2 8 JUN 2000

A Study of the Kinetics of Phase Transformations in Nb-Ti-Al Alloys

Final Report

Work Performed Under

Grant No.: F49620-95-1-0487

Submitted By

Vijay K. Vasudevan, Principle Investigator,
Keith J. Leonard and Joseph C. Mishurda,
Dept. of Materials Science and Engineering, University of Cincinnati,
Cincinnati, OH 45221-0012

To

Dr. Spencer Wu
Air Force Office of Scientific Research/NA
110 Duncan Avenue, Suite B115, Bolling AFB, Washington, D.C. 20332-0001

June 19, 2000

Abstract

The work reported herein was performed by two Ph.D. students Keith J. Leonard and Joseph C. Mishurda, under the supervision of the PI. The phase equilibria and solid state transformations within fifteen Nb-rich Nb-Ti-Al alloys were investigated. The alloys ranged in composition between 15 and 40 at.% Al with Nb:Ti ratios of 1:1.5 to 4:1. Examination of the as-cast microstructures revealed that all alloys solidified from the β phase field, with subsequent solid-state transformations occurring within four of the alloys during cooling. The range of primary β phase solidification was determined to extend beyond the limits of previous liquidus projections. The high temperature β phase field was verified in each alloy through quenching experiments. The β phase exhibited B2 ordering at room temperature with the order-disorder transition temperatures evaluated for select alloys. The site occupancy preferences within the β phase were evaluated through the ALCHEMI technique, which determined that Ti substitution occurred for Nb on Nb sublattice sites with the degree of sublattice partitioning found to depend upon alloy composition.

The phase equilibria and transformations that occurred within the alloys were explored over a complete range of temperatures, with experimental isotherms produced at 1400, 1100, 900 and 700°C, along with a plethal section between the β and σ phase fields. Formation of metastable O-Ti_2AlNb plates occurred within several of the Al lean alloys at 700°C, instead of either the δ-Nb_3Al or σ-Nb_2Al phases due to the slow diffusion growth kinetics of these phases below 900°C. The β_o to O transformation was investigated through DTA analysis, with volume diffusion ahead of the advancing precipitate found to be the rate controlling mechanism. This feature was supported by the values of n equal to values between 1.3 and 1.4, along with values of Q applicable to the diffusion limited region of the TTT diagram.

The movement of the β→δ+σ eutectoid reaction was followed through the ternary with decreasing temperatures, eventually terminating at a four-phase reaction plane near the Nb-37.5Ti-25Al composition at 980°C. The phase equilibria and microstructural control over alloys near the eutectoid transformation were evaluated. In addition, a β→δ massive transformation frequently observed in the Nb-Ti-Al system in cast materials was reproduced for the first time within furnace

and air cooled samples of Nb-25Ti-25Al following alloy homogenization.

A new phase (θ) with a body centered tetragonal structure belonging to the $I4_1/amd$ space group with lattice parameters of $\mathbf{a}_o$=5.106 Å and $\mathbf{c}_o$=28.168 Å was discovered in the 40 at.% Al alloys below 1100°C. This phase formed as lamella with the γ-TiAl phase from the β solid solution at 900 and 700°C, and was also present following treatments at 1100+900°C, 1100+700°C and within material oil quenched from elevated temperatures. No correlation existed between this phase and either the r-$TiAl_2$ phase, which also has the $I4_1/amd$ structure, or the γ1 phase, which was not observed within this work. The formation of a metastable phase with the hP18 structure through a ω-type transformation from the β_o phase was also observed instead of the $B8_2$ phase.

The high temperature phase equilibria within the 40 at.% Al alloys was also found to be very complicated, with the β phase found to transform readily into the α phase and further into α_2 or an α_2+γ lamellar structure. The degree of transformation was found to increase as Ti concentration in the alloy was decreased, with the transformation sequence dependent on the rate of cooling.

Acknowledgments

The principle investigator and supported graduate students deeply appreciate the support provided by grant # F49620-95-1-0487 from the Air Force Office of Scientific Research and of Dr. Spencer Wu, Program Monitor. The authors are also thankful to the Air Force Research Laboratory, WPAFB, Dayton, OH for providing the alloys used in this work and for the use of various facilities (arc melting, heat treatments, DTA, chemical analysis). In addition, the authors wish to thank Dr. Dennis M. Dimiduk (AFRL) for helpful discussions and assistance, Dr. Robert Wheeler (UES) for his discussion and assistance in electron microscopy, Mr. Mark Dodd (UES) for help with some of the heat treatments, Mr. Tim Shock (UES) for help with the DTA runs and Mr. Tom Kerschner (UES) for the chemical analysis of the alloys.

Table of Contents

Attached Paper:

"Examination of Solidification Pathways and the Liquidus Surface in the Nb-Ti-Al System"

1. Introduction

Since the 1980's, there has been significant research into the exploration of intermetallic alloy systems capable of operation at temperatures in excess of 1000°C as candidate materials for the replacement of Ni-based superalloys [1]. Although the main use of these materials has been associated more closely with aerospace applications, their role in land based turbines and reactors are of equal importance [2]. While the intermetallic systems are known for their exceptional strength and creep resistance at elevated temperatures, they are equally known for their brittleness at low temperatures. The Nb-Ti-Al system offers the potential for resolving problems in ductility while retaining its high temperature properties through several possible strategies, which include: ductile solid solution alloys, brittle phase reinforcement of a ductile matrix and ductile phase toughening of a brittle matrix. The development of new superalloys can be described as being an engineering design effort as much as it is a scientific one.

Alloys of the Nb-Ti-Al system, based near the Ti_3Al-Nb_3Al psuedobinary, have attracted the greatest amount of attention as potential high temperature materials. Most of the work conducted near the psuedobinary, however, has been centered on alloys with Nb concentrations less than 30 at.% [3-7]. These alloys have been extensively examined for their promising mechanical properties up to 800°C, with microstructures based on the ordered β solid solution (β_o, B2) and orthorhombic Ti_2AlNb (O, $E1_a$) phases [7]. Numerous investigations have also been conducted on Nb-rich alloys related to the phase equilibria between the β_o and Nb_3Al (δ, A15) phases [8-10], as well as the mechanical properties of these alloys [11-14]. Little experimental knowledge exists, however, on the phase transformations and equilibria at high Nb concentrations along the psuedobinary involving the β_o, δ, σ (Nb_2Al, $D8_b$) and Ti_2AlNb phases [15, 16], from which accurate determinations of the phase equilibria can be made towards the development of potential alloys.

Interest in extending the service temperatures above 800°C has also led to the investigation of alloys with higher Al concentrations, with microstructures consisting of the σ and γ-TiAl ($L1_0$) phases [17]. These duplex $\sigma+\gamma$ microstructures have been investigated for their mechanical properties up to 1000°C, in both the monolithic form [18], as well as the matrix structure for (Nb, Ti)B whisker reinforced composites [19]. The cast microstructures and phase equilibria at 1200 and 1400°C for these types of alloys have also been investigated [20-22]. The conclusions derived from these investigations, however, have resulted in conflicting interpretations as to the actual solidification pathways of these alloys. In addition, a lack of experimental evidence on the phase equilibria at temperatures above, as well as below 1200°C exists.

To better understand the structural potential of the Nb-Ti-Al alloys and the conditions under which to develop them, accurate knowledge of the solidification pathways and solid-state transformations are essential. While several phases and metastable phases involved in this system have been identified, much uncertainty lies in the stability of these structures, especially for alloys near the Nb-Al binary. The many phase transformations and crystallographic transitions found to occur in this system are not unique, in that they frequently occur in numerous other alloys systems as well. Therefore, the lessons that are learned within this system can be applied to other systems as well. The objective of this research is to expand the knowledge and understanding of the phase equilibria and phase transformations in Nb-rich Nb-Ti-Al alloys, and to provide information on the potential of these alloys for high temperature applications.

Fifteen Nb-Ti-Al alloys ranging in composition from 15 to 40 at.% Al with Nb:Ti ratios from 4:1 to 1:1.5 were investigated (Figure 1.1 and Table 1.1). All alloys were found to have solidified within the β phase field, extending the range of the solid solution phase well past the boundaries of previous liquidus projections [22]. A copy of the paper, "Examination of Solidification Pathways and the Liquidus Surface in the Nb-Ti-Al System", is included in the back of this report. Previous reports to this one have dealt with the development of the cast structures in these alloys, and therefore will not be addressed in the proceeding sections unless necessary. The following sections are divided either into specific alloy groups that share a common transformation sequence, or cover a specific topic that was examined in the course of this investigation. The three other papers which have been accepted for publication (listed in section 11) are incorporated into this report, in order to provide a better overall description of the phase equilibria and transformations occurring in this system.

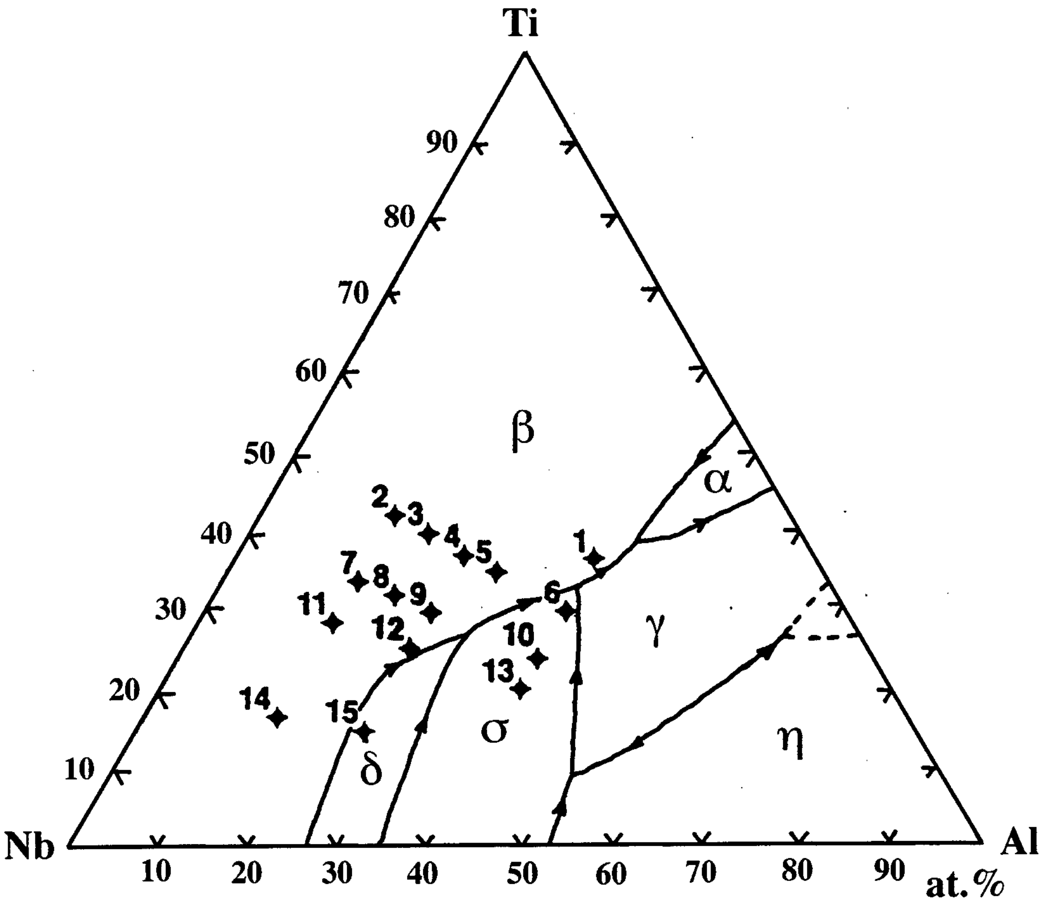

Figure 1.1 The fifteen Nb-Ti-Al alloys investigated plotted on the most recent liquidus projection [22].

Table 1.1 The nominal and actual alloy chemistries of the alloys investigated.

No.	Nominal Alloy (at.%)	Nb (at.%)	Ti (at.%)	Al (at.%)	O (wt.%)	N (wt.%)	C (wt.%)
1	Nb-36Ti-40Al	22.39	35.74	41.41	0.135	0.012	0.029
2	Nb-42.5Ti-15Al	40.78	42.58	16.06	0.129	0.016	0.044
3	Nb-40Ti-20Al	39.50	38.72	21.45	0.074	0.011	0.037
4	Nb-37.5Ti-25Al	36.45	36.92	26.50	0.026	0.010	0.020
5	Nb-35Ti-30Al	33.68	33.55	32.20	0.154	0.008	0.037
6	Nb-30Ti-40Al	29.63	29.85	40.17	0.095	0.010	0.031
7	Nb-34Ti-15Al	49.98	33.71	16.09	0.024	0.008	0.015
8	Nb-32Ti-20Al	45.75	32.04	22.01	0.037	0.012	0.023
9	Nb-30Ti-25Al	44.28	29.71	25.42	0.135	0.014	0.037
10	Nb-24Ti-40Al	34.97	24.64	40.15	0.028	0.017	0.017
11	Nb-28.3Ti-15Al	55.23	27.96	15.89	0.013	0.017	0.046
12	Nb-25Ti-25Al	49.57	24.80	25.35	0.026	0.012	0.021
13	Nb-20Ti-40Al	39.36	20.22	40.27	0.021	0.001	0.015
14	Nb-17Ti-15Al	66.68	16.66	16.09	0.077	0.015	0.020
15	Nb-15Ti-25Al	60.02	14.52	25.27	0.014	0.008	0.016

2. The High Temperature β Phase Field

2.1 β Transus Temperatures

The β transus temperatures of the fifteen alloys were determined through DTA along with quenching treatments where necessary (Figure 2.1) Of the alloys studied, DTA examination of several (alloys 7, 10, 11, 12, 13, 14, 15) was ineffective in determining the transus temperatures in addition to other high temperature reactions. For the case of alloys 7, 11 and 14, no reactions were detected due to both the slow reaction kinetics involved in the precipitation of δ from the β phase and a reduced compositional driving force of the transformation due to the relatively constant phase boundaries between β and δ with temperature. While some δ precipitation may have occurred, the fractional change was not enough to produce detectable signals. As for the other alloys (10, 12, 13, 15), the β transus temperatures were either near or well above the measurement capabilities of the DTA (~1500°C) and had to be estimated along with the afore mentioned alloys, through quenching experiments using progressively higher temperatures. The DTA thermograms, in addition to the phase equilibria involved in each alloy, will be discussed in the following sections.

Determination of the β transus temperatures allowed for both homogenization and solution treatments of the alloys in the single phase β field, with the exception of alloy 15 whose β phase field was unattainable due to furnace limitations. Water quenching from above the transus temperatures was sufficient for retaining the β phase, with only some relaxation of the lattice constants enabling a small degree of ω phase formation in certain alloys. Slower cooling rates resulted in the formation of either O, δ, α_2 or other ω-related decomposition products depending on the alloy. In all alloys, the β phase was found to order into the B2 (β_o) structure upon quenching to room temperature.

2.2 Lattice Parameters of the β/β_o Phase

The lattice parameters of the β_o phase, determined from Cohen's method based on the location of the diffracted peaks and calculated through a MATHCAD subroutine, are plotted against

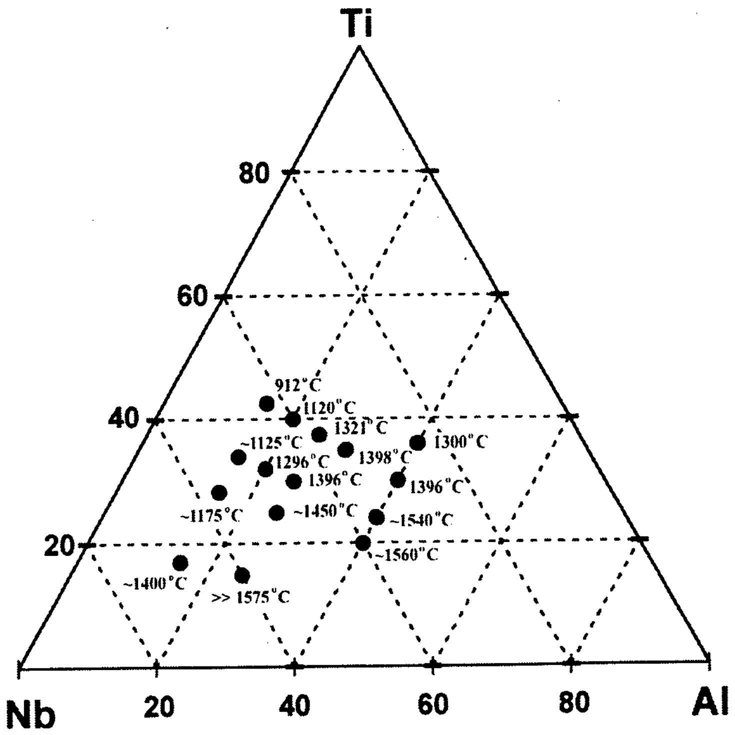

Figure 2.1 The β transus temperatures of the alloys investigated. Approximated temperatures based on quenching experiments.

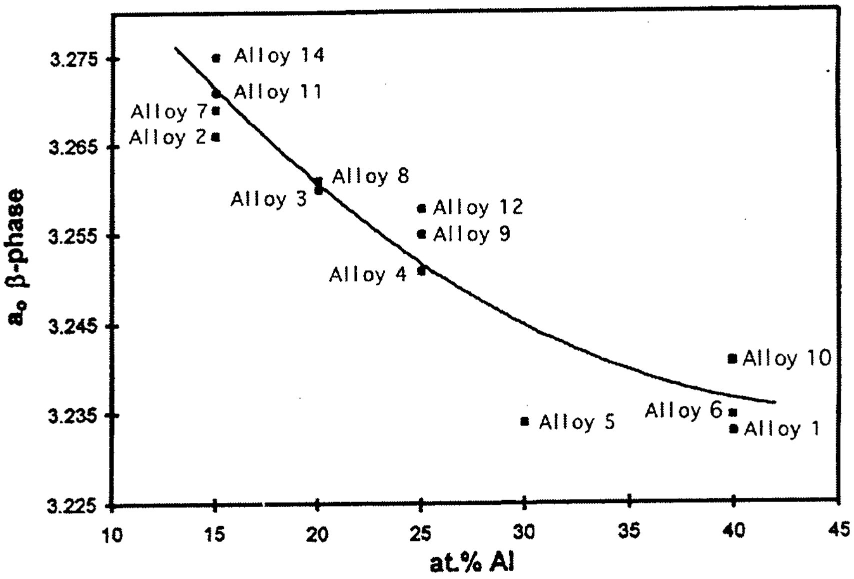

Figure 2.2 Variation of the β_o phase lattice parameter with composition.

composition in Figure 2.2. The data presented are from single phase β_o microstructures, that had been quenched from above the β transus in each alloy. A shift in the β_o lattice parameter with composition was observed, with a more significant reduction occurring with increasing Al concentration than in the decreasing Nb:Ti ratio; the latter due to the closer atomic size matching between Nb and Ti.

3. Phase Equilibria and Transformations in $\sigma + \gamma$ Alloys (1, 6, 10, 13)

3.1 Differential Thermal Analysis and Solution Treatments

The four 40 at.% alloys which were investigated were found to have solidified in the primary β phase field [23]. The high temperature β phase was determined to be retainable upon quenching with little decomposition into ω-related structures and precipitation of the α_2 phase, provided the quench rate was sufficient. The formation of α_2 needles within the β phase of alloy 1 was observed upon oil-quenching (Figure 3.1(a)). Although still being investigated, the α_2 phase appears to have formed through a martensitic reaction. The formation of α_2 was not observed in the other alloys. Alloy #'s 10 and 13 contained σ precipitation along the β grain boundaries, which was the result of quenching from 1600°C, only slightly higher than the β transus temperatures of the alloys. Furnace and sample encapsulation limitations prevented higher quench temperatures from being used.

As had been discussed in previous progress reports and compiled into a paper which has been accepted for publication, these alloys undergo a $\beta \rightarrow \sigma + \gamma$ eutectoid transformation. The eutectoid structures were most dominant within the cast material and within the samples aged at 1100°C from the metastable β_o solid solution. The decrease in the eutectoid reaction temperature with increased Ti concentration in the alloys could be tracked through the DTA thermograms of each alloy.

The DTA thermogram for alloy #1 (Nb-36Ti-40Al) is presented in Figure 3.2(a). In the DTA trace two major series of reactions on heating were detected. The first, a low temperature endothermic reaction starting at 930°C, which completes at 950°C and is followed by an exothermic peak. This reaction was only observed for the higher cooling rate (20°C/min) test. No low temperature reaction was observed on the second cycle when a slower cooling rate (10°C/min) was used, suggesting the formation of a metastable decomposition product from the β phase. The high temperature series of endothermic reactions started with an onset of 1180°C and consisted of three peaks at 1211, 1272 and 1300°C. These values changed little (~3°C) on decreasing the heating rate

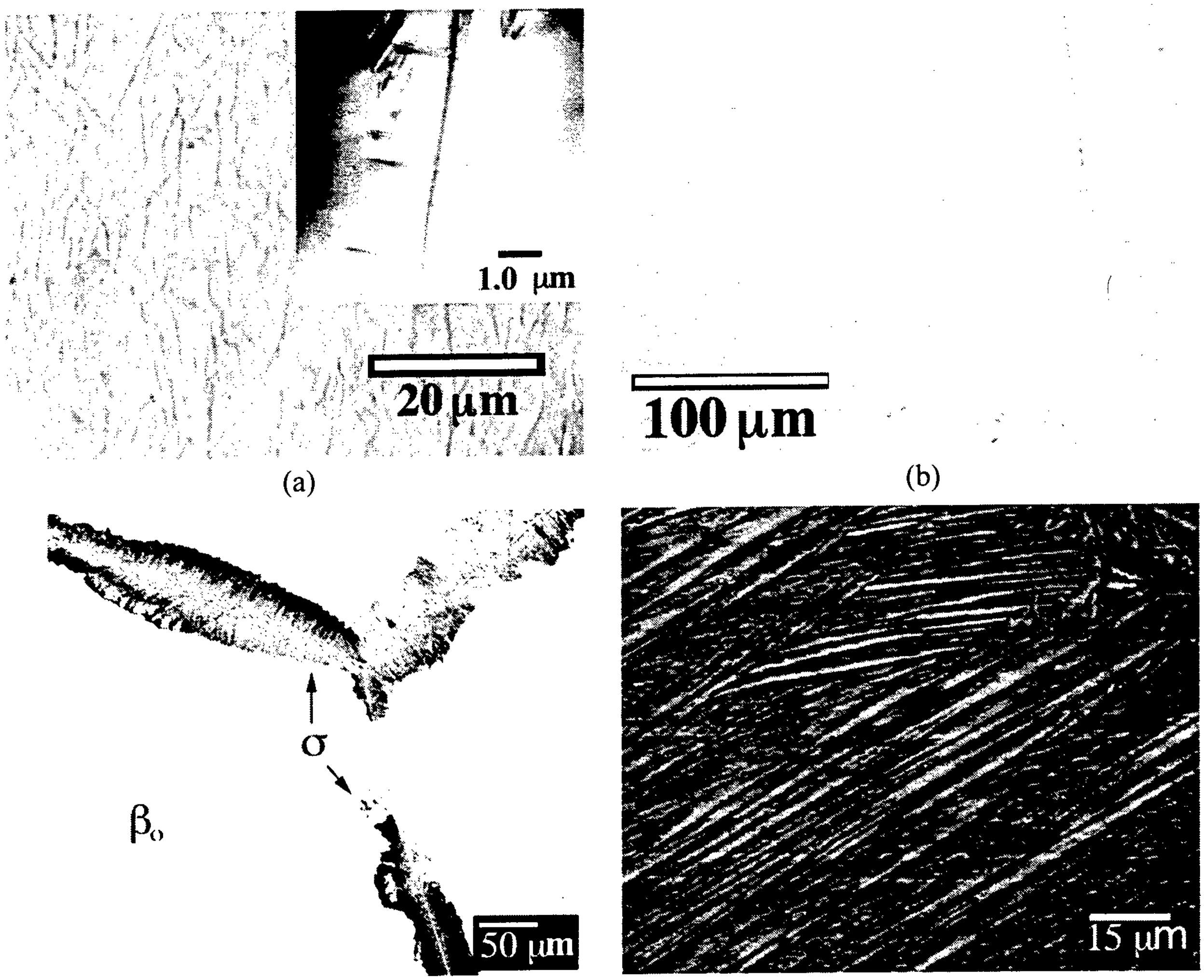

(a) (b)

(c) (d)

Figure 3.1 Solution Treated 40 at.% alloys. (a) OM of alloy 1 oil quenched from 1475°C with TEM BF-insert showing α_2 needles, (b) OM of alloy 6 oil quenched from 1475°C, (c) OM of alloy 10 water quenched from 1575C, and (d) BSE-image of alloy 13 water quenched from 1575°C.

from 15 to 5°C/min. Based on these results, the heat treatment temperatures were selected (arrows in Figure 3.2(a)) and are listed together with X-ray and EPMA results in Table 3.1.

The DTA thermogram for alloy #6 (Nb-30Ti-40Al) is presented in Figure 3.2(b). Two major transformations were observed in the DTA thermogram. The first, is a strong endothermic peak starting at 1258°C (5°C/min) and completing at 1311°C, followed immediately by a second endothermic peak which completes the transformation at 1396°C. Based on these results the heat

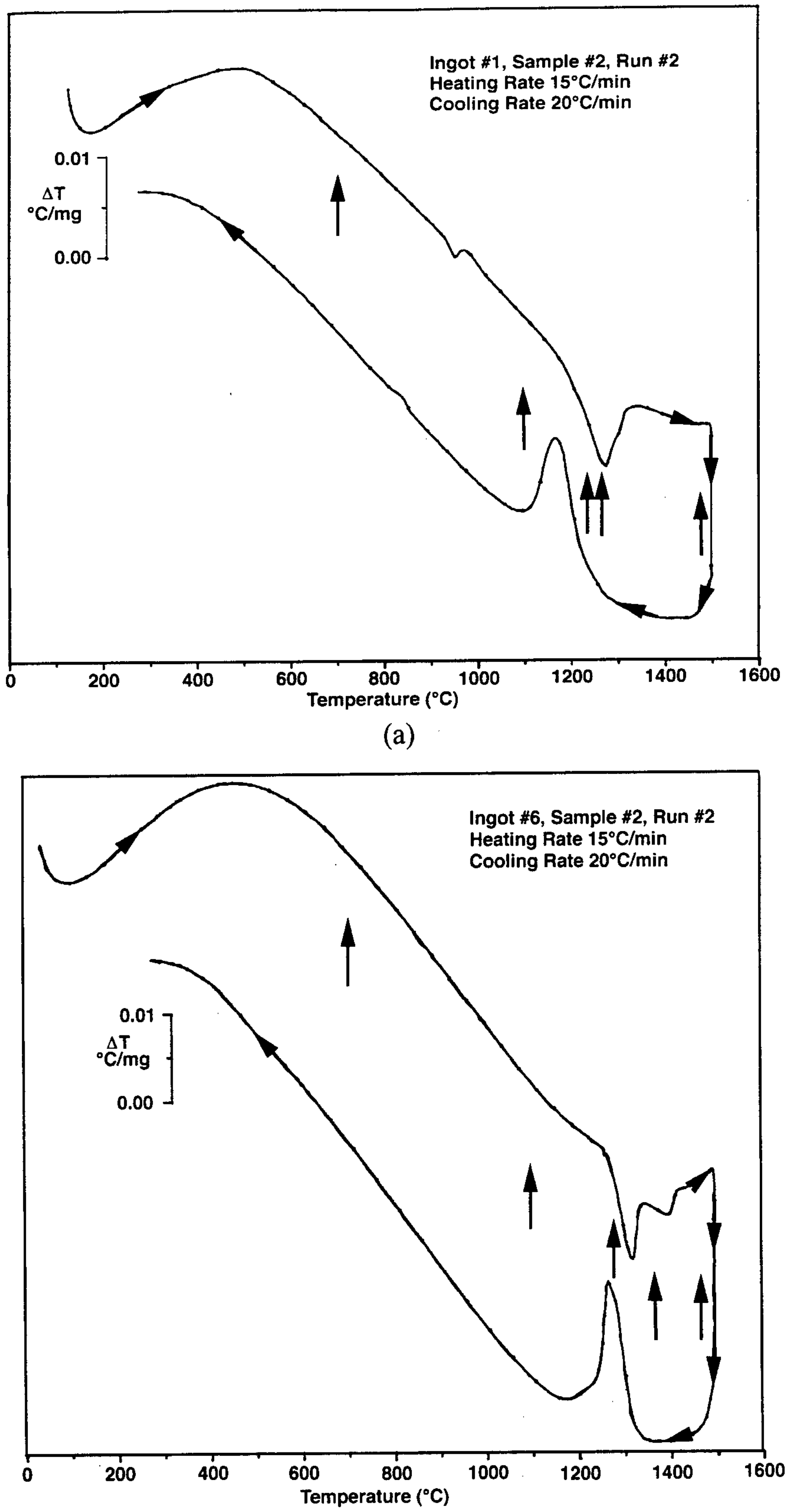

(a)

(b)

Figure 3.2 DTA thermograms of (a) alloy 1, (b) alloy 6, (c) alloy 10, and (d) alloy 13.

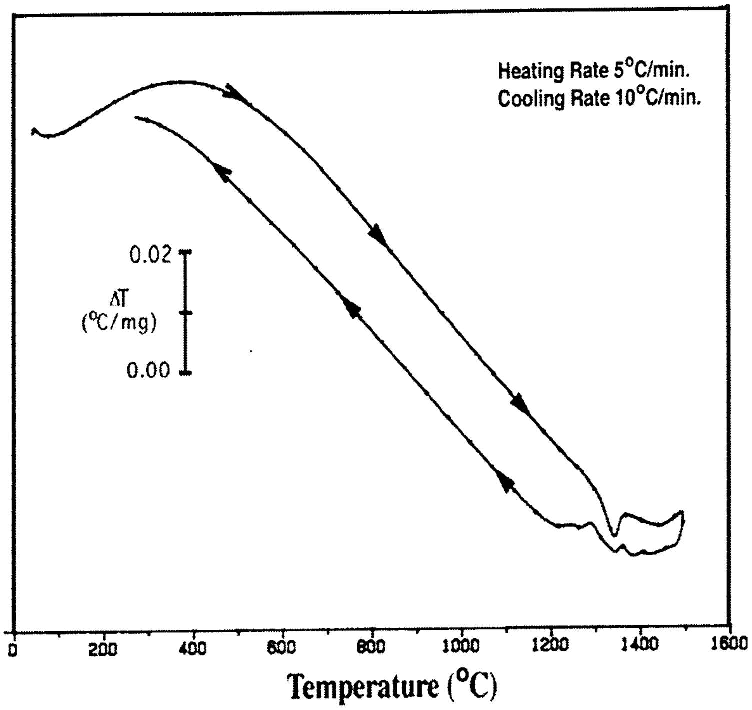

Heating Rate 5°C/min.
Cooling Rate 10°C/min.
0.02
ΔT
(°C/mg)
0.00
0
200
400
600
800
1000
1200
1400
1600
Temperature (°C)

(c)

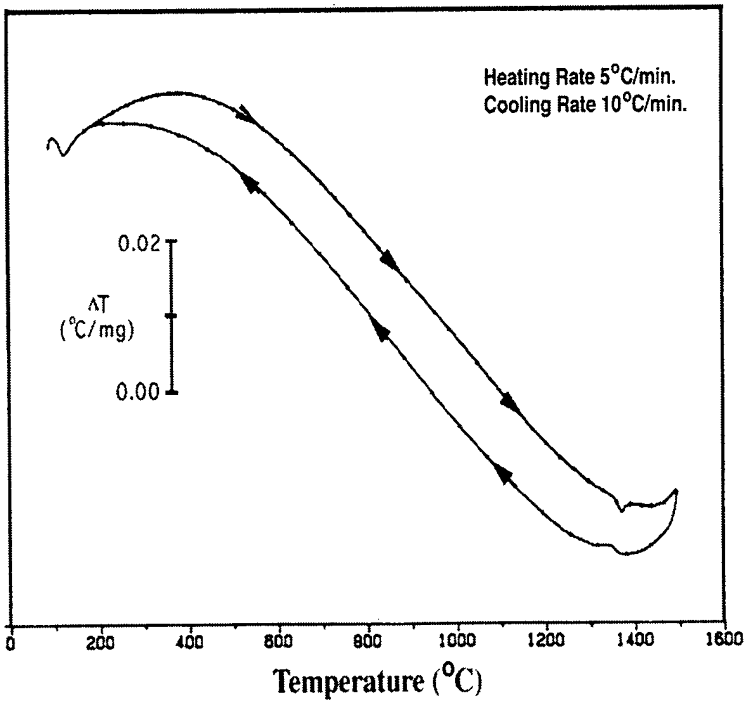

Heating Rate 5°C/min.
Cooling Rate 10°C/min.
0.02
ΔT
(°C/mg)
0.00
0
200
400
600
800
1000
1200
1400
1600
Temperature (°C)

(d)

Table 3.1 Selected Heat Treatments and Results of EPMA and X-Ray Analysis of Alloy #1

Heat Treatment	BSEI Contrast	Composition (at.%)				X-ray Results
		Ti	Al	Nb	Phase	Lattice Parameter
1475°C/6h/OQ	Grey	36.43	39.89	23.67	β	$a_o = 3.232 \pm 0.003$Å
1475°C/6h/OQ + 1268°C/32h/WQ	Grey (Matrix)	37.86	40.71	21.43	β	$a_o = 3.222 \pm 0.002$Å
	Bright	27.35	38.23	34.42	σ	$a_o = 9.909 \pm 0.010$Å $c_o = 5.138 \pm 0.005$Å
	Dark	35.15	46.97	17.88	γ	
1475°C/6h/OQ + 1248°C/32h/WQ	Grey (Matrix)	39.87	39.82	20.31	β	$a_o = 3.230 \pm 0.002$Å
	Bright	28.79	37.70	33.51	σ	$a_o = 9.933 \pm 0.010$Å $c_o = 5.123 \pm 0.006$Å
	Dark	35.15	46.97	17.88	γ	
1100°C/7d/WQ	Bright	32.55	35.26	32.19	σ	$a_o = 9.952 \pm 0.013$Å $c_o = 5.156 \pm 0.008$Å
	Grey	40.67	45.29	14.04	γ	$a_o = 4.003 \pm 0.028$Å $c_o = 4.070 \pm 0.030$Å
1475°C/6h/OQ + 700°C/30d/WQ	Grey	Structure Too Fine			hP18	$a_o = 4.608 \pm 0.003$Å $c_o = 5.494 \pm 0.008$Å
					γ	
HIP 1475°C/6h + 1475°C/3h/OQ + 700°C/150d/WQ	Grey	Structure Too Fine			hP18	$a_o = 4.600 \pm 0.003$Å $c_o = 5.490 \pm 0.001$Å
					γ	$a_o = 4.010 \pm 0.005$Å $c_o = 4.096 \pm 0.010$Å
					θ	$a_o = 5.100 \pm 0.009$Å $c_o = 28.123 \pm 0.070$Å
1100°C/7d/WQ + 700°C/30d/WQ	Bright	32.93	35.70	31.37	σ	$a_o = 9.948 \pm 0.007$Å $c_o = 5.149 \pm 0.005$Å
	Grey	41.26	45.40	13.35	γ	$a_o = 3.990 \pm 0.018$Å $c_o = 4.044 \pm 0.017$Å

Table 3.2 Selected Heat Treatments and Results of EPMA and X-Ray Analysis for Alloy #6

Heat Treatment	BSEI Contrast	Composition (at.%)				X-ray Results
		Ti	Al	Nb	Phase	Lattice Parameter
1475°C/6h/OQ	Grey	30.30	39.79	29.91	β	a_o = 3.232±0.003Å
1475°C/6h/OQ + 1360°C/14h/OQ	Grey (Matrix)	32.59	39.88	27.53	β	a_o = 3.250±0.001Å
	Bright	22.56	37.83	39.61	σ	a_o = 9.931±0.004Å c_o = 5.144±0.002Å
Repeated Measurement	Grey (Matrix)	33.01	40.12	26.86	β	
	Bright	22.88	38.03	39.09	σ	
1475°C/6h/OQ + 1285°C/32h/WQ	Grey (Matrix)	36.44	40.96	22.59	β	a_o = 3.250Å (211)
	Bright	25.89	38.35	35.76	σ	a_o = 9.920±0.003Å c_o = 5.146±0.002Å
	Dark	33.45	47.61	18.94	γ	a_o = 3.95Å (220) c_o = 4.08Å(220&202)
1100°C/7d/WQ	Grey (Matrix)	35.45	46.64	17.91	γ	a_o = 4.047±0.056Å c_o = 4.111±0.049Å
	Bright	26.26	36.70	37.05	σ	a_o = 9.922±0.006Å c_o = 5.148±0.004Å
1475°C/6h/OQ + 700°C/30d/WQ	Grey	Structure Too Fine			hP18	a_o = 4.615±0.004Å c_o = 5.486±0.009Å
					γ	a_o = 4.000±0.004Å c_o = 4.123±0.009Å
					θ	a_o = 5.108±0.004Å c_o = 28.136±0.032Å
1475°C/6h + 1475°C/3h/OQ + 700°C/150d/WQ	Grey	Structure Too Fine			θ	a_o = 5.114±0.005Å c_o = 28.161±0.040Å
					γ	a_o = 4.004±0.004Å c_o = 4.112±0.007Å
					hP18	Present
1100°C/7d/WQ + 700°C/30d/WQ	Grey (Matrix)	36.75	47.51	15.74	γ	a_o = 4.038±0.055Å c_o = 4.113±0.049Å
	Bright	25.54	35.76	38.70	σ	a_o = 9.915±0.007Å c_o = 5.145±0.005Å

Table 3.3 The phases present following isothermal treatments, their compositions and lattice parameters based on XRD for Nb-24Ti-40Al.

Heat Treatment	Phases	Composition (at.%)	Lattice Parameters (Å)
1475°C, 24hr., OQ*	γ	23.12Nb-28.38Ti-48.50Al	N/D*
	α_2	21.90Nb-36.99Ti-41.11Al	a_o = 5.643±0.01 c_o = 4.929±0.006
	σ	44.78Nb-18.44Ti-36.78Al	a_o = 9.899±0.003 c_o = 4.929±0.01
1475°C, 2hr., IBQ	α_2	25.09Nb-33.79Ti-41.12Al	a_o = 5.84±0.01 c_o = 4.652±0.004
	σ	50.92Nb-17.23Ti-31.85Al	a_o = 9.906±0.004 c_o = 5.162±0.01
1340°C, 24hr., OQ	γ	19.58Nb-30.59Ti-49.83Al	a_o = 4.011±0.01 c_o = 4.0875±0.01
	α_2	28.17Nb-34.71Ti-37.12Al	a_o = 5.776±0.006 c_o = 4.543±0.002
	σ	49.12Nb-20.97Ti-29.91Al	a_o = 9.977±0.003 c_o = 5.101±0.02
1100°C, 360hr., WQ	γ	18.94Nb-33.11Ti-47.95Al	a_o = 3.980±0.004 c_o = 4.073±0.01
	σ	44.97Nb-19.17Ti-35.86Al	a_o = 9.915±0.01 c_o = 5.165±0.03
900°C, 720hr., WQ	θ	4.51Nb-21.41Ti-35.08Al	a_o = 5.102±0.01 c_o = 28.159±0.01
	γ	18.27Nb-35.57Ti-48.16Al	a_o = 3.842±0.01 c_o = 4.077±0.01
700°C, 1080hr., WQ	θ	45.84Nb-22.98Ti-31.18Al	a_o = 5.106±0.01 c_o = 28.168±0.01
	hP18	41.76Nb-22.52Ti-35.72Al	N/D
	γ	28.60Nb-27.06Ti-44.34Al	a_o = 3.796±0.007 c_o = 4.091±0.01
1100°C, 360hr., WQ + 900°C, 720hr., WQ	θ	47.01Nb-24.46Ti-28.53Al	N/D
	σ	49.21Nb-17.85Ti-32.94Al	a_o = 9.916±0.005 c_o = 5.166±0.01
	γ	19.50Nb-30.93Ti-49.57Al	a_o = 3.976±0.01 c_o = 4.079±0.003
1100°C, 360hr., WQ + 700°C, 720hr., WQ	θ	47.12Nb-24.35Ti-28.53Al	N/D
	σ	46.19Nb-19.58Ti-34.23Al	a_o = 9.929±0.02 c_o = 5.164±0.003
	γ	19.66Nb-30.53Ti-49.81Al	a_o = 3.989±0.01 c_o = 4.118±0.03

*Also contained θ, unable to obtain accurate composition measurement

**N/D: not enough data from XRD scan to accurately determine lattice parameters treatment temperatures were selected (arrows in Figure 3.2(b)) and are listed together with X-ray and EMPA results in Table 3.2.

Differential thermal analysis of alloys 10 (Nb-24Ti-40Al) and 13 (Nb-20Ti-40Al) had detected a series of reactions occurring between 1250 and 1400°C within alloy 10, and corresponding reaction in alloy 13 between 1275 and 1450°C (Figure 3.2(c,a)). The reactions appear to occur with a greater change in energy within alloy 10 than in the lower Ti concentration of alloy 13. The main peaks in the thermograms were determined to have been associated with the $\beta \rightarrow \sigma + \gamma$ eutectoid reaction, with the smaller peaks resulting from the subsequent decomposition of the β phase which occurred on cooling.

Both alloy 10 and 13 showed large amounts of microcracking within the ingots. The microcracks did heal to some extent during homogenization; however, the amount of cracking became worse after each additional heat treatment. While there was only a nominal 4 at.% Ti difference between the two alloys, the degree of cracking within alloy 13 was much more severe. Because of the large presence of cracking within the alloy 13, TEM foils could not be prepared. The excessive cracking of the alloy also created problems in oxidation, allowing oxygen to penetrate to the center of the heat treated samples, instead of only at the sample surfaces. In addition, due to furnace capabilities, only alloys 1, 6 and 10 could be effectively solution treated. Due to these reasons, the 20Ti alloy was not examined further.

3.2 Phase Equilibria Below the β Transus

To determine the reason for the appearance of α_2 within the cast microstructure of alloy #10 and to evaluate the phase transformations recorded in the DTA scan, heat treatments were conducted within the $\beta + \sigma$ and $\beta + \sigma + \gamma$ phase fields for alloy #'s 1, 6 and 10 (Tables 3.1 through 3.3). The range of temperatures over which the $\beta + \sigma$ and $\beta + \sigma + \gamma$ phase fields were confirmed as occurring for each alloy is listed in Table 3.4. The movement of the $\beta \rightarrow \sigma + \gamma$ eutectoid reaction with decreasing temperature in the ternary diagram is shown in Figure 3.3 as eventually passing through alloy #1 at 1183°C. Heat treatmented microstructures of samples within the $\beta + \sigma$ phase

Table 3.4 Transformation temperatures from DTA analysisand heat treatments of alloys 1, 6, 10 and 13.

Alloy	Exits $\gamma+\sigma$ Field and Enters $\beta+\gamma+\sigma$	Exits $\beta+\gamma+\sigma$ and Enters $\beta+\sigma$	Exits $\beta+\sigma$ and enters β
1	1183°C	1270°C	1300°C
6	1258°C	1311°C	1396°C
10	1310°C	1430°C	~1540°C
13	1340°C	1460°C	~1565°C

field for each alloy were in some ways similar, in that on cooling from this phase field decomposition of the β_o phase occurred. The amount and type of transformation was, however, dependent on the alloy and rate of cooling.

Oil quenching alloy #6 from 1360°C, (Figure 3.3) produced a needle-like precipitation within the β phase of α_2. Similar results were also observed when alloy 6 was water quenched from the $\beta + \sigma + \gamma$ phase field at 1285°C (Figure 3.4). This also occurred in alloy #1 when water quenched from 1268 and 1248°C in the $\beta + \sigma + \gamma$ phase field (Figure 3.5). These results showed that the decomposition still occurred when the volume of β within the three-phase field is reduced. The amount of α_2 in each alloy, however, was not enough to produce measurable peaks in the XRD pattern (Figure 3.6).

The $\beta + \sigma$ and $\beta + \sigma + \gamma$ phase fields were investigated in alloy #10 by heat treatments at 1475 and 1340°C respectively, followed by both oil and iced-brine quenching from each temperature (Table 3.3). The 1475°C samples were observed through SEM analysis to contain large proeutectoid σ grains surrounded by a transformed structure (Figure 3.7). TEM analysis of the oil quenched material confirmed that the β phase had decomposed on oil quenching and was completely consumed, making it appear that the alloy was within the $\alpha + \sigma$ phase field at 1475°C instead of the $\beta + \sigma$ phase field (Figure 3.8). The microstructure consisted of large grains of σ separated by α grains, which had undergone a partial $\alpha \rightarrow \alpha + \gamma$ transformation during cooling

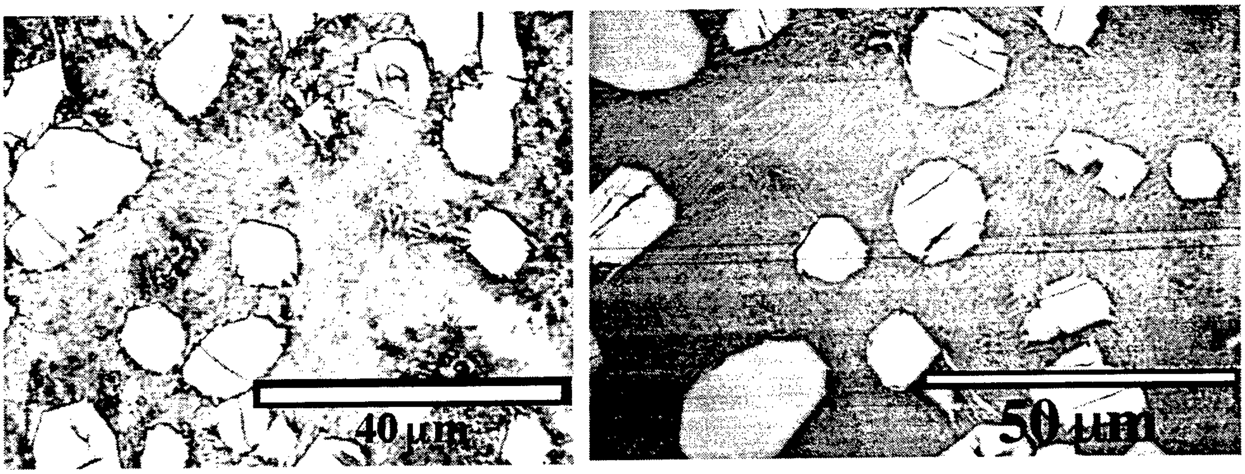

(a) (b)

Figure 3.3 Alloy #6 oil quenched from 1360°C within the $\beta + \sigma$ phase field, showing α_2 needle formation in β. (a) OM, and (b) BSE-images.

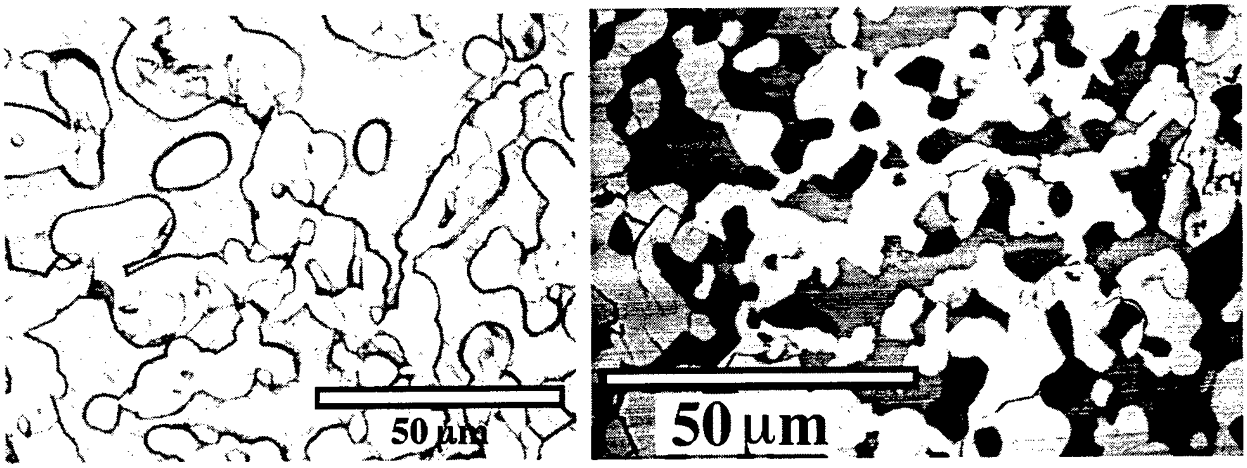

(a) (b)

Figure 3.4 Alloy #6 oil quenched from 1258°C within the $\beta + \sigma + \gamma$ phase field, showing α_2 needle formation in β. (a) OM, and (b) BSE-images.

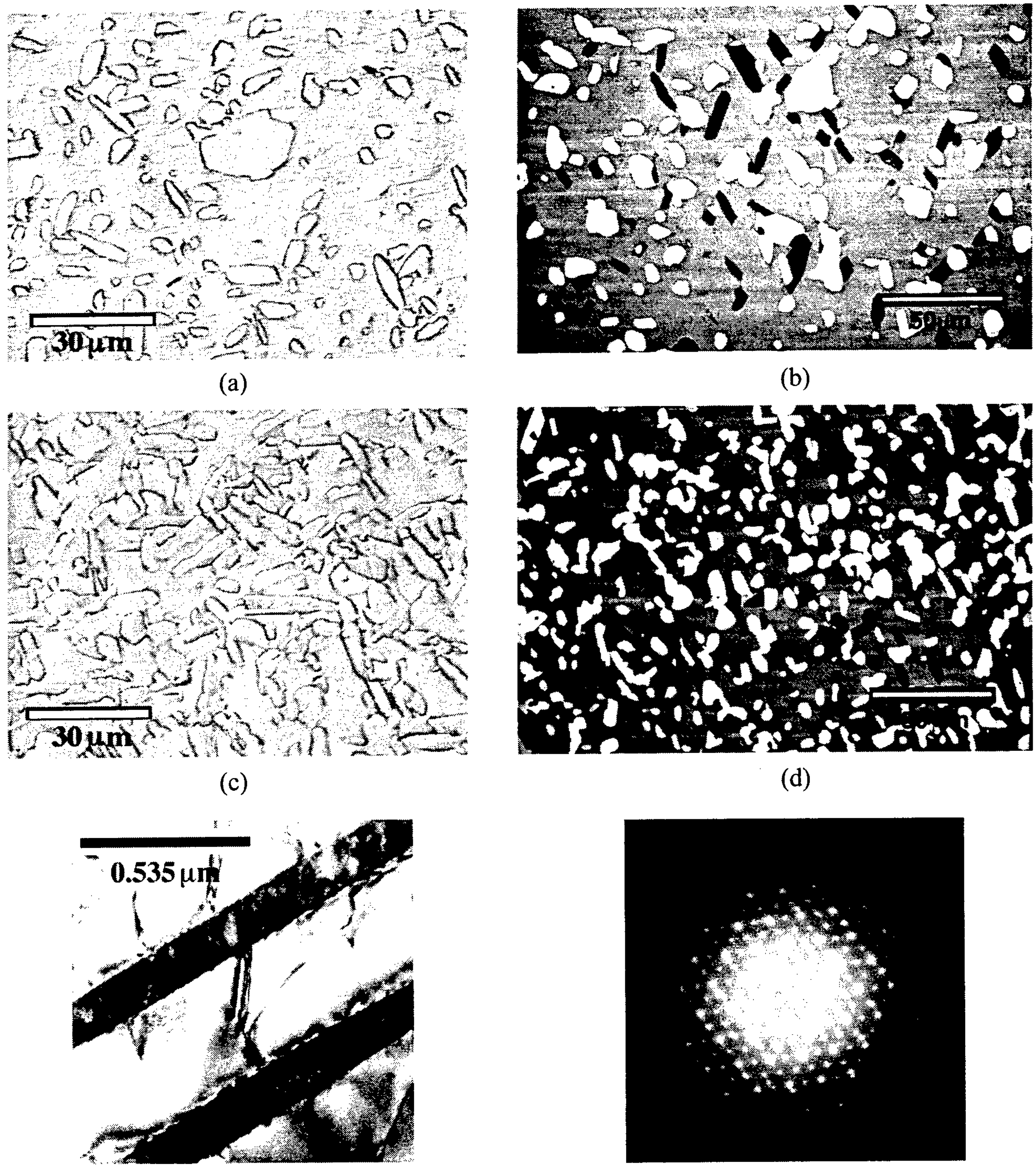

(a) (b)

(c) (d)

(e) (f)

Figure 3.5 Micrographs of alloy 1. (a) OM and (b) BSE-images of material oil quenched from the upper part of the $\beta + \sigma + \gamma$ phase field at 1268°C, (c) OM and (d) BSE-images of material quenched from the lower part of the $\beta + \sigma + \gamma$ phase field at 1248°C, (e) BF-image of α_2 needles in β, and (f) $\alpha_2[0001]$ SAD pattern.

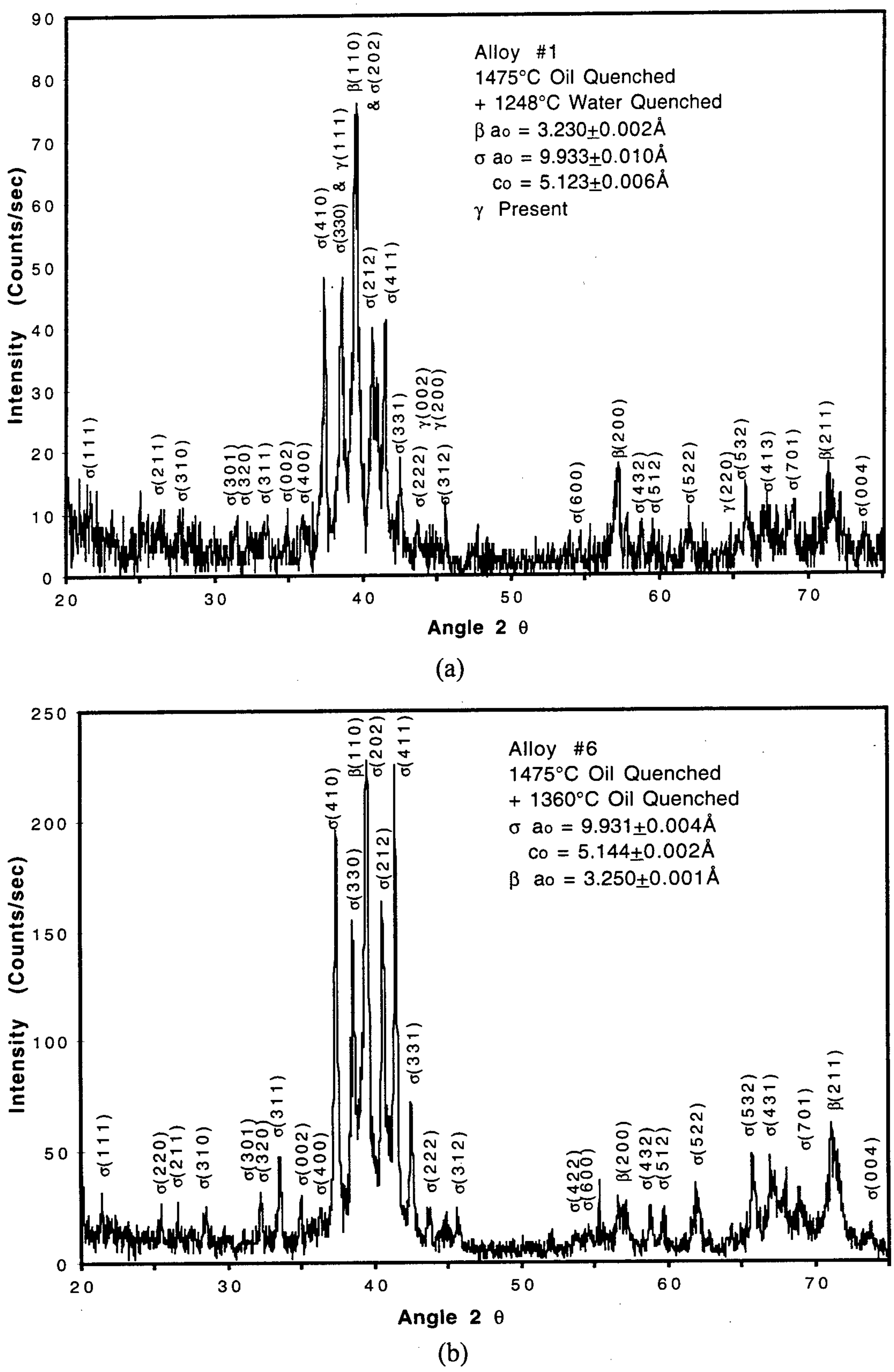

Figure 3.6 XRD patterns of (a) alloy 1, quenched from 1248°C, and (b) alloy 6, quenched from 1360°C

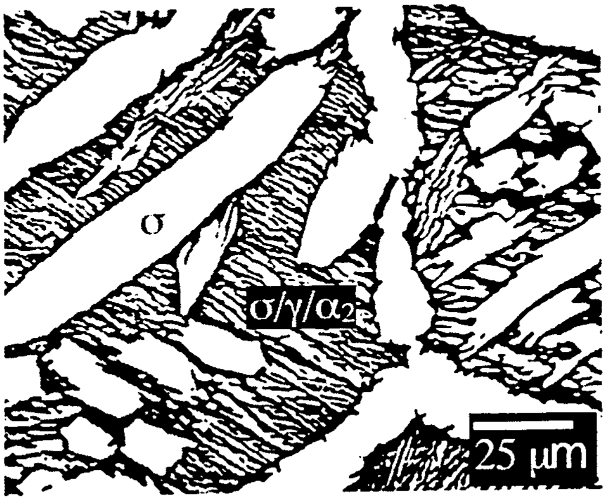

Figure 3.7 BSE-image ofalloy 10 oil quenched from 1475°C.

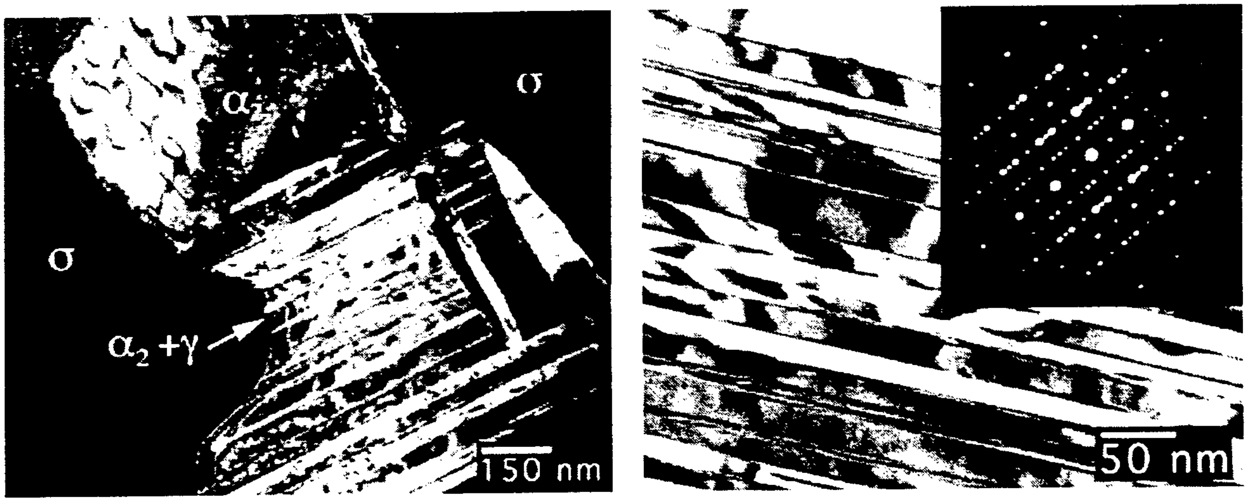

(a) (b)

Figure 3.8 Alloy 10 heat-treated at 1475°C, 48 hr., OQ: (a) DF-image of $\alpha \rightarrow \alpha+\gamma$ transformation, and (b) two-beam image, $g_\gamma=\bar{1}01$,of γ/α_2 lamella,with insert of the $\gamma[101]//\alpha_2[11\bar{2}0]$ SAD patterns.

producing twin related γ lamella oriented with their {111} planes along the basal planes of the α phase. At lower temperatures the α within the lamellae and in the untransformed portions of the grains ordered into the α_2 structure, producing an anti-phase domain structure visible under dark field conditions.

The 1475°C iced-brine quenched sample contained large σ grains with α laths that consumed the former β regions between the σ grains (Figure 3.9), the α laths having transformed into

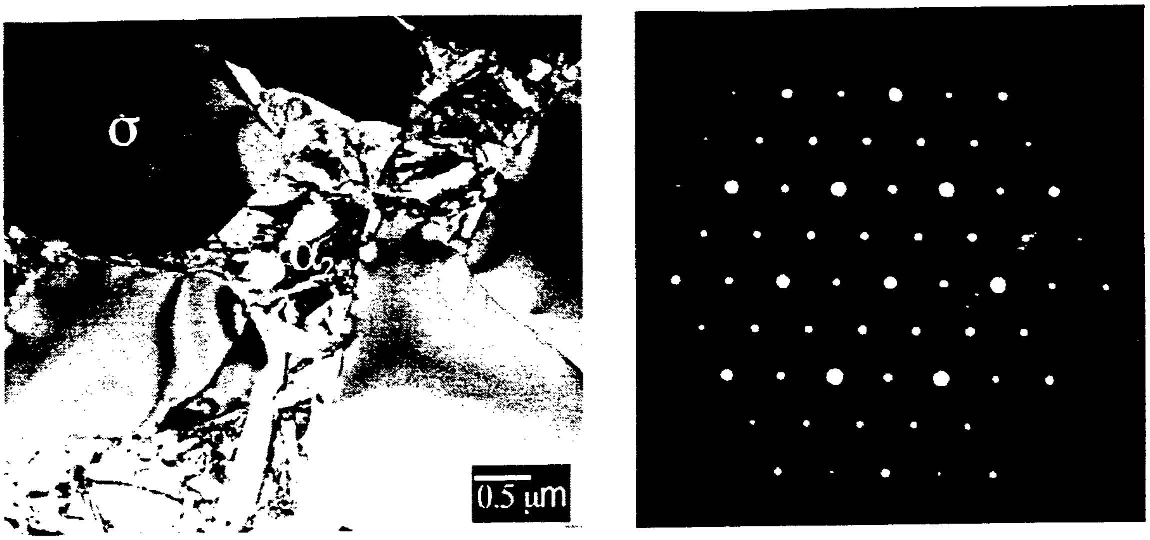

(a) (b)

Figure 3.9 Nb-24Ti-40Al aged 1475°C, 1 hr., IBQ: a) DF-image of α_2 laths between σ grains, and b) the α_2[0001] pattern.

the ordered α_2 structure upon cooling. Due to the higher rate of cooling, the α phase did not decompose into the lamellar α_2+γ structure observed in the oil quenched samples. The formation of α at 1475°C could be reasoned to have occurred as a result of a composition change within the β phase during σ nucleation and growth, shifting the composition of the β phase into the β + α phase field. Although the β + α + γ phase field is near the alloy compositions, the σ phase is not in equilibrium at any time with α_2. The formation of the α_2 phase appears instead to be the result of cooling due to β phase instabilities than actual phase equilibrium. The β to α transformation appears to be more complete the lower the Ti concentration in the alloy.

The tie-line compositions of the α/α_2, β, σ and γ phases within the two- and three-phase equilibria for all alloys are plotted in Figure 3.10. The composition of the α_2 phase in alloy 10 quenched in both oil and iced-brine had showed considerable solubility for Nb. The composition of the α_2 + γ lamellae was determined to be closer to the γ phase than that of the α_2. This correlated with X-ray and electron diffraction, in addition to DF imaging observations, which had shown that the amount of α_2 within the lamellar region was relatively small, compared with γ. The detachment

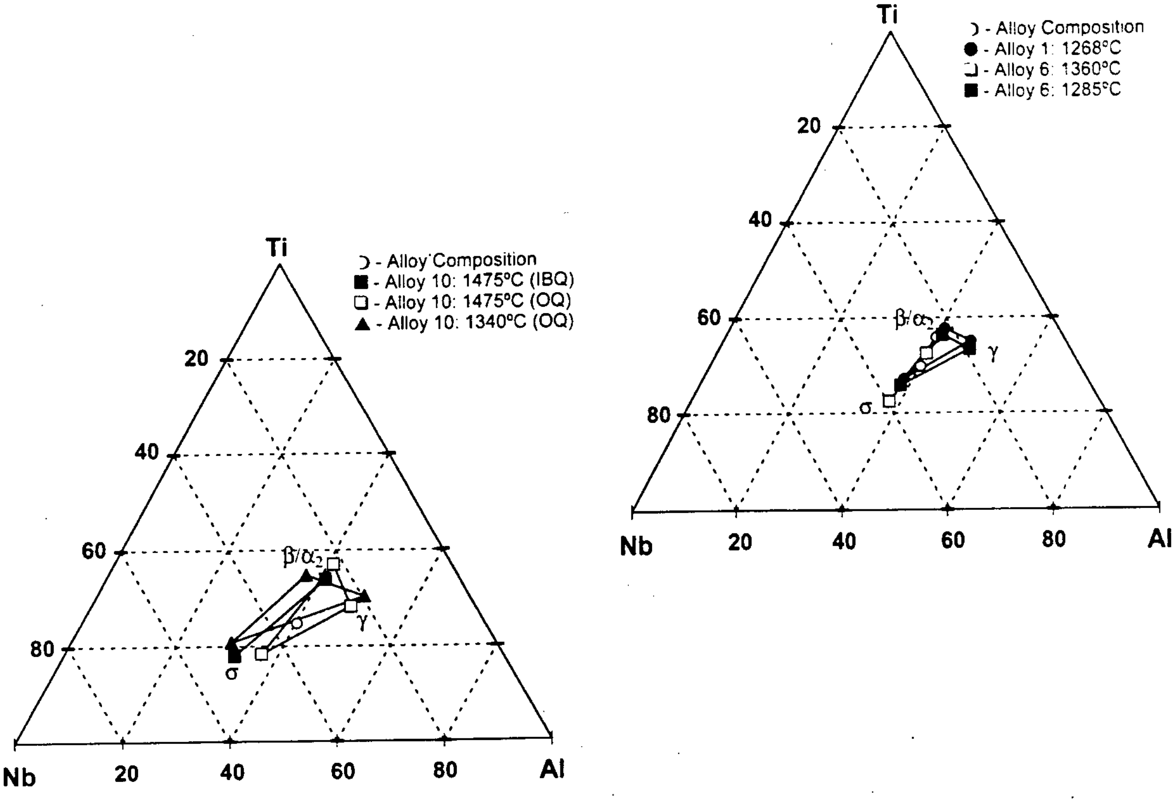

Figure 3.10 Experimental tie-lines for alloys 1, 6 and 10 within the β+σ, and β+σ+γ phase fields. β undergoes a partial to complete transformation into α/α₂ on cooling.

of the tie-line from the alloy composition in the iced-brine quenched sample, was the result of reduced aging time at 1475°C due to sample encapsulation limits.

The DTA thermogram for alloy 10 had indicated another reaction near 1340°C, which was determined through heat treatments to be due to the passage of the σ + γ + β phase field. Imaged under BSE conditions and through TEM, the oil quenched sample showed the presence of γ grains within the α_2/γ structure between the larger σ grains (Figure 3.11 and 3.12). The structure within the iced-brined quenched sample was too fine to characterize effectively. Again TEM analysis was used to accurately determine the phases present and their relationships. The oil quenched sample revealed the same α_2/γ lamellar decomposition of the α phase that had been observed in the 1475°C heat treatment (Figure 3.12). Iced-brine quenched samples also contained equiaxed grains of α_2, σ

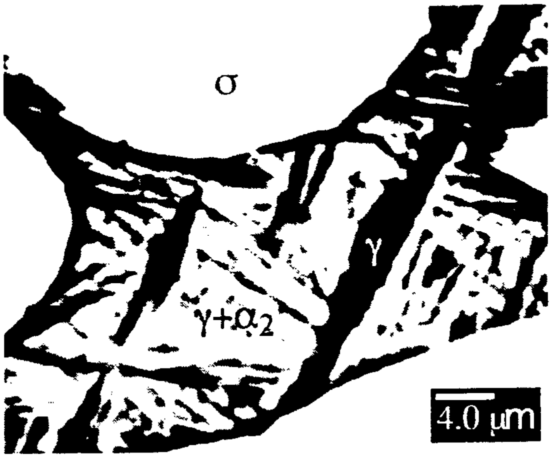

Figure 3.11 BSE-image of alloy 10 oil quenched from 1340°C.

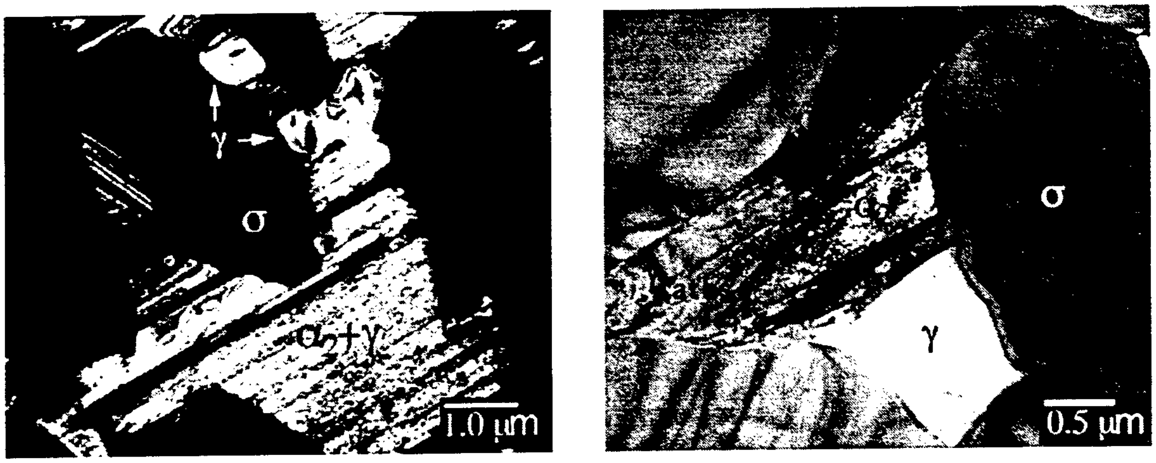

(a) (b)

Figure 3.12 TEM micrographs of alloy 10 heat treated at 1340°C: (a) DF-image of oil quenched and (b) BF-image of iced-brine quenched materal.

and some γ, but without the distinct formation of α_2/γ lamella as observed in the oil quenched samples. Some partial transformation of the α grains into γ was occasionally observed. Compositions of the phases in the oil quenched sample again showed α_2 as having substantial solubility of Nb (Figure 3.10). The composition of α_2 within the sample, however, may have been slightly skewed to higher Al concentrations than the actual values, due to electron beam interactions with neighboring γ lamella. The amount of γ, α_2 and σ that was observed in the oil quenched sample again corresponded well to the tie-line positioning.

While the formation of α_2 within the quenched microstructures occurred readily over all alloy compositions. in material that was heat treated within the high temperature phase fields and again at 1100°C; the α_2 phase disappeared with the α_2/γ lamella being replaced with {111}-type twining within the γ grains. If the formation of the α_2 phase were the result of oxygen contamination, then it would have been expected within the double-aged material as well. Chemical analysis of the heat treated material did not show any significant change in oxygen level over the homogenized material. The formation of α from β as a result of cooling, rather than a composition shift due the σ phase, is supported by the changes in γ lamellae direction observed within the oil quenched 1475 and 1340°C material (see Fig. 3.12).

3.3 A New Tetragonal Phase

In addition to the formation of the σ, γ, α/α_2 phases from the β phase at various temperatures, two other phases (θ and hP18) were observed through TEM and XRD analysis that had either not been previously reported in the Nb-Ti-Al system or fully characterized. The θ phase was present following aging treatments at 900, 700, and two-step 1100+700°C and 1100+900°C treatments (Figure 3.13). This phase was not observed within the material aged at 1100°C, where all of the 40 at.% Al alloys contained $\sigma + \gamma$ structures. The θ phase was also observed in small volumes within alloy 10 oil quenched from 1475 and 1340°C (Figure 3.14). Determination of the crystal structure, crystal point group and space group of the new phase was accomplished through XRD and analysis of the convergent beam electron diffraction patterns (CBED) and selected area diffraction patterns (SAD) from TEM (Figure 3.15).

The SAD patterns could be consistently indexed on the basis of a body-centered tetragonal structure. Through examination of symmetries observed in the CBED patterns the possible diffraction groups were deduced (Table 3.5) with the aid of existing tables [24]. From the deduced diffraction groups, the possible crystal point groups were determined and are summarized in Table 3.6. The $4mm1_R$ diffraction group identified in the [001] CBED pattern, eliminated all but the tetragonal *4/mmm* and cubic *m3m* point groups. Although the *m3m* point group does contain the $4mm1_R$ diffraction group in the <100> direction, the $2mm1_R$ symmetry identified experimentally in both the

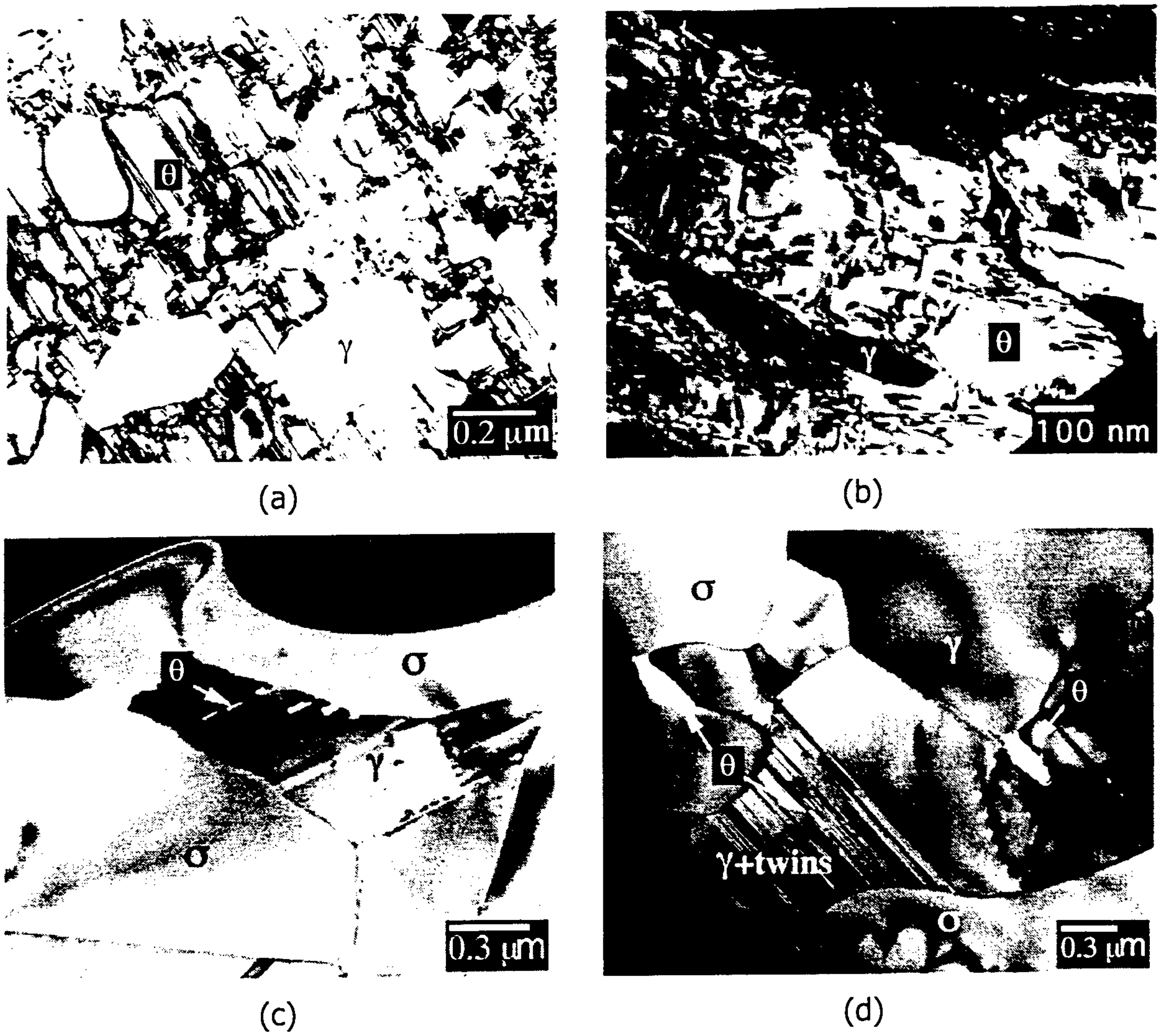

Figure 3.13 TEM micrographs showing a new tetragonal phase observed within alloy 10 aged at (a) 900°C, (b) 700°C, (c) 1100+900°C, and (d) 1100+700°C.

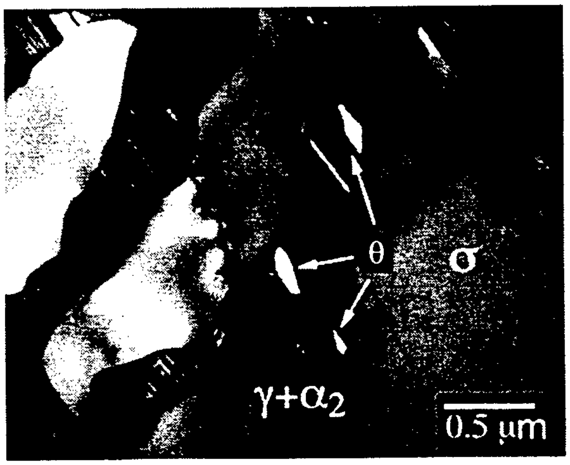

Figure 3.14 TEM DF-image of the new θ phase within alloy 10 oil quenched from 1340°C.

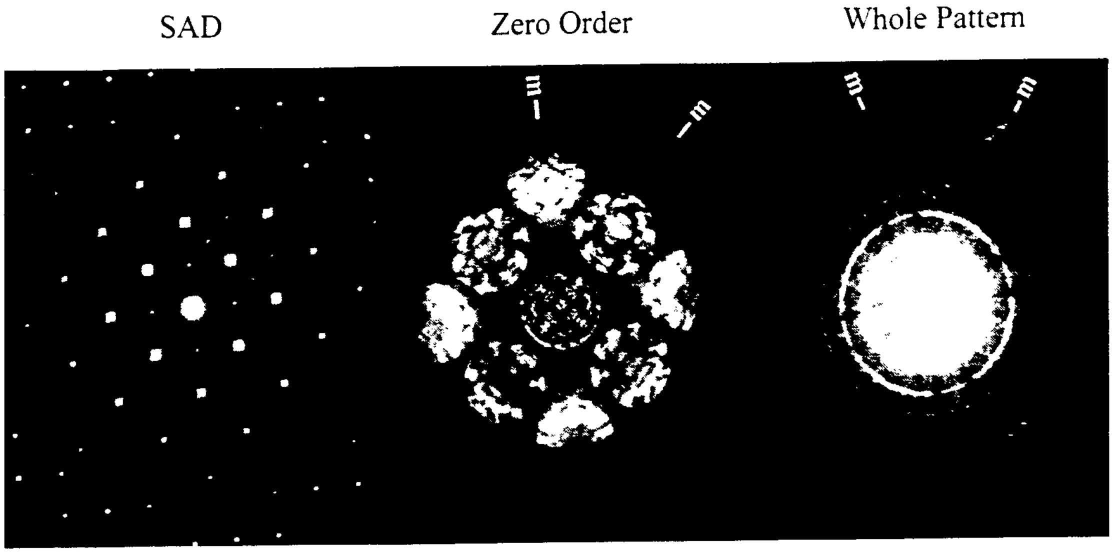

(a) [001]

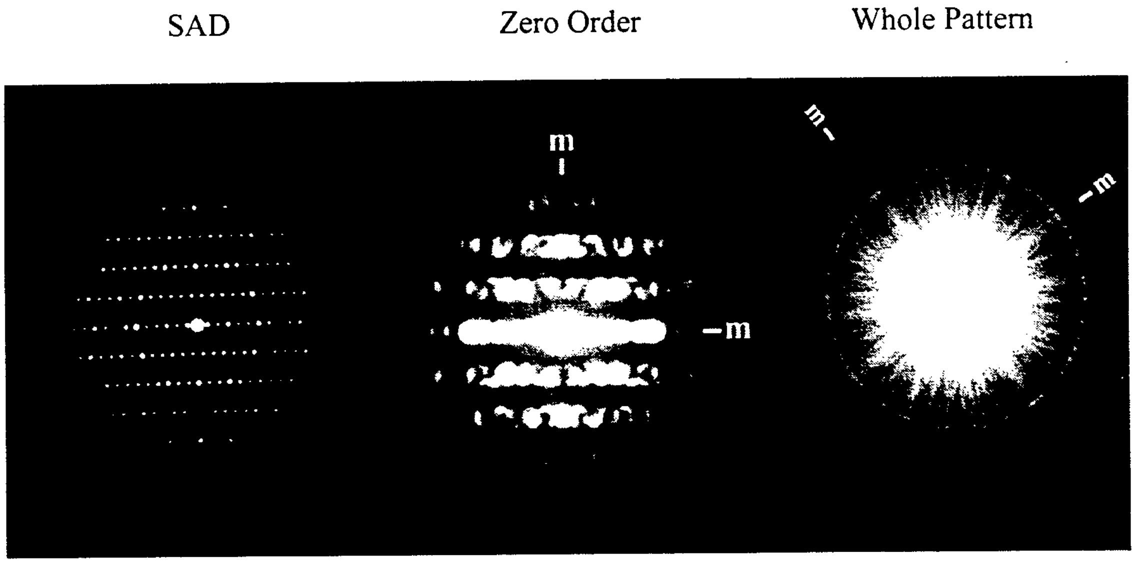

(b) [010]

Figure 3.15 Selected area diffraction, zero order and whole pattern convergent beam electron diffraction patterns of the new phase: (a) [001], (b) [010], (c) [110], (d) [101], (e) [111], (f) [120], (g) [311], (h) [331], and (i) [551]. Arrows within select whole patterns highlight features that help indicate symmetry.

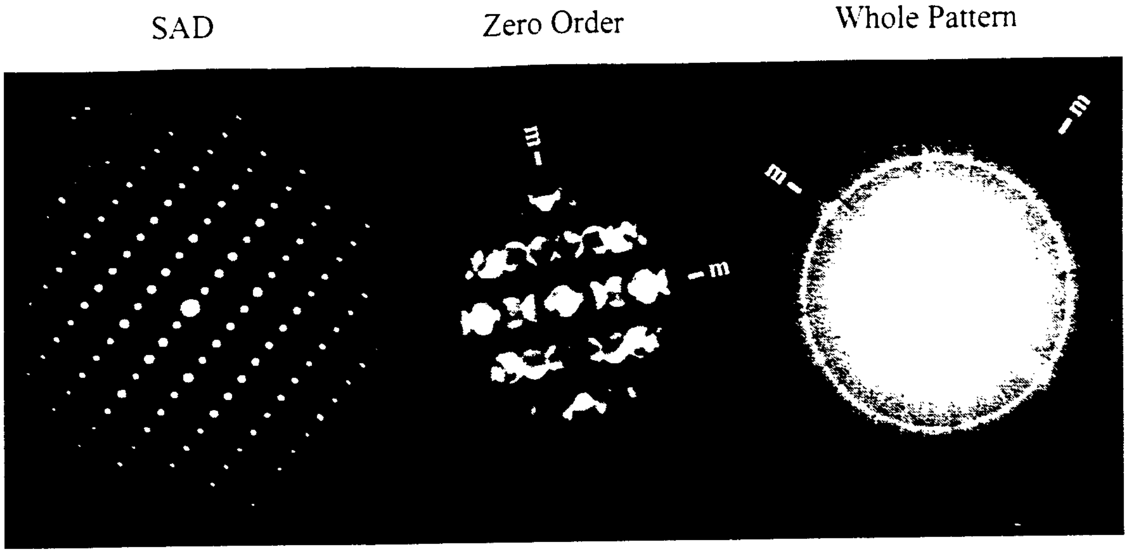

(c) [110]

(d) [101]

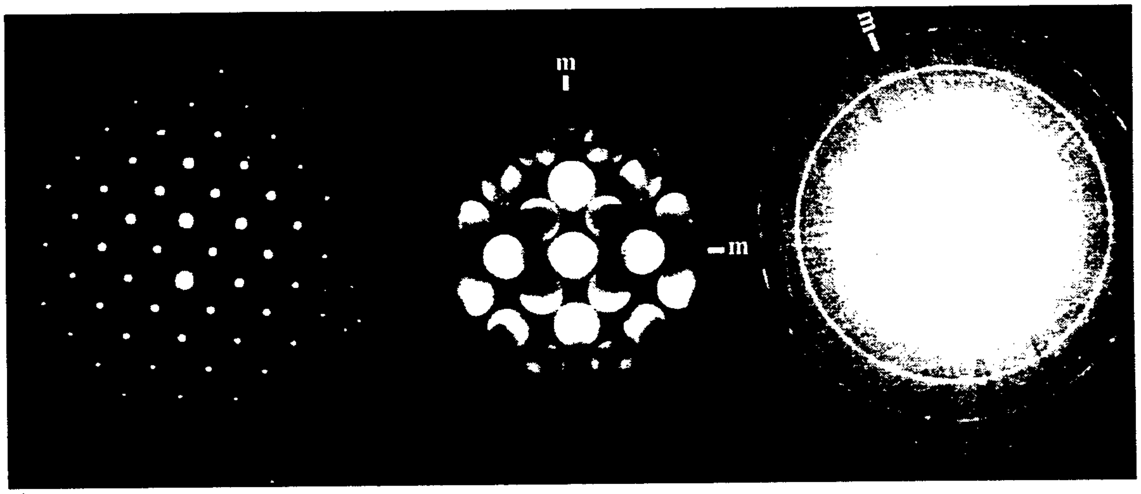

(e) [111]

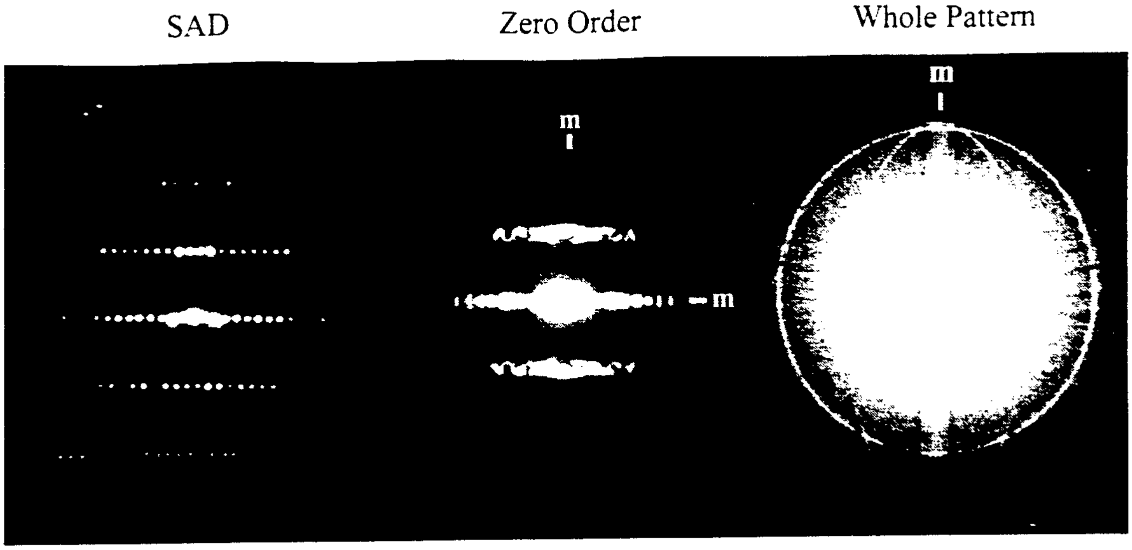

(f) [120]

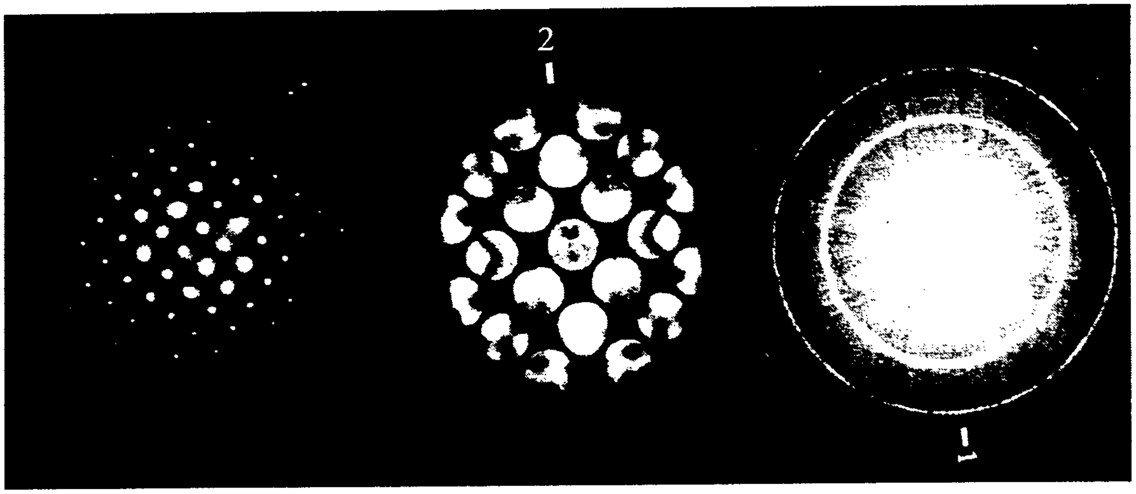

(g) [311]

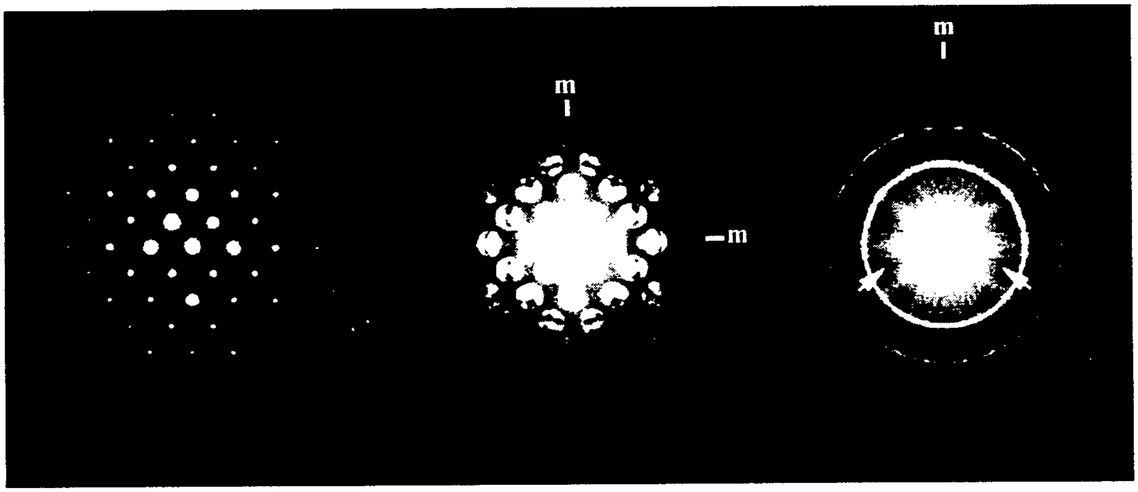

(h) [331]

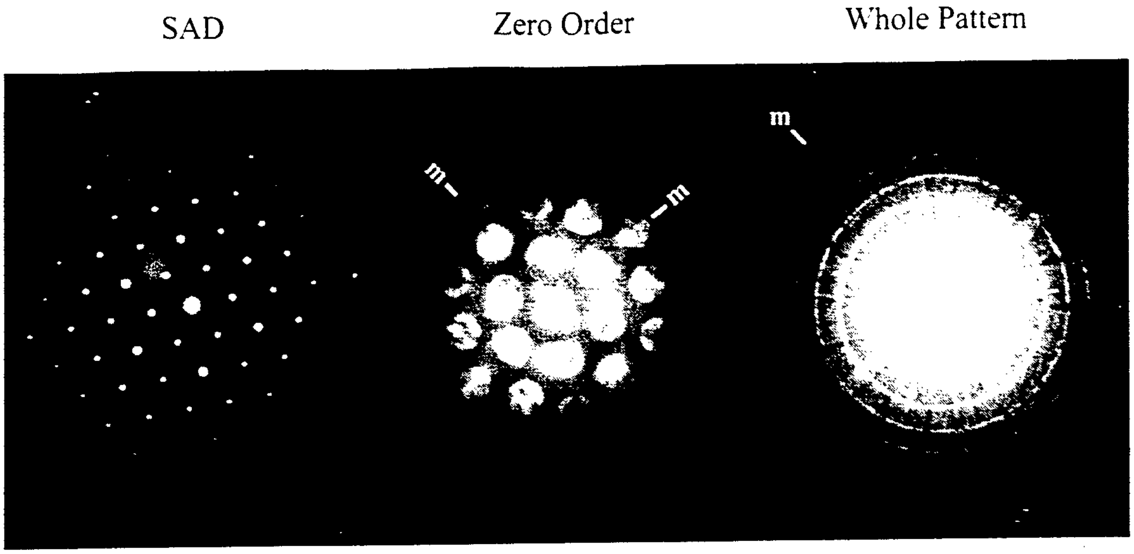
SAD Zero Order Whole Pattern

(i) [551]

TABLE 3.5 Observed Symmetries and Deduced Diffraction Groups

Zone Axis	Observed Symmetry			Deduced Diffraction Groups
	ZOLZ	Whole Pattern	BF	
[001]	4mm	4mm	4mm	4mm or $4mm1_R$
[010], [110]	2mm	2mm	—	2mm or $2mm1_R$
[311]	2	1	1	2_R
[101], [111], [120], [331]	2mm	m	m	2_Rmm_R

Table 3.6 Possible Point Groups Corresponding to the Deduced Diffraction Groups

Diffraction Groups						Possible Point Groups						
4mm						4mm						
$4mm1_R$							4/mmm					m3m
2mm			mm2						$\bar{6}m2$			
$2mm1_R$				mmm			4/mmm			6/mmm	m3	m3m
2_Rmm_R		2/m		mmm	4/m		4/mmm			6/mmm	m3	m3m
2_R	m	2/m		mmm	4/m		4/mmm	3m		6/mmm	m3	m3m

[010] and [110] patterns can only be possible if the point group is *4/mmm* tetragonal [24].

The body-centered tetragonal crystal structure of the new θ phase was confirmed through indexing of the relevant peaks in the XRD pattern (Figure 3.16), with the 2θ, interplanar spacings and {hkl}'s of these peaks being summarized in Table 3.7. The new structure followed a $h+k+\ell=even$ rule and had lattice parameters of $\mathbf{a}_0$=5.106 Å and $\mathbf{c}_0$=28.168 Å, producing (004), (101) and (103) diffracted peaks below a 2θ of 20°. The strong diffracted intensities observed for the (109), (200), (00,12) and (206) peaks in the XRD pattern correlate with the relative intensities of these reflections in the experimental SAD patterns (Figure 3.15). Within the 700°C aged material, regions of retained β_0 that have transformed into a hP18 structure were also identified in the XRD pattern. The evolution of the hP18 phase, a metastable ω-related transition of the β_0 phase beyond the ω'' structure, will be addressed in the next section. Diffraction intensities observed at low angles, however, distinguished the new phase apart from the hP18 and γ structures.

The space group of the new θ phase was identified with the aid of the International Tables for Crystallography [25], by comparing the possible reflection conditions based on calculated structure factors to those reflections observed in the experimental SAD and XRD patterns. The missing (001) and (002) reflections in both SAD and XRD patterns provided the rule $\ell=4n$ for (00ℓ), eliminating all but the $I4_1/acd$ and $I4_1/amd$ structures from the possible space groups that belong to the *4/mmm* point group. The (002) reflections, though present in the [010] and [120] zone axis patterns (Figure 4.15), were determined to have been produced from double diffraction of the (101) and $(\bar{1}01)$ reflections in [010], and the $(2\bar{1}1)$ and $(\bar{2}11)$ reflections in [120]. To determine whether the crystal had the $I4_1/acd$ or $I4_1/amd$ space group, the general rules for diffraction for each structure were further examined (Tables 3.8 and 3.9). Based on the indexed XRD and SAD patterns, it was determined that the $I4_1/acd$ space group violated too many rules, including those that could not be explained simultaneously by double diffraction events. Therefore, the correct space group of this body-centered tetragonal crystal is $I4_1/amd$, with space group number 141 and Schoenflies symbol D^{19}_{4h}.

An orientation relationship between the new tetragonal phase and the γ phase of γ[101] //

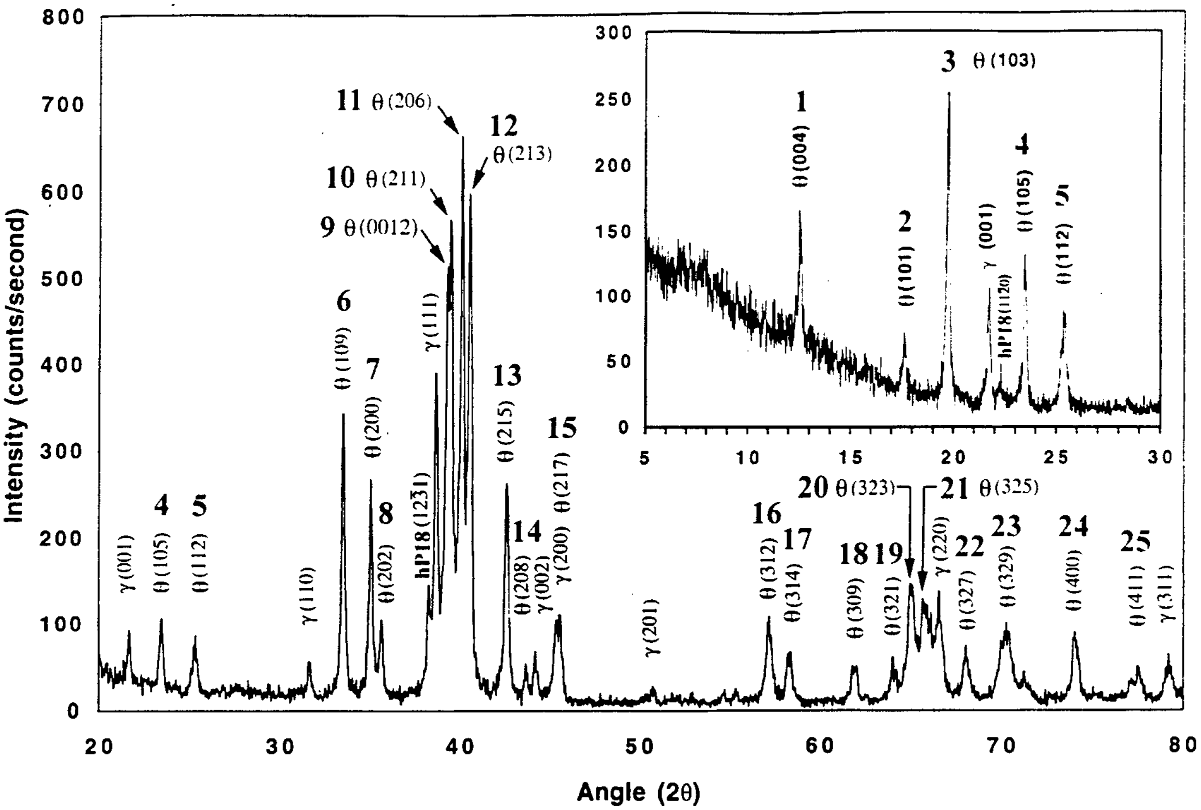

Figure 3.16 X-ray diffraction pattern of alloy #6 aged at 700C, 720h. Numbered θ phase peaks are summarized in Table 3.7.

Table 3.7 Summary of X-ray Diffraction Results from the θ Phase

Peak No.	2θ	Intensity (cps)	(hkl)	d (Å)
1	12.56	159	004	7.041
2	17.61	72	101	5.033
3	19.75	259	103	4.492
4	23.47	106	105	3.787
5	25.40	86	112	3.503
6	33.54	342	109	2.669
7	35.07	266	200	2.558
8	35.66	104	202	2.516
9	39.32	511	0012	2.347
10	39.51	566	211	2.280
11	40.12	660	206	2.246
12	40.57	595	213	2.222
13	42.63	262	215	2.119
14	43.68	53	208	2.069
15	45.59	112	217	1.989
16	57.30	100	312	1.607
17	58.51	67	314	1.576
18	61.94	48	309	1.497
19	64.04	61	321	1.417
20	65.12	144	323	1.403
21	65.82	123	325	1.376
22	68.06	74	327	1.338
23	70.28	100	329	1.292
24	74.74	90	400	1.239
25	76.77	52	411	1.212

Table 3.8 Evaluation of the I4$_1$/acd space group rules against observed reflections.

	Reflection Conditions	Rule	Violations
1	hkl	h+k+l=2n	None
2	hk0	h,k=2n	None
3	0kl	k,l=2n	$(0\bar{1}1)$ in [111] unless double diffraction: $(10\bar{1})+(\bar{1}\bar{1}2)=(0\bar{1}1)$ valid
			$(01\bar{3})$ in [331] unless double diffraction: $(11\bar{6})+(\bar{1}03)=(01\bar{3})$ valid
			$(01\bar{1})$ in [311] unless double diffraction: $(11\bar{4})+(\bar{1}03)=(01\bar{1})$ however, $(11\bar{4})$ also violates rule 4
			$(01\bar{5})$ in [151] unless double diffraction: $(\bar{1}1\bar{4})+(10\bar{1})=(01\bar{5})$ however, $(\bar{1}1\bar{4})$ also violates rule 4
4	hhl	2h+l=4n	$(11\bar{4})$ in [311] unless double diffraction: $(01\bar{1})+(10\bar{3})=(01\bar{4})$ however, $(01\bar{1})$ also violates rule3
5	00l	l=4n	(002) in [010] unless double diffraction: $(101)+(\bar{1}01)=(002)$ valid
6	h00	h=2n	None
7	h$\bar{h}$0	h=2n	$(1\bar{1}0)$ in [111] unless double diffraction: $(0\bar{1}1)+(10\bar{1})=(1\bar{1}0)$ however, $(0\bar{1}1)$ also violates rule 3

Table 3.9 Evaluation of the I4$_1$/amd space group rules against observed reflections.

	Reflection Conditions	Rule	Violations
1	hkl	h+k+l=2n	None
2	hk0	h,k=2n	None
3	0kl	k+l=2n	None
4	hhl	2h+l=4n	$(11\bar{4})$ in [311] unless double diffraction: $(01\bar{1})+(10\bar{3})=(01\bar{4})$ valid
5	00l	l=4n	(002) in [010] unless double diffraction: $(101)+(\bar{1}01)=(002)$ valid
6	h00	h=2n	None
7	h$\bar{h}$0	h=2n	$(1\bar{1}0)$ in [111] unless double diffraction: $(0\bar{1}1)+(10\bar{1})=(1\bar{1}0)$ valid

$\theta[120]$ and $\gamma(11\bar{1}) \parallel \theta(001)$ was observed within the microstructure (Figure 3.17), with the $\gamma(11\bar{1})$ and $\theta(00.12)$ being coincident. Thin defects within the θ phase were found to be parallel to the $\{101\}$ planes, and were the source of streaking observed in the [111] zone axis pattern.

The compositions of the θ phase within the 700°C, 3600h and 900°C, 720h materials, which are presented in Table 3.10, are close to the expected solubility limit of the σ phase field in the ternary diagram [15]. In the 1100+900°C and 1100+700°C materials, a shift in composition of the θ phase to lower Al concentrations relative to those in β-solutionized materials directly aged at 900 and 700°C was observed (Table 3.10). A comparison of the maximal and minimal non-isomorphic sub- and supergroups of the θ ($I4_1/amd$, D^{19}_{4h}) and σ ($P4_2/mnm$, D^{14}_{4h}) phases [25], revealed that crystallographic transitions from one to the other are not possible. The possibility that interstitial contamination was responsible for the formation/stabilization of the θ phase was also discounted, since chemical analysis revealed no substantial changes in the concentrations of the interstitial elements (O, N, C, H) in the long-term aged samples relative to the homogenized material. Furthermore, the formation of the θ phase is not believed to have been influenced by the decomposition of the β phase into the hP18 structure either, since the θ phase appeared in the Nb-24Ti-40Al alloy upon heat treating the 1100°C material again at 900 and 700°C (Figure 3.13). The θ phase was also observed in small volumes within the same alloy oil quenched from the high temperature β + σ and β + σ + γ phase fields [26]. These various observations indicate that the θ phase has some measure of thermodynamic stability below 1100°C, although the preference for this phase over σ in the materials directly aged from the β phase is still not understood.

The $I4_1/amd$ space group of the θ phase is also shared by the low temperature Hf_2Ga form of the Al_2Ti phase (Figure 3.18). Although the composition of the θ phase in the 900°C Nb-24Ti-40Al sample falls near a section line extending from the Nb corner of the diagram to the Al_2Ti stoichiometry, the compositions within the double-aged material as well as within the other alloys do not. In addition, simulations of electron diffraction patterns assuming the Al_2Ti structure for the new phase, with Nb concentration ranging from 0 to the Nb_2Al stoichiometry, did not successfully match the experimental SAD patterns [26], especially the intensities of the reflections observed. Though the

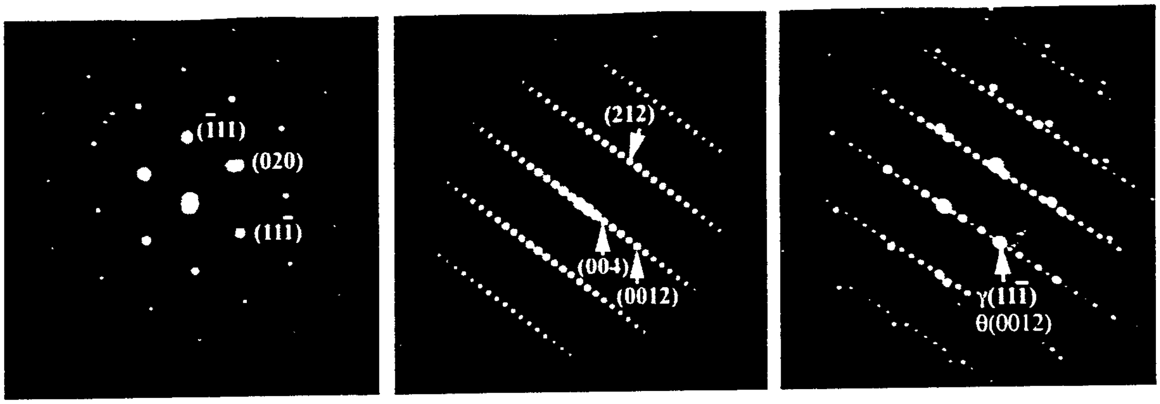

(a) (b) (c)

Figure 3.17 The $\gamma(11\bar{1})//\theta(0012)$ orientation relationship: (a) $\gamma[101]$, (b) $\theta[120]$. and (c) $\gamma[101]//\theta[120]$ zone axis patterns.

Table 3.10 Measured Compositions of the θ Phase in the Nb-Ti-40Al Alloys

Alloy	Condition	Composition (at.%)			Symbol
		Nb	Ti	Al	
Nb-36Ti-40Al	700°C	41.39	27.78	30.83	◆
Nb-30Ti-40Al	700°C	45.71	25.47	28.82	●
Nb-24Ti-40Al	900°C	43.51	21.41	34.98	■
Nb-24Ti-40Al	700°C	45.84	22.98	31.18	▲
Nb-24Ti-40Al	1100°C+900°C	46.98	24.48	28.54	□
Nb-24Ti-40Al	1100°C+700°C	48.83	24.75	26.42	○

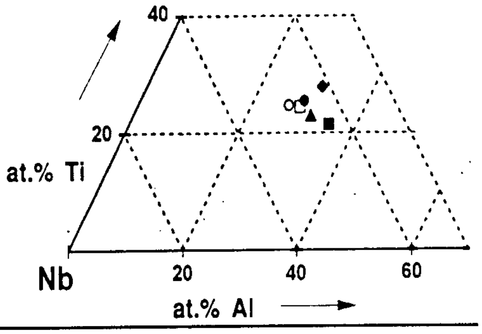

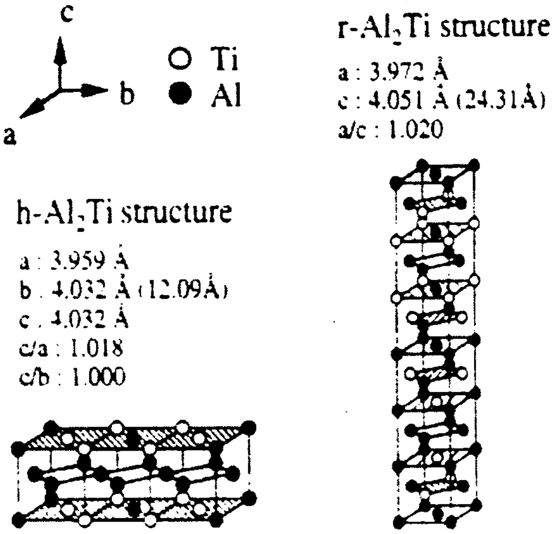

Figure 3.18 The two crystal structures of the $TiAl_2$ phase: tetragonal r-$TiAl_2$, and orthorhombic h-$TiAl_2$ [27].

composition of the θ phase lies within the range reported for the $\gamma 1$ phase at 900°C [28], its structure is also clearly not that of $\gamma 1$.

Finally, it is significant to note that the same structure, space group of $I4_1/amd$ and nearly the same lattice parameters as the θ phase has recently been determined for a transition hydride phase formed in a hydrogen-charged Ti-48Al-2Cr-2Nb gamma titanium aluminide [29, 30]. The θ phase in the Ti-48Al-2Nb-2Cr duplex alloy was induced by hydrogen charging for 60h at 13.8MPa, 800°C, and it replaced all of the α_2 phase in the microstructure. Subsequent degassing resulted in a reversible transformation to the original α_2 phase. The role of hydrogen as a transformation agent remains unclear. There are indications that hydrogen acts in the same way as niobium in stabilizing niobium-rich phases: a similar effect was observed in two Ti_3Al + Nb alloys, with a Nb concentration that was too low to stabilize the orthorhombic O-phase [31]. Introduction of hydrogen into these alloys also promoted the transformation to a phase which does not normally appear as a stable phase for the selected alloy compositions.

High resolution electron microscopy along with image simulations of the θ phase are currently being done in collaboration with Prof. Marc DeGraef at Carnegie Mellon University to determine the positions of the Nb, Ti and Al atoms and the nature of defects in this structure, with results to be reported in a forthcoming papers.

3.4 The hP18 Phase

Within the 700°C material, the lamellar $\gamma + \theta$ growth was not complete. Regions of β_0 that transformed into an ω-type structure remained within the microstructure (Figure 3.19). The ω-related decomposition product of the β_0 phase was analyzed through electron diffraction techniques. The SAD patterns observed, however, did not match the diffraction patterns of either the ω'' phase or the $B8_2$ structure.

Selected area diffraction (SAD), whole pattern and convergent beam electron diffraction (CBED) patterns of several zone axes of the β-transformed region are presented in Figure 3.20, with the lowest order zone exhibiting a hexagonal [0001] type pattern (Figure 3.20(a)). Upon

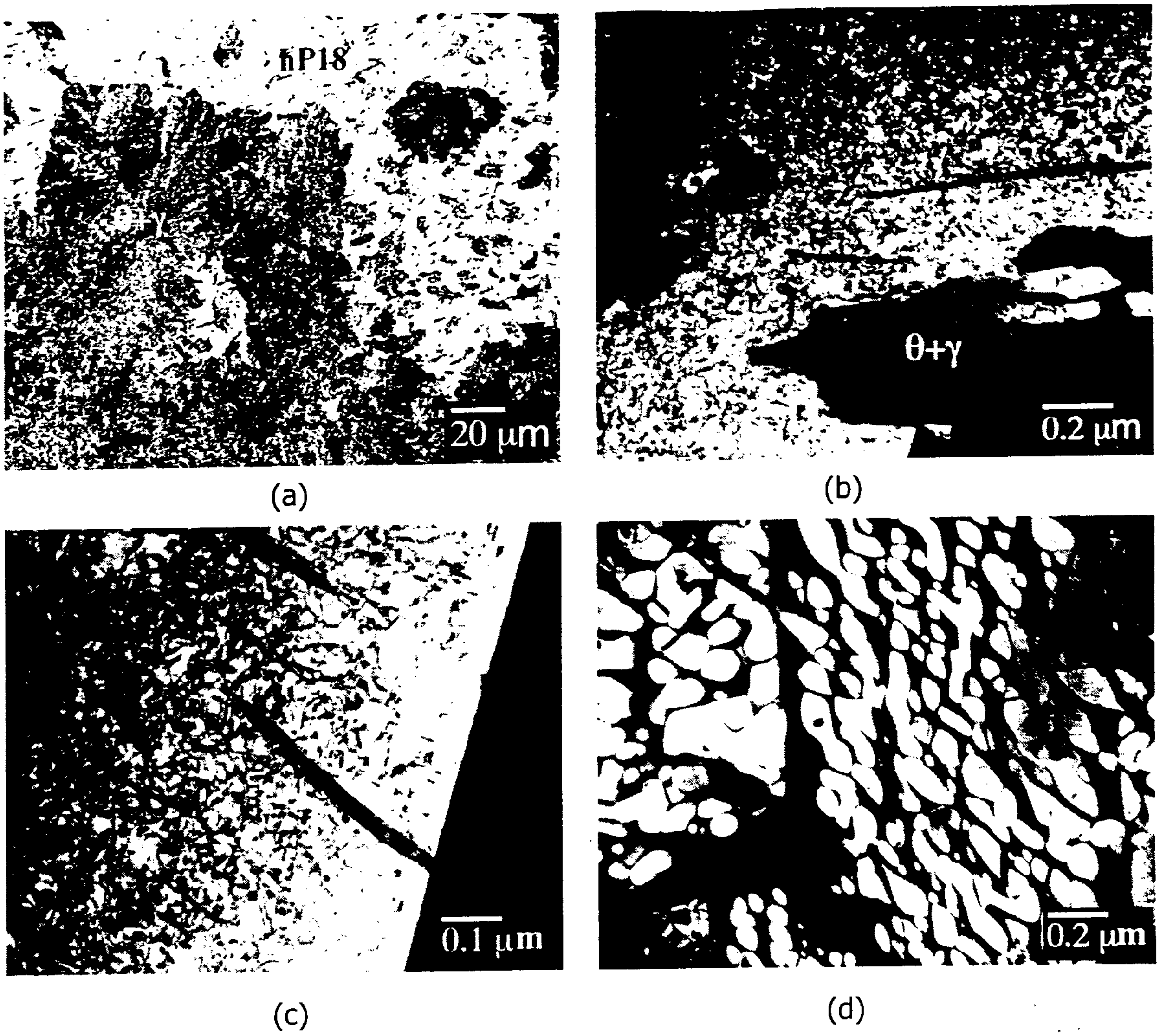

(a) (b)

(c) (d)

Figure 3.19 (a) Optical, with (b) and (c) TEM micrographs of the incomplete transformation of the β_o phase into θ and γ at 700°C in alloy 10 aged for 1080 hs. (d) DF-image illustrating two dominant domain orientations of the hP18 phase coarsened after 3600 h at 700°C in alloy 1.

tilting from the [0001] zone along the g=$11\bar{2}0$ and $10\bar{1}0$ Kikuchi lines, four additional zone axis patterns were recorded. These patterns were indexed as the $[\bar{1}103]$ and $[\bar{1}100]$ zones measured 39° and 90° from [0001] along the g=$11\bar{2}0$ Kikuchi line, and the $[\bar{1}2\bar{1}3]$ and $[\bar{1}2\bar{1}6]$ zones 35° and 57° from [0001] along g=$10\bar{1}0$. Confirmation of the hexagonal structure was also provided through XRD of the alloys (Figure 3.21).

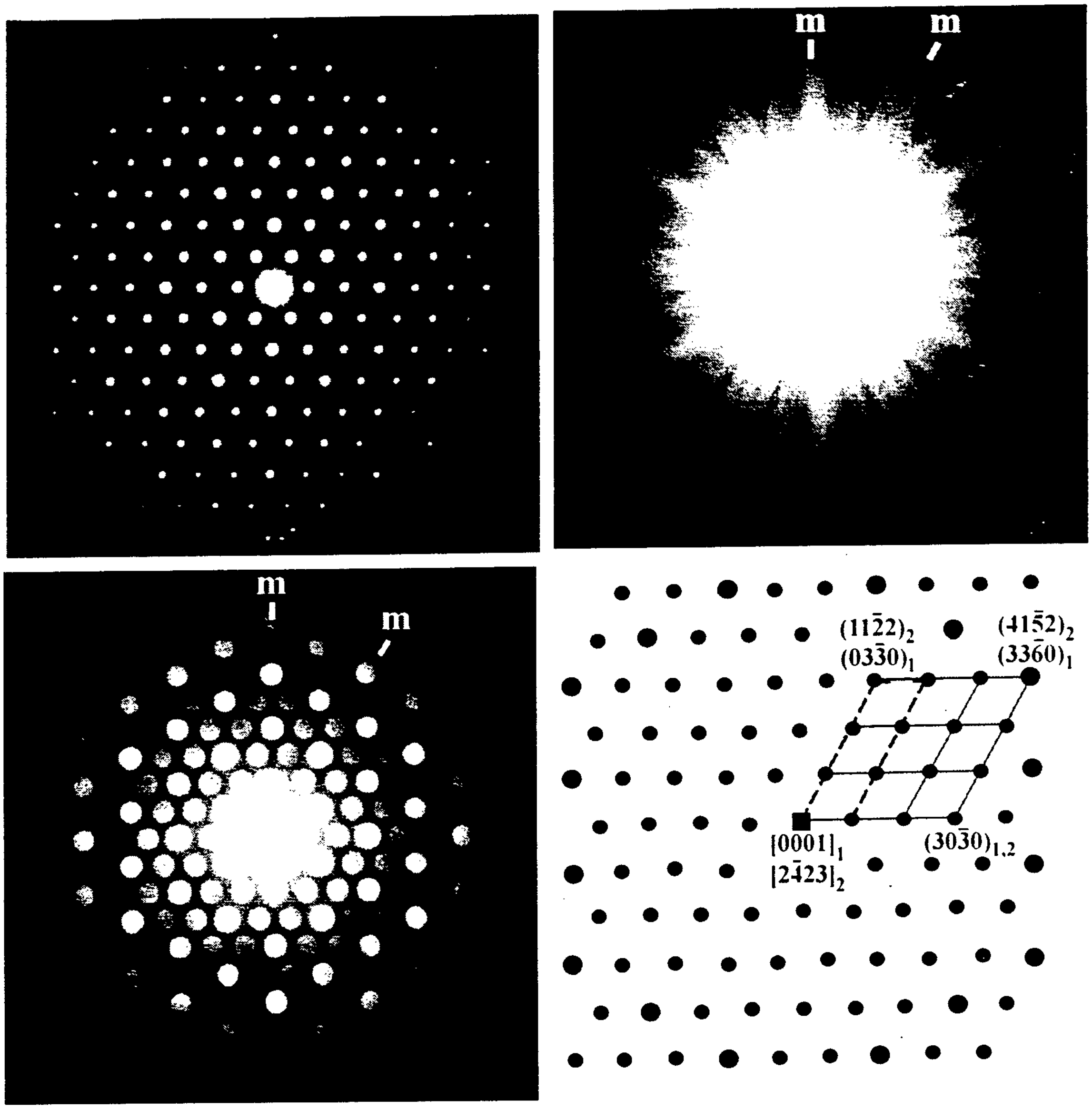

(a)

Figure 3.20 Experimental selected area diffration, whole pattern and convergent beam electron diffraction patterns of the hP18 phase with the simmulated patterns illustrating the multiple variants present within each primary zone axis: (a) [0001], (b) $[\bar{1}100]$, (c) $[\bar{1}103]$, (d) $[\bar{1}2\bar{1}6]$, and (e) $[\bar{1}2\bar{1}3]$.

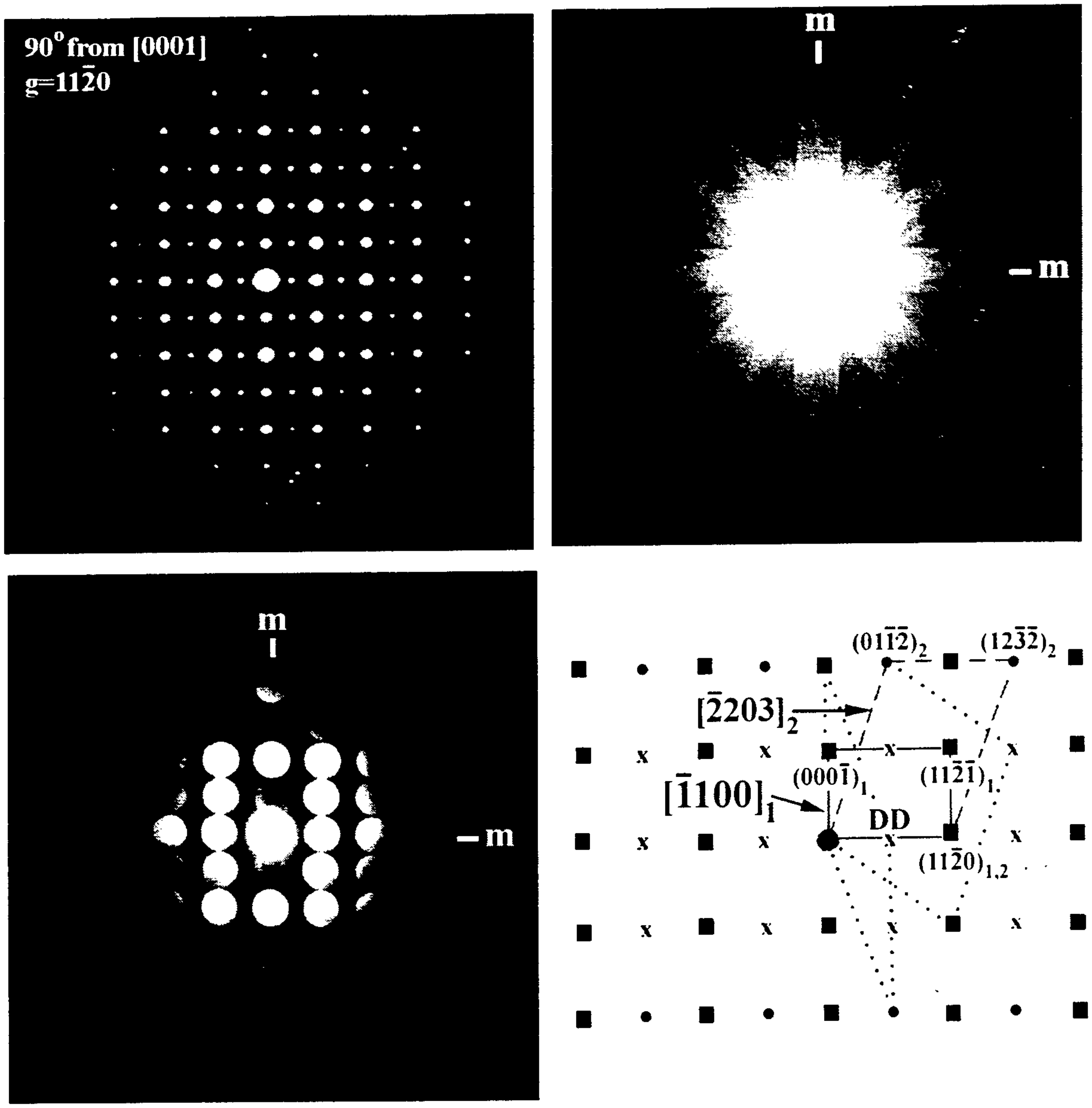

(b)

Figure 3.20 Continued.

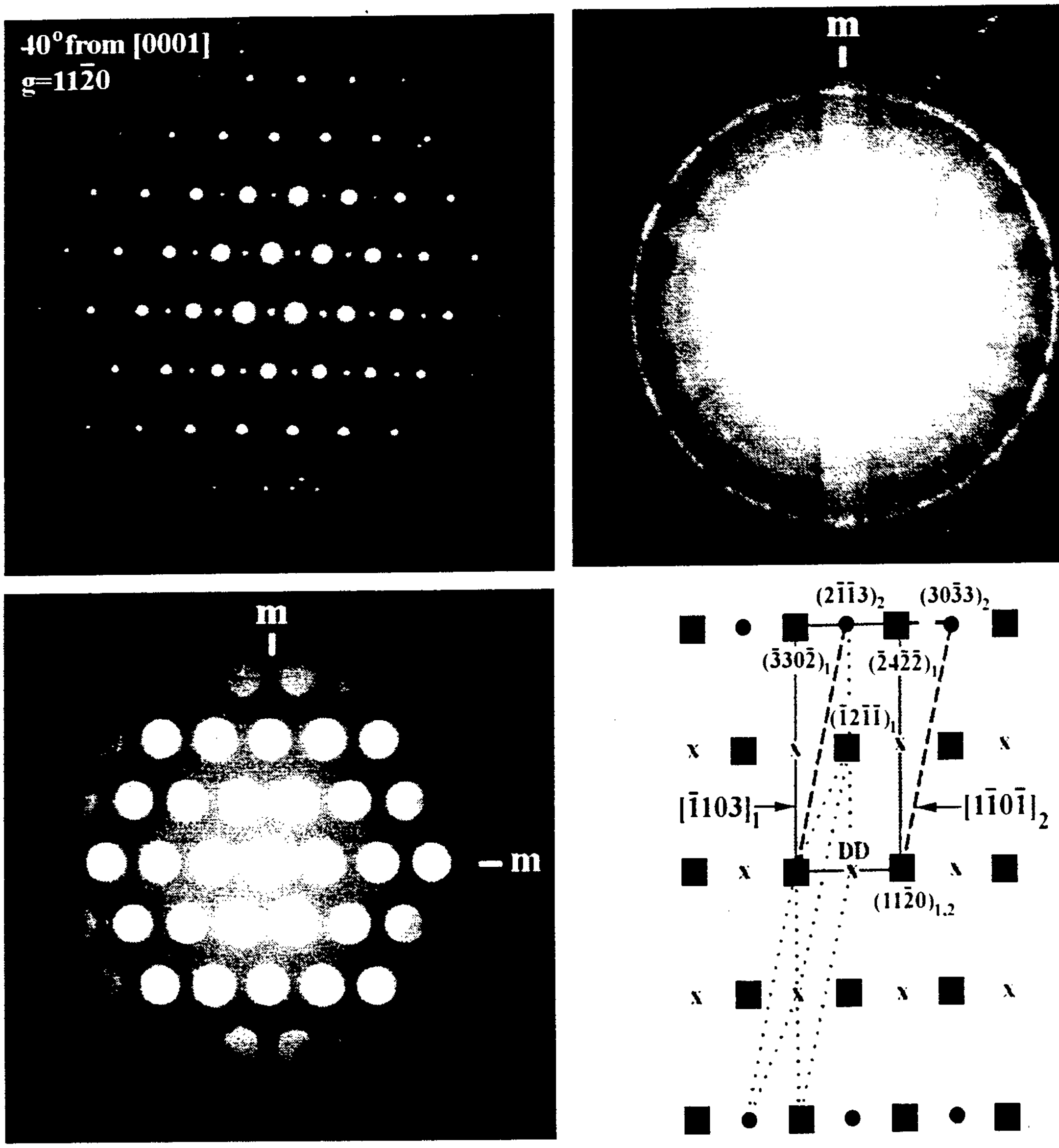

(c)

Figure 3.20 Continued.

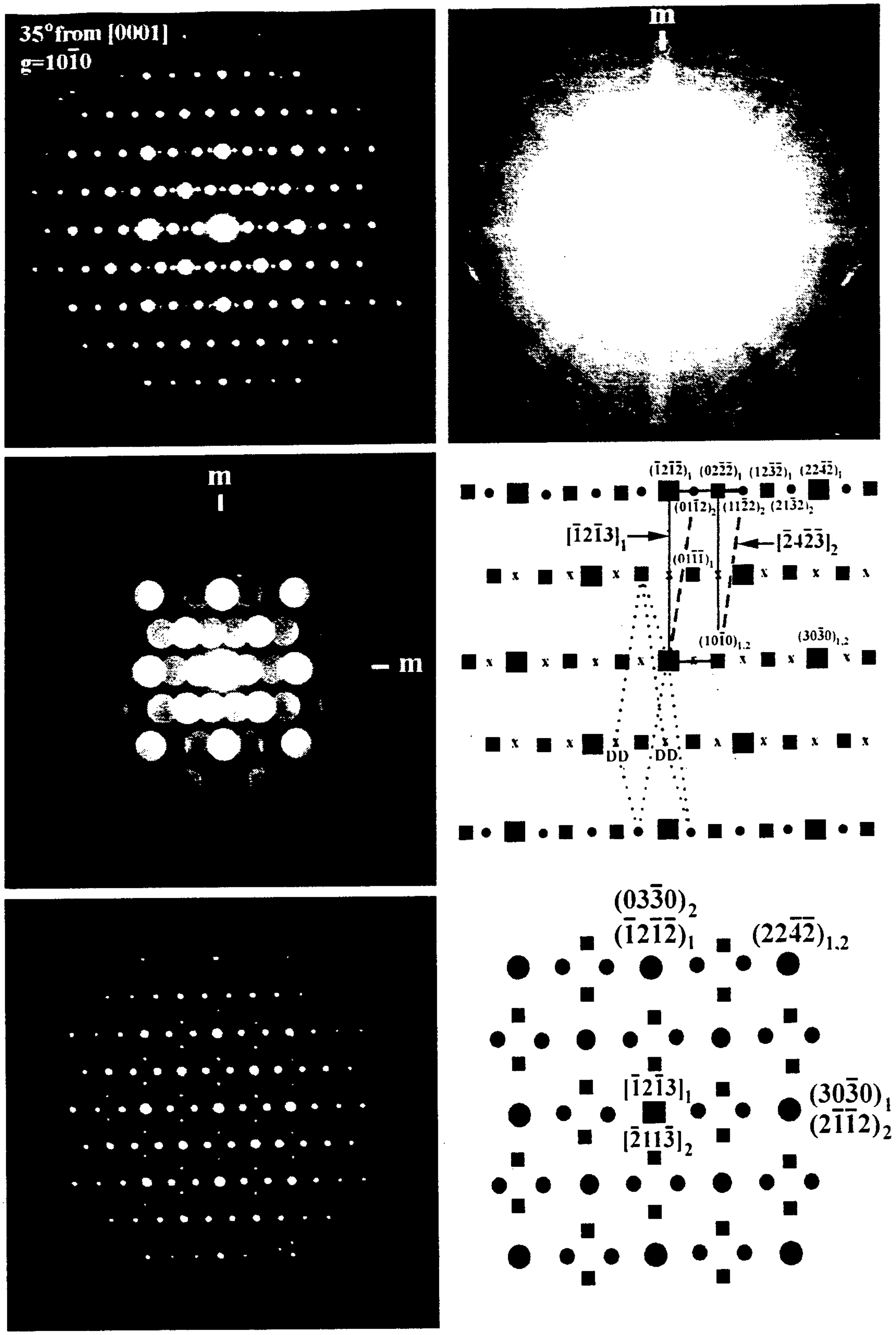

(d)

Figure 3.20 Continued.

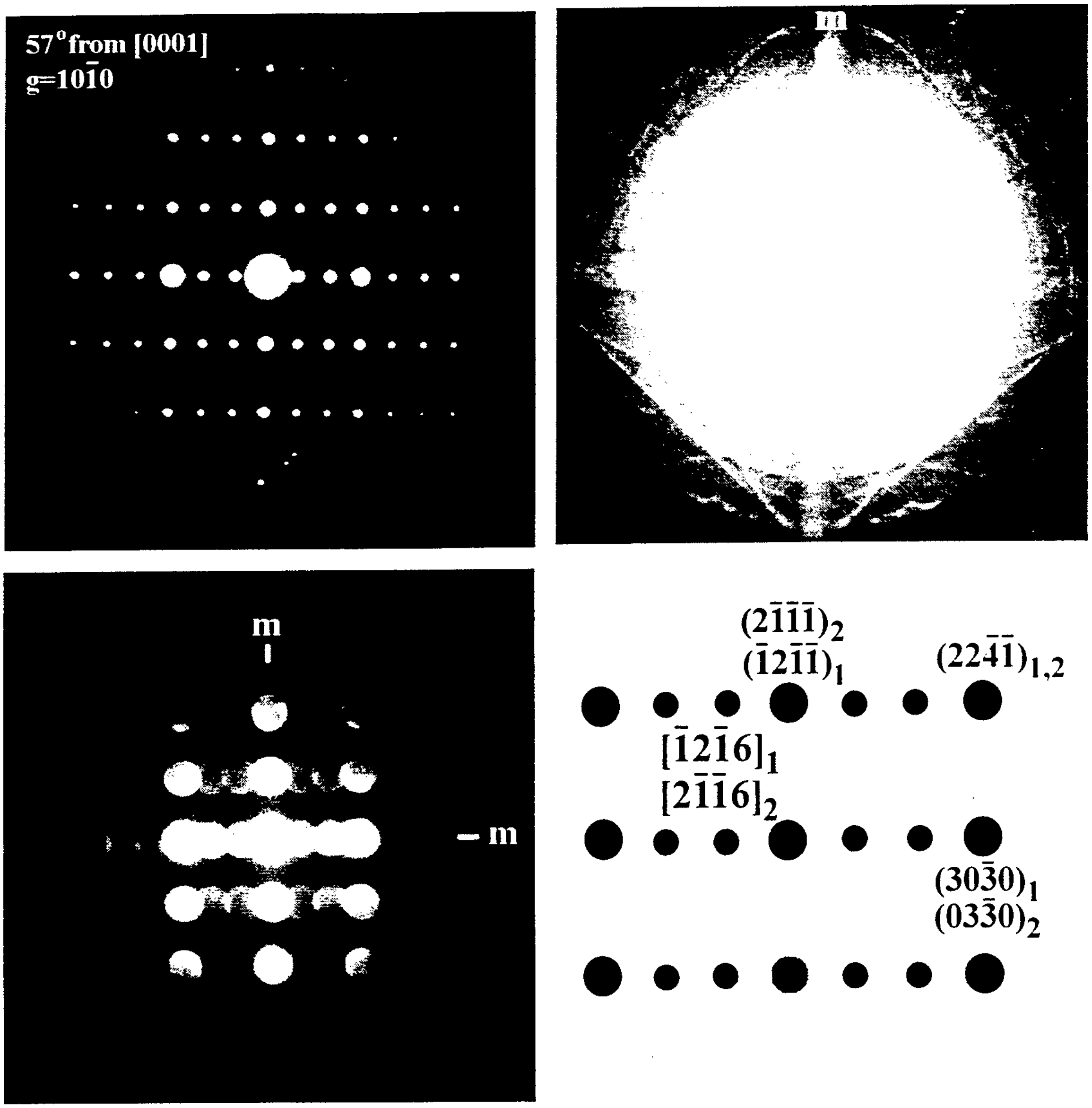

(d)

Figure 3.20 Continued.

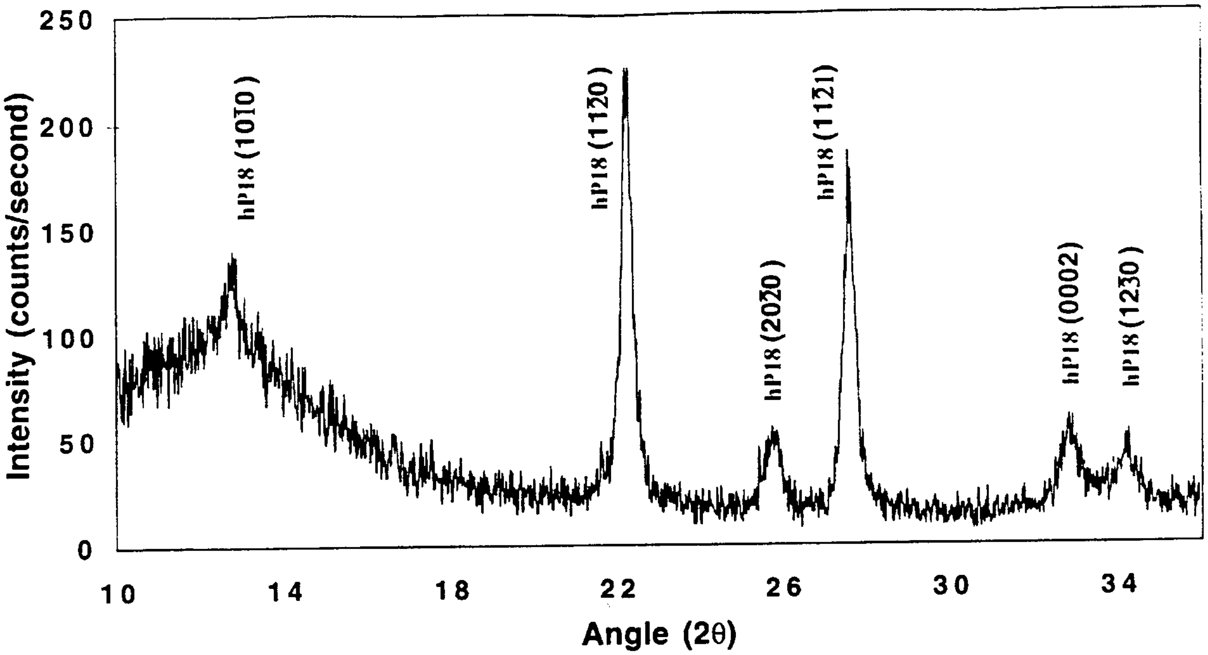

Figure 3.21 XRD pattern of alloy 1 aged at 700°C for 720 hs.

Through analysis of the SAD patterns, it was found that multiple variants of the hexagonal phase were present in each of the zone axis patterns, complicating the indexing. Multiple variants, however, are expected based on the fine domain structure observed within the materials (Figure 3.19), and because of the nature of ω-type transitions of the β phase [32]. In the [$\bar{1}$100] pattern (Figure 3.21), reflections indexed to the <$\bar{2}$203> pattern were also present, creating numerous double diffraction events, which in combination form a pattern that is deceptively simple. In addition to the presence of reflections for the <$\bar{2}$203> zone, multiple variants of <$\bar{1}$100> could also be indexed. To confirm the presence of the double diffraction reflections, tilting experiments were performed along different g-vectors near each zone. The double diffraction reflections present between the {11$\bar{2}$0} reflections in the [$\bar{1}$100] and [$\bar{1}$103] zones disappeared upon tilting off of each zone axis along the g=11$\bar{2}$0 vector (Figure 3.22(b)). Convergent beam electron diffraction of the [$\bar{1}$100] zone also identified the primary zone axis variant within the SAD pattern. The [$\bar{1}$103] zone axis recorded along the g=11$\bar{2}$0 vector, contained the <$\bar{1}$101> and other <$\bar{1}$103> patterns, producing double diffraction reflections, which again disappeared upon tilting off zone. The [0001] zone axis pattern

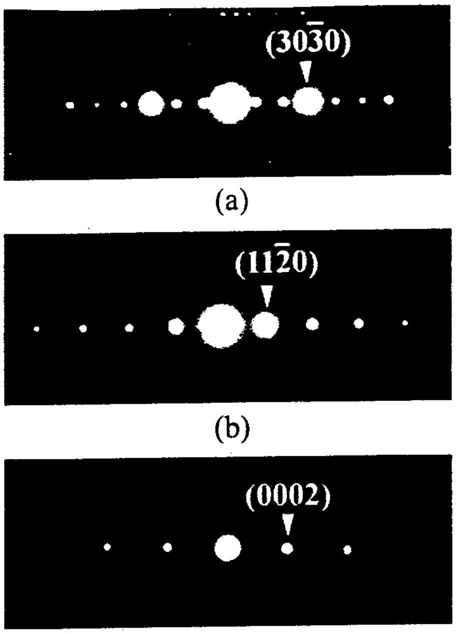

(a)

(b)

(c)

Figure 3.22 SAD patterns taken along the (a) g=$10\bar{1}0$, (b) g=$11\bar{2}0$ and (c) g=0002 vectors.

could also contain one or more of the <$\bar{2}4\bar{2}3$> patterns, whose reflections are indistinguishable from those of the [0001] pattern (Figure 3.21(a)). Confirmation for the multiple zone axes is provided by the 90° angle between [0001] and [$\bar{1}100$] of the primary zones equaling the angle between the <$22\bar{4}3$> and <$1\bar{1}00$> secondary zones. Furthermore, the 39° angle between the [0001] and [$\bar{1}103$] primary zones is also equal to the angle between the <$22\bar{4}3$> and <$01\bar{1}3$> of the secondary.

Similarly, the [$\bar{1}2\bar{1}6$] and [$\bar{1}2\bar{1}3$] zones along the g=$10\bar{1}0$ vector also contained additional variants (Fig 3.21(d,e)). The [$\bar{1}2\bar{1}3$] zone included other <$\bar{1}2\bar{1}3$> and <$2\bar{4}23$> zones, with the <$2\bar{4}23$> zones producing double diffraction events recorded within the pattern. The double diffraction effects present between the {$10\bar{1}0$} reflections of the [$\bar{1}2\bar{1}3$] pattern disappeared upon tilting off zone along the g=$10\bar{1}0$ vector (Figure 3.22(a)). While all observed reflections within the [$\bar{1}2\bar{1}6$] patterns were indexed to that zone, additional <$\bar{1}2\bar{1}6$> patterns could also be contained within the patterns since they are indistinguishable from the reflections belonging to the primary [$\bar{1}2\bar{1}6$] zone.

Therefore, no double diffraction events were observed between the $\{10\bar{1}0\}$ reflections within the $[\bar{1}2\bar{1}6]$ pattern.

The lattice parameters of the hexagonal structure, averaged from the measured interplanar spacing, were calculated to be a_o=7.93 Å and c_o=5.61 Å for the Nb-24Ti-40Al alloy, with similar values determined for the 30Ti and 36Ti alloys. These in-turn, were determined to follow an $a_o=a_\beta\sqrt{6}$ and $c_o=a_\beta\sqrt{3}$ rule with the lattice parameter of the parent β_o phase consistent with the ω* structure reported by Shao *et al.* [33] in Nb-17Al-Mo alloys and the $D8_8$ structure observed in rapidly solidified (Zr_3Al)-Nb alloys by Tewari *et al.* [32]. The indexed patterns were similar as well to those observed by Bendersky *et al.*[34] in a Ti-37.5Al-20Nb alloy. The phases observed in the latter two studies were identified as belonging to either the hP16 ($D8_8$) or hP18 forms of the *$P6_3/mcm$* structure. The [0001] and $[\bar{1}2\bar{1}6]$ zone axis patterns imaged within the Nb-Ti-40Al alloys were identical to those patterns previously observed [32-34], although the presence of additional intensities were recorded between the $\{11\bar{2}0\}$ and $\{10\bar{1}0\}$ reflections within the other zones created by the presence of multiple domains. A pattern containing two $<\bar{1}2\bar{1}3>$ zone axis variants identical to previous observations [32-34] (Figure 3.20(d)), however, was obtained by moving only a small distance within the transformed area to eliminate other $<2\bar{4}23>$ domain reflections. The formation of the $P6_3$/mcm phase from the parent β phase within the Nb-Ti-40Al alloys at 700°C appears very homogeneous when describing the collapse of the four possible {111}β planes initiating the ω-type transition and producing the multiple variants observed in the materials.

An orientation relationship of θ[111]//h[0001] θ($\bar{2}$11)//h($30\bar{3}0$), h representing the *$P6_3/mcm$*, hP18 structure, was observed across the θ+γ transformation front (Figure 3.23). Due to the multiple variants of the hP18 structure, a θ<111>//h$<2\bar{1}23>$ and θ{211}//h$\{11\bar{2}2\}$ relationship may also be possible. This could allow for several growth directions of the θ phase within the hP18 structure, facilitating its nucleation and growth. The close relationship to the β_o phase would also allow for a θ<111>//β_o<111> θ{211}//β_o{110} relationship. The transformation of the β_o phase is not believed to be a necessary precursor for the formation of the θ phase, due to θ phase precipitation occurring under conditions where β_o is not present. The θ[111] zone axis observed in parallel with hP18[0001], is difficult to visualize, given the extreme differences in lattice parameters of θ phase. It is therefore likely that the orientation relationship between the two phases is the result of a common relationship with the former β phase. The presence of ω-related particles within the Nb-24Ti-40Al alloy quenched from the β+σ phase field suggests that the β to hP18 transition is rapid.

Although the β solutionized Nb-24Ti-40Al alloy did not reveal any signs of transition, the stability of the β phase when quenched from the β+σ phase field was found to vary with aging time and quench rate. Holding the alloy for five minutes at 1500°C followed by water quenching resulted in the formation of the hP18 particles within the retained β_o phase regions of the β_o+σ material (Figure 3.24). The β_o phase itself showed diffuse ω-type streaking within the [110] SAD pattern, with a corresponding mottled texture visible when imaged under g=110 two-beam conditions. Due to the early stage of nucleation, single variants of the hP18 phase were recorded within the [111], [001] and [110] zone axis patterns of the β_o phase (Figure 3.25). The 1/3($1\bar{1}0$) reflections within the β_o zone axis patterns produced the h($30\bar{3}0$)// β_o($1\bar{1}0$) relationship unique to the $P6_3/mcm$, hP18 structure; the ω'' ($P\bar{3}m1$) and $B8_2$ (*P63/mmc*) structures hold a ($11\bar{2}0$)//β($1\bar{1}0$) relation [34-36]. Only within the [110]β pattern can multiple variants of the ω''<$11\bar{2}0$> zone produce similar 1/3$\{110\}_\beta$ reflections [36], however, these are created solely through double diffraction, which is not

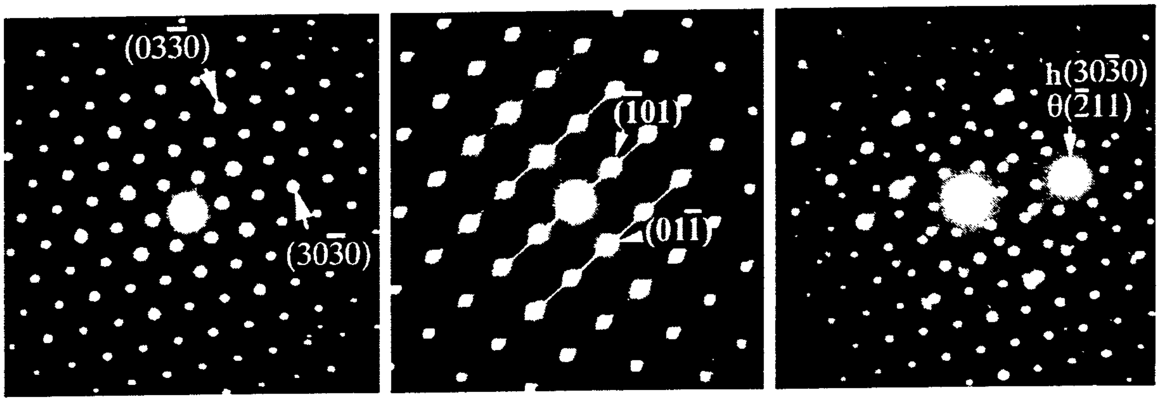

(a) (b) (c)

Figure 3.23 (a) hP18[0001], (b) θ[111] and (c) hP18[0001]//θ[111] SAD patterns showing the hP18($30\bar{3}0$)//θ($\bar{2}11$) relationship.

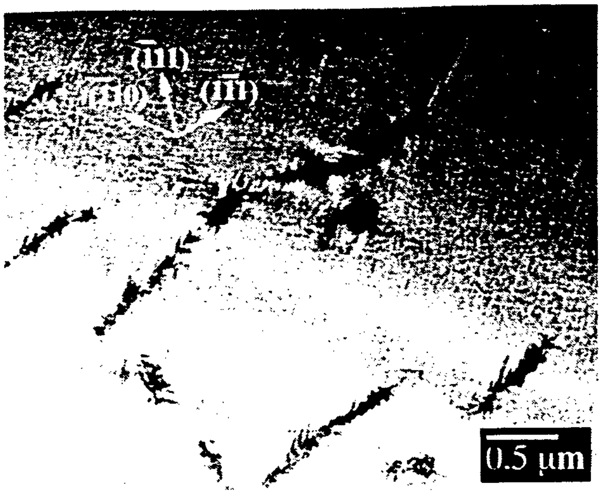

Figure 3.24 Two-beam image, g=$\bar{1}10$, of hP18 particles in β_0 of alloy 10 water quenched from 1500°C.

the case in the quenched or aged Nb-Ti-40Al alloys.

Two forms of the $P6_3/mcm$ structure, Pearson's notation hP18 and hP16, based on the number of atoms per unit cell are possible [32, 34]. The hP16 ($D8_8$) form having the Mn_5Si_3 prototype structure and observed for the Zr_5Al_3 phase by Tewari *et al.* [32], differs form the hP18 (Ti_5Ga_4) structure by the vacancy occupation of the 2(b) Wyckoff positions. The formation of the $D8_8$ phase has previously been discussed as occurring through a coupled ω-type lattice collapse of {111} planes and chemical ordering of the β lattice [32]. The $P6_3/mcm$, structure is higher in symmetry than the trigonal ω" ($P\bar{3}m1$), but lower in symmetry than the $B8_2$ ($P6_3/mmc$) phase previously observed in Nb-Ti-Al alloys [92Ben]. The two forms of the $P6_3/mcm$ space group are distinguishable by their structure factor values, specifically for the $\{10\bar{1}0\}$ plane (Table 3.11), with that of the hP16 form being zero. The Nb-36Ti-40Al alloy heat treated at 700°C for 720h, which contained the smallest amount of θ, was used for XRD analysis of the $P6_3/mcm$ phase in order to avoid difficulties associated with peak overlapping between the two phases. The $\{10\bar{1}0\}$ peak at 12.9° of 2θ was observed within the XRD pattern (Figure 3.21). Confirmation of the hP18 structure was also provided by the presence of $\{10\bar{1}0\}$ reflections observed within CBED patterns of the [0001], $[\bar{1}2\bar{1}3]$ and $[\bar{1}2\bar{1}6]$ zone axes, and within the diffraction patterns taken during tilting experiments

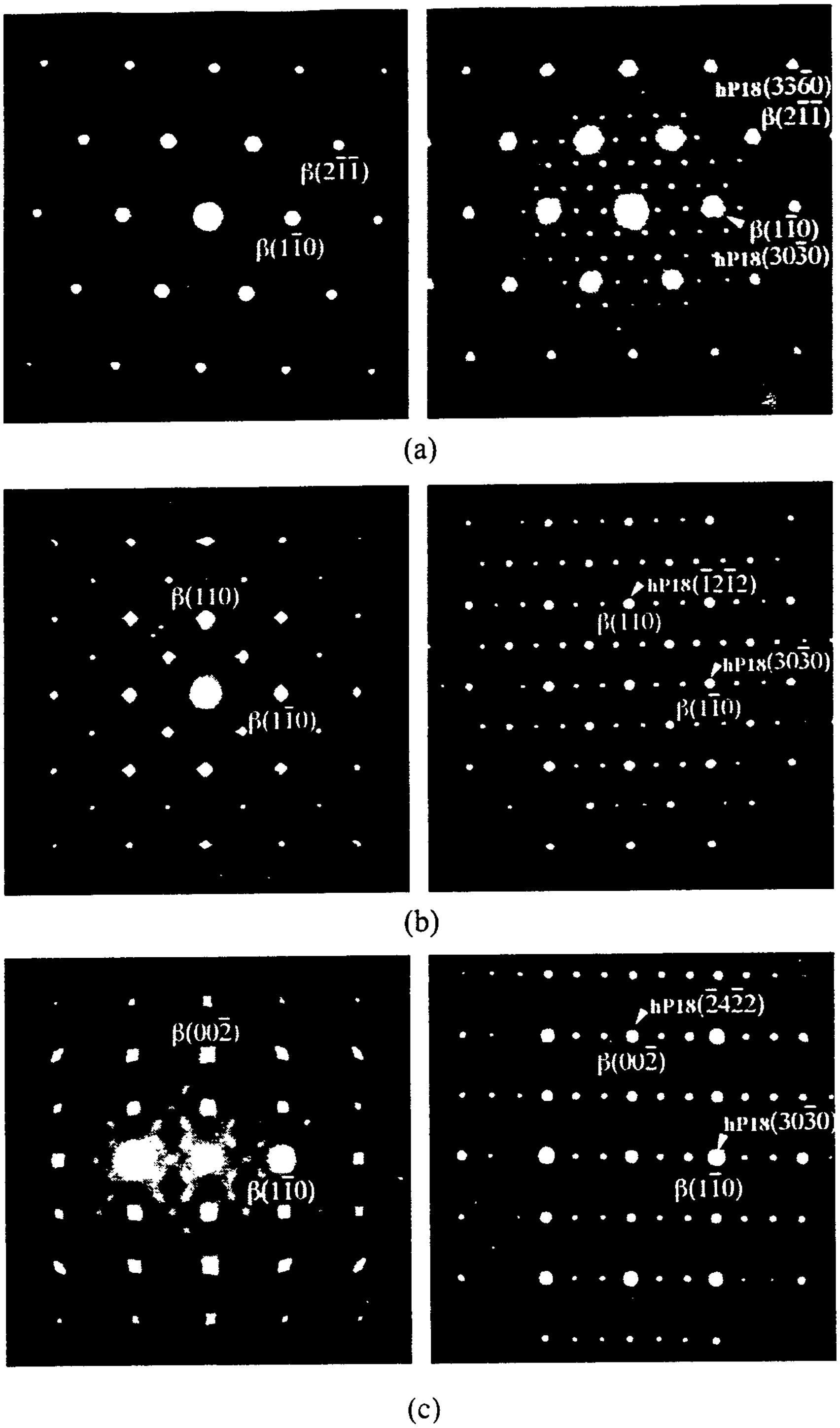

Figure 3.25 SAD patterns of the β_o matrix and hP18 particles in alloy 10 water quenched from 1500°C, (a) $\beta_o[111]$ and $\beta_o[111]$//h[0001], (b) $\beta_o[001]$ and $\beta_o[001]$//h$[1\bar{2}13]$, and (c) $\beta_o[110]$ and $\beta_o[110]$//h$[1\bar{2}16]$.

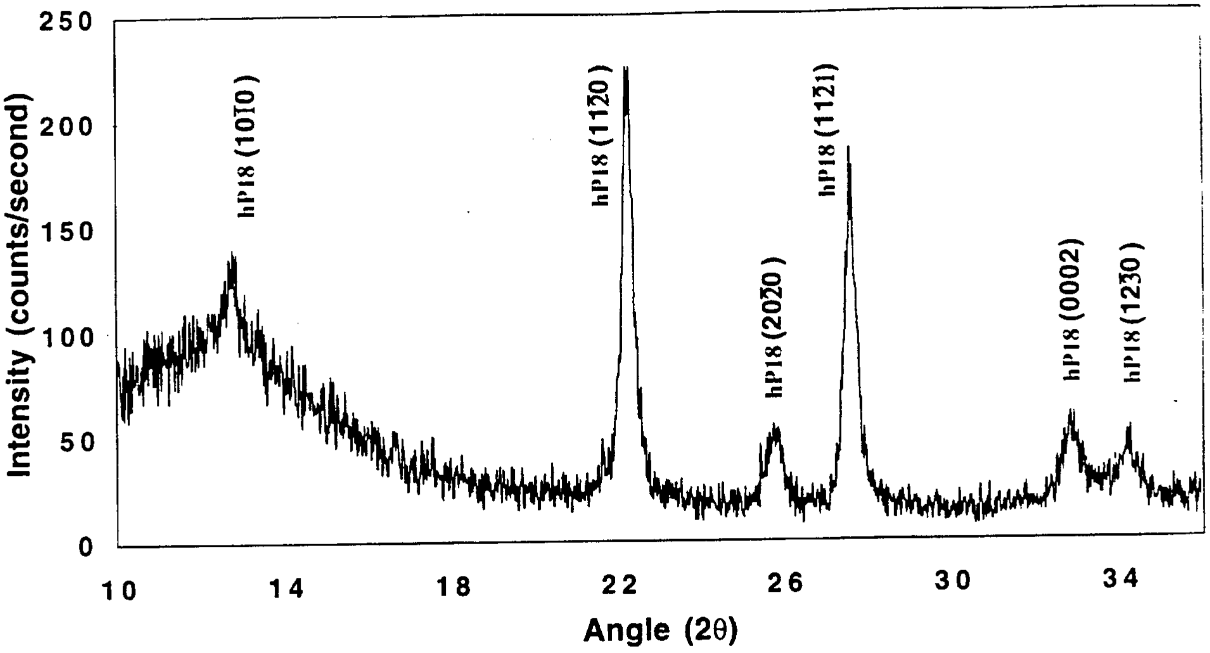

Figure 3.25 XRD pattern of alloy 1 aged at 700°C for 720 hs.

Table 3.11 Calculated structure factors for the hP16 and hP18 forms of the P6$_3$/mcm structure

		Structure Factor	
hkl	d (Å)	hP16	hP18
(10$\bar{1}$0)	6.8710	0.00	8.70
(0001)	5.6101	0.00	0.00
(10$\bar{1}$1)	4.3456	0.00	0.00
(11$\bar{2}$0)	3.9669	9.99	17.31
(20$\bar{2}$0)	3.4355	15.96	9.51
(11$\bar{2}$1)	3.2390	9.58	9.58
(20$\bar{2}$1)	2.9298	0.00	0.00
(0002)	2.8050	27.47	22.19
(12$\bar{3}$0)	2.5970	24.75	19.95

hP16 and hP18 based on Zr_5Al_3 and Zr_5Al_4 with lattice parameters of a_0=7.93Å c_0=5.61Å from the g=$10\bar{1}0$ vector (Figure 3.22(a)). In addition, the near equal structure factor values of the {$10\bar{1}0$} and {$20\bar{2}0$} planes in the hP18 form is also evident in the near equal intensities of these reflections within the CBED patterns. The zero structure factor value of the (0001) plane, indicative of a hexagonal crystal rather than the trigonal ω'', is also observed in the missing odd (000ℓ) reflections within the [$\bar{1}100$] CBED and the g=0002 vector SAD pattern (Figure 3.22(c)).

The appearance of the *P6$_3$/mcm* phase in the Nb-Ti-Al system had previously observed by Bendersky *et al.* [34], as a precipitate phase within B8$_2$ grains in a Ti-37.5Al-20Nb alloy aged at 700°C for 432h. Lattice parameters and orientation relationships relative to the B8$_2$ phase, which contained three translational variants consistent with the suggested non-isomorphic subgroup relationship to the *P6$_3$/mcm* space group, was observed. It was inconclusive, however, as to which form of the *P6$_3$/mcm* phase, hP16 or hP18, had been observed.

In the work of Tewari *et al.* [32], the D8$_8$ structure was not observed within binary Zr_3Al alloys, but did readily form with the addition of just 3 wt.% Nb. The role of Nb on stabilizing structural vacancies within the β phase was attributed to the formation of the hP16 form of the D8$_8$ phase that appeared within the Zr_3Al-Nb alloys. This structure was reported to further develop into the B8$_2$ and eventually other equilibrium phases upon aging.

The formation of the hP18 structure of the *P6$_3$/mcm* phase within the Nb-Ti-40Al alloys at 700°C may have been due to the high Nb concentration of the alloys themselves. The compositions of the hP18 phases within the Nb-Ti-40Al alloys are listed in Table 3.12. It is not believed that an ordering of the hP16 structure into the hP18 form had occurred through vacancy elimination during the low temperature aging. This is due to the occurrence of h{$10\bar{1}0$} reflections within the β_o zone axis patterns recorded from the individual hP18 particles in the oil quenched material. The presence of these reflections is required in order to account for the appearance of the double diffracted {$10\bar{1}1$} and {$02\bar{2}1$} reflections in those patterns, due to structure factors of zero in both the hP18 and hP16 forms. The small size of the hP18 particles eliminated the possibility of additional variants occurring in each zone axis direction.

Table 3.12 Measured Compositions of the hP18 Phase in the Nb-Ti-40Al Alloys

Alloy	Condition	Nb (at.%)	Ti	Al
Nb-36Ti-40Al	700°C, 720h, WQ	25.06	35.68	39.26
Nb-36Ti-40Al	700°C, 3600h, WQ	37.48	33.2	29.24
Nb-30Ti-40Al	700°C, 720h, WQ	–	–	–
Nb-24Ti-40Al	700°C, 1080h, WQ	41.76	22.52	35.72
Nb-24Ti-40Al	1500°C, 5 min., WQ	–	–	–

(WQ) Water Quenched

3.5 Phase Equilibria in the $\sigma + \gamma$ Alloys

The 1100°C aged materials exhibited a $\sigma + \gamma$ two-phase structure, with neither θ nor α_2 phases present. Alloy 10, aged a second time at 1100°C from the 1475°C oil-quenched material also contained only a $\sigma + \gamma$ structure, with the γ phase exhibiting numerous $\{111\}$-type twins (Figure 3.26). The result of the disappearance of α_2 retained from the first treatment, where the α_2 and γ phases had exhibited a $\gamma(111)//\alpha_2(0001)$ lamellar orientation. The θ phase which had been present between the γ/α_2 lamella in alloy 10 oil-quenched 1475°C material, also disappeared upon re-heating at 1100°C. The θ phase did reappear, however, when the 1100°C material was aged again at either 700 or 900°C (Figure 3.27). The θ phase was preferentially found either between γ grains, or between the γ twins as thin slivers. This was expected, due to the $\gamma[10\bar{1}] // \theta[120]$, $\gamma(111) // \theta(0012)$ orientation relationship.

It was clear that the alloys aged at 700°C (from the solutionized material, not to be confused with the 1100+700°C two-step treatment) had not attained full equilibrium, and that the remaining decomposed β_o phase might have skewed the measured θ and γ compositions. With further aging, it is likely that the θ and γ phase compositions would have approached the values closer to the 900°C aged material, as more of the β_o/hP18 structure had transformed. Prolonged aging at 700°C did show some indication of phase coarsening with the formation of γ particles within the hP18 phase regions, which were still present in the alloys for times up to 150 days (Figure 3.28). Preliminary work on the nucleation and growth characteristics of the θ and γ phases in alloy 1 indicated that the kinetics at 700°C become extremely slow and that after only 20 hours the β_o phase has shown partial transformation into the hP18 structure (Figure 3.29). Upon aging at 900°C, however, in both alloys 1 and 6 produced completely transformed $\theta + \gamma$ structures, with no retained β_o or

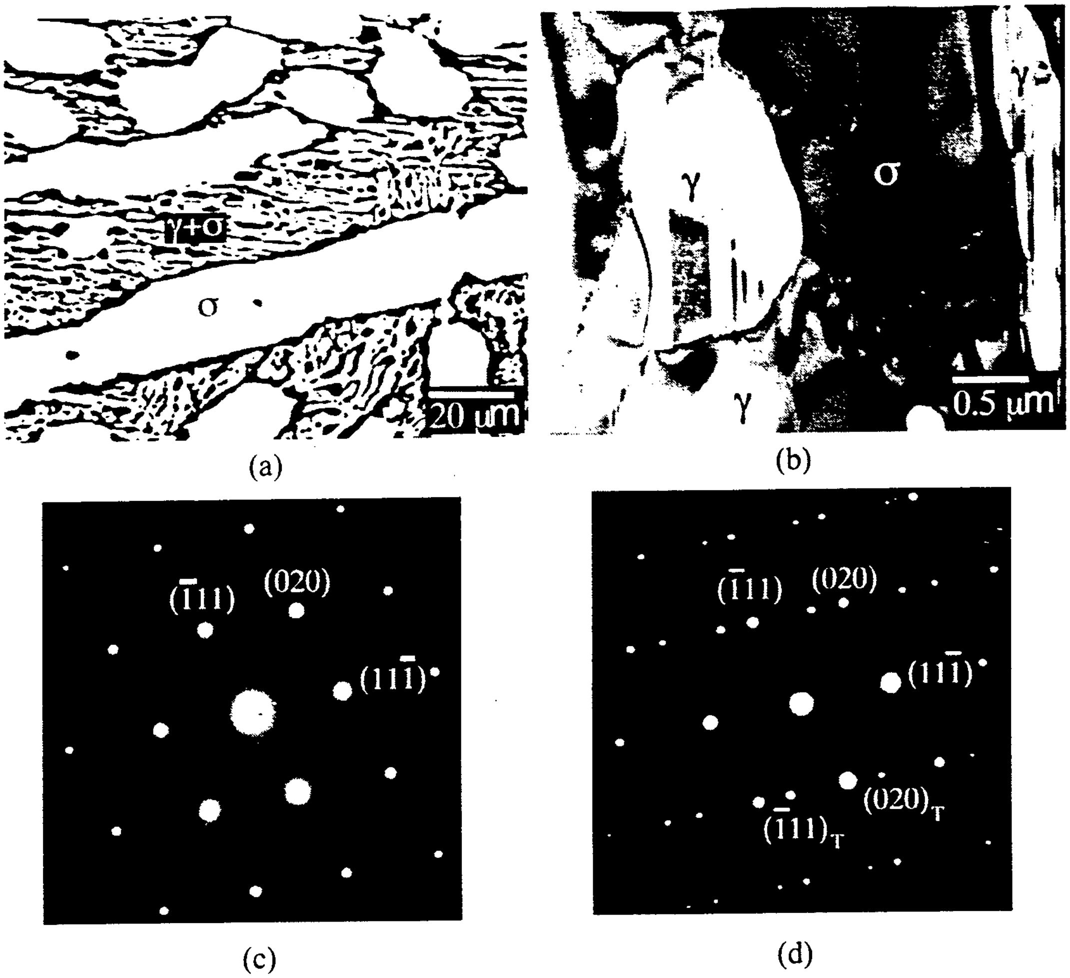

(a) (b)

(c) (d)

Figure 3.26 (a) BSE and (b) BF-images of the 1475+1100°C aged alloy 10 showing only a σ/γ microstructure; (c) The $\gamma[101]$ zone axis with, (d) $\{111\}$-type twinning resulting from the disappearance of the γ/α_2 lamellar structure from the 1475°C quench.

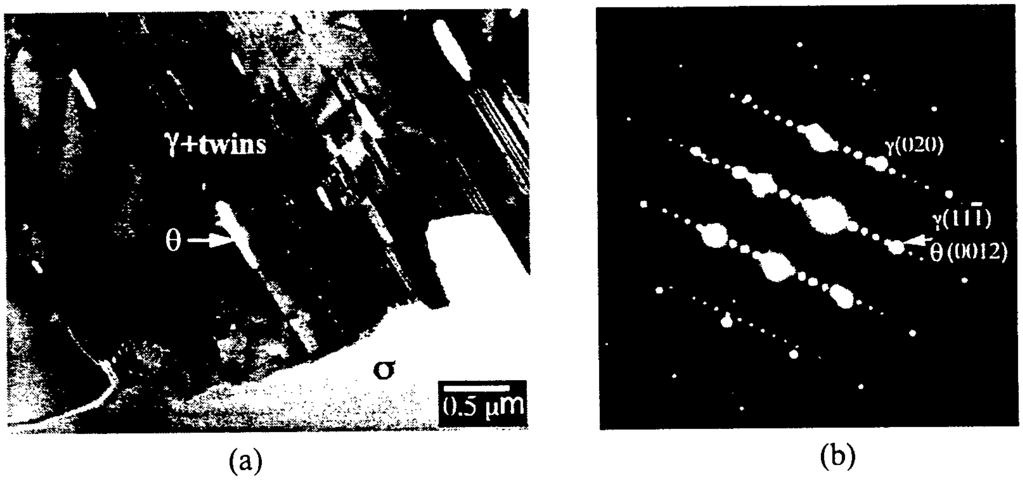

(a) (b)

Figure 3.27 (a) DF-image of the θ phase within the 1100+700°C aged alloy 10 and (b) the $\theta[120]//\gamma[101]$ zone axis SAD pattern.

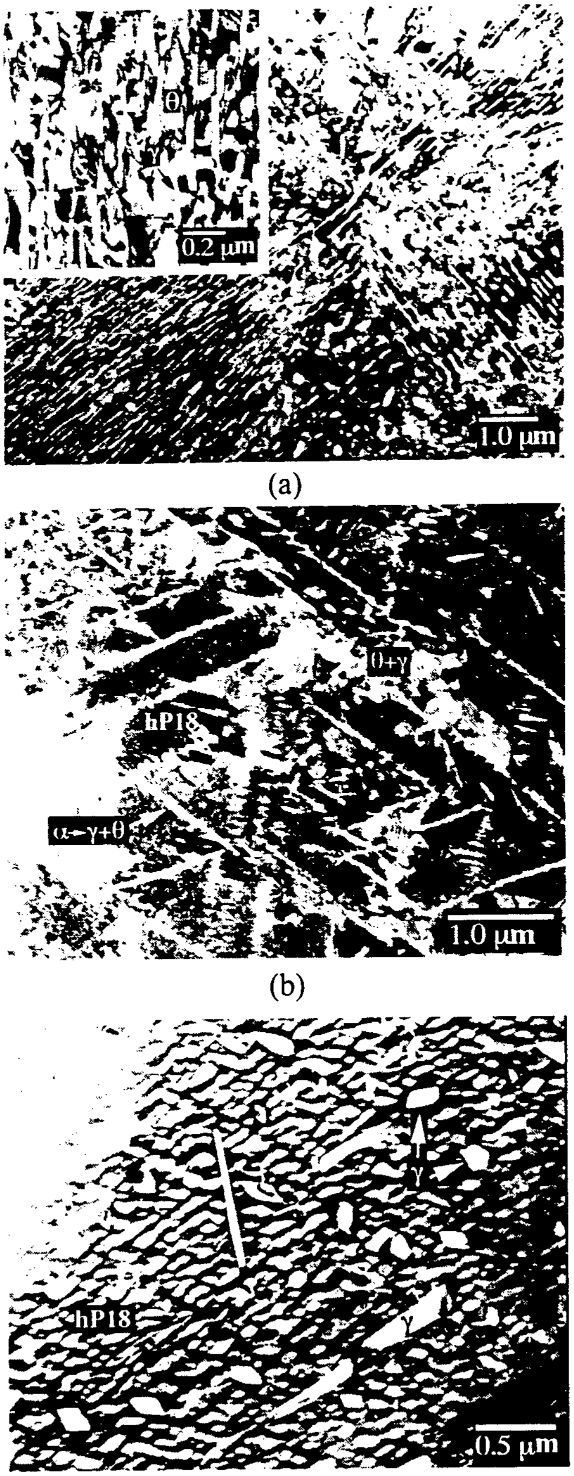

(a)

(b)

(c)

Figure 3.28 Alloy 1 aged 700°C for 150 days. (a) BF image of θ + γ structure, (b) low magnification BF-image of structure showing former α_2 plates decomposed into γ+θ surrounded by hP18, together with the lamellar-like θ+γ structure, and (c) DF-image of hP18 region that has both coarsened into two dominant domain orientations and exhibits further precipitation of the γ phase.

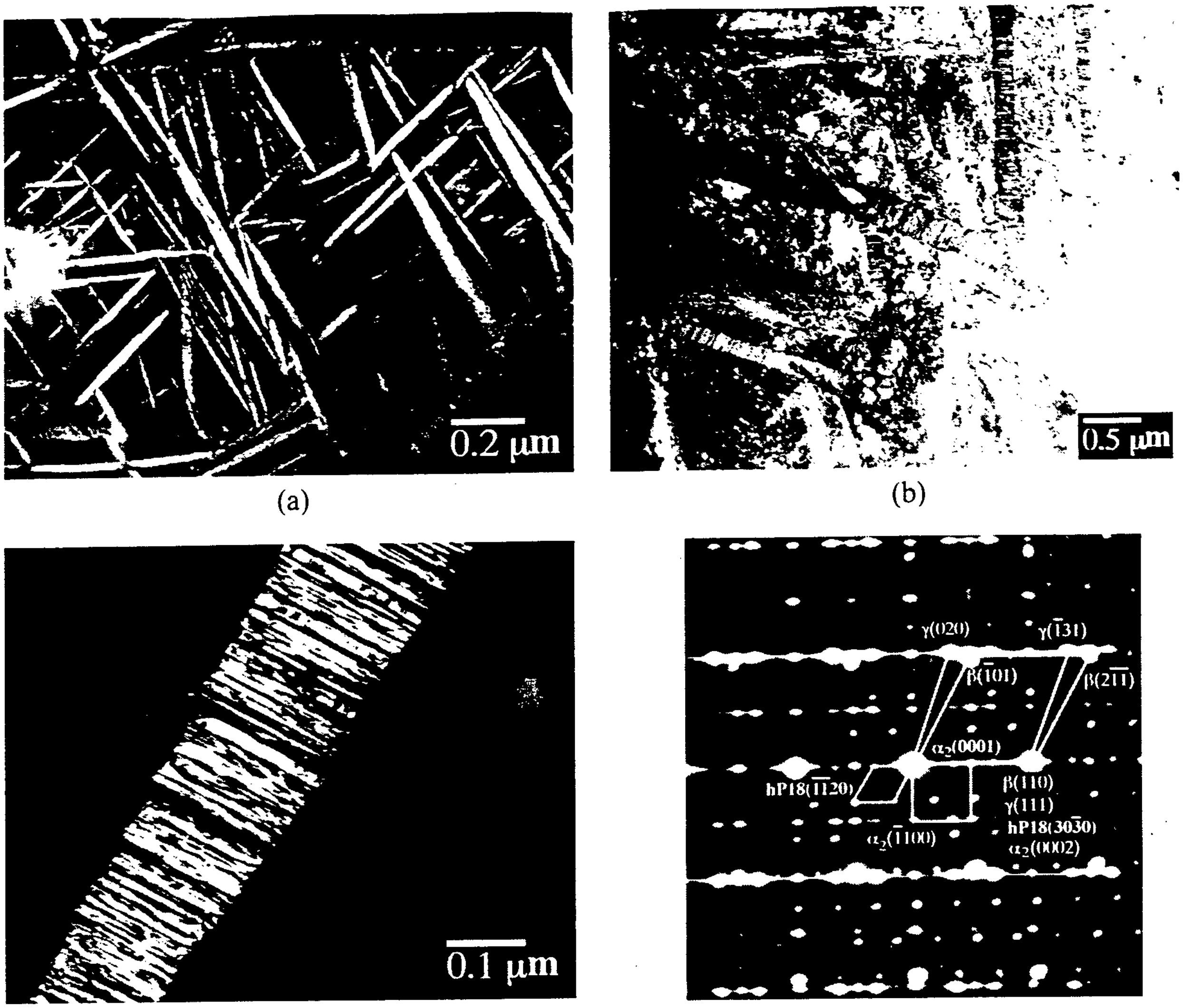

(a) (b)

(c) (d)

Figure 3.29 Alloy 1 aged at 700°C for 20h. (a) DF-image of the α_2 phase formed from the solutionizing treatment, (b) BF-image and (c) DF-image showing the decomposition of the α_2 into γ, and (c) $\beta_o[111]//hP18[0001]//\gamma[101]//\alpha_2[11\bar{2}0]$ SAD patterns.

hP18 phase regions. The α_2 needles which were formed during the solution treatment of alloy 1, appear to have neither promoted nor hindered the formation of the θ and γ phases (Figures 3.28 and 3.29). In fact, on aging at 700°C, the α_2 needles decomposed into γ twinned along the {111} directions that were perpendicular to the needles longitudinal axis (Figure 3.29(b,c)). The θ phase was also found present occasionally between the twinned γ grains within the 20-hour aged samples and continued to grow outward from the former α_2 needles after 150 days (Figure 3.28(b)). The formation of the θ and γ phases from the α_2 needles, however, is not responsible for the lamellar-like morphology observed emanating from the former β_0 grain boundaries themselves.

The retreat of the γ phase composition at 900°C towards the Ti-Al binary, in comparison with the 700°C aged material, was also a result of the further equilibration within the material that had occurred at 700°C. The positioning of the 900°C tie-line, with respect to the alloy composition, appeared to be more accurate in terms of the volume percent of the individual phases that were observed through TEM analysis. The composition of the θ phase within alloy 10 aged at 1100+700°C and 1100+900°C, was determined to be between the compositions of the O-phase and the θ phase (Table 3.10, and Figure 3.30). The compositions of the σ and γ phases within the 1100°C, 1100+700°C and 1100+900°C heat treatments showed little change.

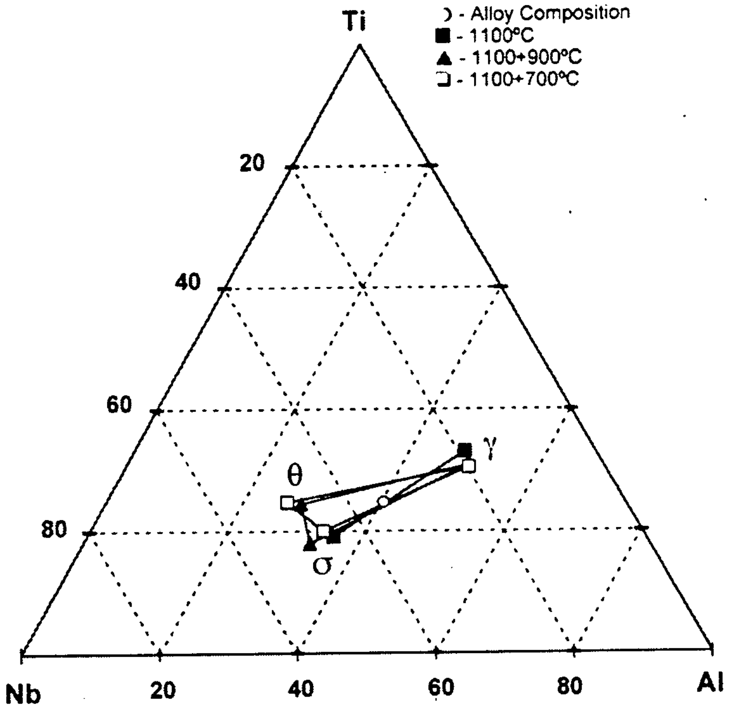

Figure 3.30 Experimental tie-line data for alloy 10 aged at 1100°C, 1100+900°C, and 1100+700°C.

4 Phase Equilibria and Transformations in $\beta + \delta$ Alloys (2, 3, 7, 8, 11 and 14)

4.1 As-cast Material

The six alloys with the two-phase $\beta + \delta$ structures were alloy #'s 2, 3, 7, 8, 11 and 14. These alloys contained cast microstructures of large equiaxed grains with dendritic segregation observed under both OM and BSE-imaging (Figure 4.1(a)). Primary dendritic coring within the microstructures was on average 0.22 mm for the alloys. The cast microstructures were all single-phase BCC β, as determined through XRD (Figure 4.1(b)). Diffracted (100) peaks, indicating an ordered B2 structure, was not observed.

While {100} peaks were not observed through XRD, {100} superlattice reflections indicating B2 ordering were observed in the <100> and <110> SAD patterns of the six alloys. The missing (100) superlattice reflections in the XRD scans, suggested a relatively low degree of long range ordering associated with the β_o phase. No decomposition products of the β_o phase were observed in these alloys, either through optical or electron microscopy.

4.2 Differential Thermal Analysis and β Transus Temperatures

The results of differential thermal analysis (DTA) for the alloy #'s 7, 11 and 14 were similar (Figure 4.2(a)). The thermograms did not reveal any clearly defining information regarding the β transus temperatures, the β/β_o ordering transition temperatures, or any information on phase transformations. The lack of a detectable signal in determining the β transus temperatures and other reactions was due to the initial single phase β_o starting structure and the slow reaction kinetics of the expected δ-Nb_3Al phase. In addition, because the phase boundaries between the β and δ phases in the Nb-Al system are relatively constant in composition with respect to temperature, and assuming this also to be true within the ternary compositions, the changes associated with the transformations may have been small. Transformations producing changes over large volumes throughout the material, or those that occurred rapidly may have not taken place that would have caused a measurable change in energy. A similar result to the before mentioned alloys was also observed for alloy #2 (Figure 4.2(b)). While changes in the slope of the thermogram heating curve were observed,

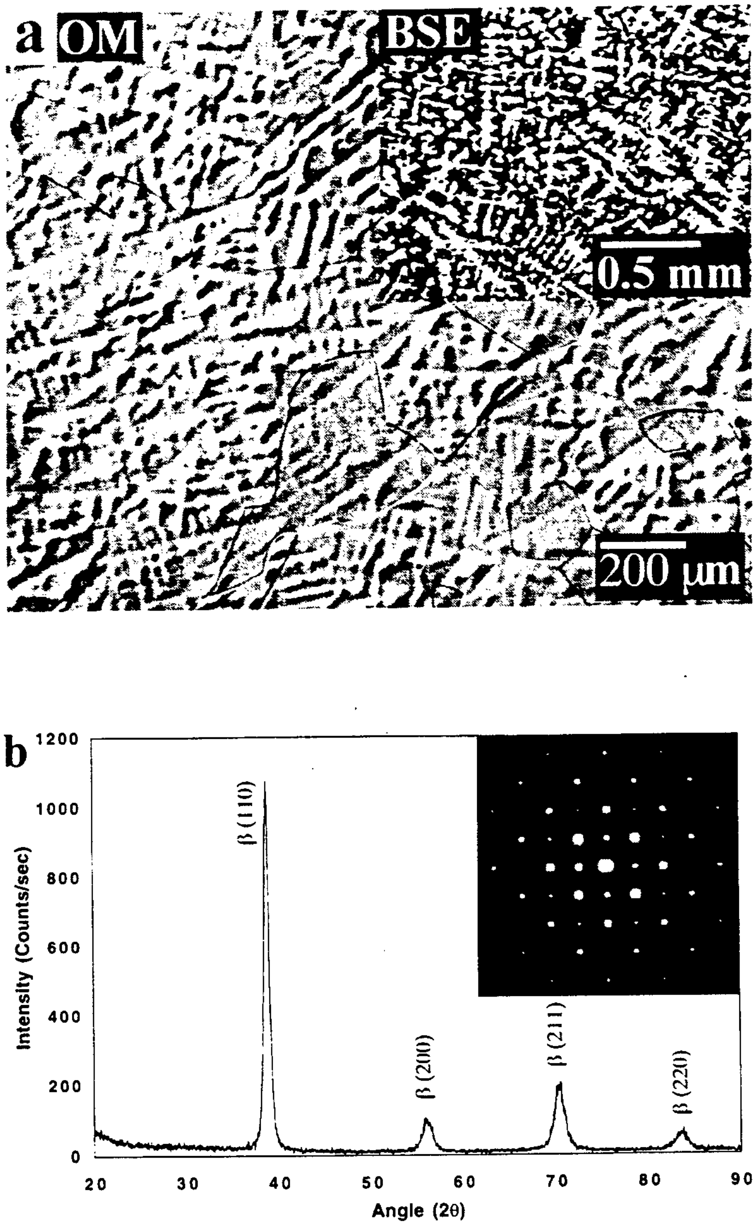

Figure 4.1. (a) OM and BSE-images of as cast alloy #11. (b) bcc XRD pattern of as cast alloy #11 with insert showing B2 (β_o) ordering in the [100] SAD pattern.

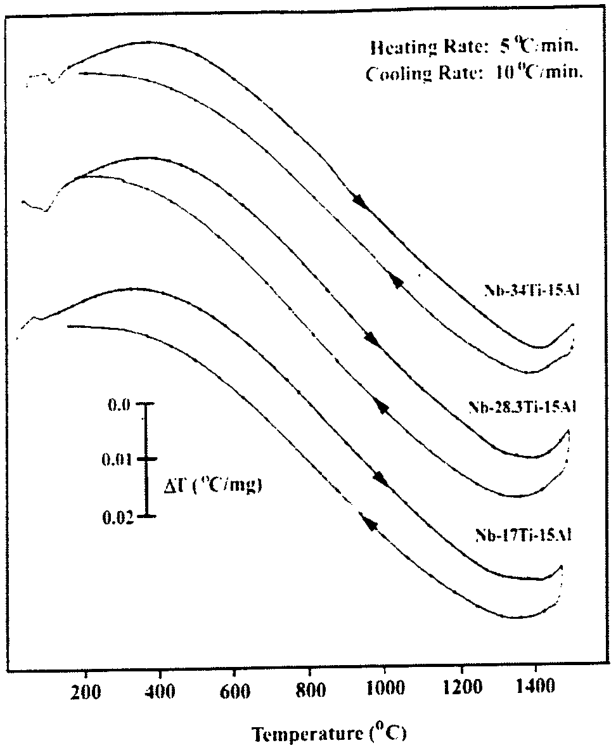

(a)

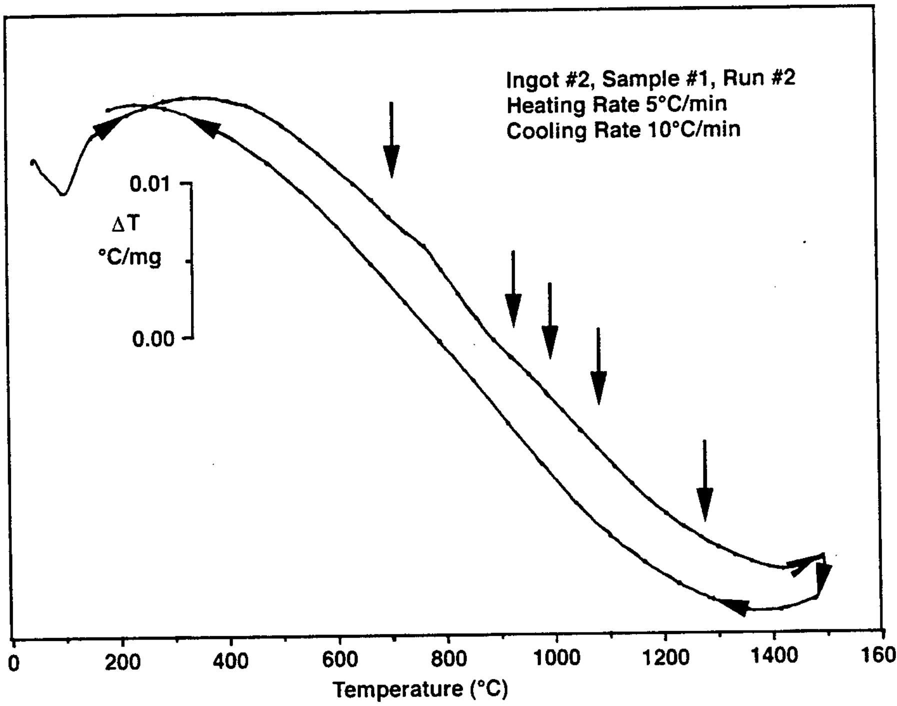

(b)

Figure 4.2. DTA thermograms of (a) alloy #'s 7 (Nb-34Ti-15Al), 11 (Nb-28.3Ti-15Al, and 14 (Nb-17Ti-15Al), (b) alloy #2, (c) alloy #3, and (d) alloy #8.

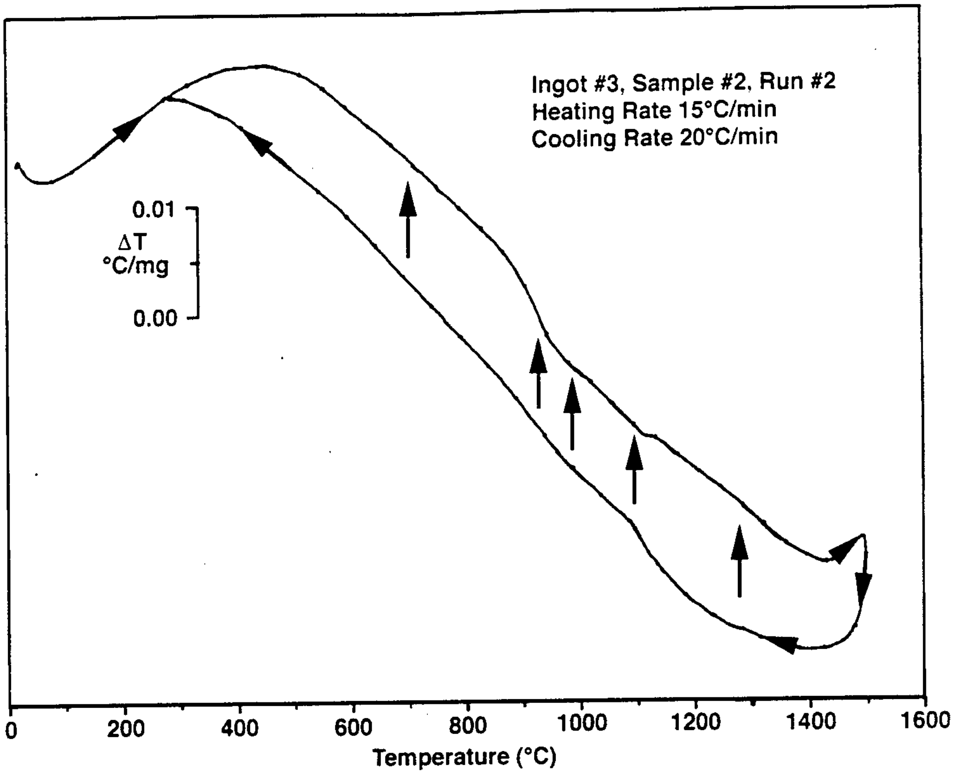

(c)

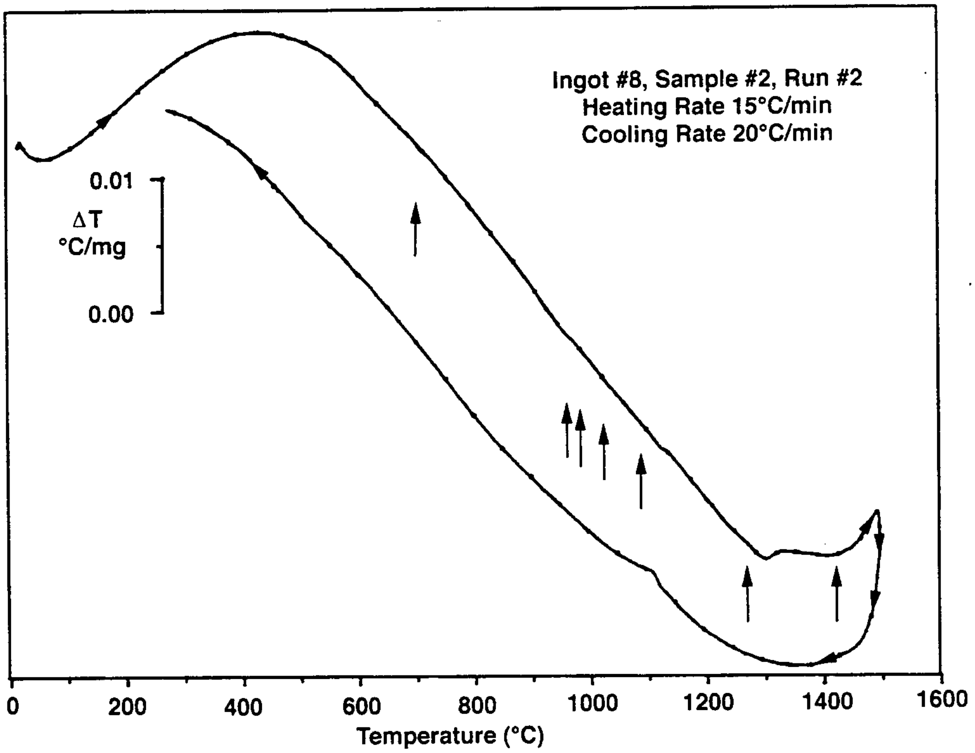

(d)

Figure 4.2. Continued.

subsequent heat treatments did not reveal any transformations. It is believed that the changes observed in the thermogram were the result of oxidation effects rather than changes due to phase boundary crossing.

The DTA scans of alloy #'s 3 and 8 were successful in detecting reactions during the thermal cycles. The thermogram of alloy #3 (Figure 4.2(c)) revealed only one major endothermic transformation on heating. The rate of heating significantly altered the onset and completion of this series of reactions, indicating an influence on the reaction kinetics; with 5°C/min., the onset and completion were 888 and 1112°C respectively.

The DTA thermogram of alloy #8 is presented in Figure 4.2(d). From the thermogram only a single major reaction was observed on heating; a long continuous shallow trough initially observed at 948°C and completing at 1296°C was associated with the precipitation of δ and the subsequent transformation into the single phase β field.

Homogenization of the alloys was conducted through hot isostatic pressing (HIP'ing) at 1475°C, 138 MPa and 6 hours for alloy #'s 11 and 14, and at 1425°C, 138 MPa, and 7 hours for alloy #'s 2, 3, 7 and 8. The furnace cooled HIP'ed material did not contain any δ precipitation, but did contain a small amount of metastable O-phase. A list of the heat treatments performed for each alloy with the corresponding phases present, composition and lattice parameters are contained in Tables 4.1 through 4.3. The photomicrographs of the alloys are presented in Figures 4.3 through 4.8.

The β transus temperatures for the alloys which could not be identified through DTA, were approximately determined through quenching experiments, and estimated from the disappearance of the δ phase with increasing temperature. The β transus temperatures of the alloys are presented in Figure 2.1 in section 2 with the other alloys of this study.

Table 4.1. Compositions and lattice parameters of the phases in alloy #14 (Nb-17Ti-15Al) following heat treatment.

Heat Treatment	Phases	Composition (at.%)	Lattice Parameters (Å)
1100C, 360 hr., WQ	β_o	74.05Nb-19.35Ti-6.60Al	$a_o = 3.277 \pm 0.01$
	δ	68.07Nb-15.66Ti-16.27Al	$a_o = 5.181 \pm 0.02$
900C, 720 hr., WQ	β_o	75.13Nb-16.85Ti-8.02Al	$a_o = 3.266 \pm 0.002$
	δ	67.11Nb-15.08Ti-17.81Al	$a_o = 5.187 \pm 0.03$
1100C + 700C, 1080 hr., WQ	β_o	74.52Nb-18.95Ti-6.53Al	$a_o = 3.259 \pm 0.003$
	δ	64.11Nb-16.94Ti-18.95Al	$a_o = 5.184 \pm 0.005$

Table 4.2. Compositions and lattice parameters of the phases in alloy #11 (Nb-28.3Ti-15Al) following heat treatment.

Heat Treatment	Phases	Composition (at.%)	Lattice Parameters (Å)
1100C, 360 hr., WQ	β_o	52.2Nb-36.43Ti-11.35Al	$a_o = 3.273 \pm 0.002$
	δ	58.03Nb-25.71Ti-16.26Al	$a_o = 5.174 \pm 0.02$
900C, 720 hr., WQ	β_o	59.07Nb-32.82Ti-8.11Al	$a_o = 3.265 \pm 0.001$
	δ	57.09Nb-25.68Ti-17.23Al	$a_o = 5.185 \pm 0.02$
1100C + 700C, 1080 hr., WQ	β_o	57.52Nb-32.95Ti-9.53Al	$a_o = 3.261 \pm 0.001$
	δ	58.53Nb-23.38Ti-18.09Al	$a_o = 5.186 \pm 0.01$

Table 4.3. Compositions and lattice parameters of the phases in alloy #7 (Nb-34Ti-15Al) following heat treatment.

Heat Treatment	Phases	Composition (at.%)	Lattice Parameters (Å)
1100C, 360 hr., WQ	β_o	49.8Nb-38.96Ti-11.24Al	$a_o = 3.274 \pm 0.001$
	δ	56.08Nb-25.24Ti-17.68Al	$a_o = 5.168 \pm 0.02$
900C, 720 hr., WQ	β_o	51.12Nb-37.38Ti-11.5Al	$a_o = 3.319 \pm 0.002$
	δ	53.15Nb-28.35Ti-18.5Al	$a_o = 5.167 \pm 0.001$
1100C + 700C, 1080 hr., WQ	β_o	50.03Nb-39.38Ti-10.08Al	$a_o = 3.315 \pm 0.004$
	δ	57.5Nb-24.99Ti-17.51Al	$a_o = 5.159 \pm 0.02$

Table 4.4. Compositions and lattice parameters of the phases in alloy #2 (Nb-42.5Ti-15Al) following heat treatment.

Heat Treatment	BSEI Contrast	Composition (at.%)				X-ray Results
		Ti	Al	Nb	Phase	Lattice Parameter
1270°C/32h/WQ	Grey	42.63	15.32	42.05	β	$a_0 = 3.263 \pm 0.004$Å
1270°C/32h/WQ + 1090°C/7d/WQ	Grey	43.66	15.44	40.90	β	$a_0 = 3.268 \pm 0.002$Å
1270°C/32h/WQ +	Grey (Matrix)	43.83	15.32	40.86	β	$a_0 = 3.267 \pm 0.002$Å
970°C/31d/WQ	Dark	60.57	24.34	15.08	α_2 (?)	
1270°C/32h/WQ +	Grey (Matrix)	43.88	14.39	41.72	β	$a_0 = 3.278 \pm 0.002$Å
925°C/30d/WQ	Dark	59.72	24.15	16.13	α_2 (?) δ	 $a_0 = 5.160 \pm 0.005$Å
1270°C/32h/WQ + 700°C/30d/WQ	Grey	Structure Too Fine			β	$a_0 = 3.269 \pm 0.001$Å
HIP 1300°C/24h + 1270°C/16.5h/WQ + 700°C/150d/WQ	Grey	Structure Too Fine			β	$a_0 = 3.270 \pm 0.001$Å

Table 4.5. Compositions and lattice parameters of the phases in alloy #3 (Nb-40Ti-20Al) following heat treatment.

Heat Treatment	BSEI Contrast	Composition (at.%)				X-ray Results
		Ti	Al	Nb	Phase	Lattice Parameter
1270°C/32h/WQ	Grey	39.19	21.43	39.37	β	$a_o = 3.261 \pm 0.002$Å
1270°C/32h/WQ + 1090°C/8d/WQ	Grey (Matrix)	45.11	20.04	34.85	β	$a_o = 3.265 \pm 0.015$Å
	Bright	29.90	22.13	47.97	δ	$a_o = 5.173 \pm 0.018$Å
	Dark (GB*) (* = near surface)	59.80	25.10	15.10	α_2 (?)	
HIP1300°C/24h + 1270°C/16h/WQ + 970°C/31d/WQ	Grey (Matrix)	47.19	19.59	33.22	β/O	
	Bright	33.15	21.90	44.95	δ	$a_o = 5.170 \pm 0.001$Å
	Dark	59.07	25.49	15.44	α_2 (?)	d = 2.2185 α_2?
HIP1300°C/24h + 1270°C/16h/WQ + 925°C/30d/WQ	Grey (Matrix)	47.85	16.24	35.00	β	$a_o = 3.266 \pm 0.004$Å
	Bright	33.13	20.94	45.94	δ	$a_o = 5.170 \pm 0.001$Å
	Dark	50.39	24.70	24.91	O (?)	d = 2.2185 α_2?
1270°C/32h/WQ +	Grey (GI)	37.32	15.40	47.29	β	$a_o = 3.273 \pm 0.009$Å
920°C/14d/WQ	Dark (GI)	41.05	24.99	33.96	O (?)	
	Grey (GB)	47.40	15.51	37.09	β	$a_o = 3.273 \pm 0.009$Å
	Bright (GB)	32.64	21.13	46.23	δ	$a_o = 5.177 \pm 0.005$Å
	Dark (GB)	51.64	23.85	24.51	O (?)	
1270°C/32h/WQ + 700°C/30d/WQ	Grey	Structure Too Fine			β(?)	$a_o = 3.261 \pm 0.003$Å
HIP1300°C/24h + 1270°C/16h/WQ + 700°C/150d/WQ	Grey	Structure Too Fine			β	$a_o = 3.289 \pm 0.014$Å
					O	$a_o = 6.103 \pm 0.025$Å $b_o = 9.522 \pm 0.068$Å $c_o = 4.695 \pm 0.013$Å

GI = Grain Interior
GB = Grain Boundary

Table 4.6. Compositions and lattice parameters of the phases in alloy #8 (Nb-32Ti-20Al) following heat treatment.

Heat Treatment	BSEI Contrast	Composition (at.%)				X-ray Results
		Ti	Al	Nb	Phase	Lattice Parameter
1425°C/7h/OQ	Grey	32.27	19.23	48.51	β	$a_o = 3.262 \pm 0.002$Å
1270°C/32h/WQ	Grey	33.33	20.02	46.65	β	$a_o = 3.258 \pm 0.002$Å
	Bright (***)	23.14	21.81	55.05	δ	$a_o = 5.179 \pm 0.0003$Å
1425°C/7h/OQ + 1090°C/7d/WQ	Grey (Matrix)	44.60	18.73	36.67	β	$a_o = 3.262$Å (211)
	Bright	30.01	20.91	49.08	δ	$a_o = 5.173 \pm 0.001$Å
	Dark (***)	59.25	24.00	16.75	α_2	
1425°C/7h/OQ + 1025°C/14d/WQ	Grey	Too Fine			β	$a_o = 3.260$Å (211)
	Bright	30.58	21.86	47.56	δ	$a_o = 5.171 \pm 0.001$Å
	Dark (*)	56.12	24.09	19.78	α_2	d = 2.2181 (40.64 2θ)
1425°C/7h/OQ + 990°C/14d/WQ	Grey (*)	44.95	16.65	38.39	β	$a_o = 3.261$Å (211)
	Bright (***)	30.92	21.76	47.33	δ	$a_o = 5.171 \pm 0.001$Å
	Dark (*)	54.66	24.50	20.84	α_2	d = 2.2178 (40.64 2θ)
1425°C/7h/OQ + 970°C/14d/WQ	Grey (*)	43.91	15.55	40.54	β	
	Bright	30.85	21.40	47.75	δ	$a_o = 5.172 \pm 0.001$Å
	Dark (*)	43.68	22.93	33.39	α_2	d = 2.2175 (40.65 2θ)
1425°C/7h/OQ + 700°C/30d/WQ	Grey	Structure Too Fine			β	$a_o = 3.272 \pm 0.003$Å
1425°C/7h + 1425°C/3h/OQ + 700°C/150d/WQ	Grey	Structure Too Fine			β	$a_o = 3.275 \pm 0.013$Å
					O	Present
1270°C/32h/WQ + 700°C/30d/WQ	Grey	33.44	21.69	44.88	β	$a_o = 3.265 \pm 0.004$Å
	Bright	23.46	23.43	53.11	δ	

*= Best value   *** = Avg. of best three measurements

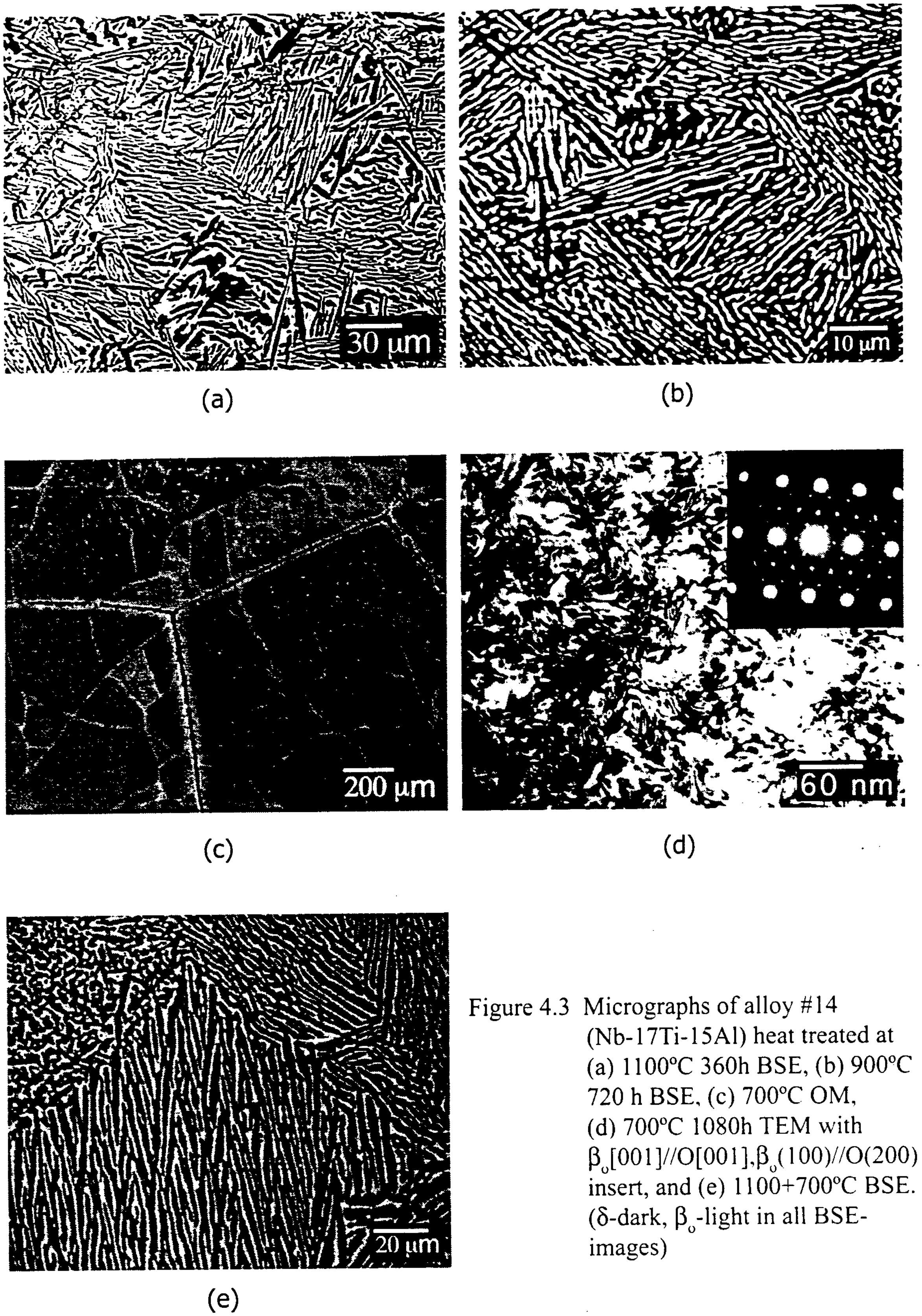

(a) (b)

(c) (d)

(e)

Figure 4.3 Micrographs of alloy #14 (Nb-17Ti-15Al) heat treated at (a) 1100°C 360h BSE, (b) 900°C 720 h BSE, (c) 700°C OM, (d) 700°C 1080h TEM with $\beta_o[001]//O[001],\beta_o(100)//O(200)$ insert, and (e) 1100+700°C BSE. (δ-dark, β_o-light in all BSE-images)

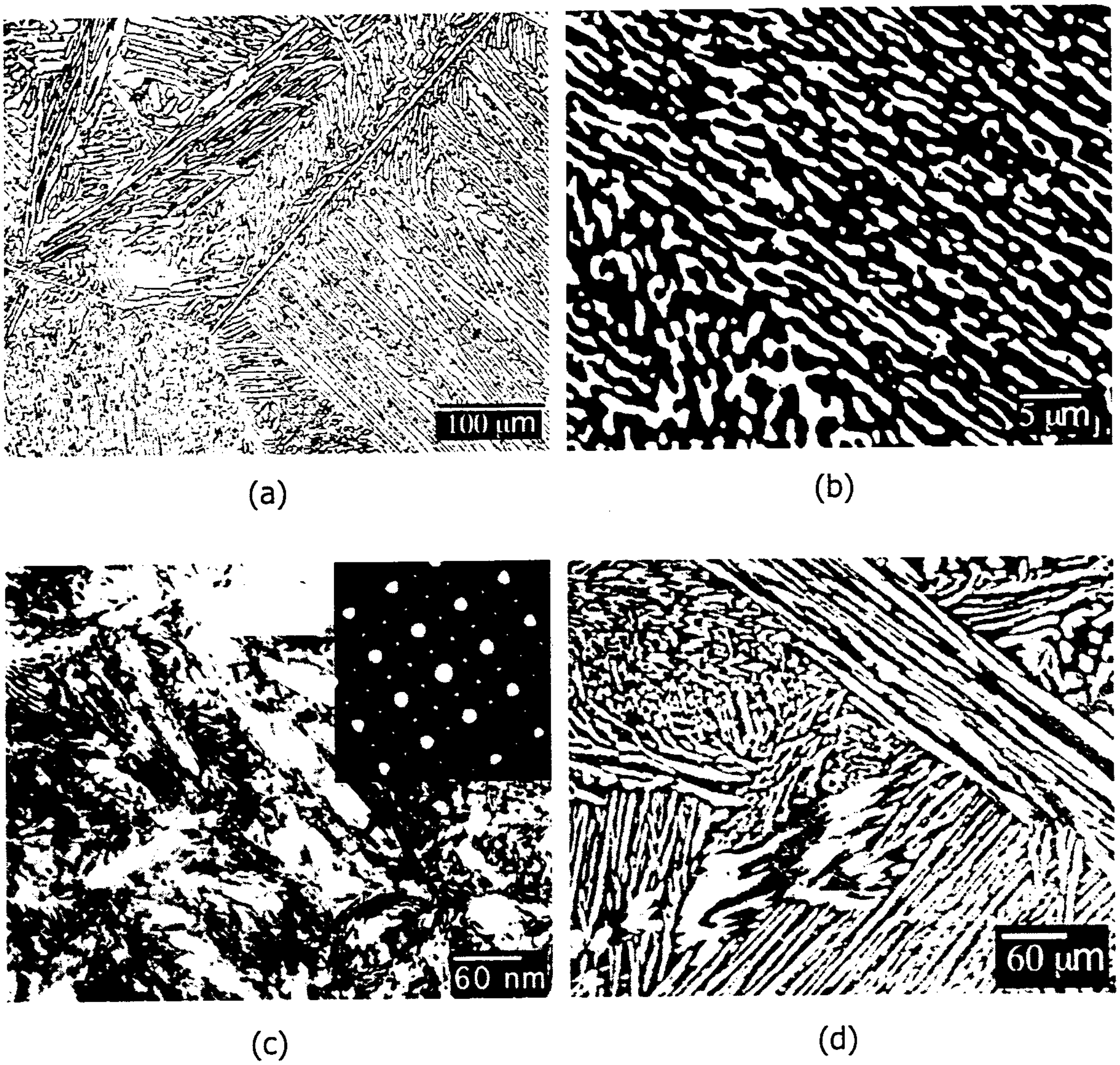

(a) (b)

(c) (d)

Figure 4.4 Micrographs of alloy #11 (Nb-28.3Ti-15Al) heat treated at (a) 1100°C 360 h OM, (b) 900°C 720h BSE, (c) 700°C 1080h TEM with $\beta_o[100]//O[100]$ and (d) 1100+700°C BSE. (δ-bright, β_o-dark in BSE-images)

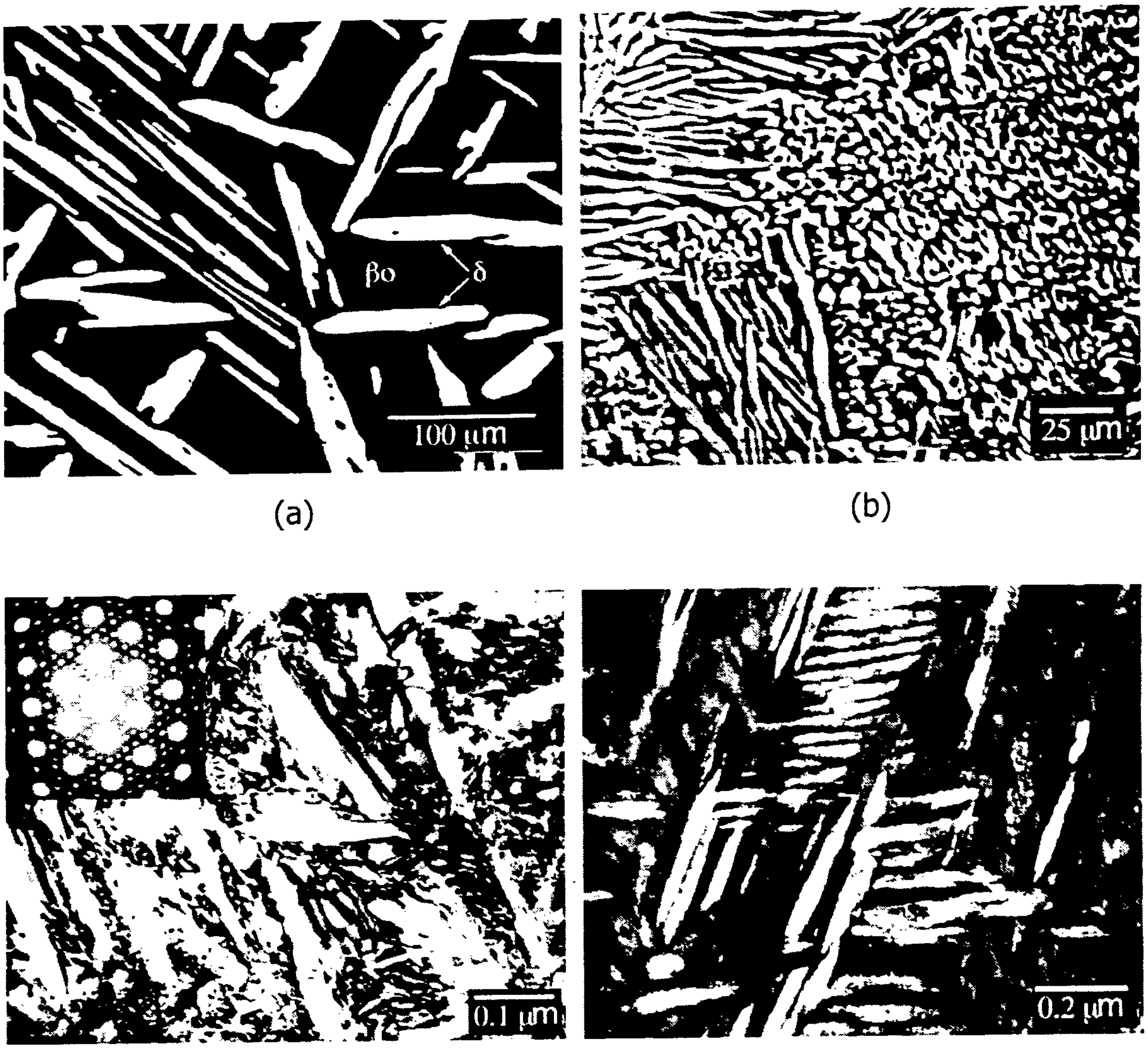

(a)

(b)

(c)

(d)

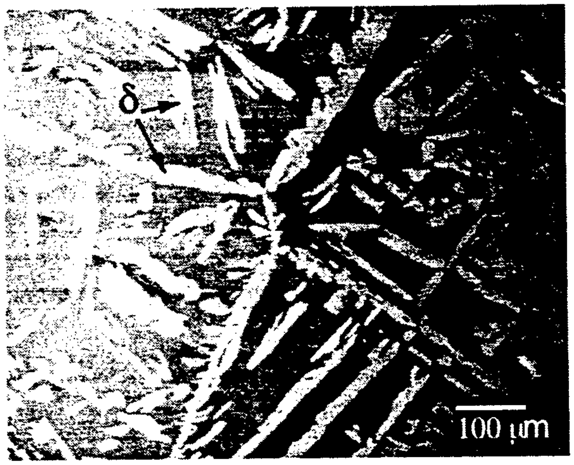

(e)

Figure 4.5 Micrographs of alloy #7 (Nb-34Ti-15Al heat treated at (a) 1100°C 360h BSE, (b) 900°C 720h BSE, (c) 700°C for 1080 hr. TEM with $\beta_0[111]//O[110]$ insert, (d) 700°C for 2280 hr. TEM, and (e) 1100+700°C BSE.

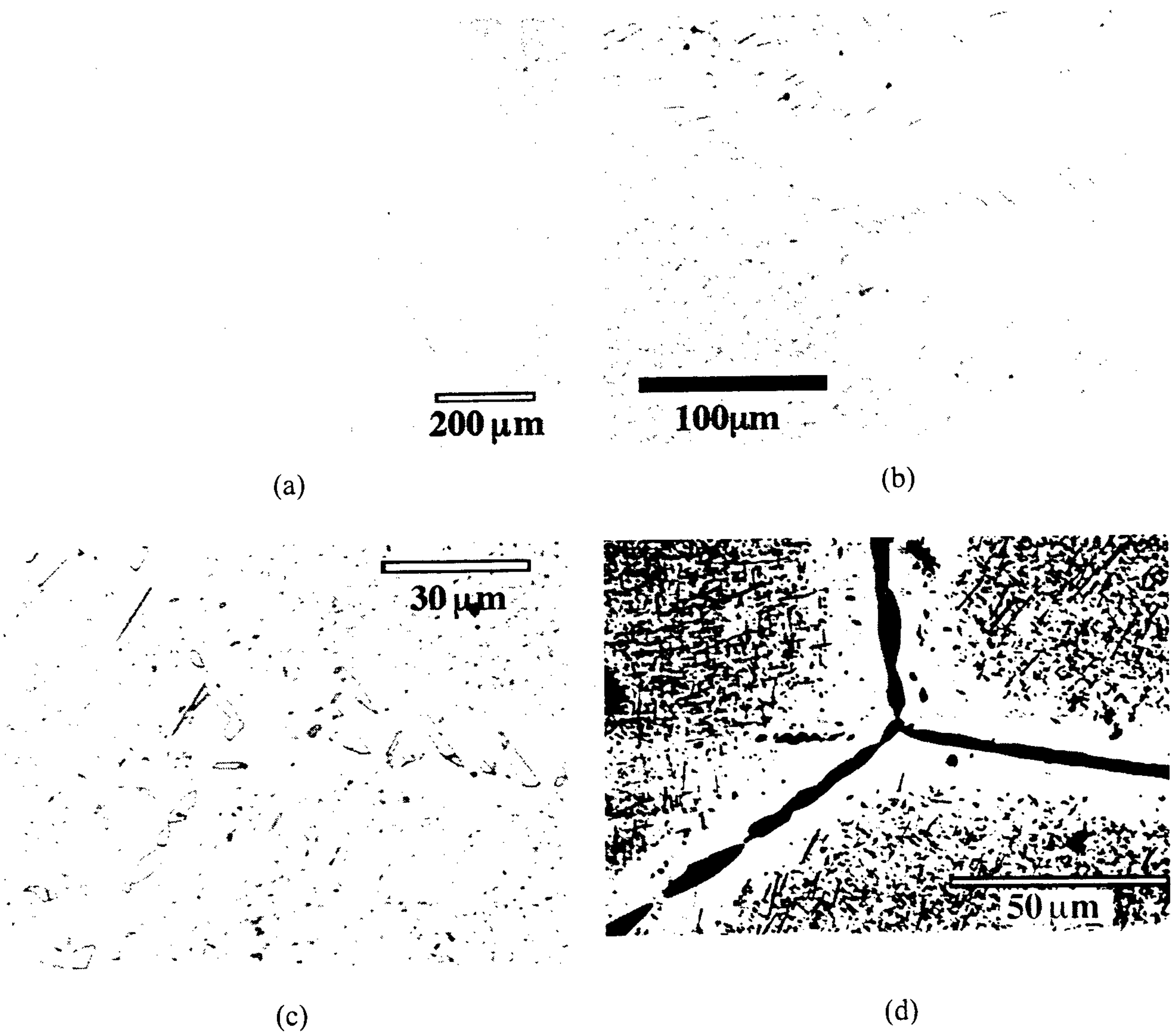

Figure 4.6. Micrographs of alloy #2 (Nb-42.5Ti-15Al): (a) 1270°C 32h OM, (b) 1270+970°C 744h OM of area near surface, (c) OM and (d) BSE-images of 1270+970°C 744h material showing the denuded zone along grain boundaries.

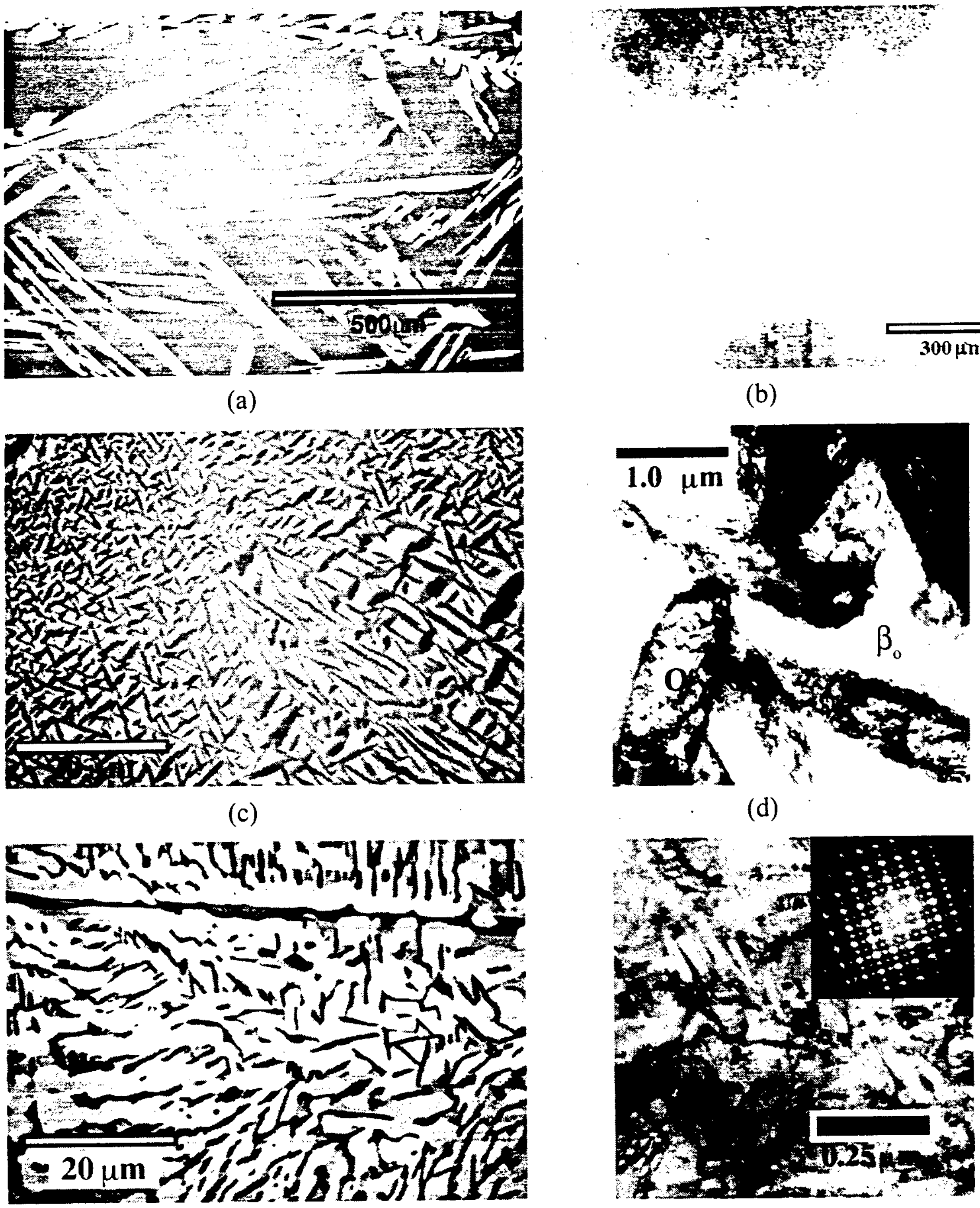

(a) (b) (c) (d) (e) (f)

Figure 4.7. Micrographs of alloy #3 (Nb-40Ti-20Al). (a) 1270+1090°C 192h BSE, (b) 1270+920°C 336h OM of grain boundary area revealing δ phase precipitation, (c) BSE image of grain interior of 1270+920°C 336h material showing O phase precipitation in β_o, (d) TEM image of grain interior region of (c), (e) BSE-image of grain boundary area in 1270+920°C 336h material showing δ(light) β_o(med.) and O(dark), and (f) TEM image of O/β_o structure in 1270+700°C 720h material with insert showing β_o[100] // O[100] SAD patterns.

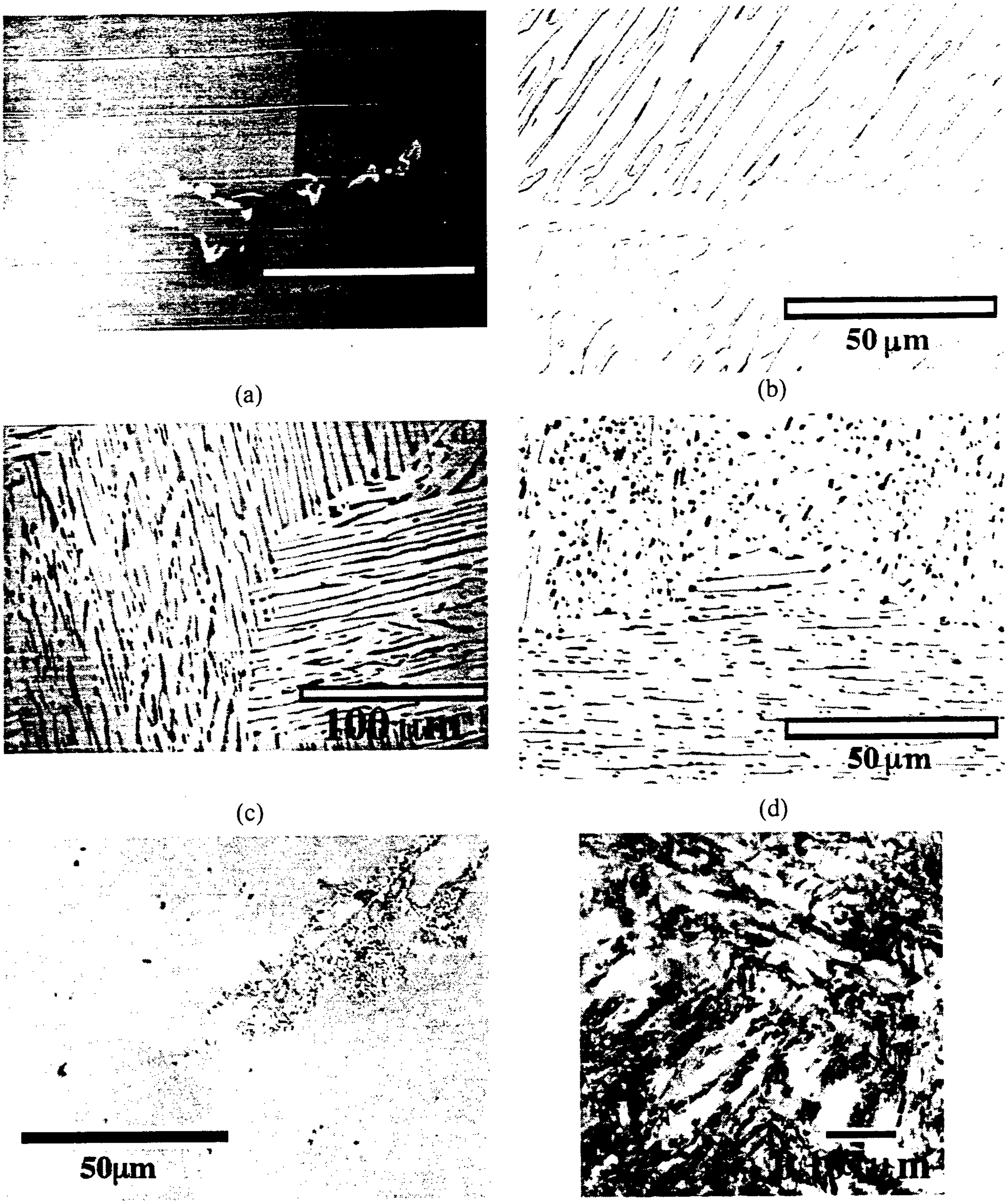

(a)

(b)

(c)

(d)

(e)

(f)

Figure 4.8. Micrographs of alloy #8. (a) BSE image 1270°C 32h, (b) OM 1090°C 168h of the interior region, (c) BSE-image 1090°C 168h near the surface showing α_2 (dark) contamination,(d) OM 970°C 336h showing three phases, (e) OM 700°C 3600h δ nucleation at grain boundaries,and (f) TEM BF-image 700°C 3600h of O laths in β_o.

4.3 The β/β_o Transition Temperatures

The approximate transition temperatures between the disordered solid solution (β) and the B2 ordered solid solution (β_o) phases were estimated for alloy #'s 7, 11 and 14. Heat treatments were conducted on the homogenized material at 900, 950 and 1000°C followed by water quenching. To prevent excessive transformations from occurring in the β/β_o phase, the heat treatments were limited to 30 minutes. Although the treatments were short, further precipitation of the orthorhombic Ti_2AlNb phase was observed in several samples. Anti-phase boundaries (APB's) were imaged under two-beam dark-field (DF) conditions, using the g=100 reflection. The average size of the ordered domains was determined from a random throw method of five dipoles. The domain sizes were calculated from the number of APB interceptions (n) occurring over the length of the dipole (L) corrected for magnification (Eq. 4.1).

$$\text{Domain size} = L/(n-1) \qquad \text{(eq. 4.1)}$$

A sudden decrease in the average domain size with progressively increasing temperature indicated that ordering had occurred on cooling. The smaller domain size was the result of the shortened time in which the ordered domains could grow below the transition temperature (Figure 4.9). It was determined that for the alloy #'s 7 and 11, the transition temperatures were between 950 and 1000°C. The transition temperature decreased to between 900 and 950°C for alloy #14.

4.4 Microhardness of the β_o Phase

Microhardness of the β_o phase also showed a dependence on composition for alloy #'s 7, 11 and 14, as illustrated in Figure 4.10. Microhardness measurements were conducted on a LECO M-400-H1 Vickers diamond pyramid indentor, under a 1 kg load held for 15 seconds. For the #7, 11 and 14 alloys that contained 15 at.% Al, decreasing the Nb:Ti ratio led to a decrease in hardness from 302 kg/mm^2 in alloy #14 to 272 kg/mm^2 in alloy #7.

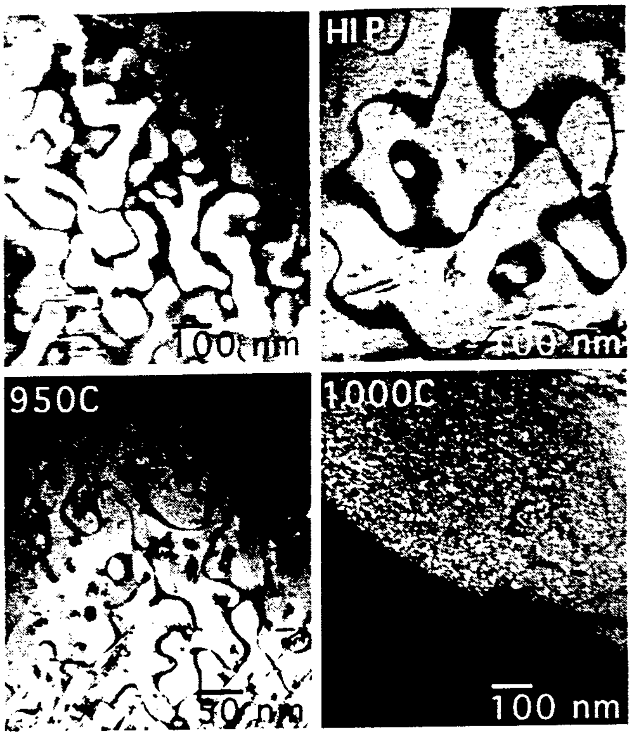

Figure 4.9. Representative changes in the ordered domain sizes with temperature as observed for alloy # 11.

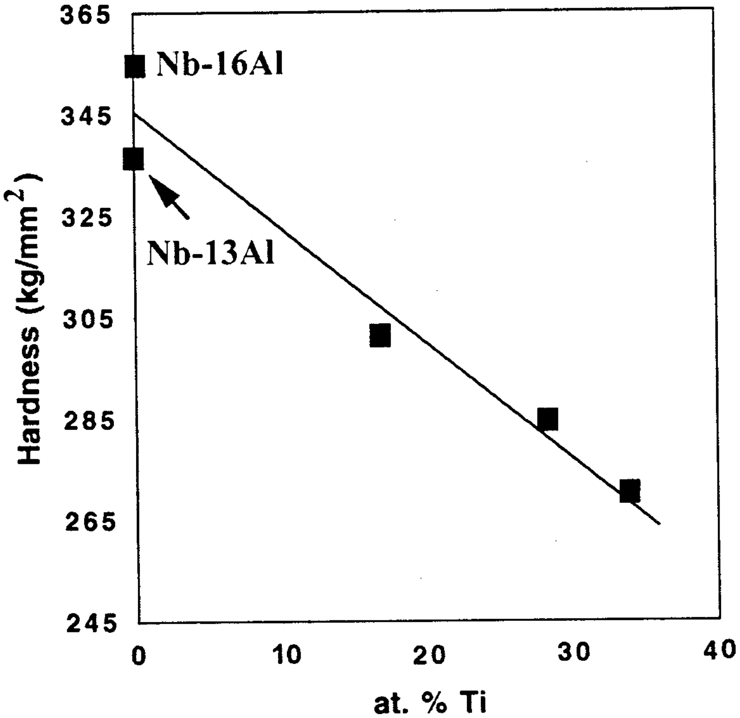

Figure 4.10. Variation in microhardness of the β_0 phase with Ti concentration for Nb-xTi-15Al alloys. Nb-13Al and Nb-16Al from ref. [12].

4.5 Phase Equilibria at 1100°C

The homogenized alloys were heat treated at 1100°C for times as long as 360 hours followed by water quenching. All alloys, except #2, were determined to be in the $\beta_o + \delta$ phase field, with tie-line information presented in Figure 4.11. At 1100°C, the microstructure of alloy #14 consisted mostly of δ (dark contrast in Figure 4.3(a)) with an almost plate-like appearance. The predominance of the δ phase in this alloy at this temperature is also reflected in the tie-line compositions with respect to the alloy composition.

The $\beta + \delta$ tie-lines of alloy #'s 11 and 7 showed a dramatic change in orientation with respect to alloy #14. The change in slope, however, was predicted [15] as the $\beta + \delta$ phase field moves away from the Nb-Al binary towards the $\beta + \delta + \sigma$ phase field. The microstructures observed in alloys #11 (Figure 4.4(a)) and #7 (Figure 4.5(a)) correspond well to the positioning of the tie-lines based on the lever rule. The composition of the β phase boundary in both alloy #'s 7 and 11 was determined to extend to a lower Al concentration than that of the calculation, although long term aging of $\beta + \delta$ alloys of binary and ternary systems [10] also have shown a decrease in Al concentration within the β phase with respect to the current phase diagrams [15, 37].

It is evident from the shape of the β+δ phase boundary (Figure 4.11) that alloy #2 was still within the single phase β field at 1100°C. On the other hand, alloy #'s 3 and 8 (Figures 4.7 and 4.8) define the limit of the $\beta + \delta$ phase field leading to the $\beta + \sigma + \delta$ three-phase field, for which alloy #9 (to be discussed in the following chapter) is positioned within at 1100°C.

4.6 Phase Equilibria at 900°C

At 900°C, alloy #'s 7 and 8 were still within the $\beta_o + \delta$ phase field, but moved even closer to the $\beta + \delta + O$ three-phase field (Figure 4.12) such that alloy #3 now falls within this field around 950°C (Figure 4.7(b)). The microstructure of alloy #7 (Figure 4.5(b)) consisted of the β_o and δ phases, with an increase in the volume of δ as compared to the structure observed at 1100°C. The microstructure of alloy #8 at 970°C consisted of the equilibrium $\beta_o + \delta$ phases but also contained some α_2, likely caused by oxygen contamination (Figure 4.8(c)). Both alloy #'s 14 and 11 were

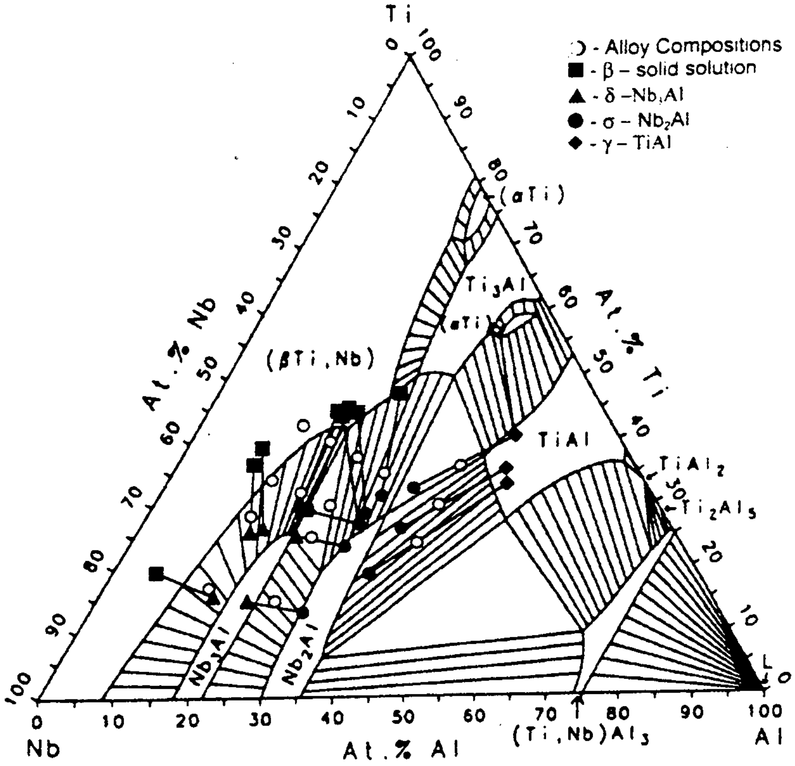

Figure 4.11. The 1100°C tie-line compositions of the β + δ alloys plotted with other alloys investigated against the calculated diagram of Kattner and Boettinger [15]

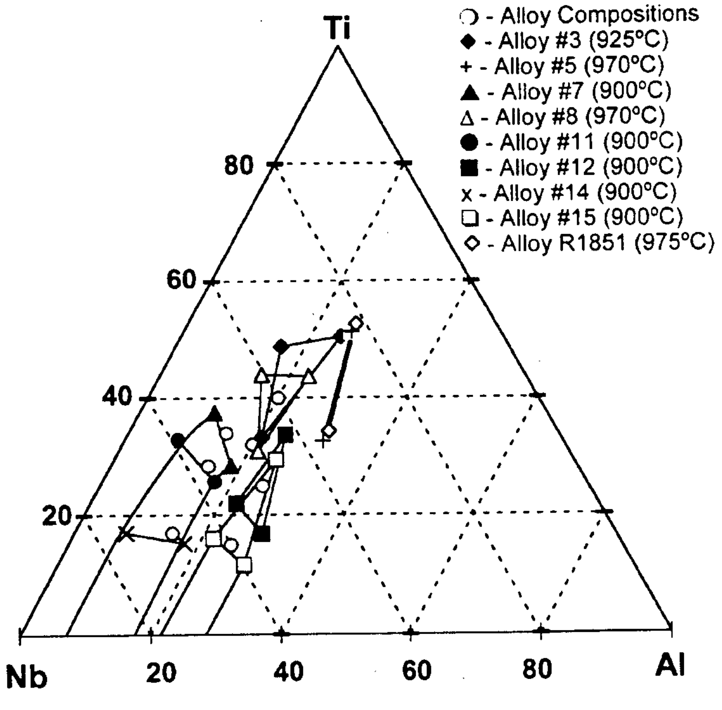

Figure 4.12. The 900°C tie-line compositions of the β + δ alloys plotted against the calculated diagram of Kattner and Boettinger [15]

within the $\beta_o + \delta$ phase field as well, and displayed similar microstructures to alloy #7 (Figures 4.3(b) and 4.4(b)).

At 900°C, alloy #3 showed a change in the microstructure from the prior β_o grain boundaries toward the grain interiors, indicating insufficient time to produce a completely homogenous microstructure throughout the sample (Figure4.7(b)). While the grain boundary regions contained the expected δ and O precipitation, with δ forming first along the β_o grain boundaries (Figure 4.7(e)), the grain interiors underwent O precipitation only (Figure 4.7(c,d)). A change in the compostion of the O phases was observed, with the O phase in the grain interior being close to the composition of the parent β_o phase.

4.7 Phase Equilibria at 700°C

Aging the six alloys at 700°C for 1080 hours did not produce the phase equilibria predicted by the calculated diagrams [15]. All alloys underwent a partial transformation into the O phase, producing plates of O within a β_o matrix (Figures 4.3(c,d), 4.4(c), 4.5(c), 4.7(f) and 4.8(f)). No compositional contrast was observed under BSEI conditions, and only a staining or darkening of the surface occurred on etching prior to OM. An apparent subgrain formation was visible through OM (Figure 4.3(c)), however, the size of the O plates within the β_o matrix were too fine to be revealed through OM but were more easily observed through TEM under DF or two-beam imaging conditions.

The O plates exhibited a martensite-like structure with multiple variants, and held a β_o[011] // O[001], β_o(100) // O(200) orientation relationship. The size of the O plates within the alloys increased with Ti concentration, due to increased diffusion rates within the material. The β_o matrix exhibited a high degree of contrast due to the strain imposed on it from the formation of the O plates, making it difficult not only to visualize the O phase in several of the alloys, but in estimating the relative volume fraction of O contained within each. Further aging of the material at 700°C for another 1200 hours, i.e. 2280 hours total, did not lead to any precipitation of the expected δ phase, except in alloy #8 along the β grain boundaries (Figure 4.8(e)). Only an increase in the size of the

O plates was observed as a result of this further aging (Figure 4.5(d)).

To avoid the formation of metastable O, and to determine the likely phase equilibria at 700°C, the 1100°C material for alloy #'s 7, 11 and 14 were heat treated again at 700°C for 1200 hours. The resulting microstructures all contained a two-phase $\beta + \delta$ structure, similar to that of the original 1100°C treatments of each alloy (Figures 4.3(e), 4.4(d), and 4.5(e)), with the exception of the alloy #14 which showed a more coarsened δ structure following the second treatment. Compositional analysis of the two-step treated samples revealed the δ and β_o compositions in alloy #'s 11 and 14 to be nearly the same as the compositions determined from the 900°C aged samples (Tables 4.1 through 4.3 and Figure 4.13). The β/δ tie-line of alloy #7, however, is slightly detached from the point marking the alloy composition. While no other phases were observed in the microstructure through BSEI and TEM, the possible presence of O, which cannot be excluded, may have shifted the compositions of β_o and δ to higher Nb concentrations.

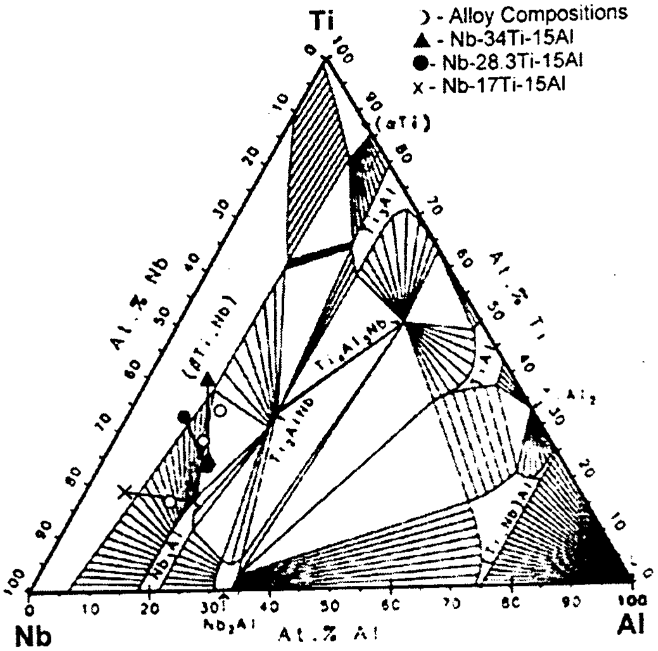

Figure 4.13. Tie-lines of alloy #'s 7, 11 and 14 double aged at 1100+700°C, plotted against the calculated 700°C diagram of Kattner and Boettinger [15].

5. Phase Equilibria and Transformations Involved in Alloys Containing the $\beta \rightarrow \sigma + \delta$ Eutectoid Reaction and the Development of the Four-Phase Plane (alloys 4, 9, 12 and 15)

5.1 The $\beta + \sigma + \delta$ Phase Field

Four of the alloys investigated (#'s 4, 9, 12 and 15) contained the $\beta \rightarrow \sigma + \delta$ eutectoid reaction which is formed by the convergence of the peritectic $L + \beta \rightarrow \delta$ and $L + \delta \rightarrow \sigma$ liquidus trough reactions (Figure 5.1). The movement of the $\beta + \sigma + \delta$ phase field through the ternary to higher Ti concentrations with decreasing temperature was recorded through DTA and subsequent heat treatments. A four-phase plane involving the $O + \beta_o + \sigma + \delta$ phases occurring at 980°C in alloy 4 has also been identified. The phase equilibria occurring above and below the $\beta \rightarrow \sigma + \delta$ eutectoid were investigated for each alloy down to 700°C.

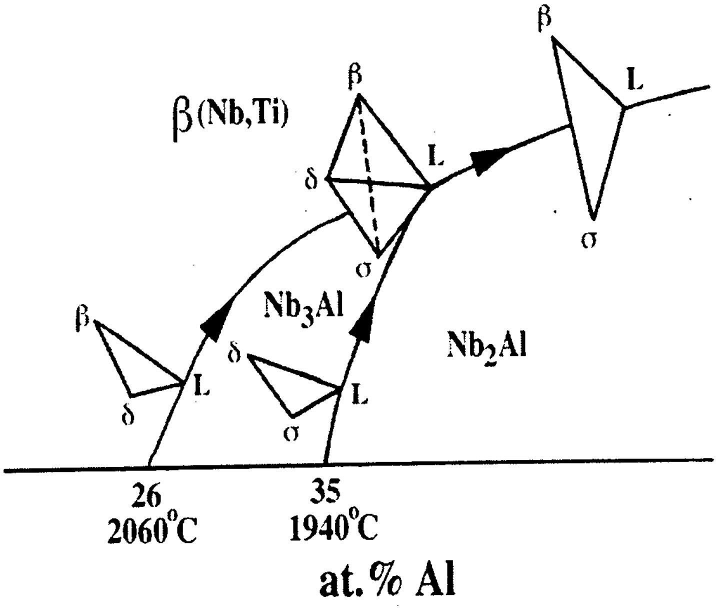

Figure 5.1. Movement of the binary peritectic reactions defining the boundary of the primary δ solidification field.

5.2 Homogenization and Solution Treatments

All four alloys, (#'s 4, 9, 12 and 15) consisted of the β phase at elevated temperatures. The single phase β field was not obtainable in alloy 15, due to furnace and encapsulation limitations.

Therefore, the material HIP'ed at 1475°C and 138 MPa for 7 hours was used as the starting structure (Figure 5.2). A typical X-ray diffraction pattern of the other three β solutionized alloys is presented in Figure 5.3(a). No $\beta_o\{100\}$ peaks were observed in the X-ray scans for the three alloys. The microstructures consisted of large equiaxed grains (Figure 5.3(b)), which were confirmed through TEM to have ordered to β_o (B2) on quenching. Anti-phase boundaries were easily observed using the $\{100\}$ superlattice reflections. Alloy 4 showed some evidence of a relaxation of lattice constants leading to the initiation of ω phase formation, as evidenced by diffuse streaking observed in the <112> directions of the $\beta_o[110]$ selected area diffraction (SAD) pattern (Figure 5.3(c)). The metastable β_o phase was used as the starting phase for the subsequent aging treatments of alloys 4, 9 and 12.

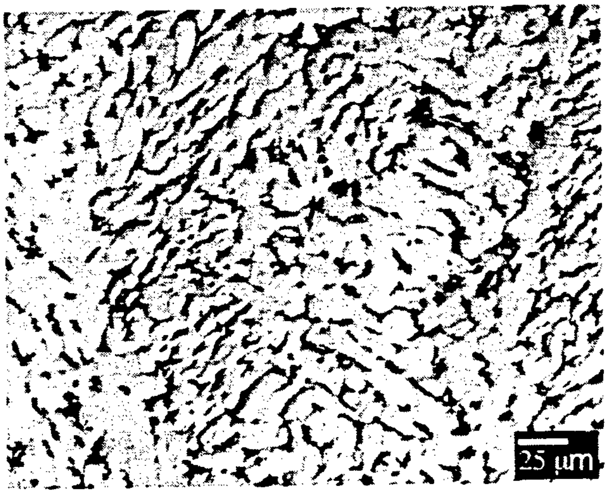

Figure 5.2. OM micrograph of alloy #15, HIP'ed at 1475°C, 138MPa for 6 hrs. (σ phase appearing dark)

5.3 Phase Transformations and Equilibria in Alloy #15

The DTA thermograms of alloys 4, 9, 12 and 15 are presented in Figure 5.4. The DTA scan of alloy 15 did not reveal any exo- or endothermic peaks up to 1500°C (Figure 5.4(a)). Although, the phase equilibria in alloy 15 did change at temperatures lower than this, the total volume fraction change was not sufficient to produce a detectable signal. Alloy 15 consisted of δ + σ above 900°C (Figure 5.5(a)) up to 1540°C, where the β + δ + σ phase field was observed through quenching

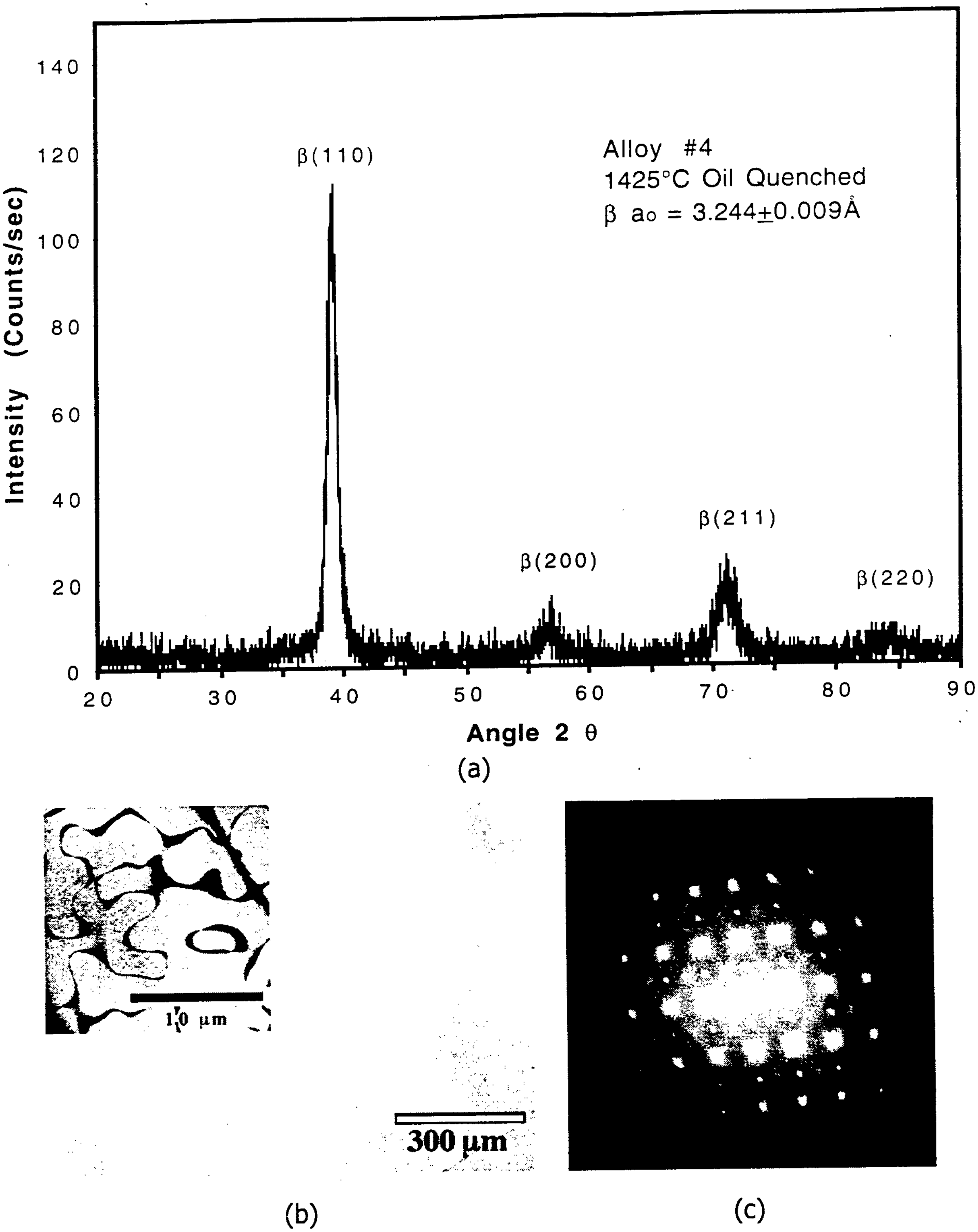

(a)

(b)

(c)

Figure 5.3. Representative structures of solutionized alloy #'s 4, 9 and 12. (a) XRD pattern of BCC β reflections, (b) TEM micrograph of alloy #4 revealing β_o (B2) ordering with insert showing APB's, and (c) β_o[110] SAD pattern of alloy #4 showing ω streaking.

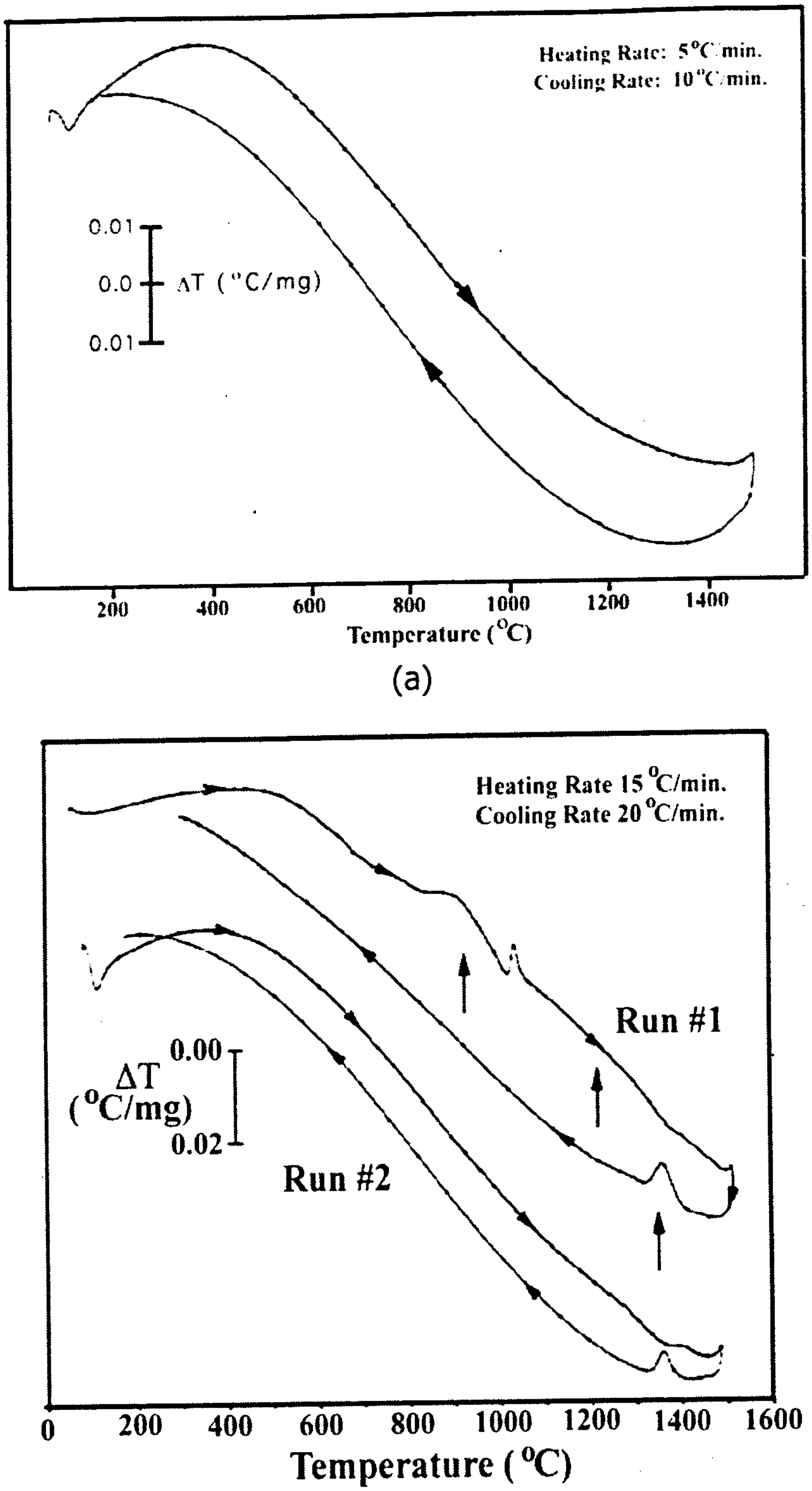

(b)

Figure 5.4. DTA thermograms of (a) alloy 15, (b) alloy 12, (c) alloy 9, and (d) alloy 4.

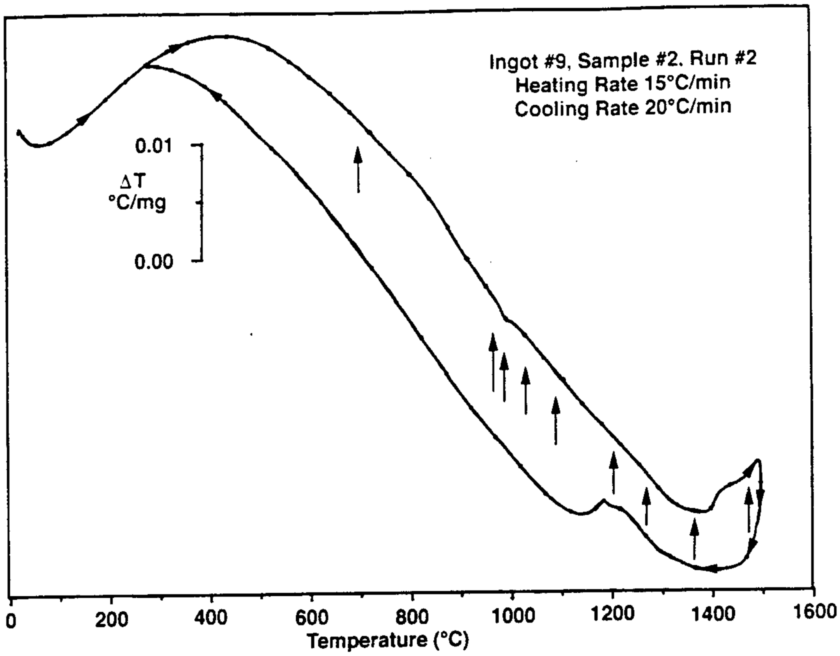

(c)

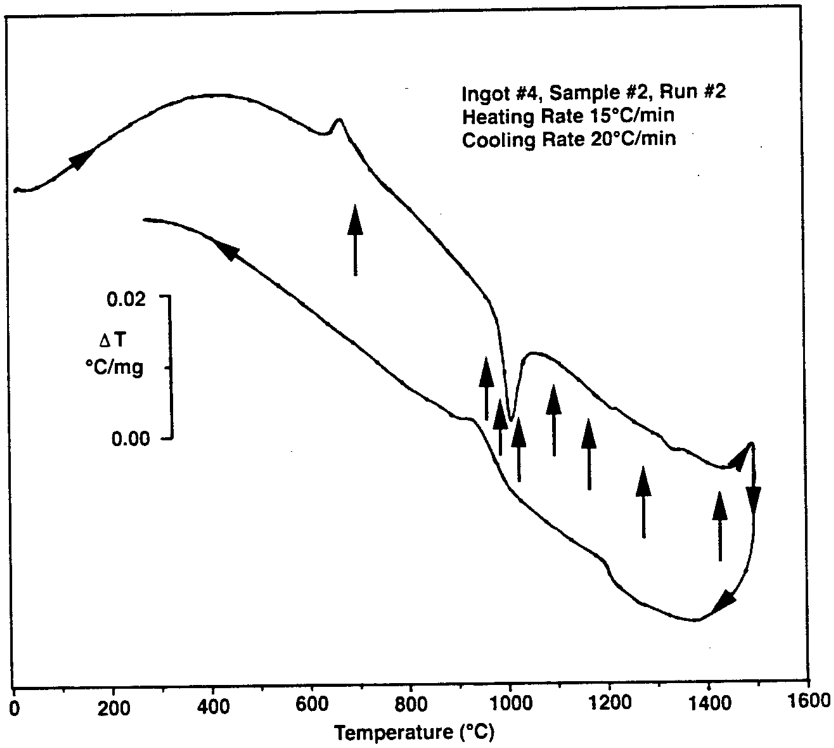

(d)

Figure 4. Continued.

Table 5.1. The phases present following isothermal treatments, their compositions and lattice parameters based on XRD for the Nb-15Ti-25Al alloy.

Heat Treatment	Phases	Composition (at.%)	Lattice Parameters (Å)
1100°C, 360 hr., WQ	δ	63.77Nb-14.91Ti-21.32Al	a_o = 5.184±0.002
	σ	57.02Nb-13.23Ti-29.75Al	a_o = 9.969±0.03 c_o = 5.172±0.002
900°C, 720 hr., WQ	δ	62.15Nb-16.05Ti-21.80Al	a_o = 5.181±0.001
	σ	59.73Nb-11.63Ti-28.64Al	a_o = 9.970±0.003 c_o = 5.185±0.002
	O	45.71Nb-29.37Ti-24.92Al	N/D*
700°C, 1080hr., WQ	δ	63.50Nb-14.17Ti-22.33Al	a_o = 5.182±0.002
	σ	61.12Nb-9.56Ti-29.32Al	a_o = 9.957±0.003 c_o = 5.174±0.002
	O	46.51Nb-29.46Ti-24.03Al	N/D

*N/D: not enough data from XRD scan to accurately determine lattice parameters

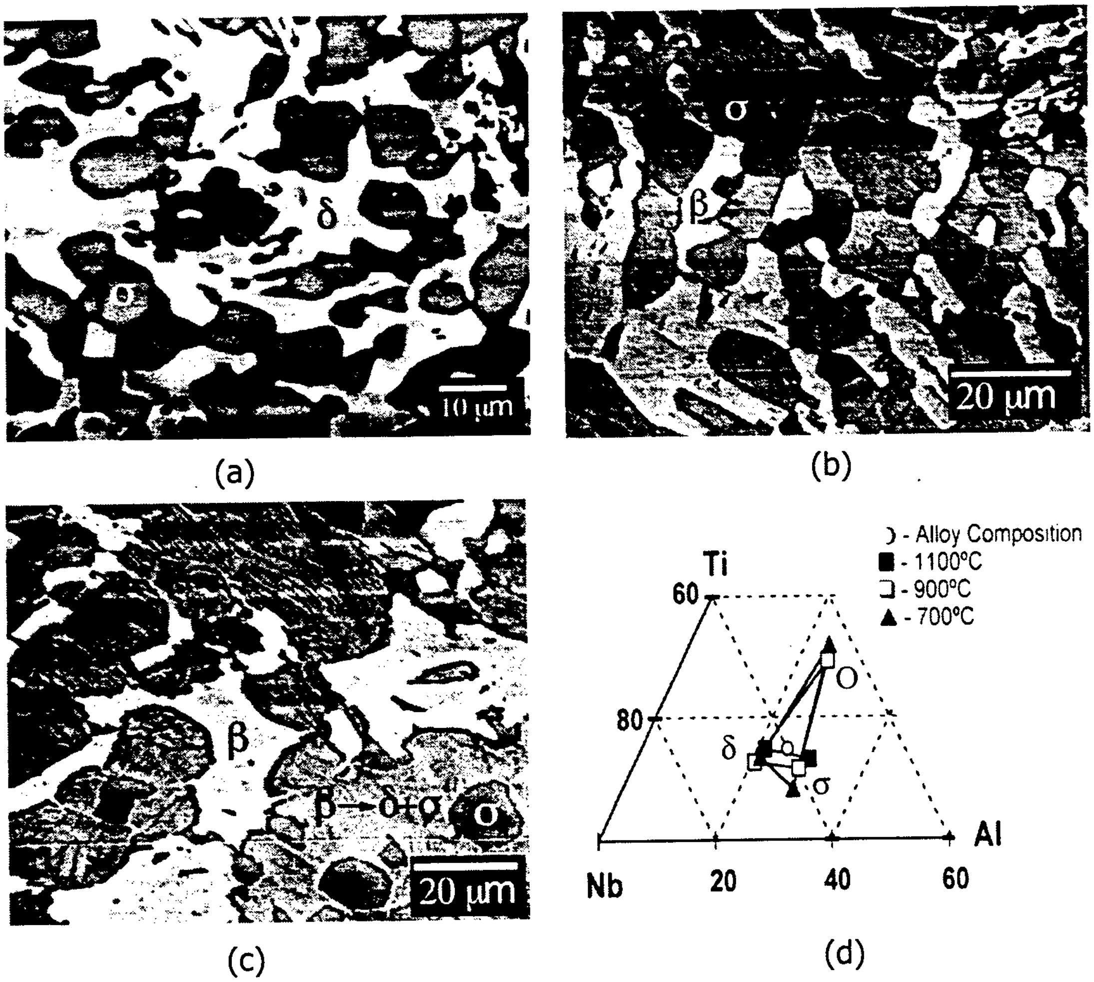

Figure 5.5. BSE-images of Alloy #15: (a) 1100°C, 360h, WQ, (b) 1540°C, 0.5h, WQ, (c)1575°C, 0.5h, WQ, and (d) experimental tie-lines of various long term treatments

experiments (Figure 5.5(b)), which remained until 1575°C where upon the β + σ phase field was located (Figure 5.5(c)). Upon quenching from 1575°C, some of the β did transform back into the δ + σ lamellar structure, the result of cooling through the eutectoid reaction. The phases present in the alloy and the temperatures over which they occured are listed in Table 5.1.

The δ + σ structure formed on aging alloy #15 at 1100°C for 360 hours, (Figure 5.5(a)) was very similar to the homogenized material with no perceptible change in the volume percentage of the constituent phases. The Ti concentration in both δ and σ phases at this temperature were nearly equal, and are represented in tie-line form in Figure 5.5(d).

Aging alloy #15 below 1100°C caused the precipitation and growth of the O phase as predicted by the calculations of Kattner and Boettinger [15]. The 900°C aged material contained small grains of O between the δ and σ (Figure 5.6(a)). The presence of O within the structure, however, could not be positively identified through XRD, due mainly in part to the large number of diffraction peaks produced from the σ crystal structure (Figure 5.7). Nevertheless, the O phase was identified through electron diffraction. A $\delta[21\bar{4}]$ // O[110], δ(201) // O(002) orientation relationship was observed between the δ and O phases (Figure 5.6(b)). No orientation relationship could be precisely identified between the O and σ phases. The 700°C aged samples had a similar microstructure to that of the 900°C material when imaged using back-scattered electrons (Figure 5.8(a)). Closer examination by TEM, however, revealed a plate like morphology located within the tri-junctions between σ and δ grains (Figure 5.8(b)). Electron diffraction patterns taken of this area revealed the plates to be that of the O phase (Figure 5.8(c)), but the intensities of the diffracted planes mimicked that of a β_o/O structure. It is impossible for the β_o phase to have been present at this temperature, and it cannot be considered as a remnant left over as a result of homogenizing at 1475°C, since the β phase was not present in this alloy until above 1500°C, and confirmed through analysis of the homogenized material both by BSE imaging and TEM analysis. The diffracted intensities produced by the multiple variants of the O phase were assumed to have caused the appearance of β_o phase reflections within the [001] and [100] zone axis patterns. The observation of O plates at 700°C and not at 900°C may indicate the mode of formation of the O grains, prior to

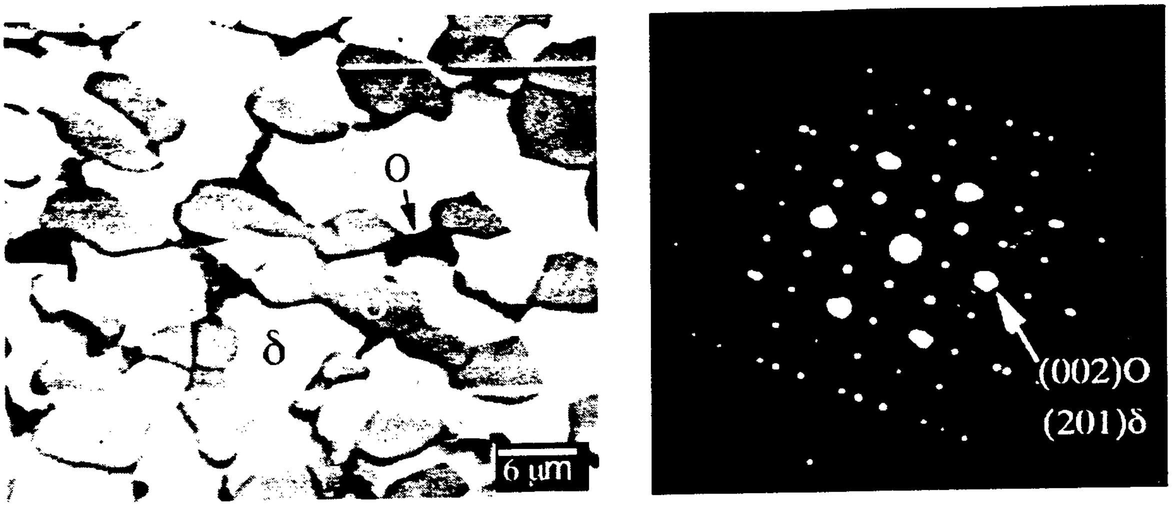

(a) (b)

Figure 5.6 Alloy #15 aged at 900°C, 720 hr., WQ: (a) BSE-image of microstructure. (b) δ[21$\bar{4}$]/O[110] zone axis patterns showing the orientation relationship between the δ and σ phases.

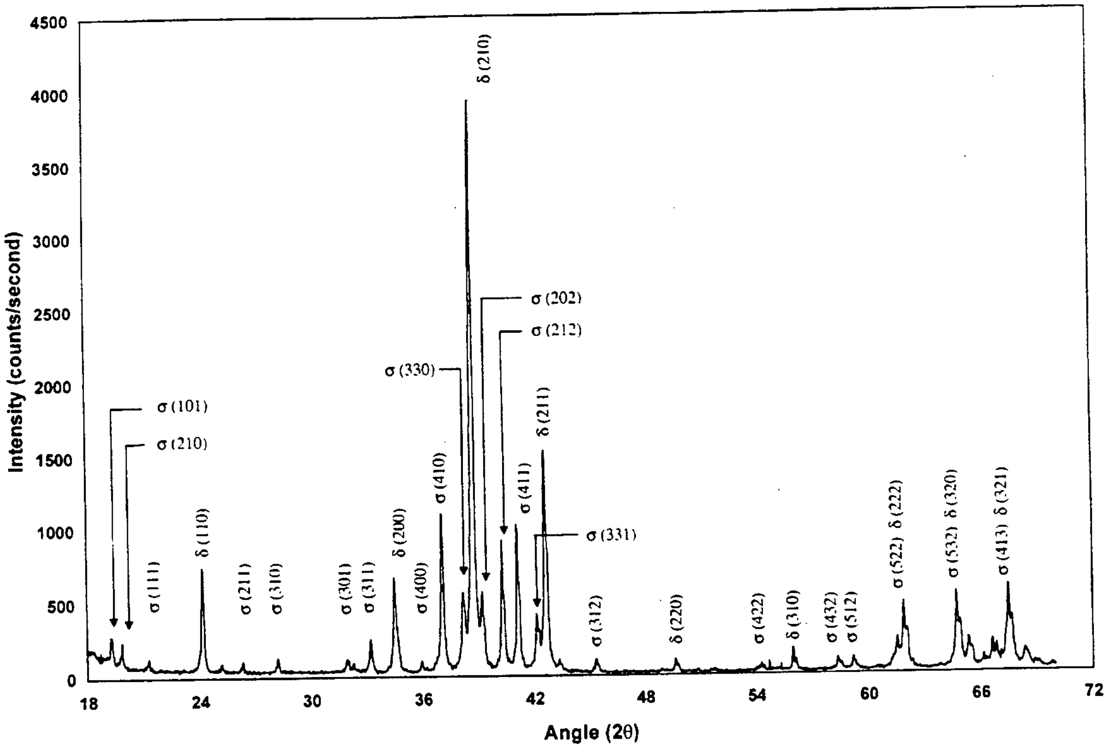

Figure 5.7. XRD pattern of alloy 15 aged at 900C for 720 hours.

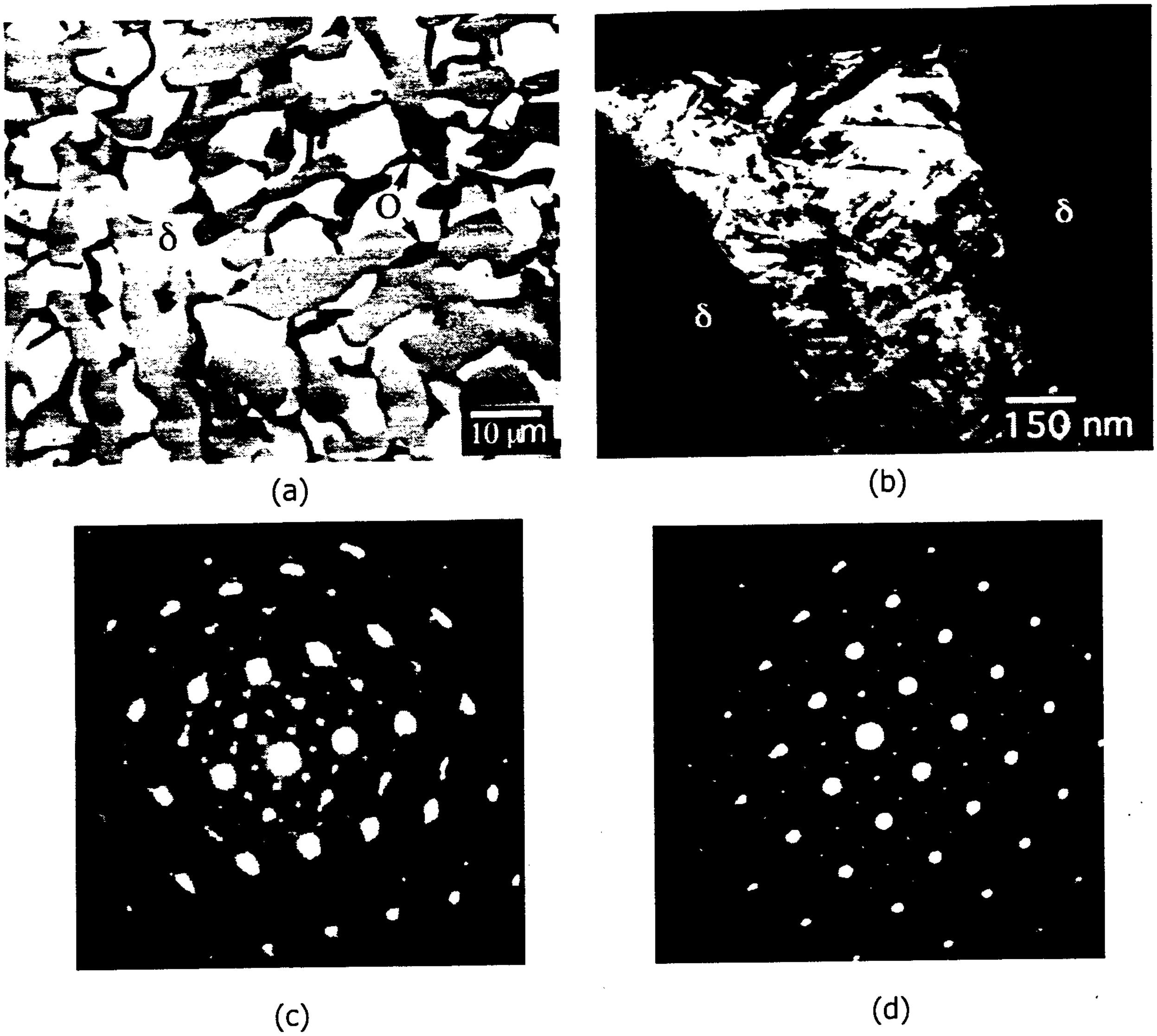

(a) (b)

(c) (d)

Figure 5.8 Alloy #15 aged at 700°C, 1080 hr., WQ: (a) BSE-image of microstructure, (b) DF-image using g=200 reflection of the O phase, and (c) [001] and (d) [100] zone axis SAD patterns of the O phase.

its coarsening at higher temperatures or longer aging times.

Both the δ and σ phases were observed to change very little in composition between 1100 and 700°C (Figure 5.5(d)). Only a slight decrease in Ti concentration was observed within the σ phase with decreasing temperature. The composition of the O phase was within the range of the Ti_2AlNb stoichiometry, however, due to the relatively small grain sizes some overlapping into other grains may have occurred within the interaction zone of the probing electron beam.

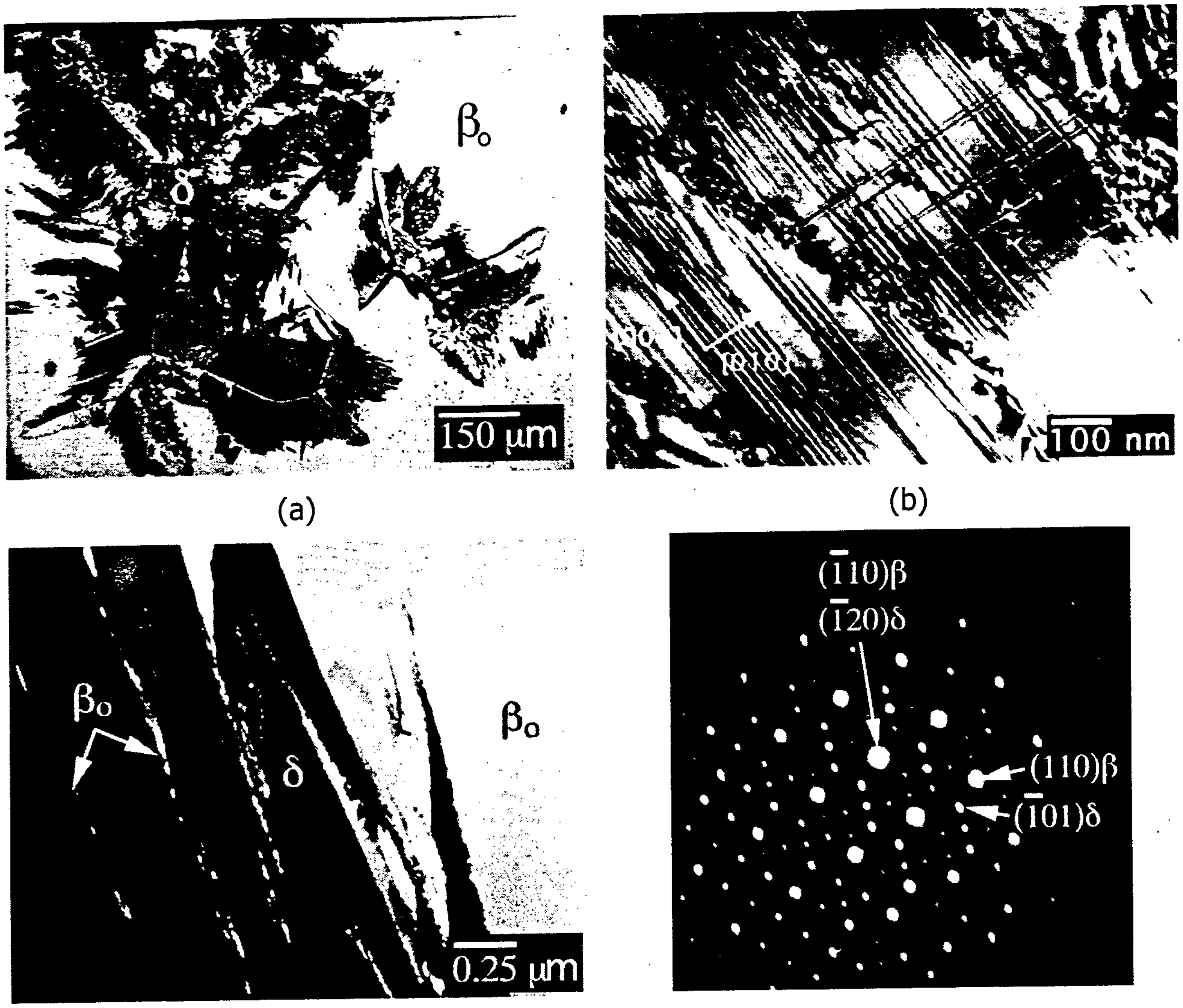

(a) (b)

(c) (d)

Figure 5.9. Microstructure of as-cast alloy #12. (a) OM showing massive δ colonies in β_o matrix; (b) BF of δ phase showing stacking faults on {100} planes; (c) DF micrograph showing separation of the δ laths β_o; and (d) $\beta_o[100]$ // δ[122] // O[100] SAD pattern.

5.4 Phase Transformations and Equilibria in Alloy #12

DTA revealed interesting, yet incomplete, results for alloy 12 (Figure 5.4(b)). At the beginning of the first thermal scan, the material was in the as-cast state and underwent reactions during heating which are a direct result of this initial (and presumably metastable) structure. As Figure 5.9(a) illustrates, nodules of δ (verified by XRD) have formed at β grain boundaries through what appears to be a $\beta \rightarrow \delta_m$ massive-like transformation. In support of a compositional invariant reaction. BSEI of the as-polished sample revealed no compositional contrast between the β_o and δ phases. The δ nodules occurred randomly throughout all ingot cross-sections examined. A closer look at the δ nodules by TEM revealed that they consisted of groups of individual heavily faulted plates (Figure 5.9(b)). Each plate was observed to have a slight mismatch with its neighbor, while being separated by a thin layer of β_o, which was clearly revealed by dark field imaging (Figure 5.9(c)). Crystallographic preferences in the growth directions of the plates and their orientation to the matrix were determined to be approximately $\beta_o[001]$ // $\delta[212]$ and $\beta_o[111]$ // $\delta[001]$ (Figure 5.9(d)). The $\beta_o(\bar{1}10)$ and $\delta(\bar{1}20)$ reflections were observed to coincide in the SAD patterns, leading to a $\{120\}\delta$ growth habit along the $\{110\}$ in β_o. While the zone axes corresponding to the above SAD patterns from the two phases tended to be tilted by 4-6° at the edge of the nodules, a near-exact matching of the zones was observed in the thin β_o layers between the δ_m plates. The thin faults within the δ plates were found to be parallel to the $\{100\}$ planes and produced streaking along the <100> directions in the SAD patterns. Quantitative EDS in the TEM showed no measurable difference in composition between the δ and β_o, with values of both remaining near that of the bulk alloy composition, which lends further support for a $\beta \rightarrow \delta$ massive transformation.

The exothermic peak observed on heating in the DTA thermogram for alloy 12 (Figure 5.4(b)), beginning from about 700°C, is believed to be due to the decomposition of the metastable retained β_o present in the cast structure to the O-phase. The subsequent endothermic peak which terminates at about 1000°C then corresponds to the transformation of O back to β_o; the peak above this temperature is thought to be due to the growth of the δ phase along with the σ to consume the β until reaching the $\beta \leftrightarrow \sigma+\delta$ eutectoid reaction near 1340°C (Figure 5.10(a)). Above the three-phase $\beta+\sigma+\delta$ field, the material enters the two-phase $\beta+\sigma$ field (Figure 5.10(b)). The β transus, which could not be discerned in the DTA trace, was determined through quenching experiments to lie between 1425 and 1475°C. In the first cooling run in the DTA, the alloy developed a lamellar $\delta+\sigma$ microstructure below the eutectoid (~1340°C). With this as the starting structure, reactions related to the decomposition of the metastable β_o in the cast microstructure are no longer seen in the second heating run.

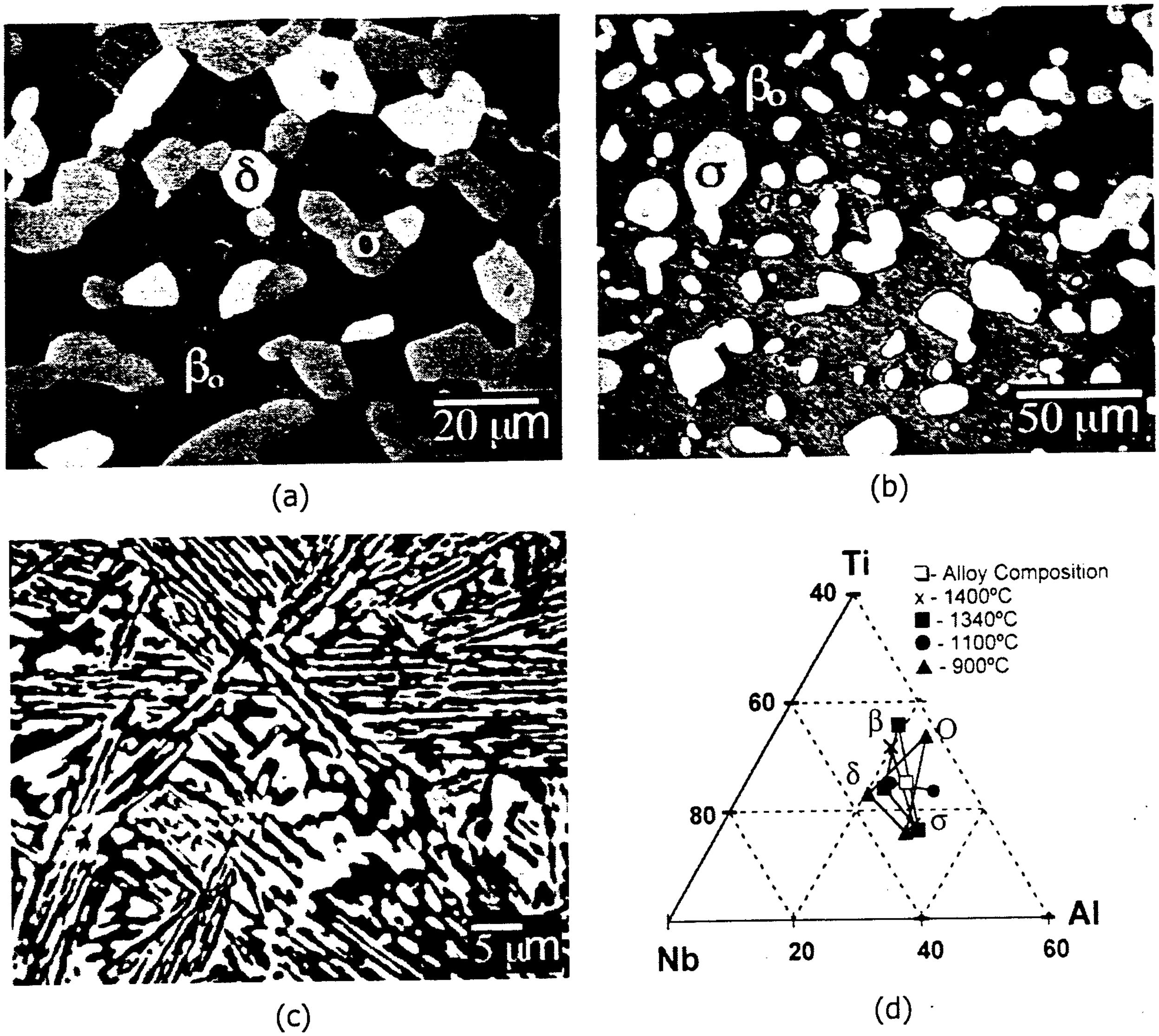

(a) (b) (c) (d)

Figure 5.10. BSE-images of Alloy #12. (a) 1340°C, 24h, OQ, (b) 1400°C, 24h, OQ, (c) 1100°C, 360h, WQ, (δ-light, σ-dark) and (d) experimental tie-lines for the various heat treatments.

The solutionized alloy 12 was aged at 1100°C for 360 hours, which led to complete transformation of the β_0 phase into a lamellar δ + σ structure (Figure 5.10(c)). No O phase was present in the material at this temperature, in agreement with the calculations of Kattner and Boettinger [15]. The compositions of the phases present are listed in Table 5.2 and tie-line information plotted in Figure 5.10(d).

Table 5.2 The phases present following isothermal treatments, their compositions and lattice parameters based on XRD for the Nb-25Ti-25Al alloy.

Heat Treatment	Phases	Composition (at.%)	Lattice Parameters (A)
1400°C, 24hr., OQ	β_o	48.59Nb-31.71Ti-19.7Al	a_c = 3.246±0.003
	σ	52.31Nb-17.36Ti-30.33Al	a_o = 9.918±0.002 c_c = 5.139±0.003
1340°C, 24hr., OQ	β_o	45.25Nb-35.80Ti-18.95Al	a_o = 3.245±0.002
	δ	53.51Nb-24.07Ti-22.42	a_o = 5.175±0.001
	σ	52.10Nb-16.37Ti-31.53Al	a_o = 9.964±0.002 c_o = 5.169±0.001
1100°C, 360 hr., WQ	δ	52.03Nb-25.12Ti-22.85Al	a_o = 5.178±0.001
	σ	46.17Nb-23.5Ti-30.33Al	a_o = 9.956±0.002 c_o = 5.150±0.002
900°C, 720 hr., WQ	δ	55.61Nb-21.97Ti-22.42Al	a_o = 5.179±0.001
	σ	54.34Nb-16.82Ti-28.84Al	a_o = 9.964±0.002 c_o = 5.179±0.001
	O	45.15Nb-33..55Ti-24.3Al	N/D*
700°C, 1080hr., WQ	O	49.25Nb-24.74Ti-26.01	a_o = 6.093±0.02 b_o = 9.508±0.004 c_o = 4.605±0.01

*N/D: not enough data from XRD scan to accurately determine lattice parameters

The O phase was observed in the 900°C aged alloy 12 as small 80 nm sized particles evenly distributed between the grains of the lamellar $\sigma + \delta$ structure. When imaged under dark field conditions using the O(200) reflection, these grains could clearly be seen (Figure 5.11(a)). The O phase grains were observed to have a faceted morphology, suggestive of an orientation relationship. A $\delta[001] // O[5\bar{8}6] // \sigma[001]$ relationship was observed, together with a $\delta(210) // O(221) // \sigma(330)$ matching of the planes (Figure 5.11(b)). While the index of the O phase zone was rather high, a comprehensive investigation of the foils revealed no other low-index relationships. It is believed that the O phase had formed from the parent β_o phase at the same time the $\delta + \sigma$ lamella were growing, and therefore shared only a common orientation with the lamella to that of the β_o phase than with each other.

The lamellar structure produced through cooperative growth of the δ and σ phases from the β_o phase, was observed to produce numerous fringe effects across the interface due the incident beam direction in relation to the angle of the boundary (Figure 5.11(c)). Double diffraction effects

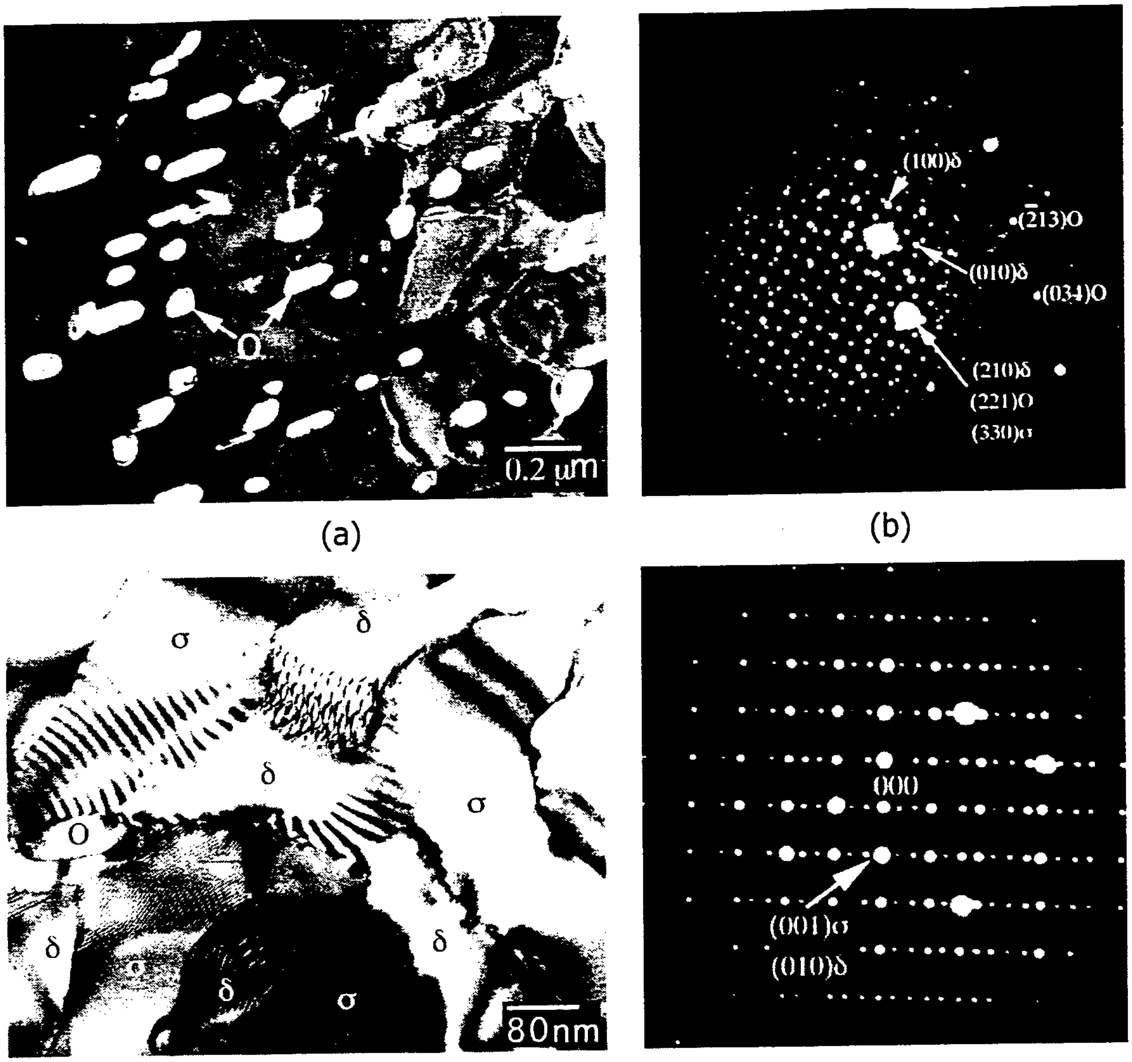

(a) (b)

(c) (d)

Figure. 5.11 Alloy #12 aged at 900°C, 720 hr., WQ: (a) DF-image using O phase reflections, (b) δ(210)//O(221)//σ(330) orientation relationship, (c) BF-image of Fresnel fringes appearing along the σ/δ interfaces, and (d) the δ[100]//σ[310] SAD patterns with δ(001)//σ(001) relationship also observed between σ and δ.

created from the interface were observed in analyzing the σ[310] // δ[100] σ(001) // δ(001) orientation relationship, also observed between the lamella (Figure 5.11(d)). No relationship with respect to the O phase was observed under this condition.

A complete β_o to O transformation of the solutionized material was observed following aging of the β quenched material at 700°C for 1080 hours. The microstructure consisted of twin related plates of O, with an APB structure visible under certain two-beam conditions (Figure 5.12(a)).

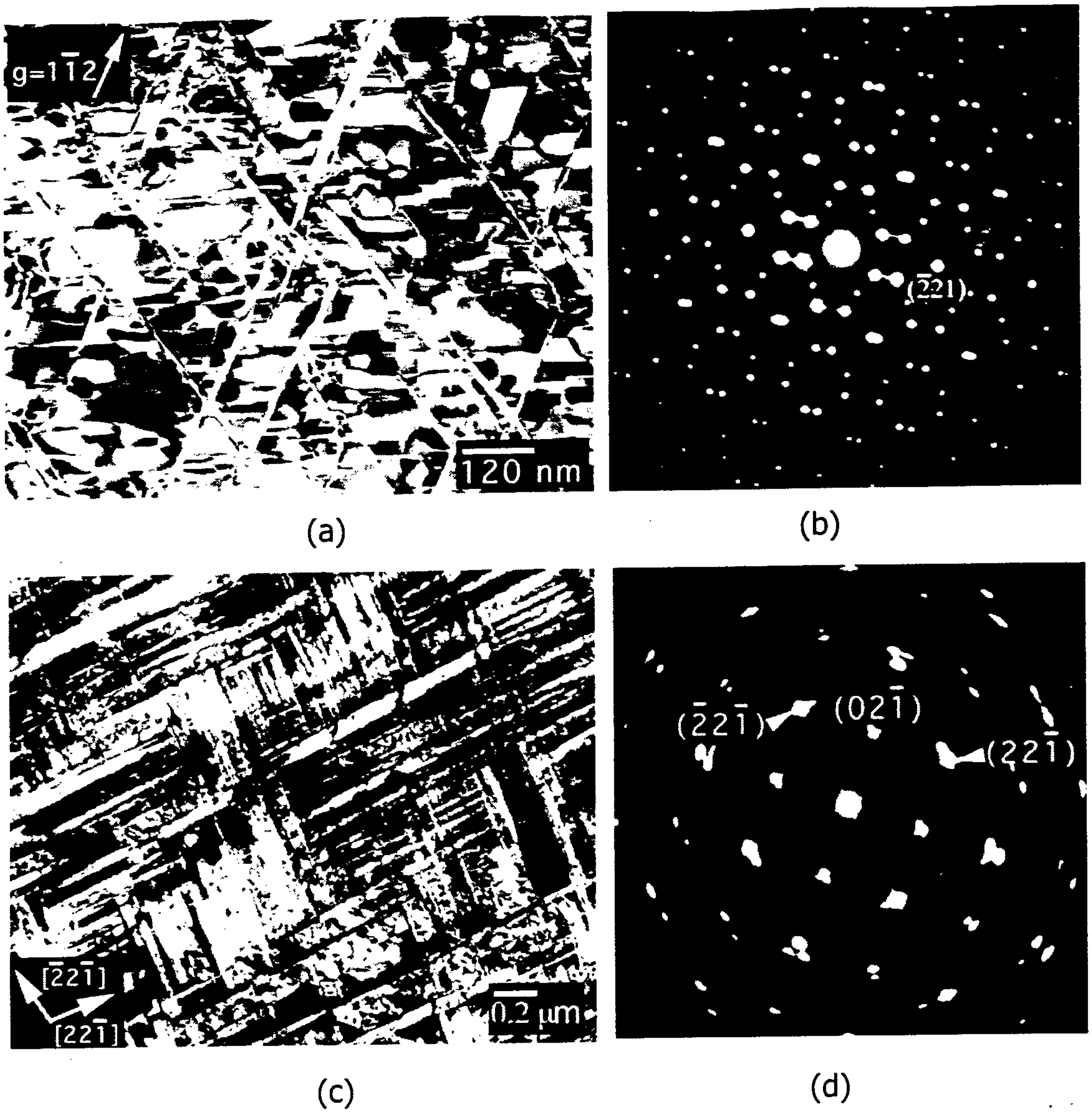

Figure. 5.12 Representative micrographs of O plate morphology in alloy #12 aged at 700°C, under (a) two-beam conditions using g=1$\bar{1}$2, and (b) BF-conditions along the [012] zone axis. {221}-type twinning observed within the (c) [110] and (d) [012] SAD patterns.

The amount of twinning appeared to vary from sample to sample and within each TEM foil observed (Figure 5.12(c)). No other morphological structures of the O phase were present within the sample, including regions near the former grain boundaries. The {221}-type twinning of the O plate structure was clearly deduced through examination of the [110] and [012] SAD patterns (Figure 5.12(b,d)).

While electron diffraction identified the microstructure as completely consisting of the O phase, XRD analysis revealed peak placements nearly identical to that of the β phase (Figure 5.13). The only marked difference between the two was that of additional peak intensities at 37.22° and 42.54° 2θ, identified as the (040) and (112) planes of the O phase. The close orientation relationship between β_o and the martensite-like O phase produced from it can account for the close matching in peak intensities observed in XRD. The highest intensity β peak corresponding to the (110) plane when transformed to the O structure becomes the (221) plane, and still exhibits the maximum intensity of all the diffracted planes within the O structure, this point made more noteworthy by the abundance of {221} type twinning observed within the O structure. The position of the (221)O peak and its relative intensity were found to agree with published values [38]. The other O phase peaks, similar in position to their β counterparts, were also produced in the same manner. The observation of a complete O phase structure reproducing a β-like XRD pattern, was also observed by Narayanan in a Nb-37Ti-26Al alloy solution treated and aged at 900°C [39].

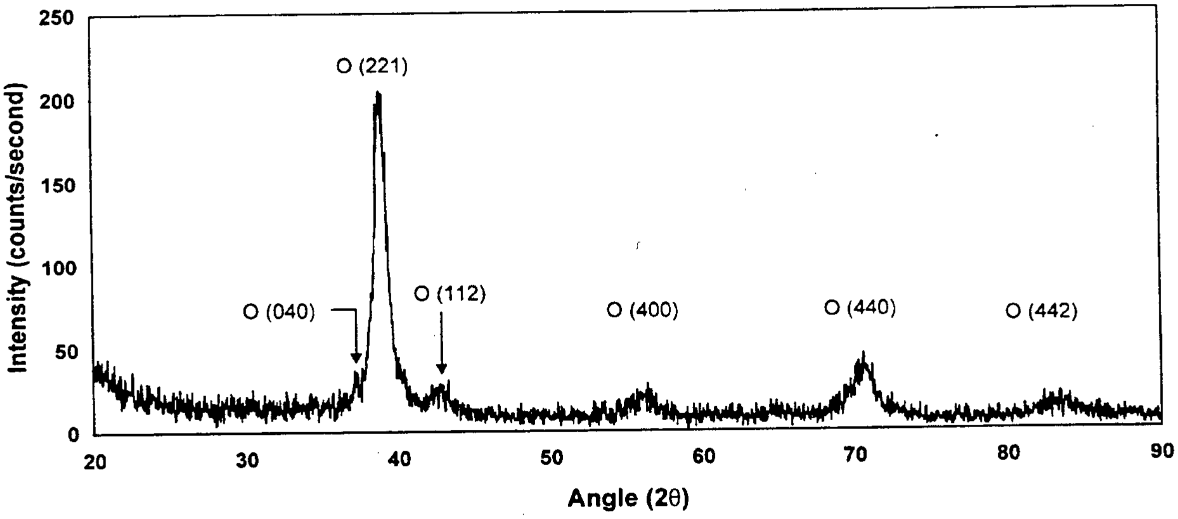

Figure. 5.13 XRD scan of Alloy #12 aged at700°C, 1080 hr., WQ.

Analysis of the displacement vector of the APB's observed within the microstructure was conducted near the [110] zone of the twin plate labeled A in Figure 5.14. Under two-beam conditions, the APB's were visible under the $g=1\bar{1}1$ and $1\bar{1}2$ conditions and invisible under 002. The $g=2\bar{2}\bar{1}$ vector, being perpendicular to the twin plane, produced no net image of the internal structure. Based on the conditions of visibility and invisibility, the displacement vector of the APB's was determined to be 1/2<001>. While imaged under the g=002 condition, a diffuse image of fine, slightly curved lines were observed (Figure 5.15). The lines are presumably an artifact produced from the electron beam interaction within the sample and likely to be resulting from strain within the structure due to the transformation from β_o, or manifested from slight changes within the ordering structure of the O phase itself [40].

To determine the ordering state of the O phase, whether it is the binary O1 or the ternary O2, convergent beam analysis of the [001] zone was conducted. Analyzing a relatively thin area in order to reduce dynamical diffraction contrast within the disks, the kinematical convergent beam pattern of the [001] zone showed the intensities of the (020) and (110) reflections to be distinct in contrast (Figure 5.16(b)). Therefore, ternary ordering of the O phase (O2) at 700°C had occurred, in which Nb, Ti and Al atoms were located on separate sublattices in the orthrhombic crystal.

A second heat treatment was performed on the 700°C aged samples to determine if ternary ordering of the orthorhombic structure occurred above this temperature. Upon treating the material at 800°C for one hour followed by water quenching, the intensities of the (020) and (110) reflections in the [001] CBED pattern were observed to be similar (Figure 5.16(c)), suggesting binary ordering of the O phase (O1), where Nb atoms randomly occupy the Ti sublattice sites within the crystal structure. Structure factor considerations that had produced the differences between the (020) and (110) intensities within O2 structure become averaged out in the O1 structure when Nb and Ti atoms randomly occupy the former Ti and Nb sublattices.

Based on the phase rule, alloy #12 should have been within a two-phase region at this temperature, whereas existing calculated diagrams [15] suggested σ + O. The rapid formation of the O plates and the already reduced diffusion rates are believed to have reduced the rate of σ

nucleation. No σ formation was observed along the prior β grain boundaries.

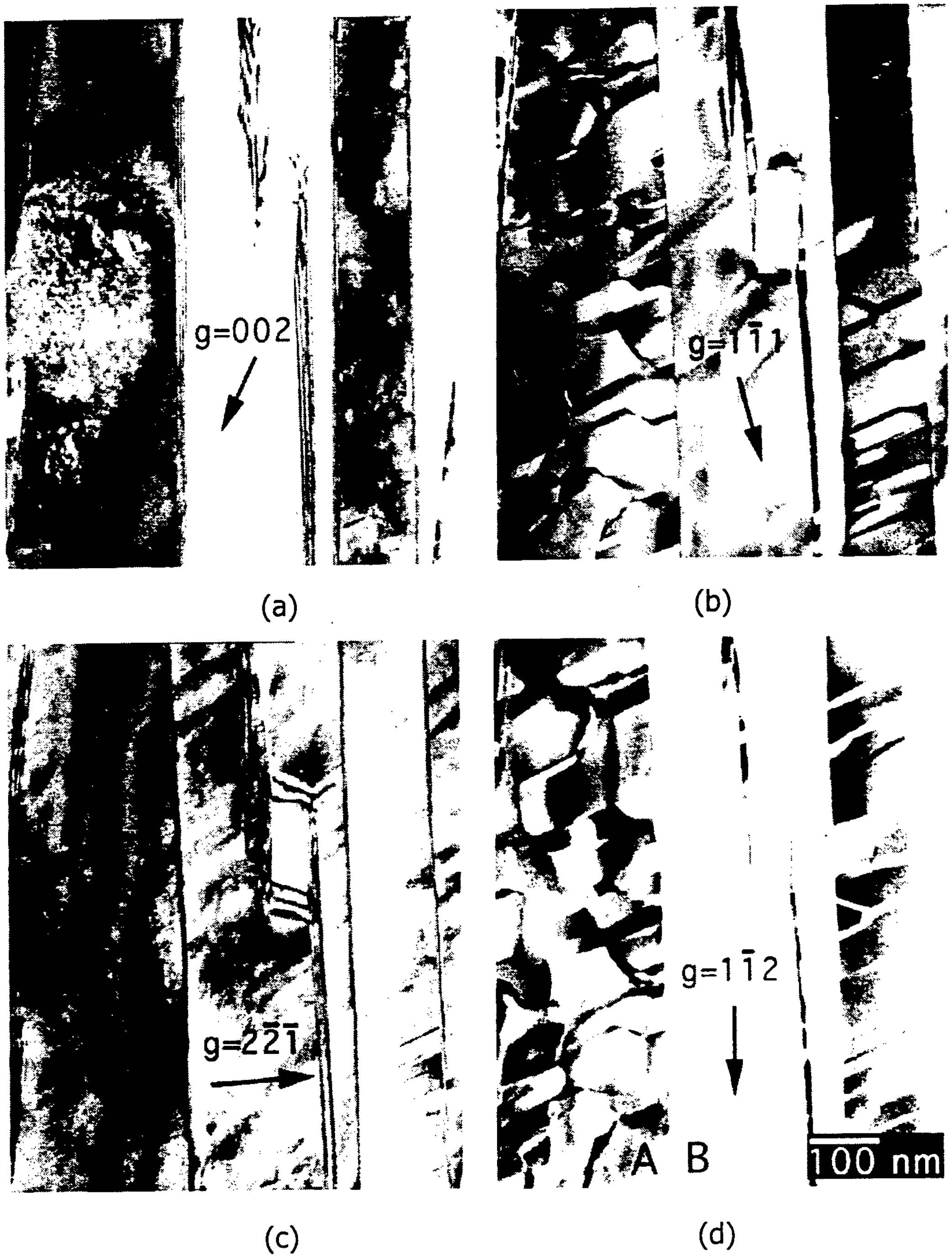

Figure. 5.14 Analysis of APB's of lath A in 700°C material under two-beam conditions near the [110] zone axis: (a) g=002, (b) g=1$\bar{1}$1, (c) g=2$\bar{2}\bar{1}$ and (d) g=1$\bar{1}$2.

Figure 5.15 Strain induced effects observed under g=002 two-beam conditions within 700°C material.

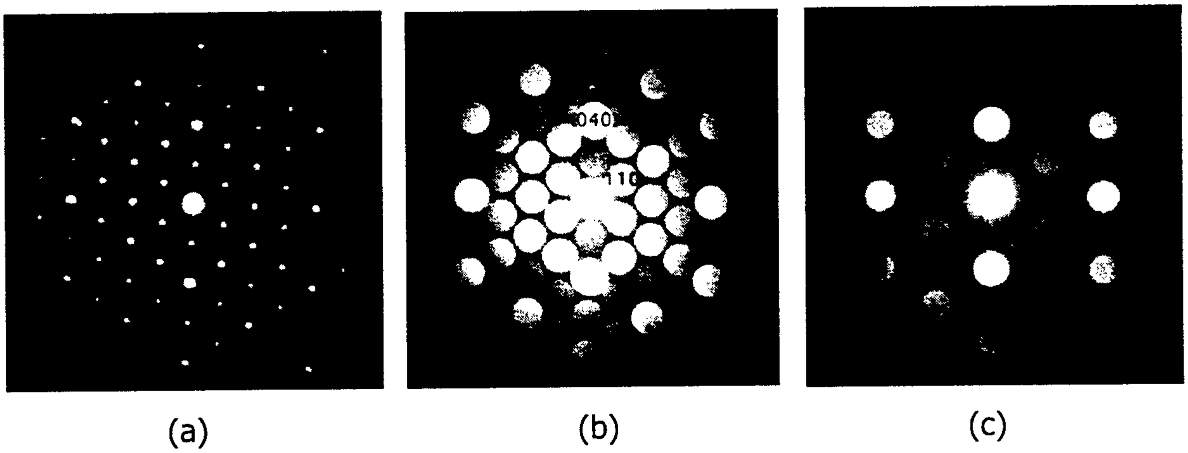

(a) (b) (c)

Figure 5.16 Electron diffraction patterns of the O phase in the Nb-25Ti-25Al alloy: (a) [001] SAD pattern, (b) [001] CBED at 700°C, and c) [001] CBED after 800°C treatment.

5.5 Phase Transformations and Equilibria in Alloy #9

As the alloy compositions are changed to increasingly higher Ti concentrations, the β → δ + σ eutectoid occurs at lower temperatures. The DTA thermogram for alloy 9 is presented in Figure 5.4(c). From the thermogram only a single extended major reaction could be observed on heating: this long continuous shallow trough has a small peak at 991°C and continues until completion at 1396°C (the β transus). However, it should be noted that the cooling curve shows a more complex cooling peak, which is indicative of a transition from a two to three phase region. Based on these results and those of other neighboring alloys the heat treatment temperatures were selected (arrows in Figure 5.4(c)) and are listed in Table 5.3. The results of X-ray analysis and microprobe analysis are also presented in Table 5.3, with micrographs of the resulting structures shown in Figure 5.17.

It was determined through heat treatments that alloy #9 enters into the β + σ phase field from single-phase β at around 1360°C (Figure 5.17) and remains so until passing through the β → δ + σ eutectoid reaction just below 1100°C (Figure 5.18). Changes in the volume fraction of σ with temperature were observed through heat treatments of alloy #9 within the β + σ phase field (Figure 5.17). The alloy formed a two-phase δ + σ structure on aging the β_0 solutionized material between 990 and 970°C, but showed some O phase formation on extended aging at 970°C (Figure 5.19).

(a) (b)

Figure 5.17. BSEI micrographs of alloy#9 heat treated in the β + σ phase field. (a) 1360°C,14h, OQ, and (b) 1270°C, 32h, WQ.

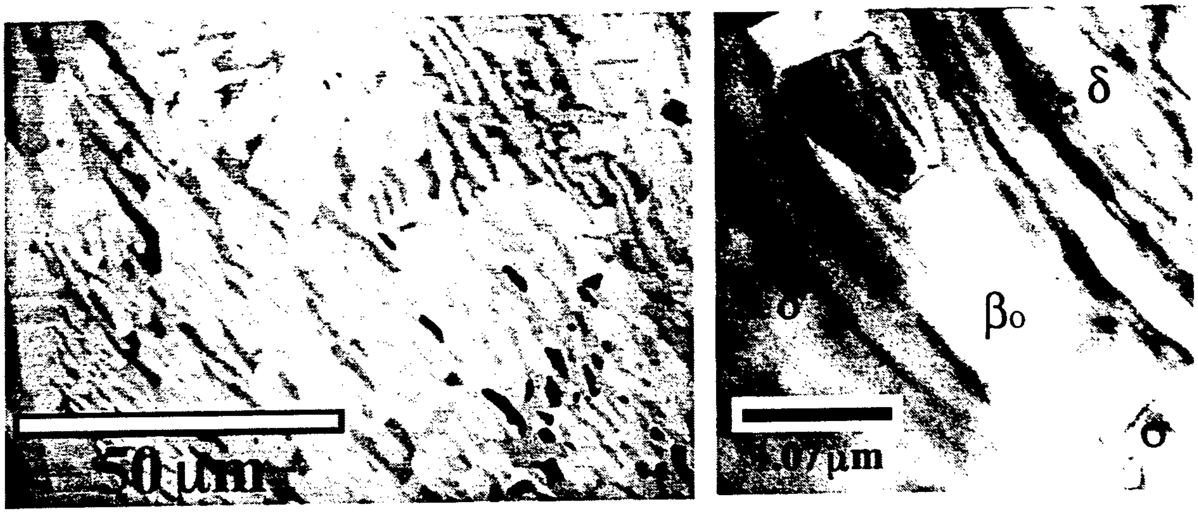

(a) (b)

Figure 5.18. Alloy #9 aged at 1090°C, 168h. (a) BSE-image of β_0 (dark grey), σ (medium grey) and δ (light grey) structure with α_2 (black) observed near the sample surface due to contamination. (b) BF-image of structure.

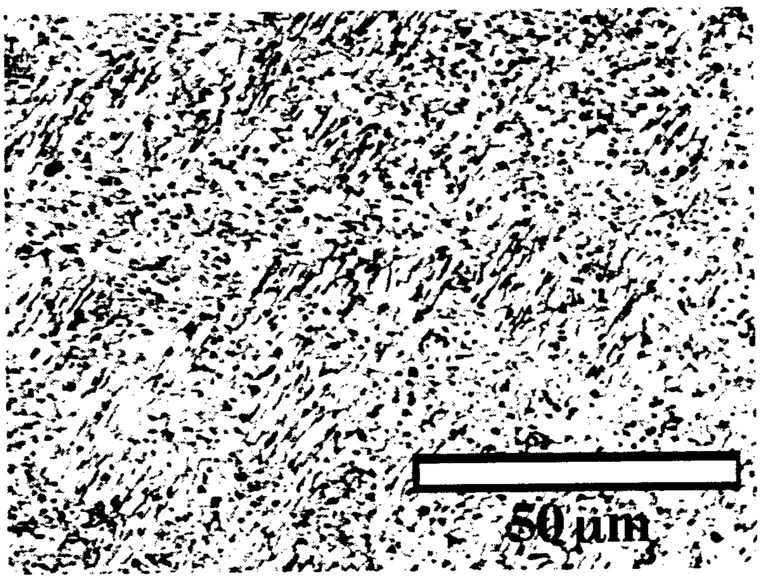

Figure 5.19. OM image of alloy #9 aged at 970°C for 720hs.

Table 5.3 Alloy #9 Selected Heat Treatments and Results of EPMA and X-Ray Analysis

Heat Treatment	BSEI Contrast	Composition (at.%)				X-ray Results
		Ti	Al	Nb	Phase	Lattice Parameter
1475°C/6h/OQ	Grey	30.26	24.65	45.09	β	$a_o = 3.258 \pm 0.003$Å
1475°C/6h/OQ + 1360°C/14h/OQ	Grey (Matrix)	32.29	24.96	42.76	β	$a_o = 3.257 \pm 0.002$Å
	Bright	20.86	31.53	47.76	σ	$a_o = 9.944$Å $c_o = 5.195$Å
HIP 1475°C/6h + 1270°C/32h/WQ	Grey (Matrix)	35.33	21.66	43.01	β	$a_o = 3.258 \pm 0.003$Å
	Bright	22.81	30.53	46.67	σ	$a_o = 9.969 \pm 0.013$Å $c_o = 5.151 \pm 0.008$Å
1475°C/6h/OQ + 1200°C/48h/WQ	Grey (***)	37.77	20.58	41.65	β	$a_o = 3.266 \pm 0.001$Å
	Dark (****)	24.65	30.59	44.76	σ	$a_o = 9.969 \pm 0.009$Å $c_o = 5.149 \pm 0.005$Å
	Bright (***)	26.28	22.41	51.31	δ	Present
1475°C/6h/OQ + 1090°C/7d/WQ	Dark (Matrix)	43.84	19.82	36.34	β	$a_o = 3.254$Å (211)
	Grey (Matrix)	27.02	30.52	42.46	σ	$a_o = 9.951 \pm 0.004$Å $c_o = 5.138 \pm 0.003$Å
	Bright	29.23	22.15	48.62	δ	$a_o = 5.170 \pm 0.001$Å
near surface	Dark (**)	59.24	24.10	16.66	α_2	
1475°C/6h/OQ + 1025°C/14d/WQ	Grey (Matrix)	31.81	27.16	41.03	σ	$a_o = 9.966 \pm 0.004$Å $c_o = 5.141 \pm 0.003$Å
	Bright	30.67	23.00	46.33	δ	$a_o = 5.169 \pm 0.001$Å
	Dark (*)	57.50	25.07	17.43	α_2	
1475°C/6h/OQ + 990°C/14d/WQ	Grey (Lath*)	27.13	31.72	41.15	σ	$a_o = 9.959 \pm 0.001$Å $c_o = 5.143 \pm 0.001$Å
	Bright	29.88	23.21	46.91	δ	$a_o = 5.169 \pm 0.001$Å
	Dark (*)	48.35	25.94	25.72	α_2 or O (?)	
1475°C/6h/OQ + 970°C/14d/WQ	Grey(Matrix*)	28.48	29.15	42.37	σ	$a_o = 9.960 \pm 0.001$Å $c_o = 5.143 \pm 0.001$Å
	Bright (*)	30.81	21.98	47.21	δ	$a_o = 5.170 \pm 0.001$Å
	Dark (*)	36.80	23.19	40.00	O (?)	
1475°C/6h/OQ + 700°C/30d/WQ	Grey	Structure Too Fine			O	$a_o = 6.171 \pm 0.001$Å $b_o = 9.467 \pm 0.002$Å $c_o = 4.665 \pm 0.001$Å
1475°C/6h + 1475°c/3h/OQ + 700°C/150d/WQ	Grey	Structure Too Fine			O	$a_o = 6.156 \pm 0.020$Å $b_o = 9.470 \pm 0.052$Å $c_o = 4.692 \pm 0.010$Å
					β_o	$a_o = 3.266 \pm 0.015$Å

*= Best value **= Avg. of best two measurements

*** = Avg. of best three measurements ****= Avg. of best four measurements

5.6 Phase Transformations and Equilibria in Alloy #4

The DTA thermogram for alloy 4 is presented in Figure 5.4(d). From the thermogram three major reactions can be observed on heating. The first is an exothermic peak with an onset at 640°C and peak at 667°C. This reaction is only observed for the specimen with the higher cooling rate (20°C/min) and is believed to be related to the metastable decomposition of retained β phase to O. The next major transformation is a strong endothermic peak starting at 980°C and peaking at 1008°C associated with the $\beta \rightarrow \sigma + \delta$ reaction. This reaction is followed by a long extended trough, the $\beta + \sigma$ phase field, completing near 1321°C marking the β transus temperature. Based on these results the heat treatment temperatures were selected (arrows in Figure 5.4(d)) and are listed in Table 5.4. The results of X-ray analysis, and microprobe analysis are also presented in Table 4, with micrographs of the resulting structures shown in Figures 5.20 through 5.21.

Heat treatments conducted between 1270 and 1025°C (Figure 5.20) confirmed the temperature range of the $\beta + \sigma$ field identified from the DTA. A significant volume increase was observed for the σ phase between 1270°C (Figure 5.20(a)) and 1100°C (Figure 5.20(b)), as the material is undercooled further below the β transus. Three-phase structures were produced through aging the materials at 970°C; however, the calculated annealing time of 14 days for the transformation of the metastable β_o phase to the equilibrium structures proved to be inadequate as an inhomogeneous transformation of the β_o grains occured (Figure 5.21(a)). The grain interiors were observed to form O' plates, the O phase having the same composition as the parent β, formed presumably through a martensite-type of transformation. The δ phase covered the grain boundaries and grew with the σ phase into the grain interiors (Figure 5.21(b)). As the $\sigma + \delta$ transformation front continued into the grain interiors, the change in composition of the β_o phase led to further precipitation of O, with a composition different than that of the O' in the grain interiors (Figure 5.21(c,d)). At longer aging times at 970°C, the material equilibriated into a four-phase structure of β, δ, σ and O.

On aging at 700°C for 30 days, alloys 4 and 9 contained microstructures similar to those observed in alloy #'s 3, 7, 8, 11 and 14, also at 700°C (Figure 5.22(a)). The alloys contained a β_o

Table 5.4 Alloy #4 Selected Heat Treatments and Results of EPMA and X-Ray Analysis

Heat Treatment	BSEI Contrast	Composition (at.%)				X-ray Results
		Ti	Al	Nb	Phase	Lattice Parameter
1425°C/7h/OQ	Grey	37.09	24.85	38.06	β	$a_0 = 3.244 \pm 0.009$Å
1270°C/32h/WQ	Grey (Matrix)	40.52	25.20	34.28	β	$a_0 = 3.255 \pm 0.002$Å
	Bright (GB)	26.28	31.86	41.86	σ	$a_0 = 9.960 \pm 0.012$Å
						$c_0 = 5.146 \pm 0.008$Å
1425°C/7h/OQ + 1150°C/7d/WQ	Grey (Matrix)	44.28	23.03	32.70	β	$a_0 = 3.258 \pm 0.001$Å
	Bright	28.51	31.22	40.27	σ	$a_0 = 9.969 \pm 0.010$Å
						$c_0 = 5.146 \pm 0.005$Å
HIP1425°C/7h + 1425°C/3h/OQ + 1100°C/7d/WQ	Grey (Matrix)	44.47	21.60	33.93	β	$a_0 = 3.260 \pm 0.001$Å
	Bright	28.63	30.68	40.69	σ	$a_0 = 9.977 \pm 0.010$Å
						$c_0 = 5.148 \pm 0.006$Å
1425°C/7h/OQ + 1025°C/14d/WQ	Grey (Matrix)	46.42	20.63	32.95	β	$a_0 = 3.271 \pm 0.002$Å
	Bright	30.43	29.66	39.91	σ	Present
	Dark (GB***)	58.85	24.45	16.70	α_2 (?)	
1425°C/7h/OQ + 990°C/14d/WQ	Grey (GI**)	46.87	20.21	32.92	β	$a_0 = 3.259$Å (211)
	Bright (GI)	30.78	29.82	39.40	σ	$a_0 = 10.086$Å
						$c_0 = 5.157$Å
	V. B. (GB**)	33.32	21.77	44.91	δ	
	Bright (GB**)	29.98	30.40	39.62	σ	
	Dark (GB*)	56.85	24.21	18.93	α_2 (?)	
1425°C/7h/OQ + 970°C/14d/WQ	Grey (GI)	38.85	25.91	35.24	β	$a_0 = 3.261$Å (211)
	Bright (GI)	28.72	30.84	40.44	σ	$a_0 = 10.285 \pm 0.077$Å
						$c_0 = 5.157 \pm 0.036$Å
	V. B. (GB)	31.94	22.51	45.55	δ	
	Bright (GB)	28.54	31.08	40.38	σ	
	Dark (GB)	47.42	25.66	26.92	O (?)	
HIP1425°C/7h + 1425°C/3h/OQ + 970°C/31d/WQ	Grey Matrix	46.10	20.00	33.90	O/β_o	Present
	Bright	29.25	30.79	39.97	σ	$a_0 = 10.005 \pm 0.018$ Å
						$c_0 = 5.165 \pm 0.009$ Å
	V. B.	32.81	22.01	45.18	δ	$a_0 = 5.167 \pm 0.004$ Å
	Dark	57.94	25.6	16.46	α_2 (?)	
1425°C/7h/OQ + 700°C/30d/WQ	Grey	Structure Too Fine			O	$a_0 = 6.188 \pm 0.028$Å
						$b_0 = 9.600 \pm 0.082$Å
						$c_0 = 4.670 \pm 0.019$Å
HIP1425°C/7h + 1425°C/3h/OQ + 700°C/150d/WQ	Grey	Structure Too Fine			β_o	$a_0 = 3.266 \pm 0.007$Å
					O	$a_0 = 6.116 \pm 0.036$Å
						$b_0 = 9.458 \pm 0.089$Å
						$c_0 = 4.663 \pm 0.017$Å
1270°C/32h/WQ + 700°C/30d/WQ	Grey (Laths)	39.64	26.11	34.25	O	$a_0 = 6.125 \pm 0.009$Å
						$b_0 = 9.554 \pm 0.011$Å
						$c_0 = 4.675 \pm 0.002$Å
	Bright (GB)	25.57	32.46	41.97	σ	$a_0 = 9.956 \pm 0.008$Å
						$c_0 = 5.147 \pm 0.006$Å

* = best value, ** = Avg. of best two measurements, *** = Avg. of best three measurements

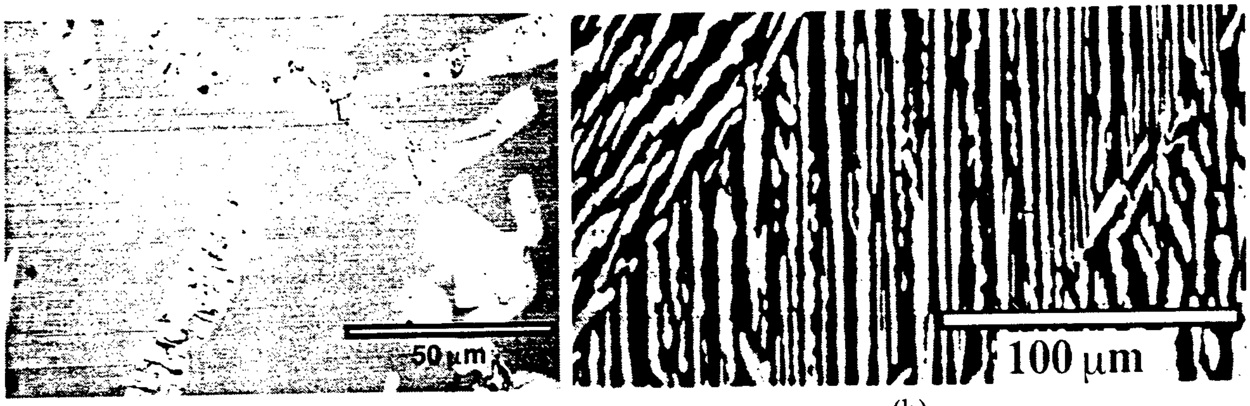

(a) (b)

Figure 5.20. BSE-images of alloy #4 heat treated in the β + σ phase field (σ-bright, β-dark). (a) 1270°C, 32h, WQ, and (b) 1100°C, 168h, WQ.

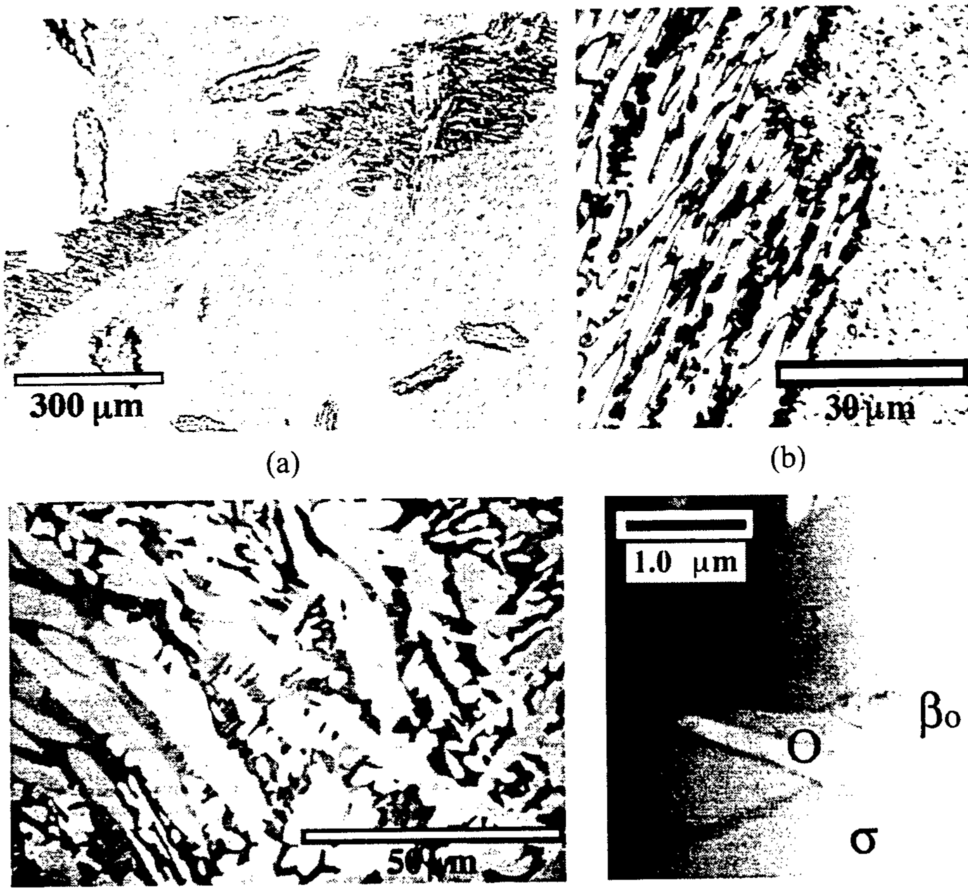

(a) (b)

(c) (d)

Figure 5.21. Alloy #4 aged at 970°C, 336h. (a) OM of grain boundary region, (b) OM higher magnification of region in (a), (c) BSEI of four-phase structures (δ-light, σ-medium, β-dark, O-darkest), and (d) TEM BF-image,

matrix that decomposed into O' laths, with the same $\beta_o[111]$ // O[110] type orientation relationship as observed before. No change in phase equilibria occured after aging alloys 4 and 9 for times up to 150 days.

(a) (b) (c)

Figure 5.22. TEM micrograghs of (a) alloy #4, and (b) alloy #9, heat treated at 700°C for 720 hs. (c) $\beta_o[111]$ // O[110] SAD patterns.

5.7 The $\beta \rightarrow \sigma + \delta$ Transformation

The $\beta \rightarrow \sigma + \delta$ eutectoid transformation in ternary space was determined to move to higher Ti concentrations with reduced temperature (Figure 23). The DTA signal corresponding to this transformation was very strong for alloy #4 and weaker in the other alloys (Figure 5.4). The difference is believed to be due to the presence of the four-phase plane occurring at 980°C, which provided an additional energy release as the β_o further transformed to the O phase.

The high temperature phase equilibria of these four alloys offers interesting microstructures of σ and β_o. However, this structure is not stable due to the continued decomposition of the β_o phase at lower temperatures to produce either the δ phase at the grain boundaries or metastable O within the grain interiors. The formation of the δ phase in the form of a eutectoid $\sigma + \delta$ structure, was also observed on oil quenching alloy 12 from the $\beta + \sigma$ phase field (Figure 5.24); the result of cooling through the $\beta + \sigma + \delta$ phase field. This was not visible within the BSE-image (Figure 5.10(b), however, etching revealed the structure in OM (Figure 5.24(a)) and subsequent TEM examination (Figure 5.24(b.c)). The kinetics of formation of the δ phase in these alloys can be very sluggish at temperatures below 1000°C as evidenced by the 970°C structure of alloy 4 (Figure 21). In addition, all the alloys were found to be susceptible to alteration of phase equilibria with α_2 formation due to impurity effects, namely oxygen.

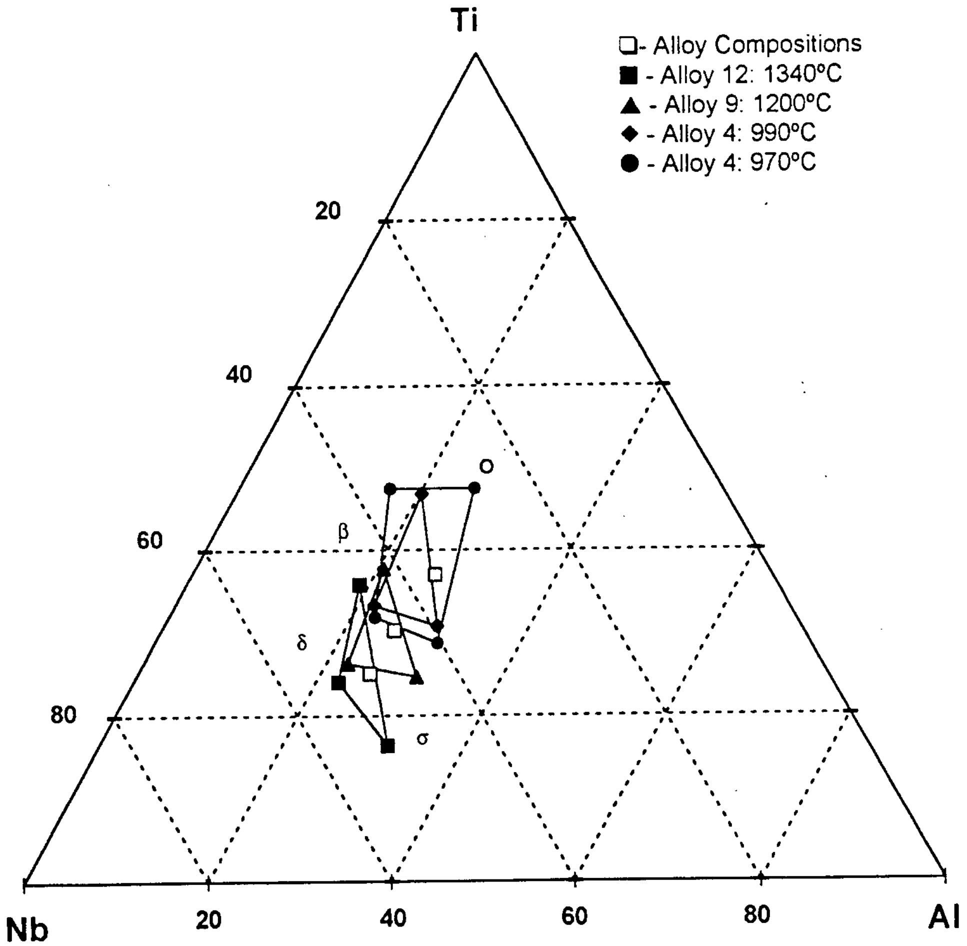

Figure 5.23. The movement of the β + σ + δ phase field through the ternary with reduced temperatures, leading to the four phase β + O + σ + δ phase field at 980°C.

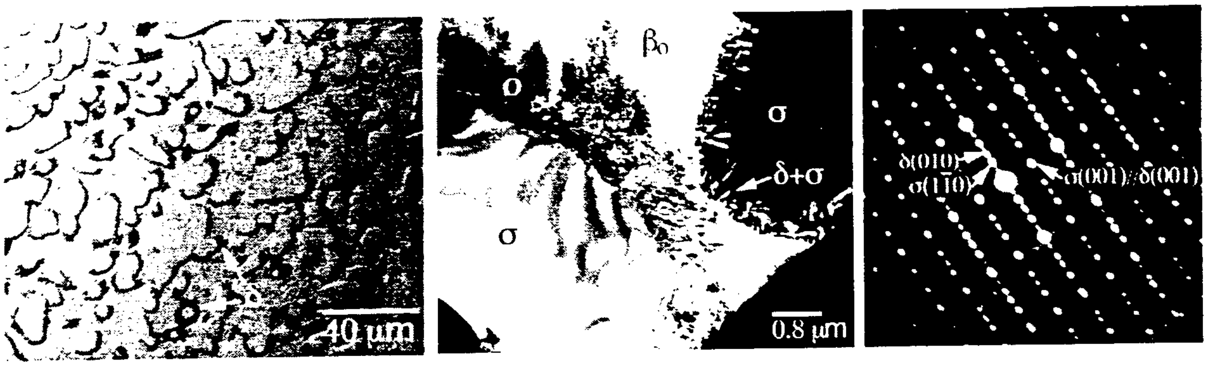

(a) (b) (c)

Figure 5.24 Alloy #12 aged at 1400°C, 24 hr., OQ: (a) OM of transformed structure at σ/β interface, (b) TEM image of the σ/β interface with (c) σ[110]//δ[100] SAD patterns of the σ+δ eutectoid product.

5.8 The β→δ Transformation.

The formation of the δ phase was also found to occur relatively easily through a masive-like transformation in alloy 12, and was further investigated by cooling experiments after alloy homogenization through HIP'ing at 1475°C, above the β transus temperature. Water quenching from above the β transus was effective in suppressing any transformations involving the high temperature β phase, other than the ordering to the β_o (B2) structure.

Air-cooling from above the β transus did result in the formation of the σ and δ phases, although the cooling rate was sufficient to suppress the formation of lamellar δ + σ from the eutectoid reaction. The air-cooled microstructure contained laths of both σ and δ located near the β_o grain boundaries (Figure 5.25(a)). The σ laths typically grew separate from the δ laths, and were produced during cooling through the β + σ phase field (Figure 5.25(b)). The δ laths, however, possessed the exact same characteristics in morphology, orientation to the β_o phase, and internal defect structures as had been observed within the cast material (Figure 5.25(c,d)). Unlike the σ laths, no compositional difference was detectable between the δ and β_o phases, providing further evidence for a β→δ massive reaction.

Furnace cooling from 1475°C did result in the formation of the lamellar δ + σ eutectoid product (Figure 5.26(a)), but again produced the massive-like δ structure (Figure 5.26(b,c)). The δ

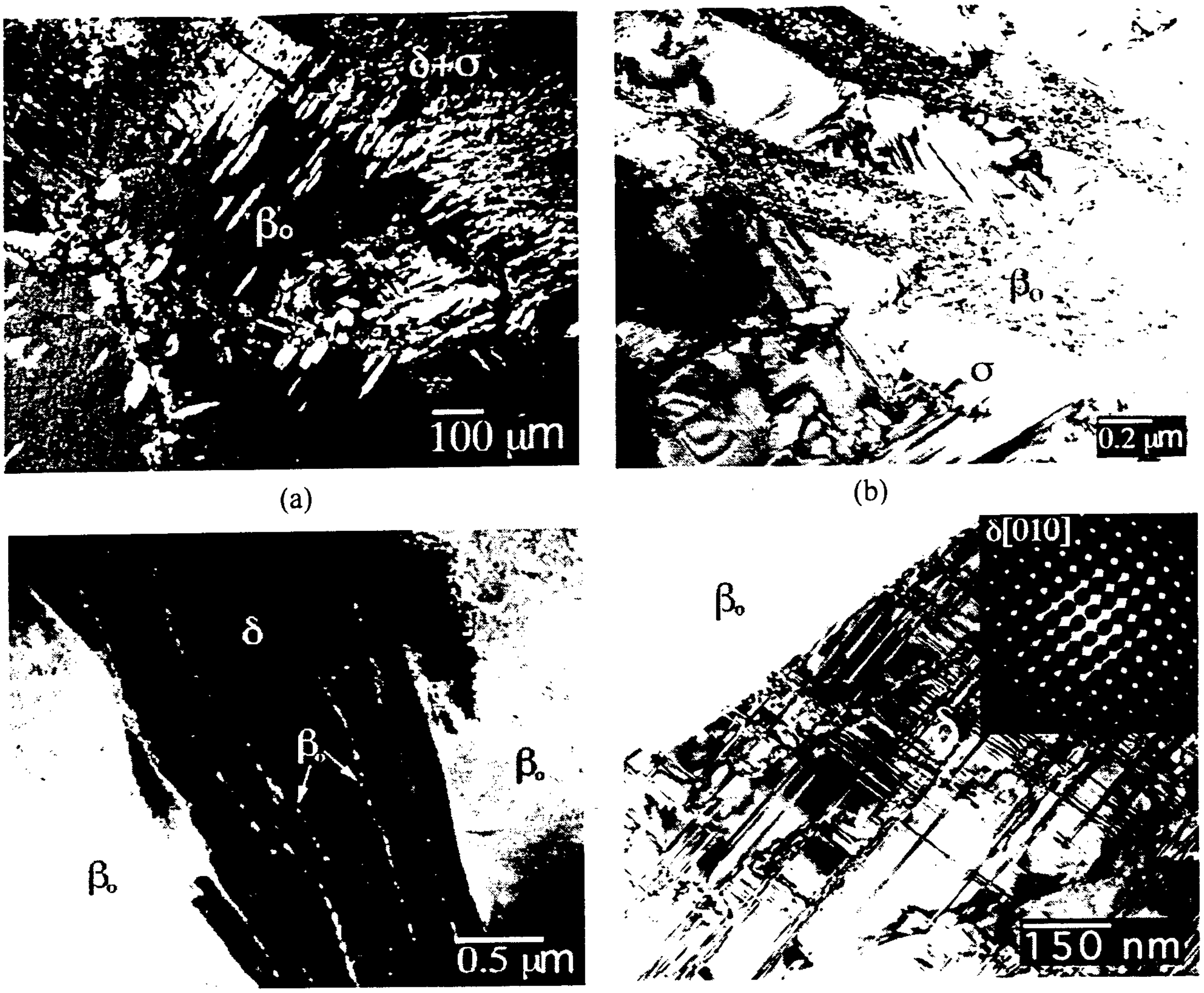

(a) (b)

(c) (d)

Figure 5.25 Alloy #12 air cooled from 1475°C: (a) polarized light micrograph, (b) BF-image showing σ laths within β_o, (c) DF-image of δ_m structure, and (d) thin faults in δ_m with insert of δ_m[010] zone pattern showing resulting streaking in the <100> directions.

laths were found along the β_o grain boundaries in regions that had not undergone the eutectoid transformation. The slower cooling rate also led to the nucleation and growth of the orthorhombic (O-Ti_2AlNb) phase along the δ/β_o interface and separately within the regions of retained β_o (Figure 5.26(d)).

The formation of the δ phase was also observed within material oil quenched from 1475°C. While water quenching from above the β transus resulted in a complete retention of the supersatu-

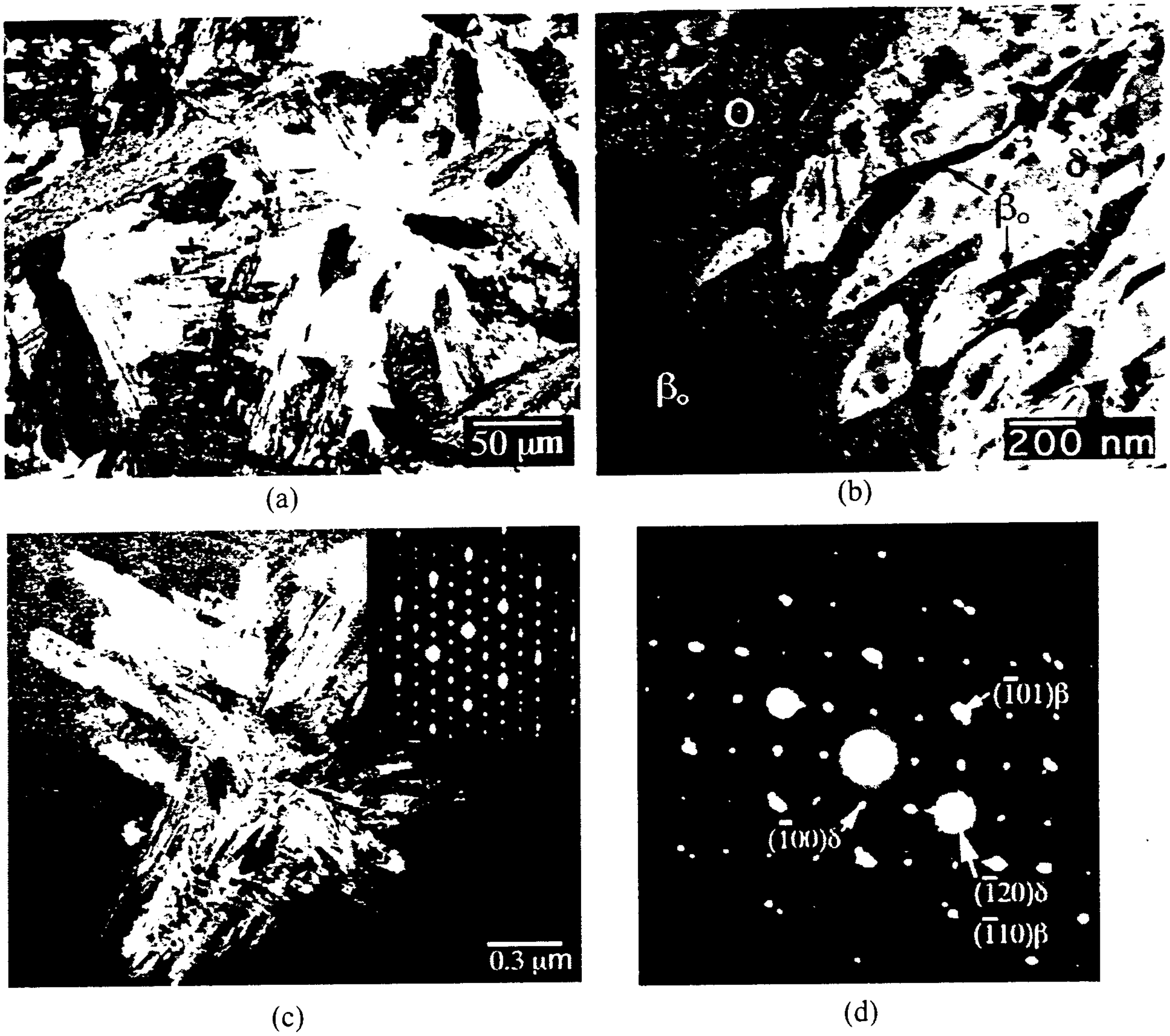

(a) (b) (c) (d)

Figure 5.26. Alloy #12 furnace cooled from 1475°C: (a) OM, (b) DF-image of δ_m structure with O phase precipitation at δ_m/β_o interface, (c) $\beta_o[111]//\delta_m[001]$ $\beta_o(\bar{1}10)//\delta_m(\bar{1}20)$ relationship, and (d) DF-image of O phase colony within the retained β_o grain with insert showing $\beta_o[011]//O[001]$ relationship.

rated β_o structure, oil quenched samples revealed the precipitation of δ along the β_o grain boundaries (Figure 5.27). No differences in composition were detected between the β_o and δ phases in the oil quenched material either through EPMA or TEM-EDS analysis.

The formation of massive-like δ colonies has been observed before in both binary Nb-Al [37, 41] and ternary Nb-Ti-Al systems [10], but has only been reproduced in binary alloys under extreme cooling conditions. The formation of the δ colonies in the ternary was suggested to have occurred by Al enrichment near the grain boundaries, due to segregation from casting [10]. The

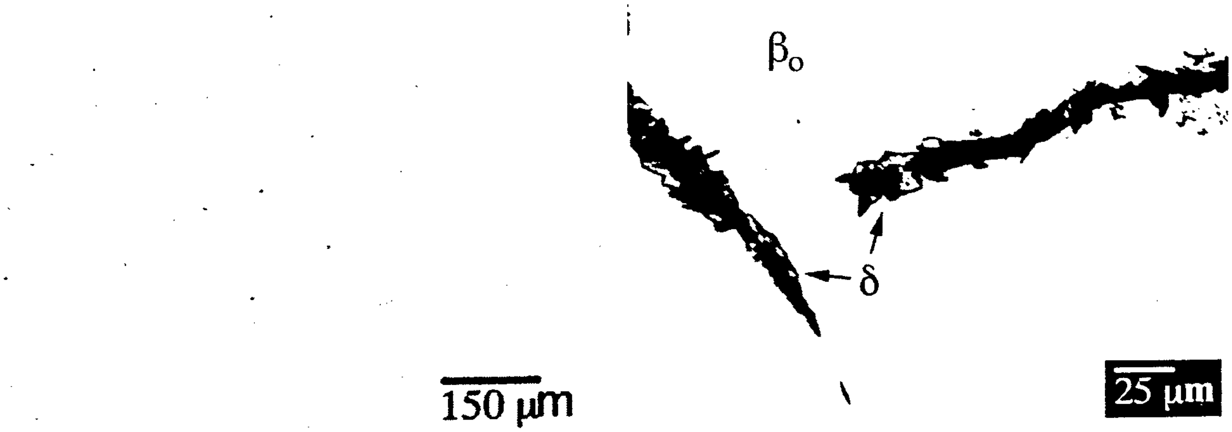

(a) (b)

Figure 5.27. Optical micrographs of alloy #12 (a) water quenched from 1475°C and (b) oil quenched from 1475°C.

compositionally invariant reaction that had formed the δ colonies along the grain boundaries in the cast and post homogenized treatments in the Nb-25Ti-25Al alloy does suggest that the massive transformation is a real effect. The separation of the laths by thin layers of β_o and a $\beta_o(\bar{1}10)//\delta(\bar{1}20)$ relationship, suggests that the massive-parent interfaces maybe semi-coherent in this case, in apparent support of observations made in other systems [42, 43]. The presence of the β_o phase between the δ laths may have allowed for a reduction in the strain energy associated with the transformation. This, coupled with the orientation relationship to the β_o phase, may have made the transformation kinetically favorable over a broad range of cooling rates.

5.9 The Four-Phase $\sigma + \delta + \beta + O$ Plane.

The first evidence for the existence of a four phase plane in the Nb-Ti-Al system was seen in the DTA thermogram of alloy #4, as a significant endothermic reaction peak starting at 983°C. The heat treatments at 990 and 970°C of alloy #4 above and below the reaction, showed a clear shift in the tie lines and phase relationships (Figure 5.28). At 990°C, alloy #4 consisted of $\beta_o + \sigma + \delta$, whereas alloy #5 contained $\beta_o + \sigma +$ O. At 970°C alloy #3 contained $\delta + \beta_o +$ O, with alloy #4 consisting of $\delta + \sigma +$ O. Therefore, the four-phase reaction cna be written as: $(\delta+\sigma+\beta_o) + (\sigma+\beta_o+O)$

=> $(\delta+\beta_o+O) + (\delta+\sigma+O)$. From the tie lines of alloys 8 and 9, it is clear that they have missed the four phase plane. Alloy 8 remains $\beta_o + \delta$ (except for the formation of α_2 due to impurities), with alloy #9 passing through the $\beta_o + \sigma + \delta$ three-phase field leaving a $\sigma + \delta$ structure. Alloy #3 has either just missed the four-phase reaction plane or is right on its edge. Therefore, alloy #4 is the best alloy to study, as it is at the heart of the four phase reaction.

TEM examination of the transformation front in alloy #4 at 970°C, revealed the significance of the effect of the four phase plane on the transformation (Figure 5.21). The first transformation that occured was the decomposition of the metastable β_o phase into the intermediate metastable O' phase. The subsequent transformation of O' to the equilibrium structure is controlled through bulk diffusion, as evidenced by the compositional gradient ahead of the interface. The transformation of O' to the equilibrium $\sigma + \delta + O$ did not occur through a continual compositional gradient within the O' phase. This was evident in the BSE-image of the reaction interface revealing a contrast between the O' and O phase. A clear compositional jump was confirmed by TEM-EDAX analysis (Table 5.4). There must be a reaction path governed by the metastable phase equilibria remnant from the four phase reaction plane, due to the composition of the metastable O' phase. Instead of δ forming with a gradual shift in the O' phase composition, β_o was formed in the diffusion field ahead of the σ phase. It should be pointed out that the O phase has a narrow solubility of aluminum, a fixed ratio of Al:(Ti+Nb). Therefore, the excess titanium and niobium ahead of the reaction front would promote the stability of β_o in accordance with the metastable phase equilibria. The composition of this β_o phase should be close in composition to the β_o phase at the four-phase reaction plane. The next step in the reaction is the nucleation and growth of the new equilibrium O at the σ interface. Finally the δ phase forms in-between the σ and O phases as all the β phase is consumed, producing a final microstructure which consists of elongated σ grains partially surrounded by δ and with fine O phase particles between.

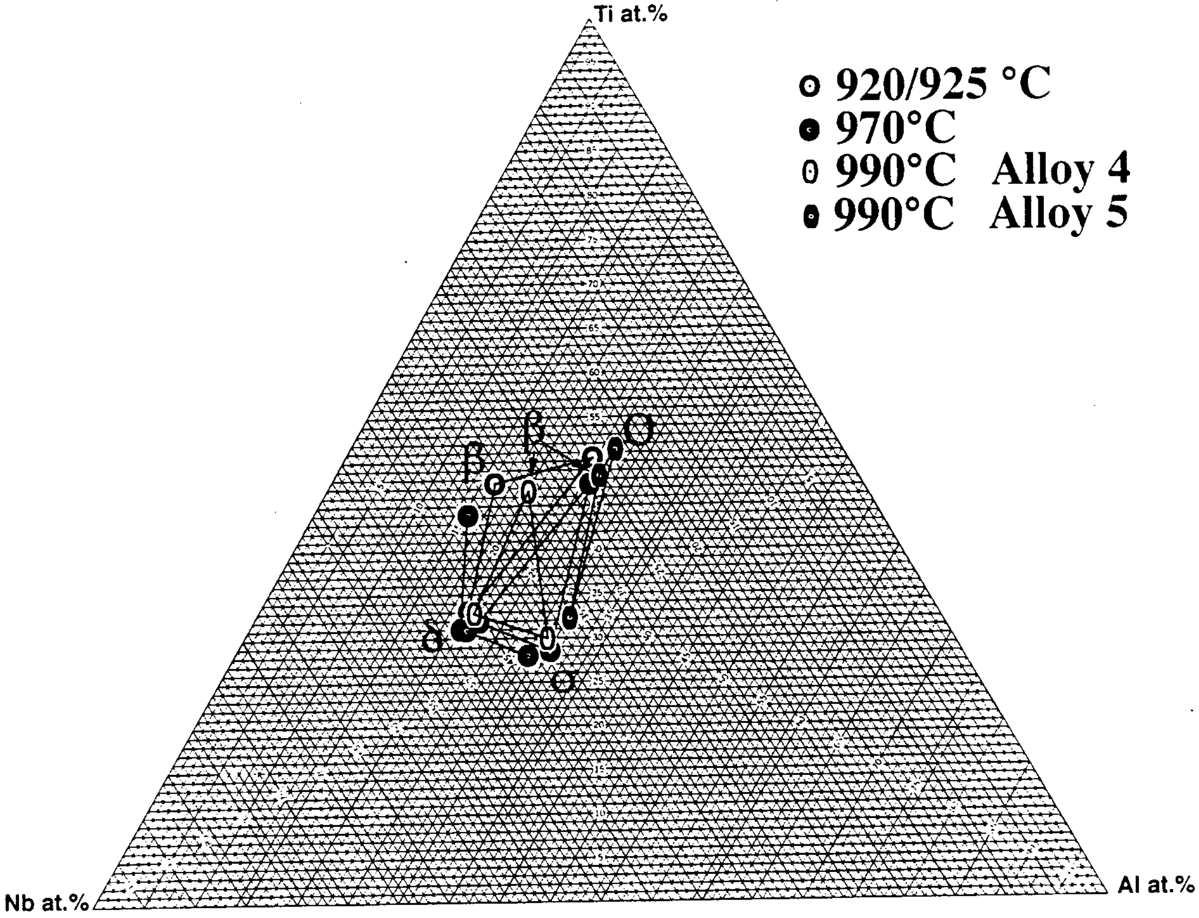

Figure 5.28. The tie lines above and below the four phase reaction plane at 980°C (983°C).

6. Alloys with β + σ Structures and the β to O Reaction Kinetics

6.1 Phase Equilibria and Transformations in Alloy #'s 5, R1850 and R1851

The composition of alloy #5 (Nb-35Ti-30Al) lies near the compositions of alloys 4 (Nb-37.5Ti-25Al) and 9 (Nb-30Ti-25Al), and in several ways shares many microstructural similarities with these alloys. Alloy #5, however, is unique and is covered specifically in the first part of this section. Alloys 4 and 9 contained the β → δ + σ eutectoid reaction, which was also present in alloys 12 and 15, and therefore were discussed in the previous section. Alloy #5, not to mention alloys 3 and 9, are important to alloy #4 when discussing the four-phase equilibrium occurring at 980°C, which will be addressed later in this section.

The DTA Thermogram for alloy #5 is presented in Figure 6.1. From the thermogram two major reactions can be observed on heating. The first, a small endothermic peak with an onset of 980 and peak at 1003°C and the second a long continuous trough with a completion temperature of 1398°C. Based on these results and transformation observed in other near by alloys the heat treatment temperatures were selected (arrows in Figure 6.1) and are listed in Table 6.1. The results of X-ray analysis, microprobe analysis are also presented in Table 6.1. The results of microprobe analysis are presented in Table 6.2 for alloys R1851 and R1850; additional alloys that were produced based on the 30Nb-42Ti-28Al composition, near that of alloy #5. Both alloys are of the same nominal composition, however, R1850 has a higher nitrogen concentration than R1851.

The high temperature single phase field in all alloys was identified as the β phase, with alloy #5 being the only alloy in this investigation to exhibit the β_o(100) XRD peak (Figure 6.2). Although, anti-phase boundaries were observed during the TEM examination of the solutionized structures of alloys 4 and 9, they were not observed in alloy 5. Streaking in the β_o[110] SAD pattern from the ω phase were also observed in alloy #5 (Figure 6.2(b)). The appearance of the (100) superlattice intensity in the XRD pattern and the missing APB's suggest that the β/β_o transition temperature occurred at higher temperatures than in alloys 4 and 9. Oil quenching from the β phase field of the homogenized alloys 4 and 9 also produced some ω phase formation.

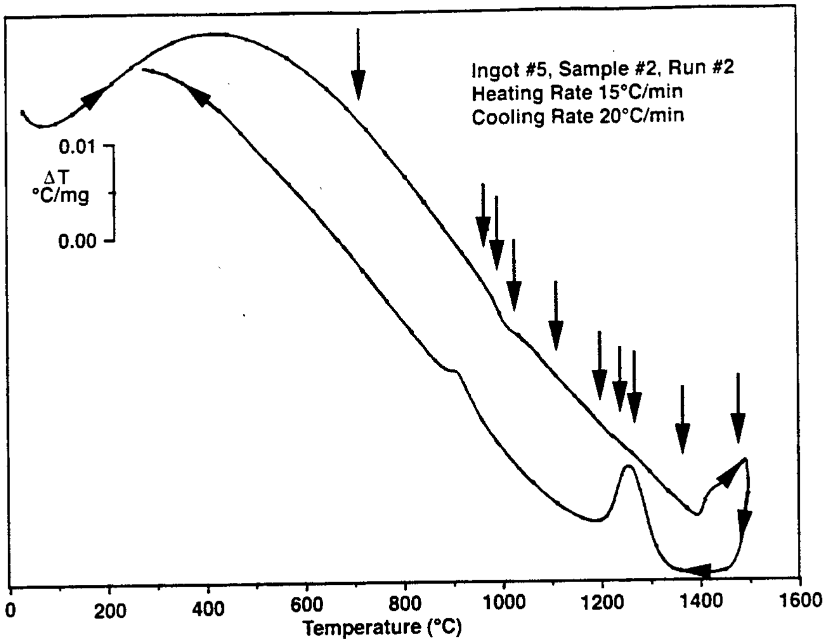

Figure 6.1 DTA Thermogram of Alloy #5 (Ti35-Al30-Nb35). Arrows represent the selected heat treatments.

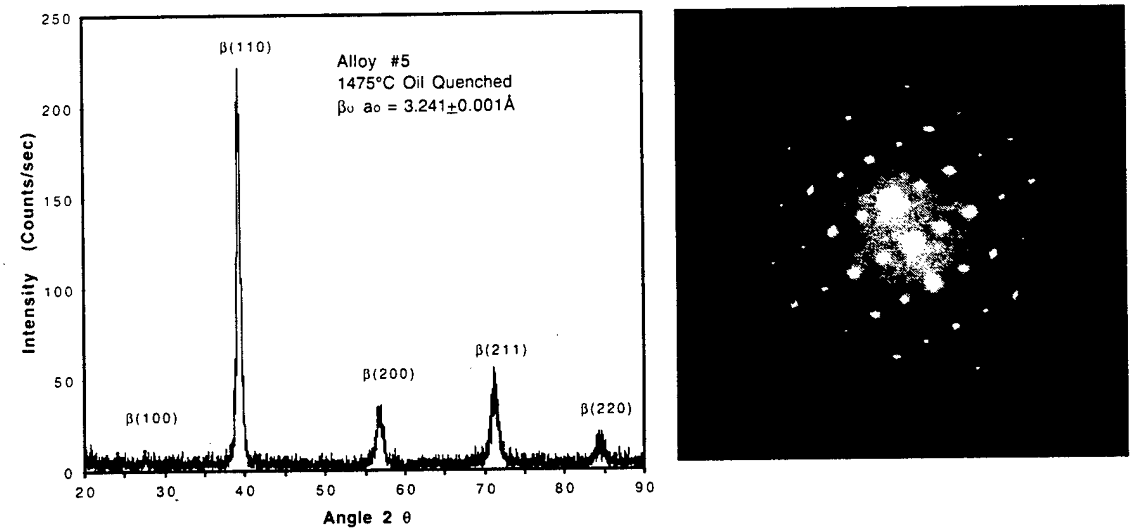

(a)

(b)

Figure 6.2 Alloy #5 β solutionized at 1475°C. (a) XRD pattern of B2 structure, and (b) the β_o[110] SAD pattern showing ω streaking.

Table 6.1 Alloy #5 Selected Heat Treatments and Results of EPMA and X-Ray Analysis

Heat Treatment	BSEI Contrast	Composition (at.%)				X-ray Results
		Ti	Al	Nb	Phase	Lattice Parameter
1475°C/6h/OQ	Grey	35.00	29.71	35.29	β	a_o = 3.241±0.001Å
1475°C/6h/OQ +	Grey (Matrix)	36.21	30.12	33.66	β	a_o = 3.243±0.001Å
1360°C/14h/OQ	Bright	24.03	32.92	43.05	σ	a_o = 9.989±0.006Å
						c_o = 5.159±0.003Å
1475°C/6h/OQ +	Grey (Matrix)	43.50	29.16	27.34	β	a_o = 3.251±0.001Å
1268°C/32h/WQ	Bright	27.63	33.46	38.90	σ	a_o = 9.956±0.007Å
						c_o = 5.145±0.004Å
1 mm	Grey (Matrix)	43.61	26.54	29.86	β	
From	Bright	26.26	32.74	41.00	σ	
Surface	Dark	56.03	27.84	16.13	α_2	
1475°C/6h/OQ +	Grey (Matrix)	44.11	28.42	27.47	β	a_o = 3.247±0.001Å
1248°C/32h/WQ	Bright	28.38	32.88	38.74	σ	a_o = 9.950±0.008Å
						c_o = 5.141±0.005Å
1200°C/48h/WQ	Grey (Matrix)	45.86	27.50	26.64	β	a_o = 3.241Å (211)
	Bright	30.37	32.31	37.32	σ	a_o = 9.954±0.004Å
						c_o = 5.143±0.002Å
HIP1475°C/6h +	Grey (Matrix)	47.30	25.98	26.72	β	a_o = 3.246±0.012Å
1475°C/3h/OQ +	Bright	31.41	31.44	37.15	σ	a_o = 9.946±0.006Å
1100°C/7d/WQ						c_o = 5.142±0.004Å
	Dark (***)	56.47	26.92	16.62	α_2	
1475°C/6h/OQ +	Grey (****)	38.53	29.71	31.77	β	a_o = 3.254Å (211)
1025°C/14d/WQ	Bright	32.67	31.18	36.15	σ	a_o = 9.962±0.003Å
						c_o = 5.143±0.002Å
1475°C/6h/OQ +	Grey (**)	48.30	26.62	25.08	β	a_o = 3.254Å (211)
990°C/14d/WQ	Bright (***)	32.22	31.19	36.59	σ	a_o = 9.957±0.006Å
						c_o = 5.144±0.004Å
1475°C/6h/OQ +	Grey	51.23	25.95	22.82	O (?)	
970°C/14d/WQ	Bright	32.58	30.55	36.87	σ	a_o = 9.947±0.007Å
						c_o = 5.138±0.005Å
1475°C/6h/OQ +	Grey	Structure Too Fine			O	a_o = 6.154±0.009Å
700°C/30d/WQ						b_o = 9.505±0.026Å
						c_o = 4.653±0.006Å
					ω”	a_o = 4.592±0.007Å
						c_o = 5.497±0.003Å
HIP1475°C/6h +	Grey	Structure Too Fine			ω”	a_o = 4.601±0.011Å
1475°C/3h/OQ +						c_o = 5.479±0.004Å
700°C/150d/WQ					σ	a_o = 9.915±0.041Å
						c_o = 5.132±0.020Å
					O	Present
1200°C/48h/WQ +	Grey	44.46	28.72	26.82	O	O (111) present
700°C/30d/WQ	Bright	29.21	33.60	37.19	σ	a_o = 9.947±0.007Å
						c_o = 5.149±0.004Å

= Avg. of best two measurements * = Avg. of best three measurements
****= Avg. of best four measurements

Table 6.2 Alloys R1851 and R1850 Selected Heat Treatments and Results of EPMA

Heat Treatment	BSEI Contrast	Composition (at.%)			
		Ti	Al	Nb	Phase
R1850	Grey (Matrix)	48.71	27.24	24.05	β
1350°C/26h/FC +	Bright	32.88	31.50	35.62	σ
1100°C/7d/WQ	Dark (***)	55.47	27.58	16.95	α_2
R1851	Grey (Matrix)	48.43	28.36	23.21	β
1350°C/26h/FC +	Bright	32.49	32.35	35.16	σ
1100°C/7d/WQ	Dark (**)	56.62	27.77	15.61	α_2
R1851	Grey (Matrix)	50.85	26.10	23.05	β
1350°C/26h/OQ +	Bright	34.37	30.74	34.89	σ
1025°C/14d/WQ	Dark	57.18	26.97	15.85	α_2
R1851	Grey (Matrix)	53.01	26.11	20.88	O
1350°C/26h/OQ +	Bright	35.15	30.49	34.36	σ
990°C/14d/WQ					
R1851	Grey (Matrix)	52.58	25.93	21.48	O
1350°C/26h/OQ +	Bright	34.28	30.71	35.01	σ
975°C/30d/WQ					

** = Best two measurements
*** = Best three measurements

The evolution of the σ + β morphology with reduced temperature is best exemplified by alloy 5, although similar effects were seen in alloys 4 and 9 as well (Chapter 5). Even with moderate undercooling the elongated nature of the σ grains in the β_o matrix can be observed (Figure 6.3). This morphology is the result of a crystallographic preference of σ phase nucleation and growth within the β_o phase. As the temperature is reduced the volume fraction of σ increases and the elongated nature of the σ grains persists, yielding a very desirable microstructure (Figure 6.3(b)). X-ray diffraction confirms the presence of only two phases σ and β_o (Figure 6.4). Prolonged heat treatment of the σ + β_o morphology at 700°C for 30 days resulted in the β phase being replaced by the O phase (Figure 6.4(b)). Similar observations were found for alloy #4 annealed 1200°C WQ + 700°C WQ (Figure 6.5).

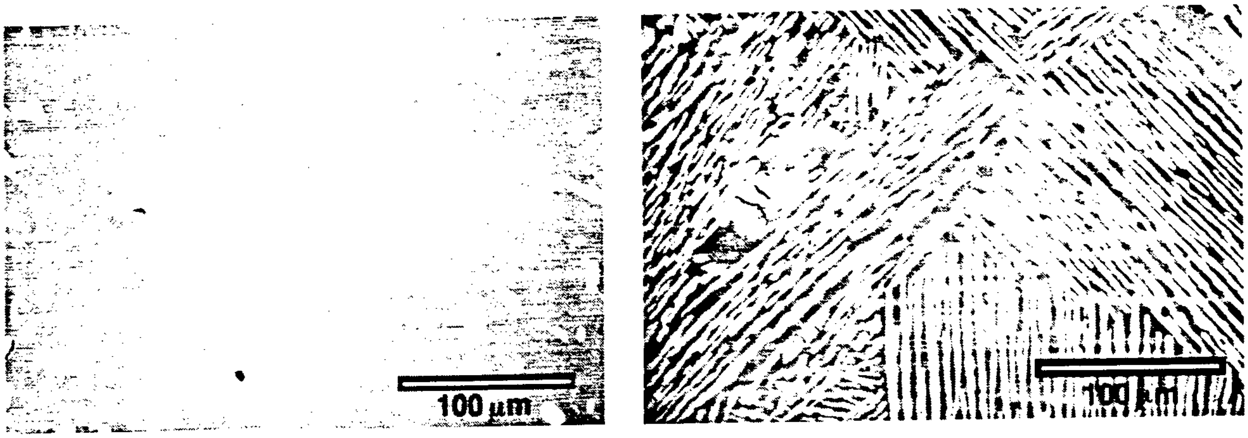

(a) (b)

Figure 6.3 BSE-images of $\sigma + \beta_o$ structure in alloy #5 aged at (a) 475/1360°C OQ, and (b) 1475/1248°C WQ

At 990°C, the $\beta_o + \sigma + O$ three-phase field passes through alloy #5. TEM examination revealed a two-phase structure of σ and O, however, the O phase was found to have two different compositions based on its location in the microstructure (Table 6.3, Figure 6.6). The lamellar structure examined consisted of σ with a second phase, with the σ phase being the majority phase. Compositionally the second phase corresponded to either the β_o phase or the O phase based on EPMA results, depending on the location in the sample. All of the diffraction patterns from this region, however, corresponded to the O phase structure (Figure 6.6(b)). This suggested that the β_o phase had transformed to O' during quenching due to the proximity of the heat treatment temperature to the β_o to O transformation temperature.

By 970°C the three-phase field passed through the alloy and a two-phase equilibrium between σ and O was established. Again, desirable microstructures were obtained, this time between the σ and O phases (Figure 6.7). The slightly higher aluminum content of alloy R1851 shifted the phase equilibria into the $\beta + \sigma + \alpha_2$ three-phase field at this temperature (Figure 6.8).

Alloy #9 starts off in a similar fashion as alloy #5, in that a $\sigma + \beta$ lamellar morphology was obtained above 1270°C (Figure 6.9(a)). However, as the temperature is reduced, the δ phase initialy precipitates along the grain boundaries. A further decrease in temperature produced an increase in the volume fractions of σ and δ (Figure 6.9(b,c)). TEM examination revealed that with the shift in

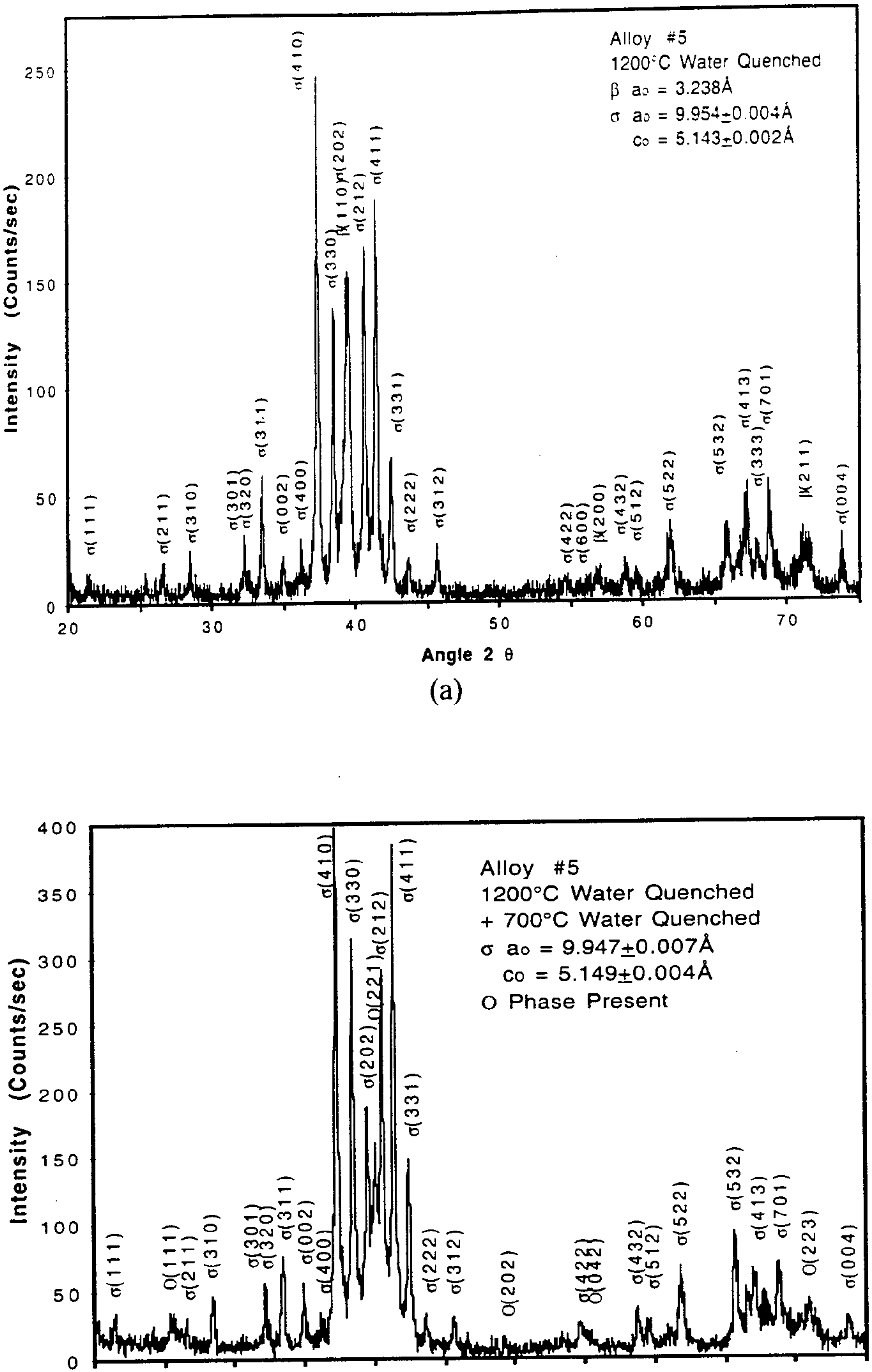

(a)

(b)

Figure 6.4 X-ray Diffraction Traces of Alloy 5 consisting of σ + βo phases at (a) 1200°C, and (b) σ + O phases after 1200°C + 30 Days at 700°C.

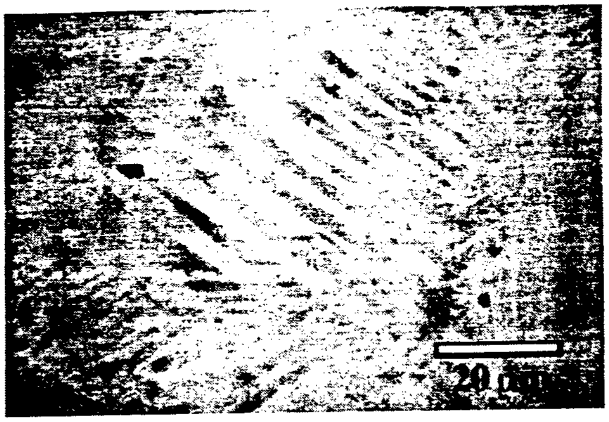

Figure 6.5 BSE-image of alloy #4 aged at 1270 +700°C.

Table 6.3 TEM Composition Analysis of Alloy #5 HT 1475 + 990°C WQ

	Composition (at.%)		
Phase	Ti	Al	Nb
O'	51.19	26.37	22.44
O	48.88	25.22	25.90

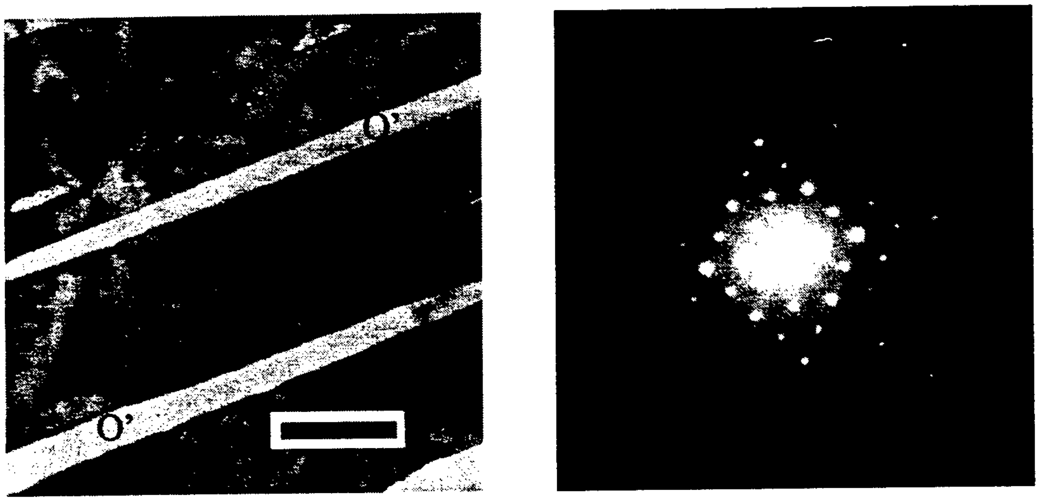

(a)

(b)

Figure 6.6 TEM images of Alloy #5 (Ti35-Al30-Nb35) Heat treated at 1475 + 990°C WQ. (a)Bright Field, on a σ[001] Zone, and (b) O[011] SAD pattern from the O' region.

composition of β at 1090°C, the β phase becomes disordered, as confirmed by the presence of anti-phase boundaries formed on cooling (Figure 6.10(b)). The lower temperature phase equilibria indicates that the β + σ + δ three-phase field passes completely through alloy #9, leaving behind a σ + δ two-phase structure. The presence of the α_2 phase was also observed as a result of impurities (O and N). The volume fraction of α_2 was observed to increase as the amount of β within the structure was reduced (Figure 6.11(a,b)).

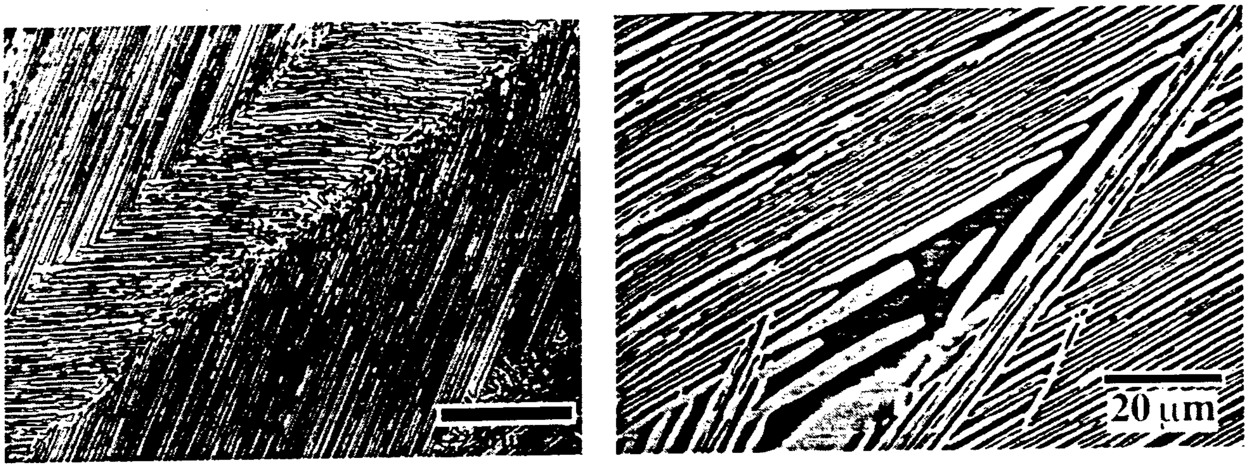

(a) (b)

Figure 6.7 Alloy R1851 heat treated at 1350°C OQ + 975°C 30 Days WQ, σ in O phase matrix. (a) OM, and (b) BSE-images.

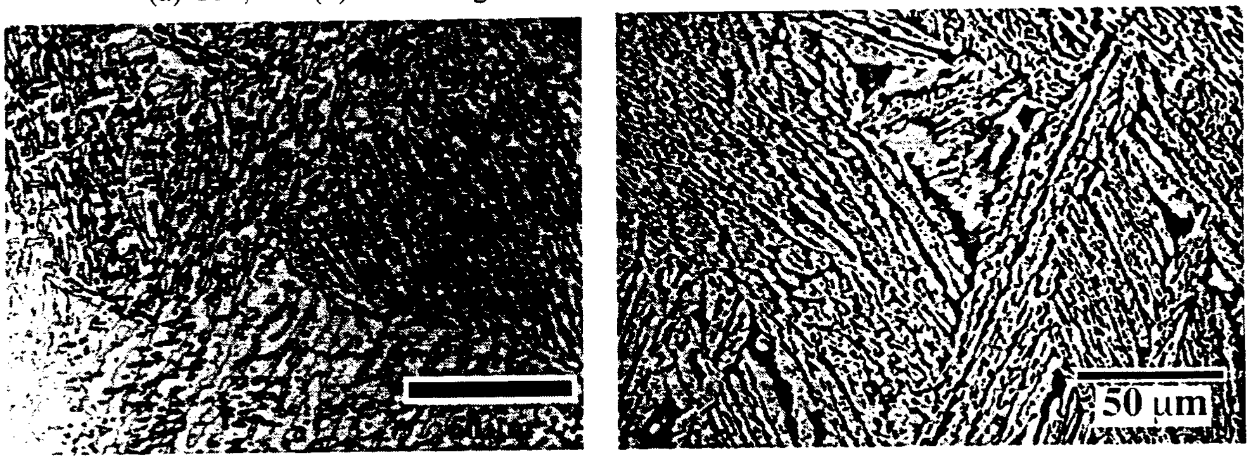

(a) (b)

Figure 6.8 Alloy R1851 HT 1350°C OQ + 1025°C 14 Days WQ, $\sigma + \alpha_2$ in β_o matrix. (a) OM, and (b) BSE-images.

The influence of interstitial contamination was first observed as a reaction layer about 1 mm from the surface, where three phases were present while the interior consisted of two-phases (Figure 6.11(c)). The stabilization of the α_2 phase due to impurities, which in some cases lead to the presence of four phases in equilibrium, was confirmed through EDS analysis (Table 6.4). Comparison of alloys R1851 to R1850 heat treated at 1100°C (Figure 6.13) further confirmed that impurities were contributing to α_2 stabilization. While both alloys have the same base composition, alloy R1850 had 0.12 wt.% N, and therefore contained a greater volume fraction of the α_2 phase than R1851.

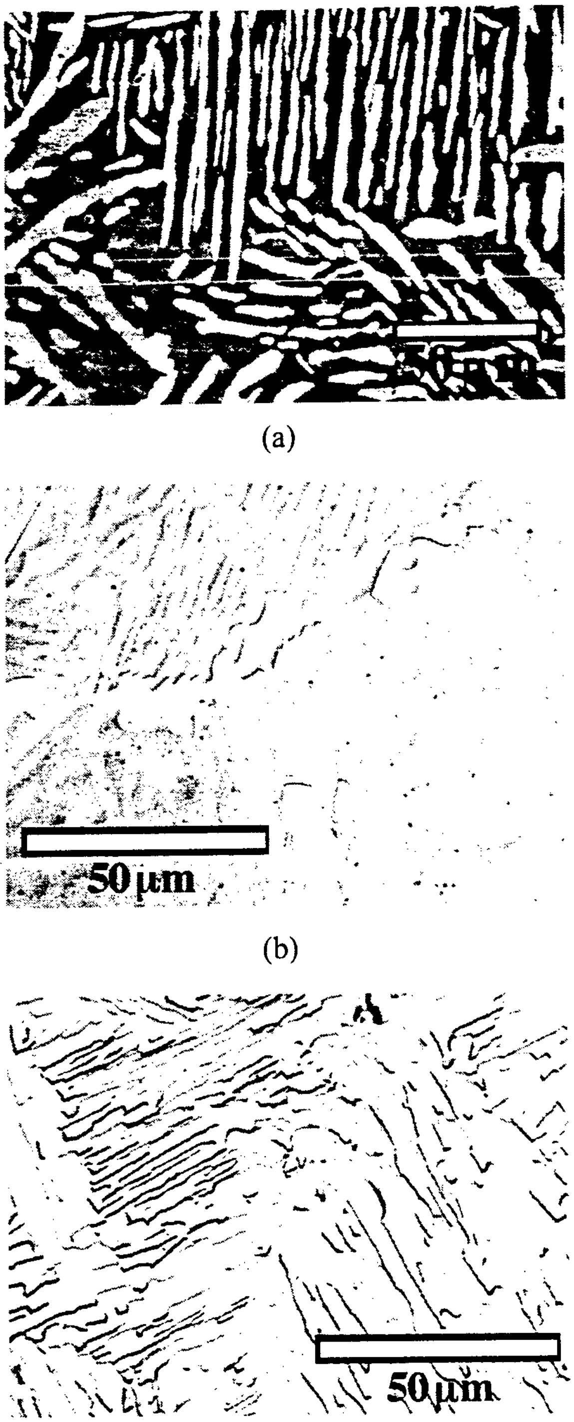

(a)

(b)

(c)

Figure 6.9 Alloy #9 (a)1475/1270°C WQ ,BSE-image of σ in β_o, (b) 1425 + 1200°C WQ, OM σ in β_o matrix with δ at grain boundaries, (c) 1425 + 1090°C WQ, OM, three phases $\sigma + \delta + \beta_o$, and (d) XRD pattern of 1090°C aged material.

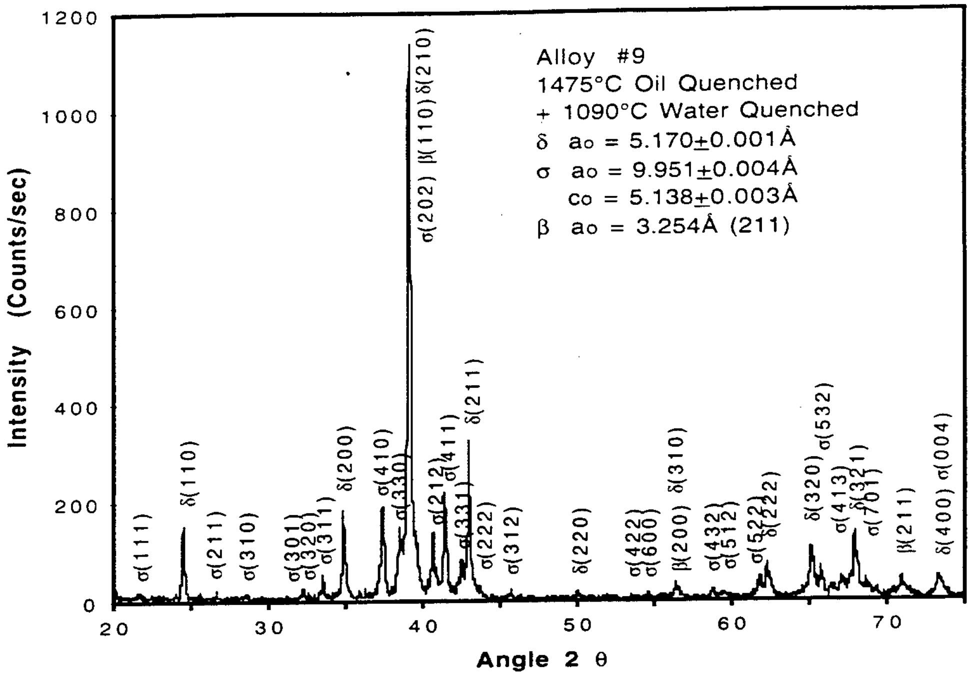

(d)

Figure 6.9 Continued.

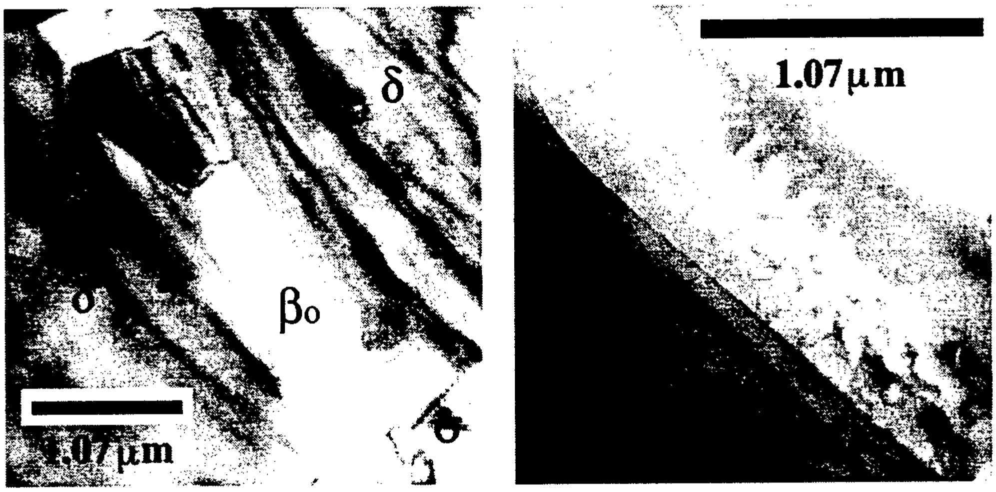

(a) (b)

Figure 6.10 TEM images - Alloy 9 (Ti25.86-Al29.65-Nb44.49), heat treated 1475°C + 1090°C WQ. (a) Bright Field, σ and δ in β matrix, and (b) Bright Field, Anti phase domains in β_o Phase.

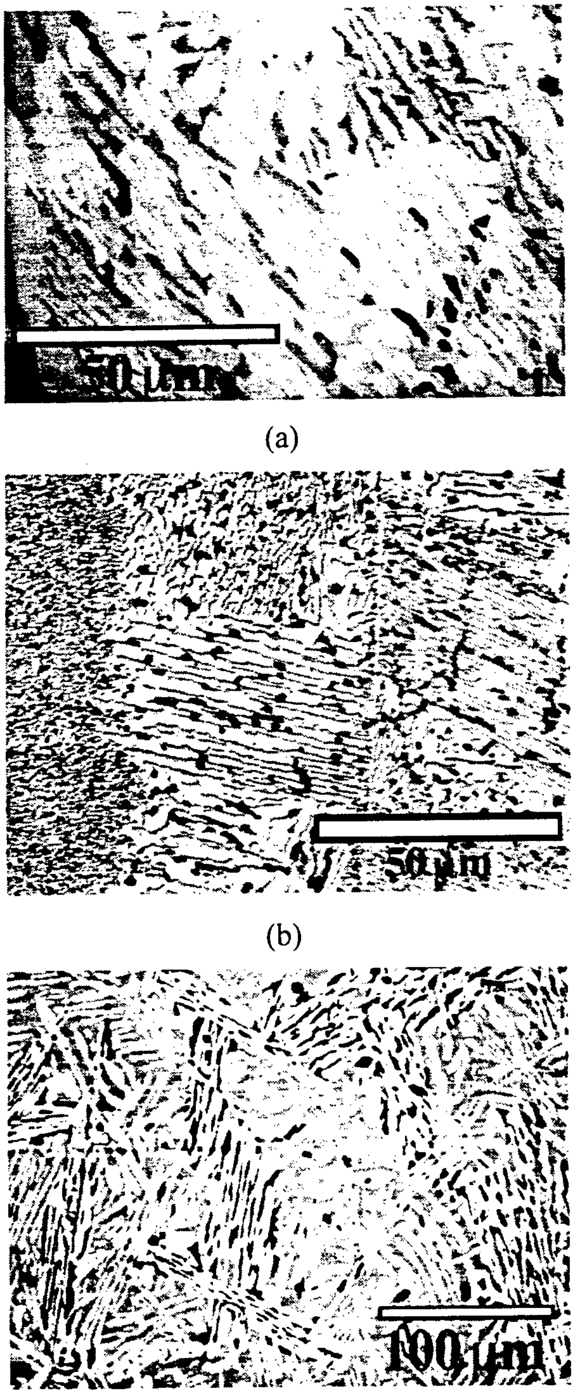

(a)

(b)

(c)

Figure 6.11 Suspected contamination effects in heat treated alloys. (a) BSE alloy #9 HT 1475/1090°C WQ, four phases near surface, (b) OM alloy #9 HT 1425/1025°C WQ, $\sigma + \delta + \alpha_2$, (c) BSE alloy #5 HT 1475/1248°C WQ, three phases 1 mm from surface, $\beta_o + \sigma + \alpha_2$.

(a)

Table 6.4 TEM Composition Analysis of α_2 Phase in Alloy #4 HT 1425 + Second Heat Treatment

	Composition (at.%)			
Phase	Ti	Al	Nb	Notes:
α_2	53.39	26.19	20.42	1025°C WQ
α_2	53.59	25.95	20.46	1025°C WQ
σ	29.27	33.35	37.38	

Note: β phase used as internal standard (EPMA)

	Ti	Al	Nb	Notes:
α_2	56.47	24.86	18.67	990°C WQ
α_2	53.60	27.83	18.57	990°C WQ
β	44.33	22.34	33.32	

Note: σ phase used as internal standard (EPMA)

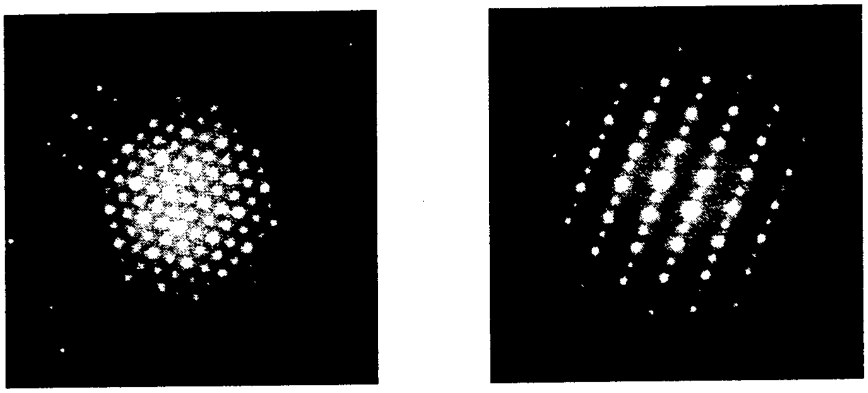

(b) (c)

Figure 6.12 TEM of α_2 phase formation due to interstitial contamination. (a) BF-image of α_2 precipitate in σ matrix in alloy #4 HT 1425 + 990°C WQ, (b) α_2 [0001], and (c) α_2[1126] patterns.

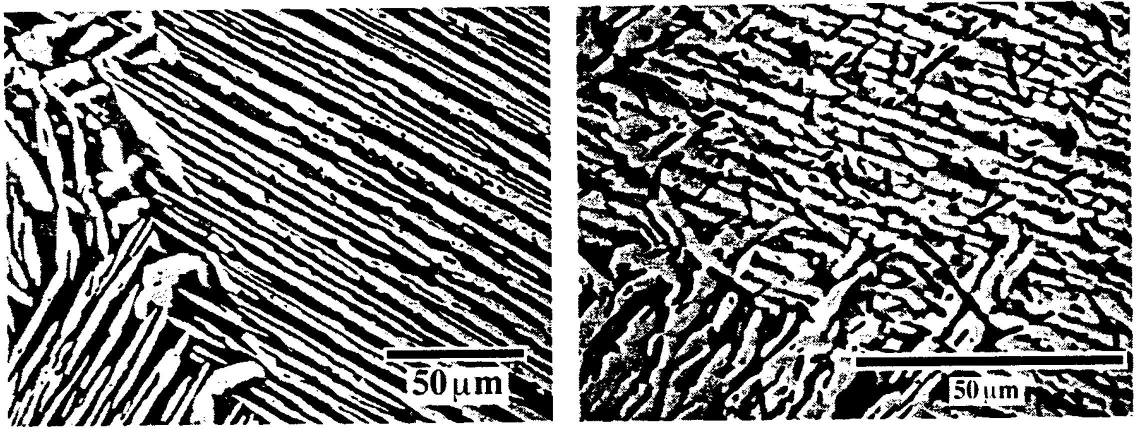

(a) (b)

Figure 6.13 BSE images of R1851 and R1850 alloys heat treated at 1350°C FC + 1100°C 7 Days WQ. (a) R1851 (N = 0.007 wt.%), $\sigma + \beta_o$ with only a small amount of α_2, and (b) R1850 (N = 0.120 wt%), $\sigma + \beta_o$ with increased volume fraction of α_2.

The 700°C heat treatment of alloy #5 did not result in full equilibrium being established even after 150 days. Alloy #5, which contained a higher concentration of aluminum than alloy #4, placed itself off the O phase compositional line and after 150 days yielded only a partial transformation to the equilibrium structure (Figure 6.14(a)). TEM examination of the grain interior revealed a fine structure of the O and ω" phases (Figure 6.14(b)), confirmed through X-ray diffraction (Figure 6.15). The grain boundary region consisted of σ and O, as confirmed through both X-ray and electron diffraction (Figure 6.16 and Table 6.5). Alloy #9, which was expected to have σ present at this temperature based on alloy #5, consisted instead of the β and O phases (Figure 5.22(b) and Figure 6.17).

A cooling rate study was performed on the R1851 alloy equilibriated at 1100°C for 7 days to produce the σ + β structure. Through water quenching (approximately 600°C/sec) the β_o phase was retained except for some ω phase formation. As the cooling rate was reduced in the air-cooled samples (approximately 160°C/sec), the β_o to O phase transformation was only partial (Figure 6.18). The O phase formed along the σ / β_o interfaces (Figure 6.18(c)) and within the β_o grain interiors (Figure 6.18(d)), nucleating at approximately 1μm intervals. No ω phase formation was observed within the retained β_o (Figure 6.18(e)).

Upon furnace cooling (19°C/min at 1000°C), Figure 6.19, the β_o phase was completely displaced by O with no apparent effect to the σ phase morphology or distribution (Figure 6.19(b-d)). Thus, the desirable lamellar σ morphology could be retained following the β to O transformation.

6.2 The σ + β Two Phase Equlibria Near Alloy #5

Alloy #5 is an interesting material in that all of the tie lines can easily be projected on a single plethel section within the limits of experimental error. This plethel section, shown in Figure 6.20, illustrates the tie lines between the β and σ phases with decreasing temperature. An abrupt change in slope of the tie lines is observed between 970 and 990 °C; there is also a corresponding endothermic peak on the DTA thermogram (Figure 6.1) which starts at 981°C and peaks at 1000°C

(@5°C/min). This peak corresponds to the transformation of β to O as a three phase field of $\beta - \sigma + O$ passes through the alloy very abruptly. Based on the movement of the tie lines from the TEM analysis of alloys 4 and 5 this transformation changes in characteristics from eutectoid to a $\beta_o + \sigma \rightarrow O$ peritectoid reaction (Figure 41). This alloy is very near the four phase plane observed in alloy #4 of $\sigma + \delta + \beta + O$ and accounts for the existence of the $\sigma + \beta + O$ phase field required to combine with the $\sigma + \delta + \beta$ phase field to produce the two $\delta + \beta + O$ and $\delta + \sigma + O$ three-phase fields. The tie lines established between $\beta + O$ at 990°C are in good agreement with previous data at 1000°C [93Row]. The identification by TEM of two O phases with different compositions is believed to be due to the βo phase at 990°C transforming to O phase just prior to the water quench as a result of the close proximity of the heat treatment temperature to the transformation temperature. Alloy R1851 (which has a slightly higher aluminum content) clearly shows the presence of $\alpha_2 + \beta + \sigma$ at 1025°C and is in agreement with others [98Hel]. This suggests a narrow four phase plane between 1000 and 990°C involving $\alpha_2 + \beta + \sigma + O$. The 700°C heat treatment confirmed the presence of $\sigma + O$ structure.

The microstructural morphology observed in these alloys offers a very interesting insitu composite structure (Figure 6.3 and 6.7), alternating layers of σ in a β_o matrix or after low temperature heat treatments σ in an O matrix; these two morphologies may offer excellent mechanical properties. It is apparent that the β_o to O phase transformation at 981°C in these alloys will result in residual stresses in the alloy as evidenced by the auto catalytic mechanism operating for O phase formation in the β grains (Figure 6.18(d)). It is hoped the information gathered here will assist in the optimization of alloy composition and thermal processing to maximize performance of these materials.

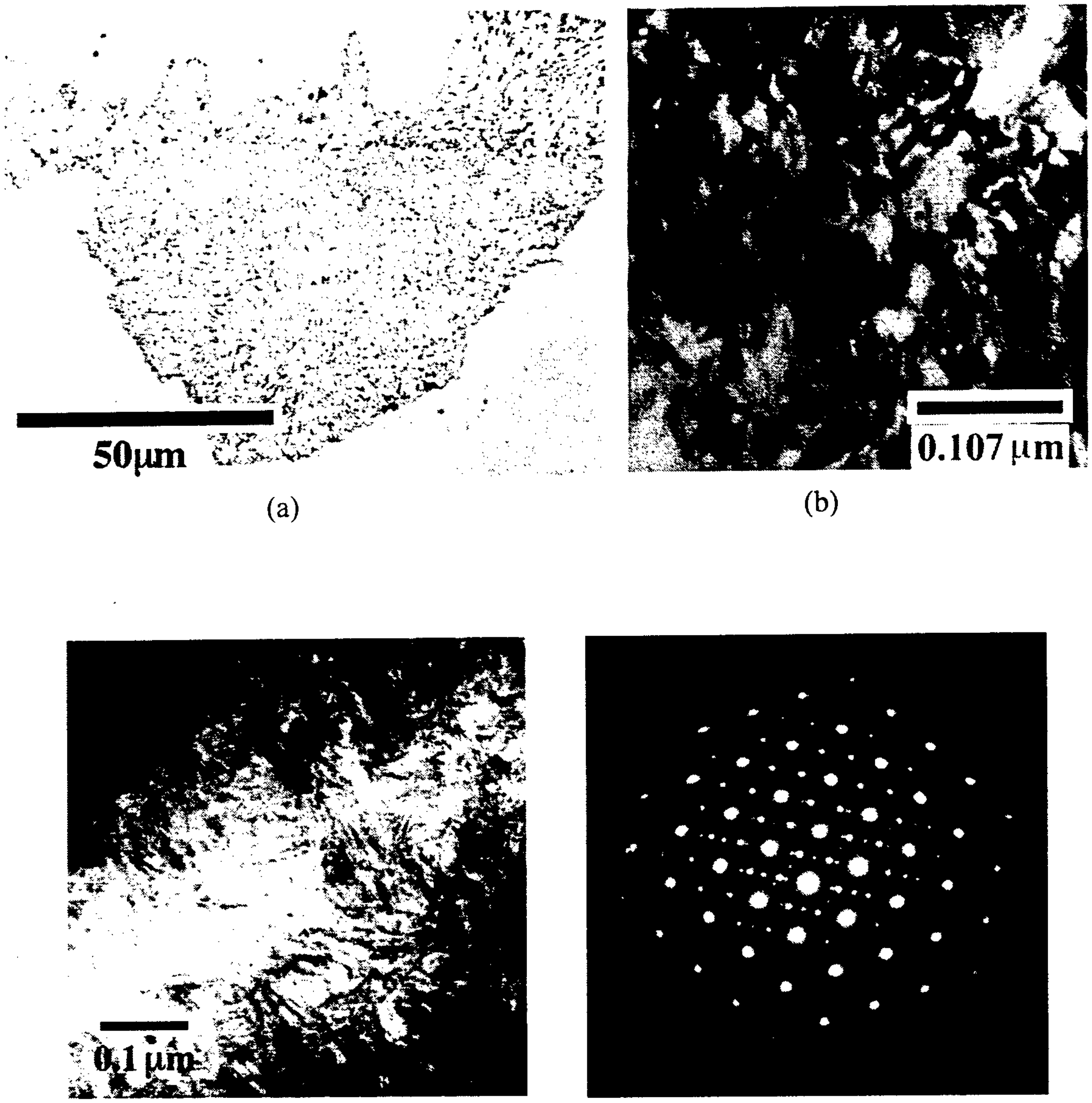

(a) (b)

(c) (d)

Figure 6.14 Alloy #5 heat treated at 700°C for various times. (a) OM 150 Days, σ + O at prior grain boundaries (b) BF-image, 30 days on a ω"[110] Zone, (c)BF-image, 150 days, and (d)β_o [111] with 3 - O<110> and ω"[001] SAD patterns, of prior β_o region.

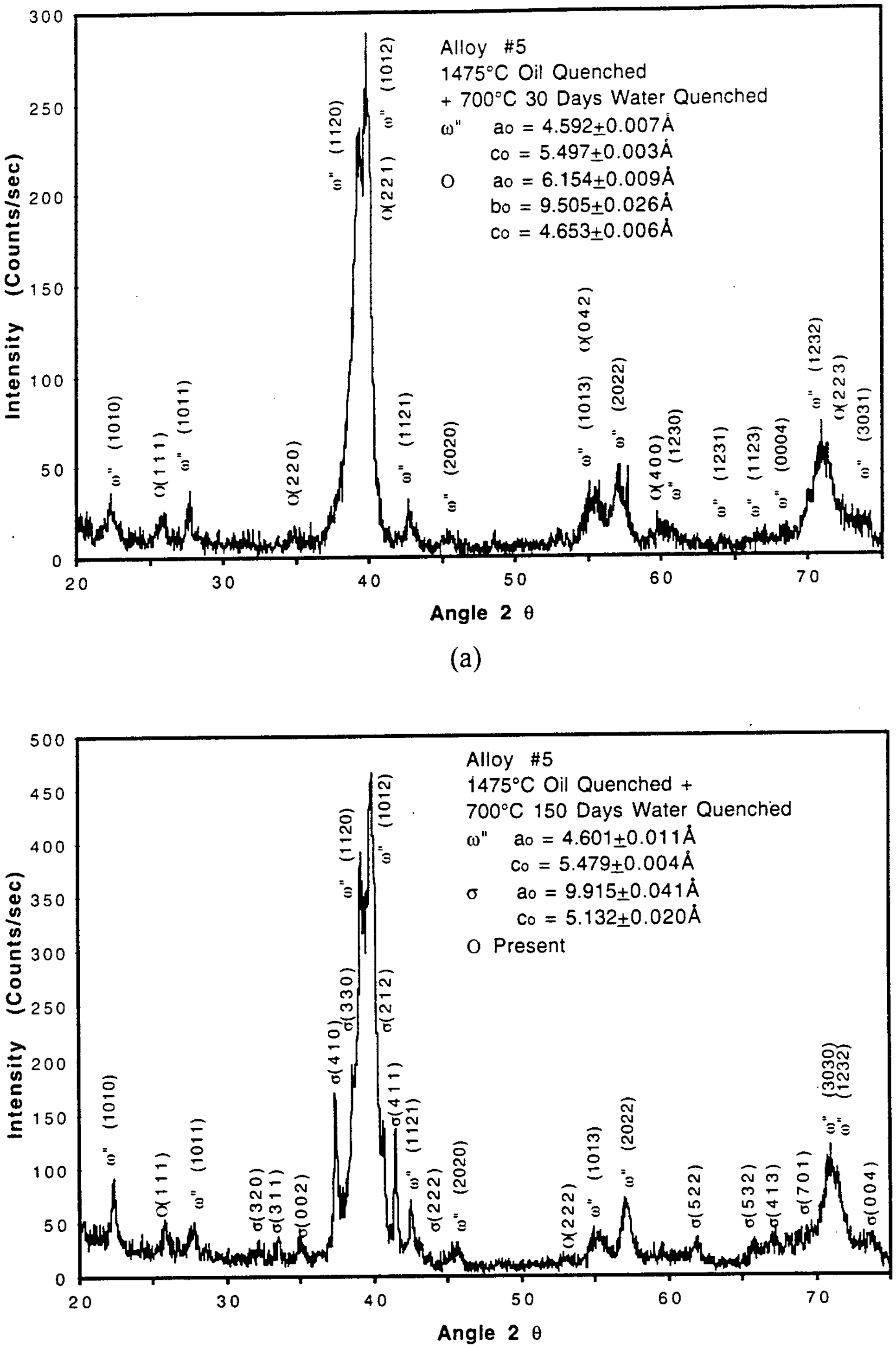

(a)

(b)

Figure 6.15 XRD patterns of alloy #5 aged at 700°C for (a) 30 days, and (b) 150 days.

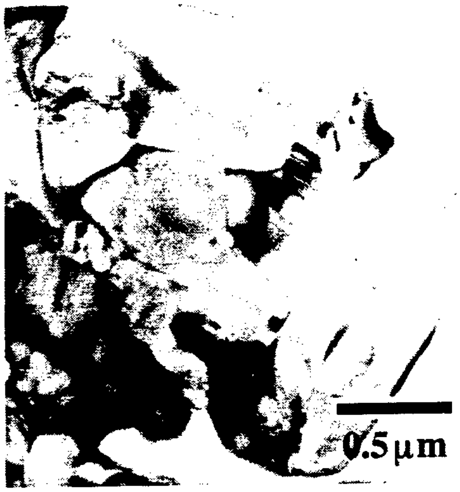

(a)

Table 6.5 TEM Composition Analysis of Alloy #5 HT 1475 + 700°C 150 Days WQ

	Composition (at.%)			
Phase	Ti	Al	Nb	Location
σ	27.77	26.47	45.76	G.B.
σ	27.44	27.60	44.96	G.B.
σ	27.11	26.34	46.55	G.B.
O	40.49	22.31	37.20	G.B.
O	37.01	23.26	39.74	G.B.
O	35.19	20.73	44.08	G.B.
O	35.05	20.39	44.56	G.B.

Note: External Standard.

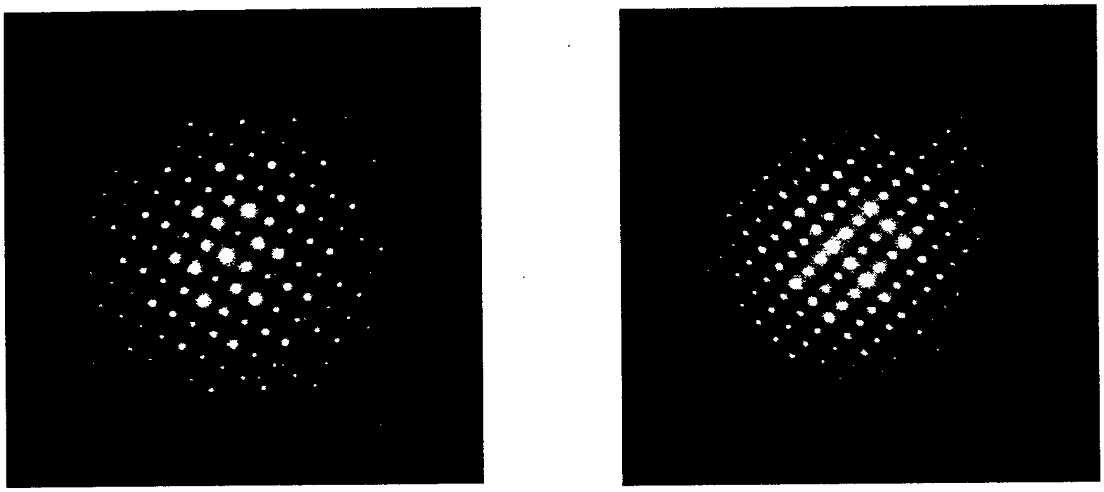
(b) (c)

Figure 6.16 TEM images of Alloy #5 (Ti35-Al30-Nb35) heat treated 700°C for 150 days. (a) BF-image of grain boundary region with σ + O, (b) O[110], and (c) σ [110] SAD patterns.

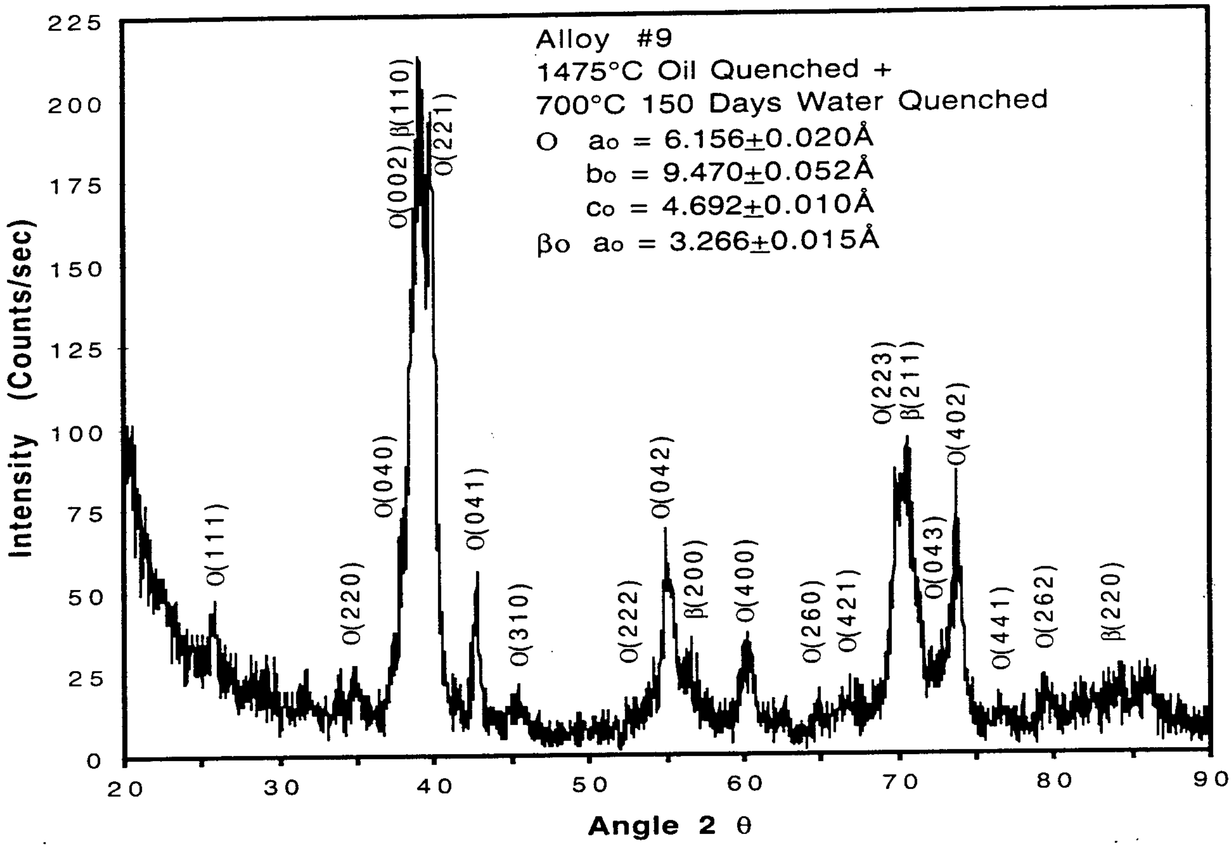

Figure 6.17 XRD pattern of alloy #9 heat treated at 700°C for 150 days WQ.

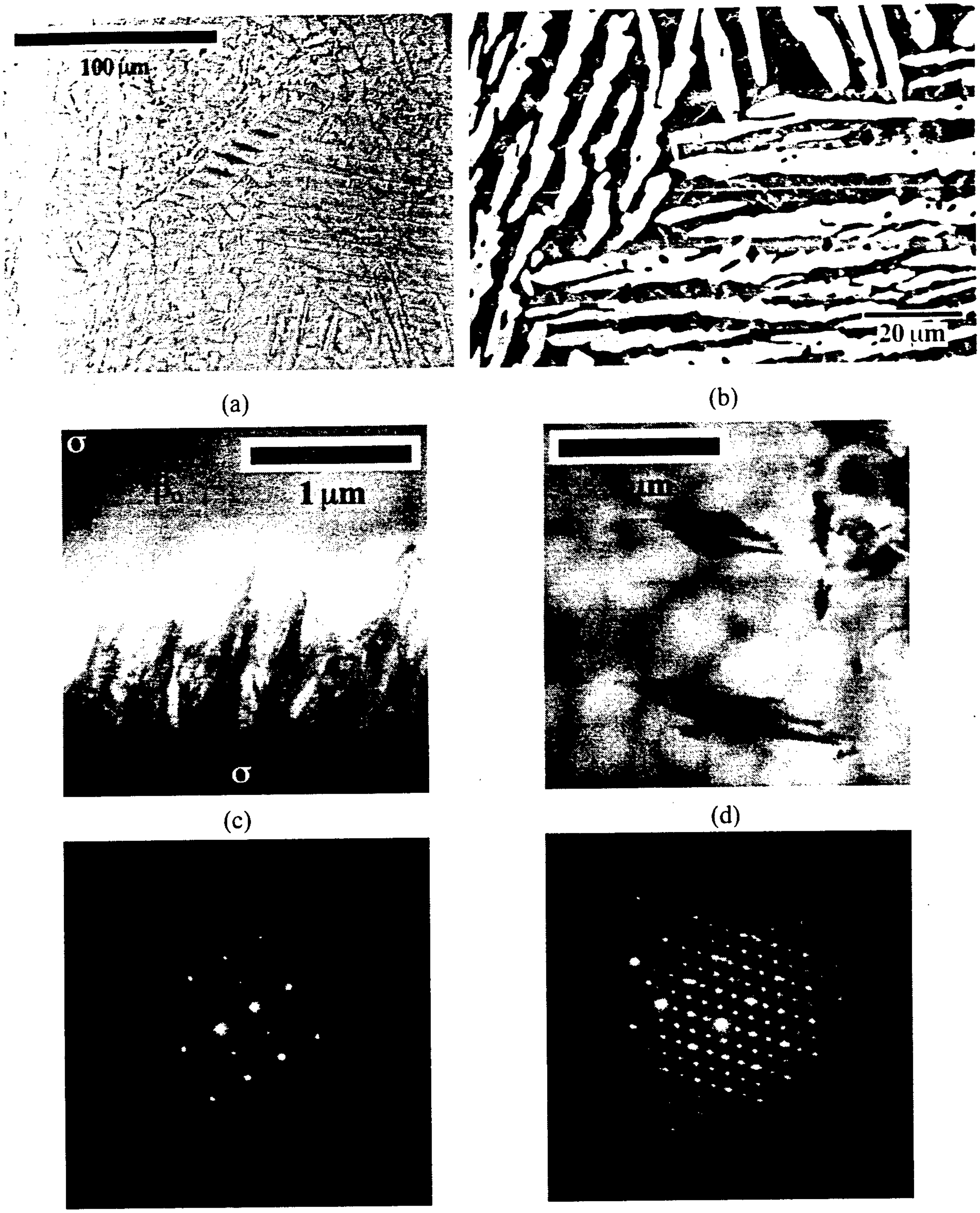

(a) (b)

(c) (d)

(e) (f)

Figure 6.18 Alloy R1851 Heat Treated at 1100°C for 7 Days and Air Cooled. (a) OM, (b) BSE-image, (c) BF-TEM of O nucleation at σ/β_o interface, (d) BF-image of O nucleation in grain interior, (e) $\beta_o[110]$, and (f) O[001] SAD patterns.

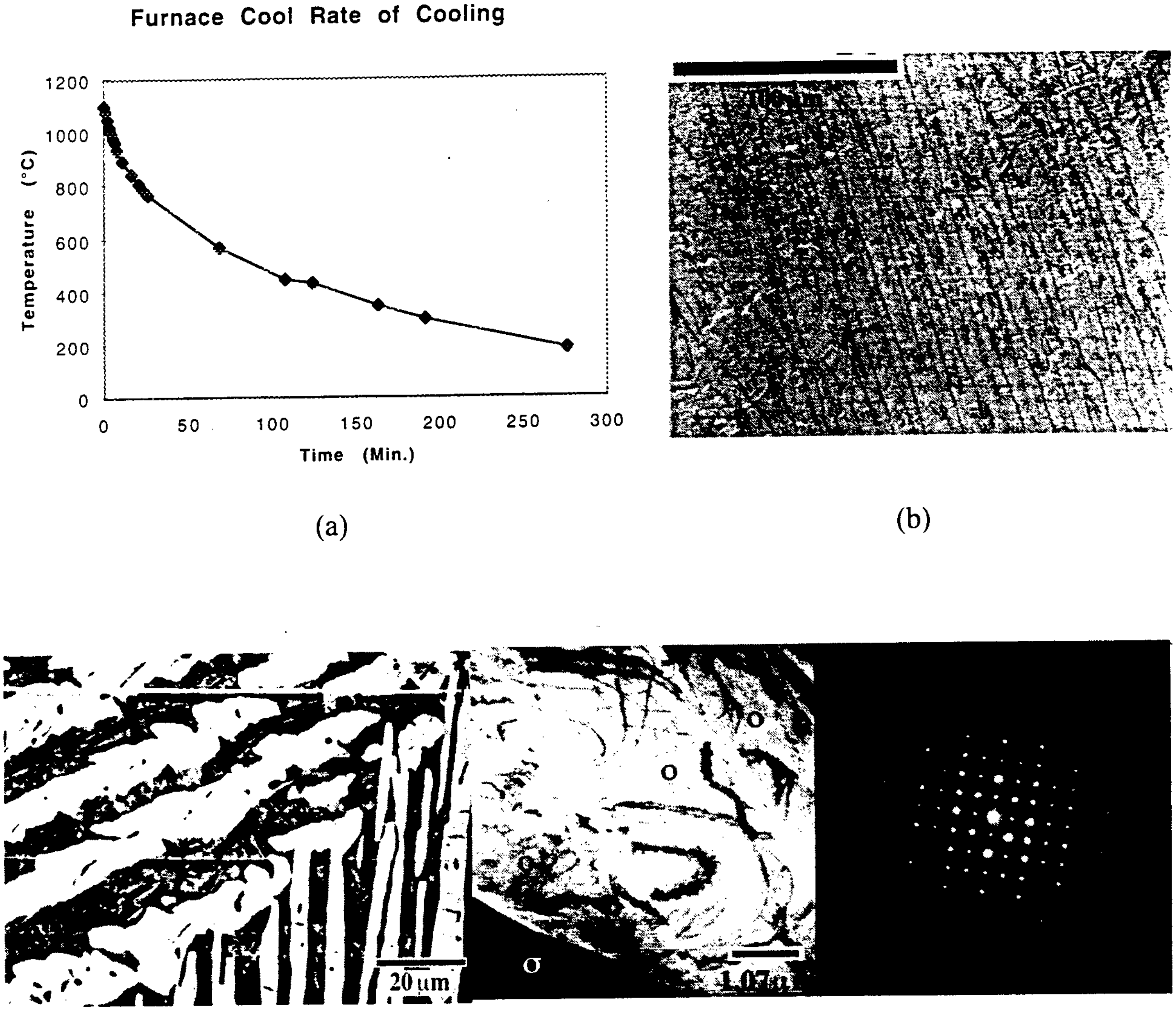

(a) (b)

(c) (d) (e)

Figure 6.19 Alloy R1851 Heat Treated at 1100°C for 7 Days and Furnace Cooled. (a) Cooling rate recorded, with an initial cooling rate of 40°C/min, slowing to 19°C/min passing through 1000°C, (b) OM, (c) BSE, (d) BF-TEM image of O phase at σ interface, and (e) O[100] SAD pattern.

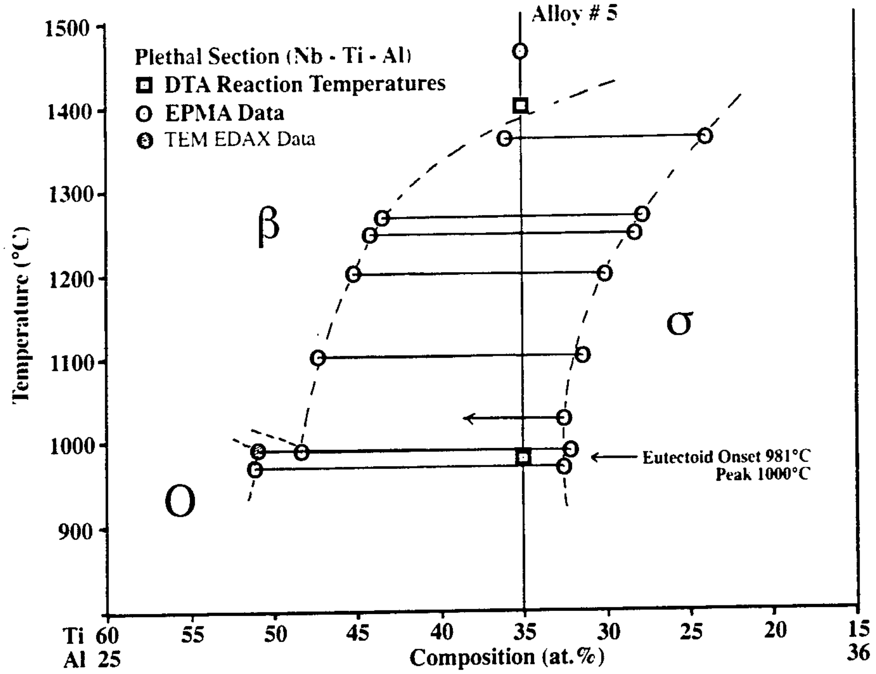

Figure 6.20 Plethel section showing projected tie lines for alloy # 5 with decreasing temperature.

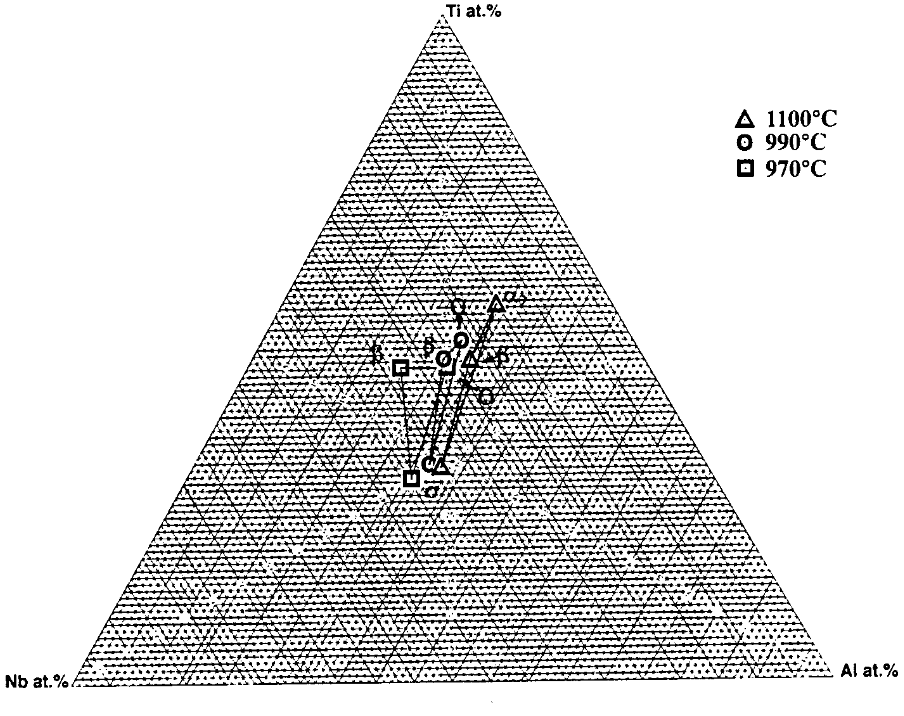

Figure 6.21 The β_o + σ + O three phase field movement with reduced temperature. Note: Shift from eutectoid to peritectoid with reduced temperature.

5.3 Kinetics of the β_o to O' Transformation and a Quick Estimate of Reaction Kinetics

The retention of the metastable β phase with high quench rates (434°C/sec) (Figure 6.22) in alloys prone to form O phase is a clear indication that the transformation is not a compositionally invariant martensitic transformation, which could not be suppressed under these conditions [44]. It is apparent, however, that a critical cooling rate is necessary to permit nucleation (in vicinity of 295°C/sec). Alloy #4 has a composition which lies within the low temperature phase region of the O phase; the suppression of this transformation with rapid quenching (water cooling) indicates at least some rearrangement of atoms across the interface is necessary for the transformation to occur. The necessary atomic rearrangements of niobium and aluminum to specific sites can be deduced from a comparison of the B2 and O2 site occupancies [7, 40]. While the decomposition of the metastable β phase in both alloys 5 and 9 requires expulsion of excess titanium and niobium respectively, the auto catalytic mechanism observed in alloy 5 likely involves the cooperative shift of planes of atoms with a corresponding stress field generated. A comparison of the crystal structures for the B2 and O2 phases reveals the possible nature of this shift and the resulting stress field due to lattice distortion [7, 40].

The decomposition of the metastable β phase to the metastable O' is orders of magnitude faster than the equilibrium nucleation and growth of the complex intermetallic phases, as evidenced by the low temperature transformations observed in several of the alloys. This intermediate transformation product O' consumes some of the energy available from the metastable β phase decomposition to the equilibrium transformation products. Indeed an examination of the first cycle DTA runs performed on the as-cast samples reveals the existence of an exothermic peak in alloys 4, 5 and 9 (Figures 5.4(c,d) and 6.1). It is possible to determine the reaction kinetics from the thermal analysis traces.

The establishment of the reaction kinetics for a transformation is usually obtained by a series of isothermal holds at specific intervals of time with the progress of the transformation being monitored and the volume fraction transformed (α) with time (t) determined, given by:

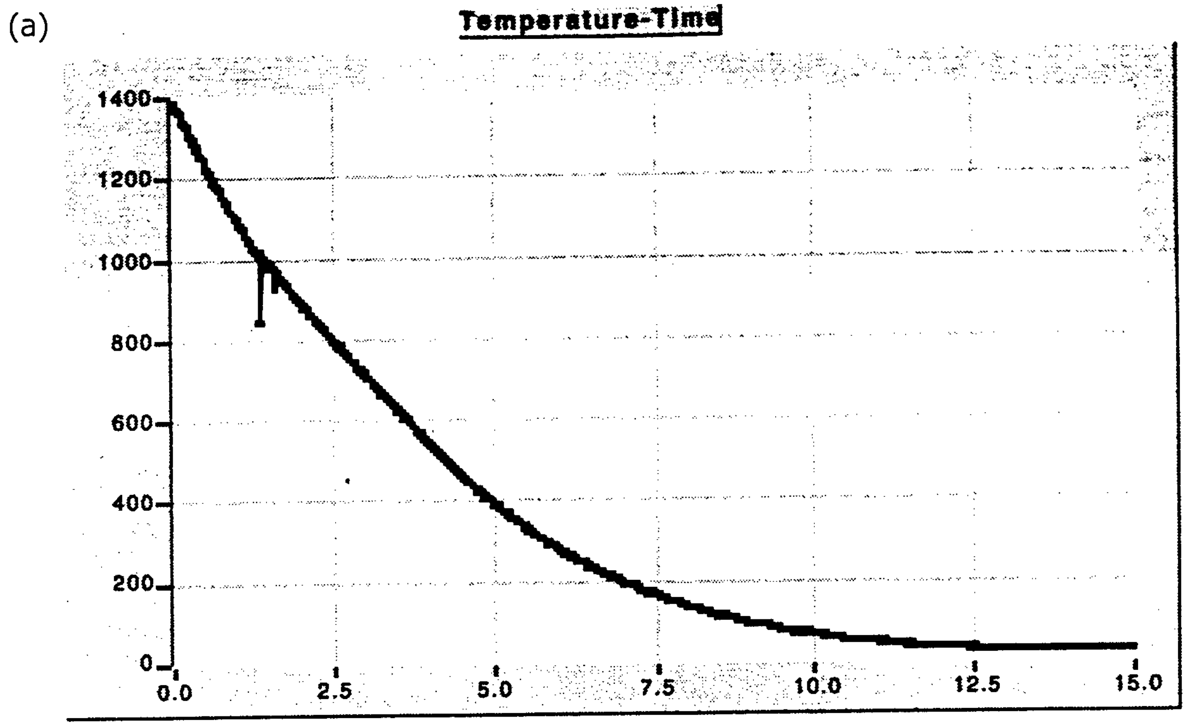

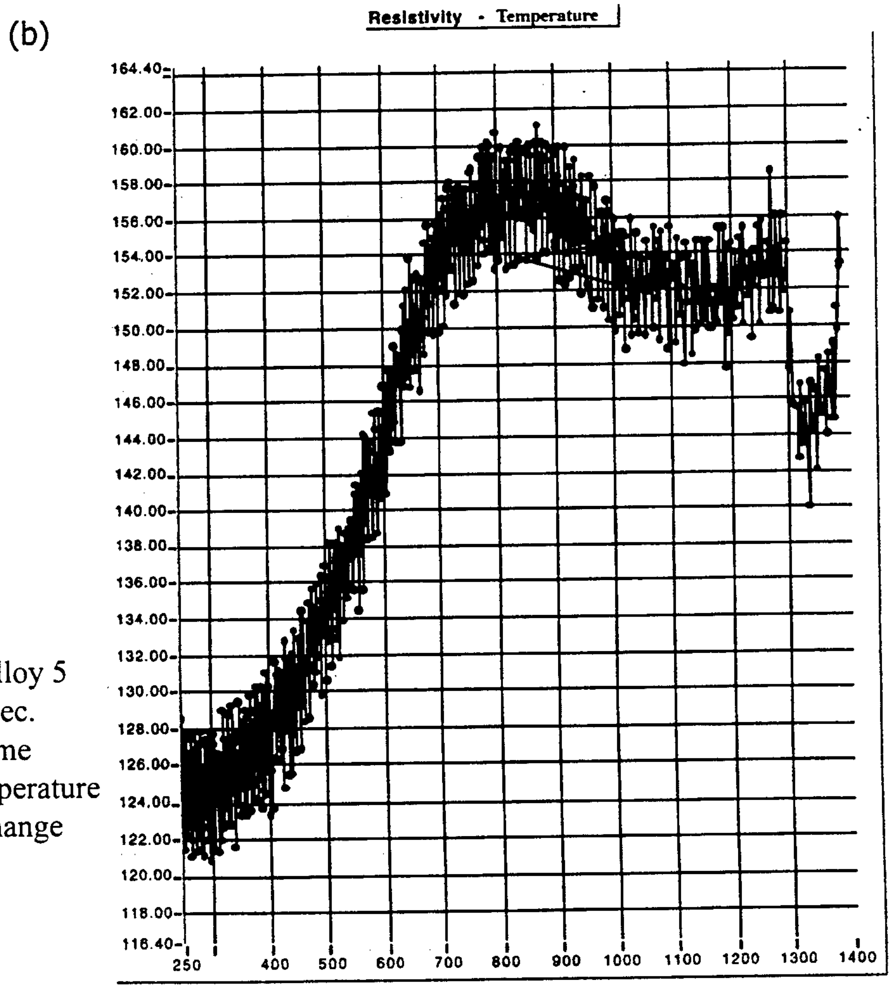

Figure 6.22
TERMS Results for alloy 5
Cooling Rate 295°C/sec.
A) Temperature vs Time
B) Resistivity vs Temperature
Note: resistivity change

$$d\,\alpha/dt = k\,g(\alpha) \qquad \text{(eq. 6.1)}$$

Where:
$k = A\,e^{(-Q/RT)}$
and $g(\alpha)$ is the derivative function of the volume fraction transformed based on an assumed model of the transformation mechanism.

However, it is far simpler to extract the same information from one dynamic thermal analysis test or more reliably from two different thermal analysis runs with different heating rates [45]. The kinetic analysis of the dynamic results involves relating the observed change in volume fraction transformed with change in temperature to the change in time based on the heating rate (ϕ) employed. The usual equation follows [45]:

$$d\alpha/dT = (d\alpha/dt)(dt/dT) = (1/\phi)(d\alpha/dt) \qquad \text{(eq. 6.2)}$$

This equation itself is subject to controversy [45, 46], as two key areas are of concern: 1) the effects of thermal gradients and 2) the assumed constant rate of the transformation. The concern for the thermal gradients controlling the transformation rate are alleviated by the exothermic nature of the transformation being studied. As the transformation progresses, the heat necessary to facilitate the transformation will be provided by the transformation itself, as opposed to the rate of heat flow into the sample. Therefore, the rate equation will reflect the true transformation and not an aspect of heat transfer. The usual approach for dynamic analysis is to use very slow heating rates to minimize the effect of thermal gradients [45], although it has been found that there is better agreement between isothermal and dynamic approaches for exothermic transformations when faster heating rates are employed.

The usual approach for establishing the volume fraction transformed is to use the entire peak, which is related to the energy released from the transformation [47]. This approach is generally applied to solutions (rapid heat transfer) and with slow heating rates (<1.5°C/min). However, with the large bulk sample necessary for the detection of solid-state transformations, a thermal lag is clearly present as the heat released must diffuse out of the sample. A typical approach used by metallurgists [21] for obtaining the onset and completion of a transformation is to set the onset as the extrapolated slopes of the base line to the face of the peak and the completion as the extrapolated slopes to the leading and trailing faces of the peak. This approach is applied to determine the volume fraction transformed (Figure 6.23). It assumes, in agreement with the necessary requirements for the calculations, a linear rate of the transformation with time. This, of course, is not true as the expected volume fraction transformed with time will be sigmoidal in shape. However, for the values to about 0.5 volume fraction, an approximate linear relation should hold.

The assumed relationship between volume fraction transformed and time is given by the Avrami-Erofe'ev equation [45]:

$$\alpha = 1 - \exp(-kt^\wedge n) \qquad \text{(eq. 6.3)}$$

Where:
- α = Volume fraction transformed
- t = time
- k is given be the Arrhenius rate equation:
  - $k = A\exp(-Q/RT)$
- n is a constant which:
  - (a) can be related to the growth rate [48]
    - n = 1 for one dimension, 2 for two dimensions, and 3 for three dimensions
  - or (b) to the diffusion [49]
    - n = 1.5 for spherical, 1 for rods, and 0.5 for plates

The first step is to calculate the value of n. This can be done by converting the temperature change for each incremental volume fraction transformed to a time interval using the heating rate; this was done over the region of apparent linearity. Then linear regression analysis was performed with $\ln(-\ln(1-\alpha))$ as the dependent variable and $\ln(t)$ as the independent variable, which gave the slope (n). A sample plot is shown for alloy 4 (Figure 6.24). The calculated values of n for all three

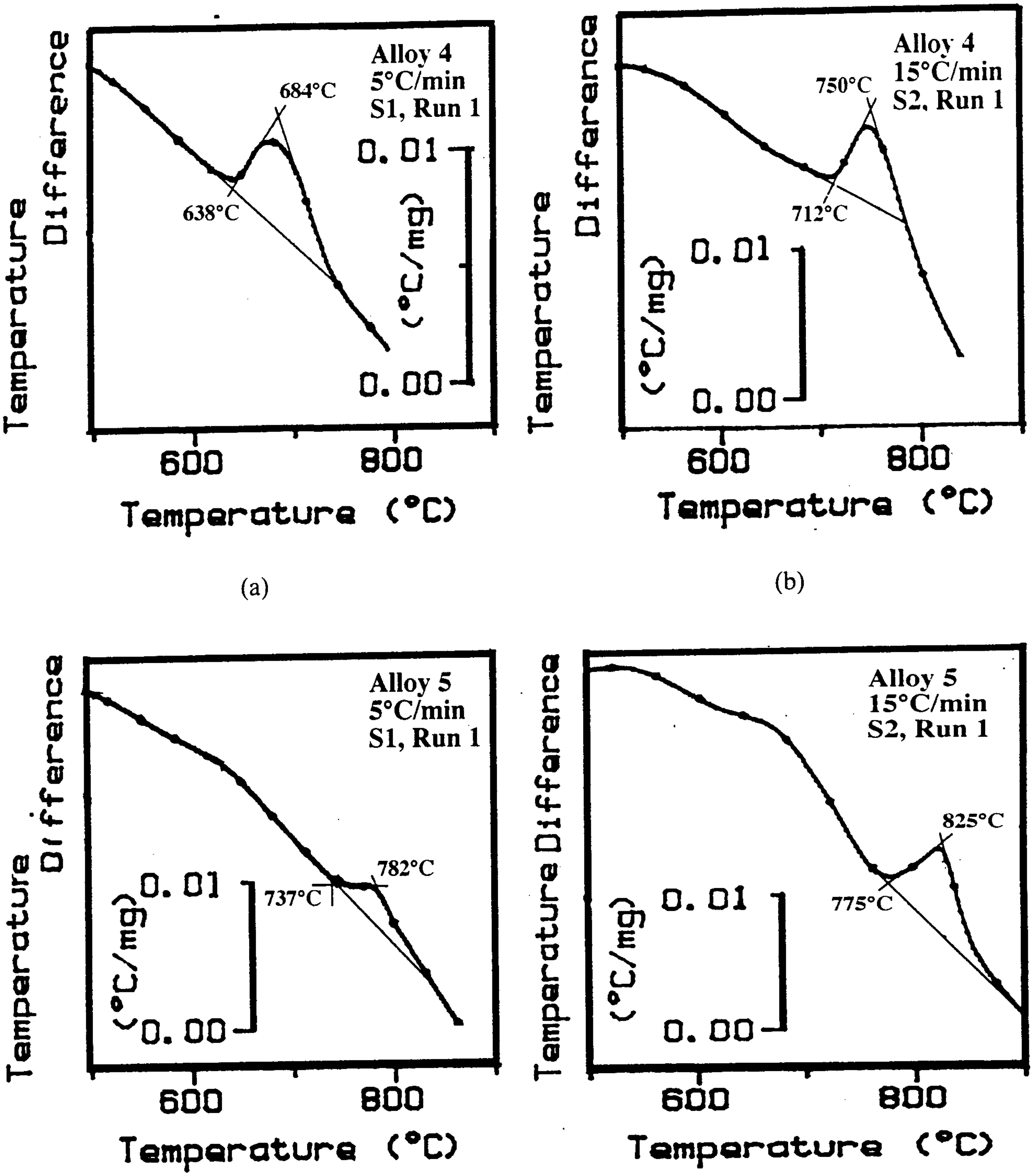

(a) (b)

(c) (d)

Figure 6.23 Representative DTA Thermograms of Low Temperature Exothermic peaks

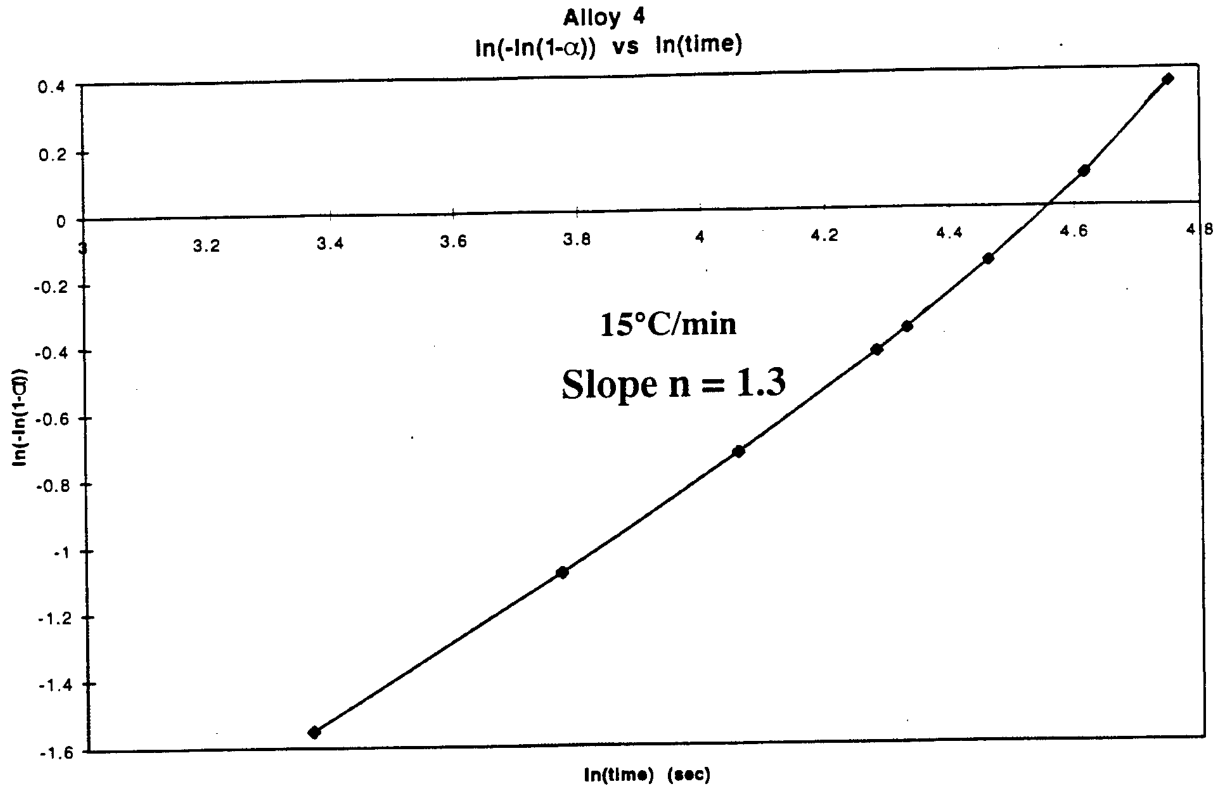

Figure 6.24 Representative Plot of ln(-ln(1-α)) vs ln(t) used to calculate n for Alloy 4.

alloys are listed in Table 6.6. These values of n are consistent with a volume diffusion limit for growth of a slightly less than spherical precipitate [49]. Next, the values of k are calculated using the assumed model and calculated values of n. The temperature necessary for the 0.5 volume fraction of the transformation was then determined for both heating rates and a linear relationship was assumed between ln(k) and 1/T with the slope (-Q/R) and the intercept (ln(A)) calculated for alloys 4 and 5 (Table 6.6). Since only two points were employed linear regression analysis was used with all the volume fraction transformed values from both heating rates and an estimate of the error was obtained for both the slope and the intercept (Figure 6.25). The calculations for alloy 9 indicated an R squared value less than 1: since closer examination of the data reveals a shallow peak for the 5°C/min heating rate, a linear regression analysis was performed only for the 15°C/min data (Table 6.6). The calculated values of n, A and Q were then used to calculate the C-curve for diffusion limited growth region for alloys 4, 5 and 9 (Figure 6.26).

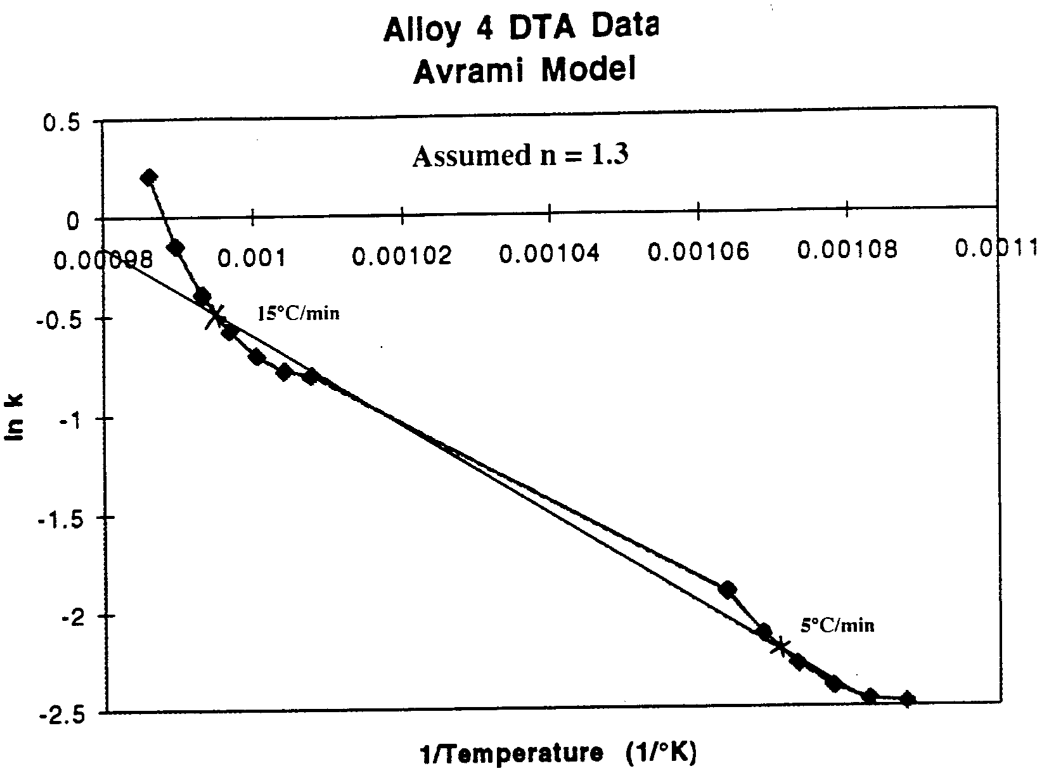

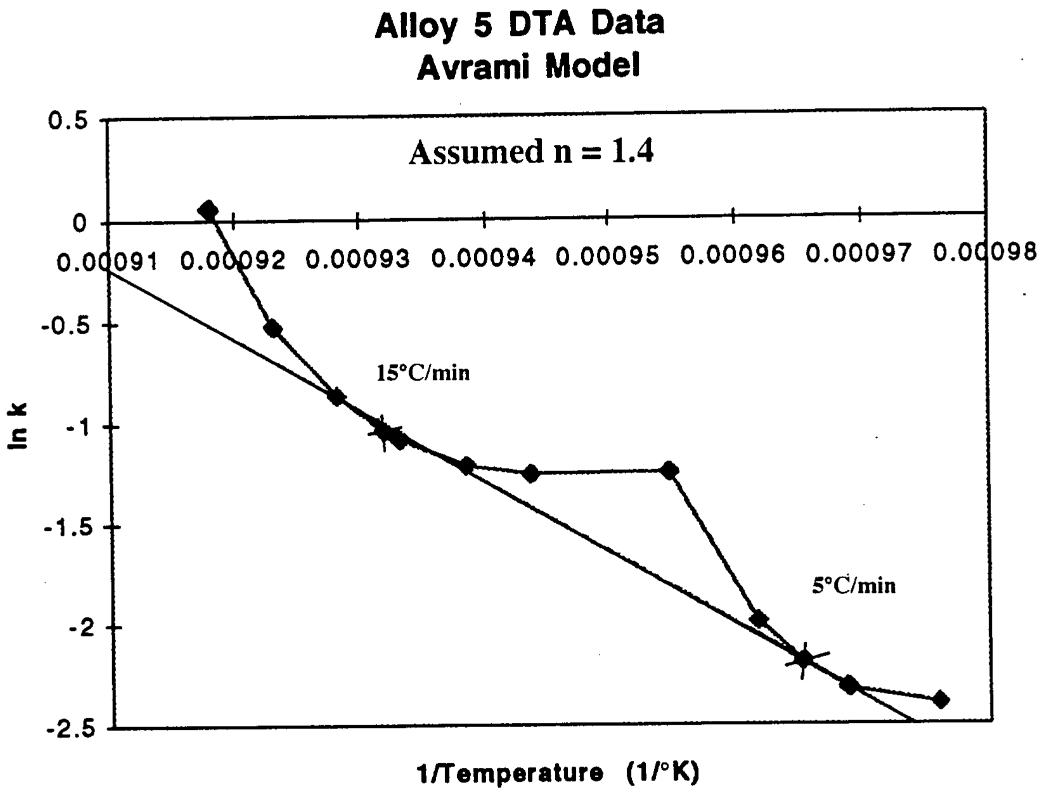

Figure 6.25 Representative Plots of ln(k) vs 1/T Based on Calculated Values of n for alloys 4 and 5

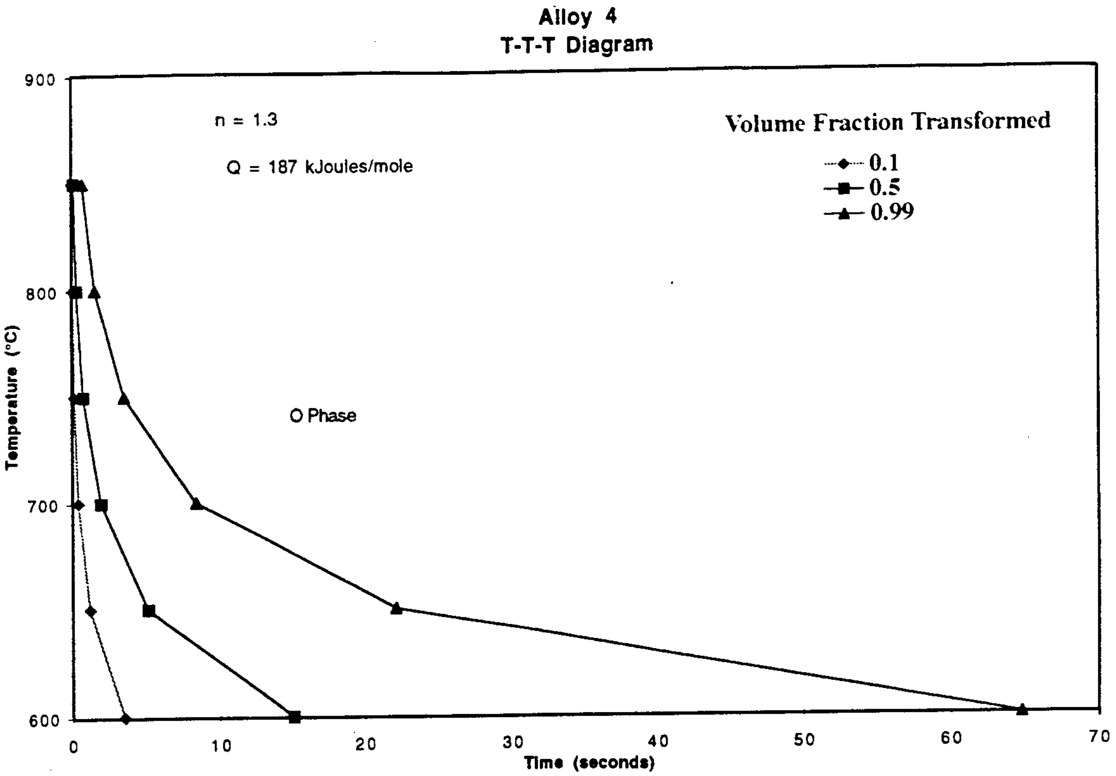

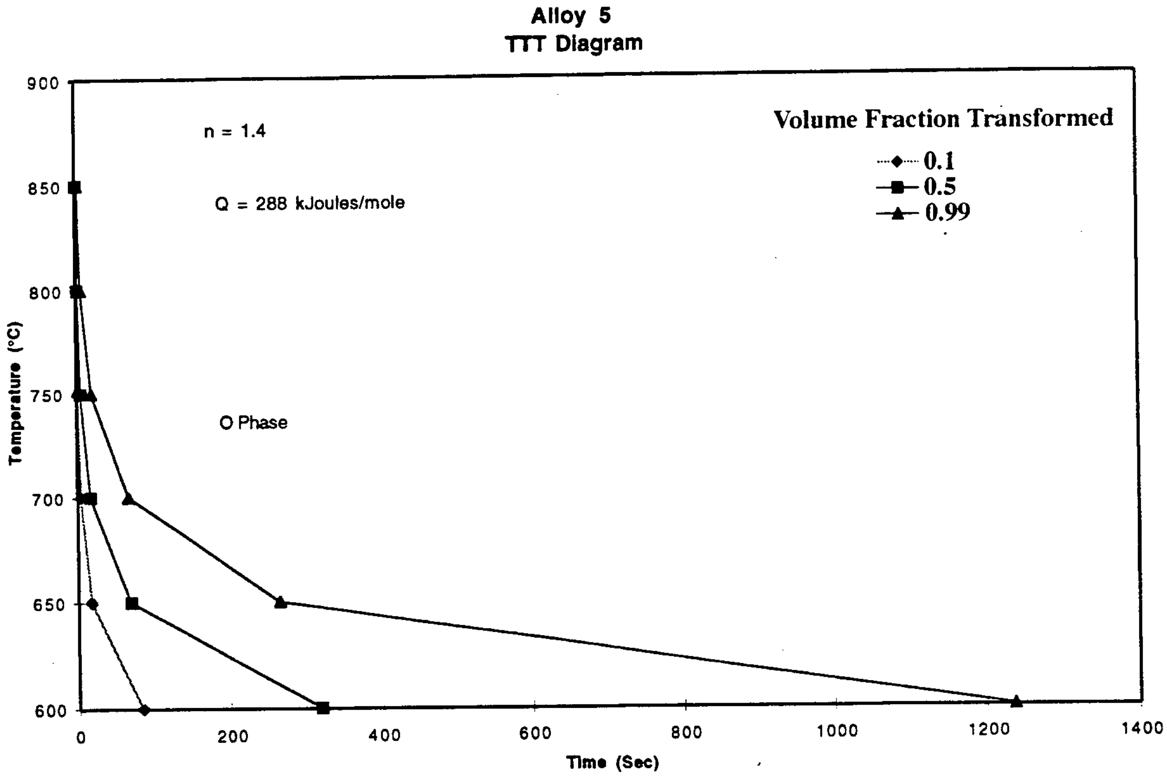

Figure 6.26 Representative Calculated T-T-T Curves for alloys 4 and 5.

Table 6.6 Kinetic Analysis for the Metastable β to Metastable O' Transformation

Alloy	Rate °C/min	Onset °C	Undercooling °C	ln (A) ln (1/sec^n)	-Q/R
4	5 & 15	638/712	348/274	21.834±0.153	-22462±998
5	5 & 15	744/775	242/211	31.273±0.223	-34671±3457
9	15	792	172	26.240±0.094	-29873±5603

	n	Q (Joules/mole)	Time of Transformation Observed DTA	Calculated at On set
4	1.3	194,940±8,220	351 sec / 116 sec	48 sec / 12 sec
5	1.4	288,270±28,740	365 sec / 165 sec	37 sec / 18 sec
9	1.4	248,380±46,580	--- sec / 150 sec	--- sec / 8 sec

The calculated values of Q are in the same order of magnitude as that used in the diffusion calculation (164 kJoules/mole) in the β phase and thus the actual T-T-T curve should be within the proximity (one order of magnitude) of that calculated curve. However, the self check of calculated time for the transformation versus the actual time for the transformation determined during thermal analysis are not in agreement (Table 6.6) . The calculated time necessary for the transformation at the onset temperature should be longer than the actual time observed in the DTA as the transformation rate should be accelerating with an increase in temperature, assuming the temperature is still in the diffusion limited regime. The calculated times for the transformations are faster by one order of magnitude than those observed. This may be accounted for by the thermal lag into the sample, resulting in the onset occurring at a lower temperature than the thermocouple is registering and should thus be compensated for by the calculation extrapolation. If the slope of the ln(k) v.s. 1/T line is made slightly more negative, then the same times that were observed in the DTA may be calculated; this adjustment is within the 2-σ error estimate of the reported values. The direction of error with this approach overestimates the rate of the actual transformation.

The kinetics for alloy 4 are nearly an order of magnitude faster than alloys 5 and 9. This observation is supported by three other factors: the observed onset temperatures are lower, the degree of undercooling is greater, and the need to diffuse away excess aluminum or niobium is reduced. As the transformation temperatures are in the diffusion limited region of the T-T-T C-curve. the need to diffuse away the excess aluminum or niobium would be the rate controlling step. The overall observed behavior is consistent with a nucleation and growth mechanism of the transformation of β to O phase in agreement with previous research efforts [50].

7. The Site Occupancy Preferences within the β_o Phase

The site occupancy preferences of the β_o phase were determined from the homogenized material of three of the 15 at.% Al alloys (#'s 7, 11 and 14), the Nb-25Ti-25Al alloy (#12) and the Nb-24Ti-40Al alloy (#10). The latter two alloys required solutionizing treatments in order to obtain a single-phase β_o structure. For each alloy investigated, spectra were collected at 10 distinct {200} excitations between the symmetry and the {600} Bragg orientations near the <100> beam direction. Foil thickness of the alloys in the channeling region were approximately 100 to 125 nm, as determined from the Kossel-Möllenstedt fringes in the zero order Laue zone CBED patterns [51] (Figure 7.1). Each spectra was recorded at a count rate of approximately 1500 s^{-1}. To attain sufficient collimation of the electron beam, a condenser aperture of 20 µm in diameter was used. The counts from the K_α peaks for each deviation were measured from ROI (regions of interest) windows at a 1.2 Full-width Half Maximum setting. Following subtraction of the background and hole counts, the intensities of the K_α peaks of the elements for each scan were converted to apparent compositions using *k*-factors of 1.601 for k_{AlTi} and 0.804 for k_{TiNb}, previously established from a single phase alloy standard.

The measured Al:Ti, Ti:Nb and Al:Nb ratios of the K_α intensities for the $s_{100}<0$, $s_{100}>0$ channeling conditions and kinematic conditions are listed in Table 7.1 for the five alloys. It was observed that as the amount of Ti decreased from 34Ti to 28.3Ti in alloys 7 and 11, a greater percent difference in the ratios of Al:Nb relative to Al:Ti occurred between the two channeling conditions. This change indicated a stronger preference for the separation of Nb and Al to different sublattices in alloys 11 (Nb-28.3Ti-15Al) and 14 (Nb-17Ti-15Al) than in alloy 7 (Nb-34Ti-15Al). Alloy #12, not only showed the strongest preference of Al/Ti separation, but also the greatest percent changes in all ratios between the channeling conditions, including the Ti:Nb ratio, which was determined to have a small change above the range of error associated with the ratios. This was not observed in the other alloys, where the change in Ti:Nb ratio was within the limits of statistical error. In the 40% Al alloy (#10), the percent change between the Al:Ti and Al:Nb ratios were relatively similar. The alloy, however, exhibited a strong preference towards both the separation of Al and Ti atoms,

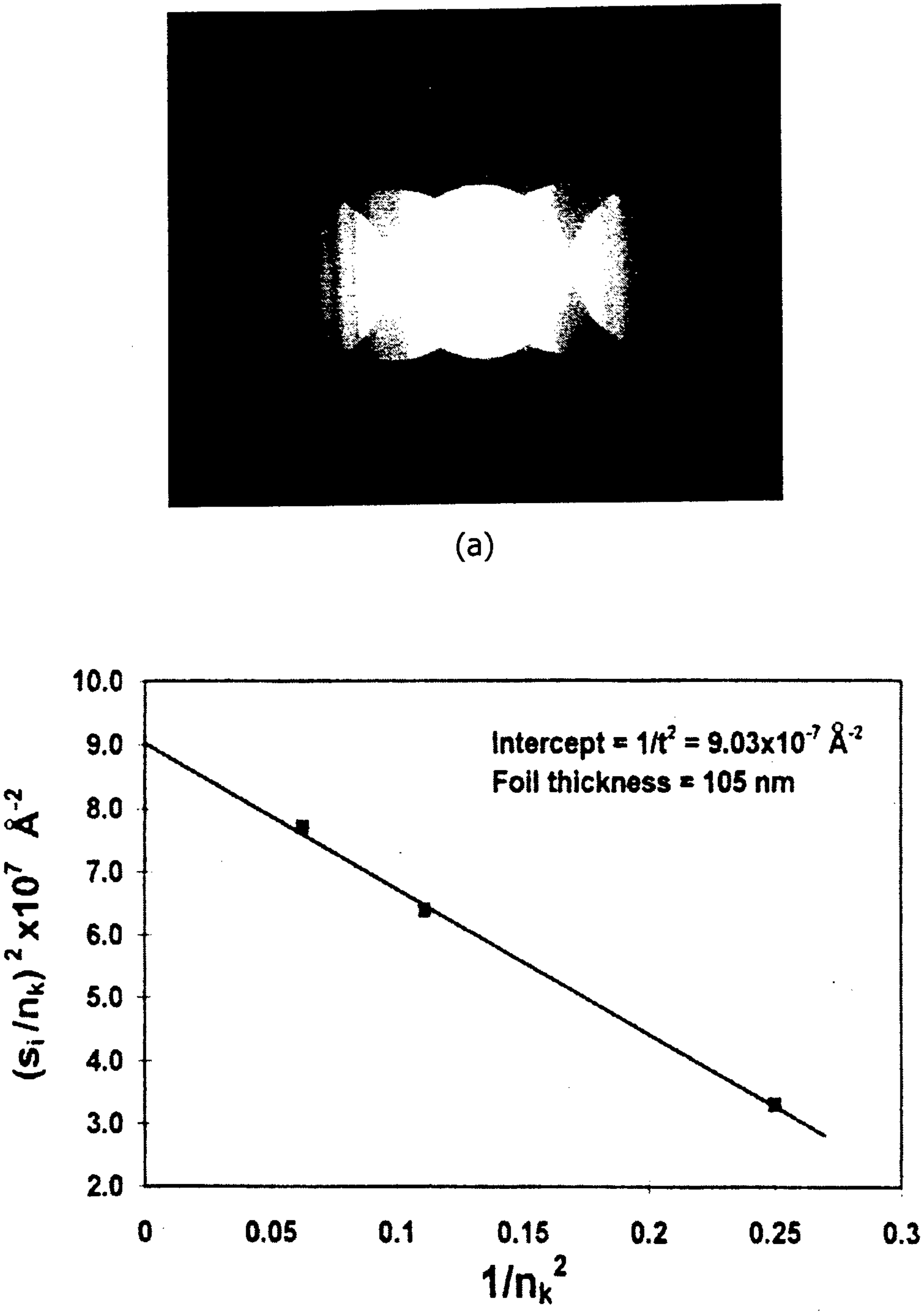
(a)

(b)

Figure 7.1 Representative foil thickness measurements using (a) the Kossel-Möllenstedt fringe spacing within the g=100 ZOLZ CBED pattern, (b) to determine the line intercept of the $(s_i/n_k)^2$ vs. $1/(n_k)^2$ relationship; intercept = 1/(foil thickness)^2.

Table 7.1 The measured Al:Ti, Ti:Nb and Al:Nb ratios of the Kα intensities and apparent compositions for the channeling and kinematic conditions within the β_o phase of the alloys examined.

Alloy	Condition	Al/Ti	Ti/Nb	Al/Nb	Nb	Ti	Al
Nb-34Ti-15Al	$s_{100}<0$	0.2478±0.0199	0.8384±0.043	0.2078±0.0163	51.15	35.08	13.77
	$s_{100}>0$	0.3160±0.0288	0.8264±0.0517	0.2612±0.023	49.64	33.56	16.80
	kinematic	0.2925±0.0228	0.815±0.0425	0.2384±0.018	50.62	33.75	15.64
Nb-28.3Ti-15Al	$s_{100}<0$	0.2942±0.0269	0.6394±0.037	0.1881±0.016	56.60	29.60	13.80
	$s_{100}>0$	0.4459±0.0518	0.6721±0.0569	0.2997±0.0323	51.60	38.37	20.04
	kinematic	0.3548±0.0345	0.6487±0.0425	0.2302±0.028	54.68	29.02	16.31
Nb-17Ti-15Al	$s_{100}<0$	0.4544±0.0258	0.3054±0.0109	0.1388±0.0065	69.95	17.47	12.58
	$s_{100}>0$	0.5753±0.0286	0.3176±0.0106	0.1827±0.0074	66.82	17.36	15.82
	kinematic	0.4824±0.0251	0.3096±0.0103	0.1494±0.0064	69.12	17.50	13.38
Nb-25Ti-25Al	$s_{100}<0$	0.4602±0.0283	0.6251±0.0278	0.2877±0.0162	53.08	27.14	19.78
	$s_{100}>0$	0.8286±0.0701	0.515±0.0357	0.4267±0.0313	50.65	21.34	28.01
	kinematic	0.6564±0.065	0.5853±0.0458	0.3842±0.034	50.59	24.22	25.19
Nb-24Ti-40Al	$s_{100}<0$	1.4751±0.0271	2.847±0.0772	4.1997±0.1064	39.45	27.50	33.05
	$s_{100}>0$	2.2309±0.0426	2.6712±0.0806	5.9591±0.1572	35.18	23.01	41.08
	kinematic	2.0382±0.0387	2.8591±0.086	5.8274±0.1557	34.93	24.45	40.61

as well as Al and Nb atoms. The Ti:Nb ratio remained relatively unchanged, similar to the 15% Al alloys, but all less than that observed in Alloy 12 (Nb-25Ti-25Al).

By plotting the apparent compositions, calculated from the various EDS spectra obtained from tilting between channeling conditions, the OTL slopes of the alloys were determined. While the end points of the OTL were not resolved, the trend in sublattice preferences were clearly illustrated (Figure 7.2). In general, it was observed that Ti substitution occurred for Nb on Nb sublattice sites. Although, some separation of Nb and Ti had been observed in the K_α intensity ratios of alloy 12, the strength of Al partitioning to opposite sublattice sites to those of Ti and Nb was still greater than the separation between Ti and Nb. The slope of the OTL in alloy 12 was found to be the largest, with a significant difference over those of alloys 7 and 10, which were similar. The slopes of the OTL's in the 15 % Al alloys between the 34Ti and 28.3Ti compositions (alloys 7 and 11), also illustrated the change observed in the partitioning of elements that was indicated from the changes in the percent difference in K_α ratios between the channeling conditions of the two alloys.

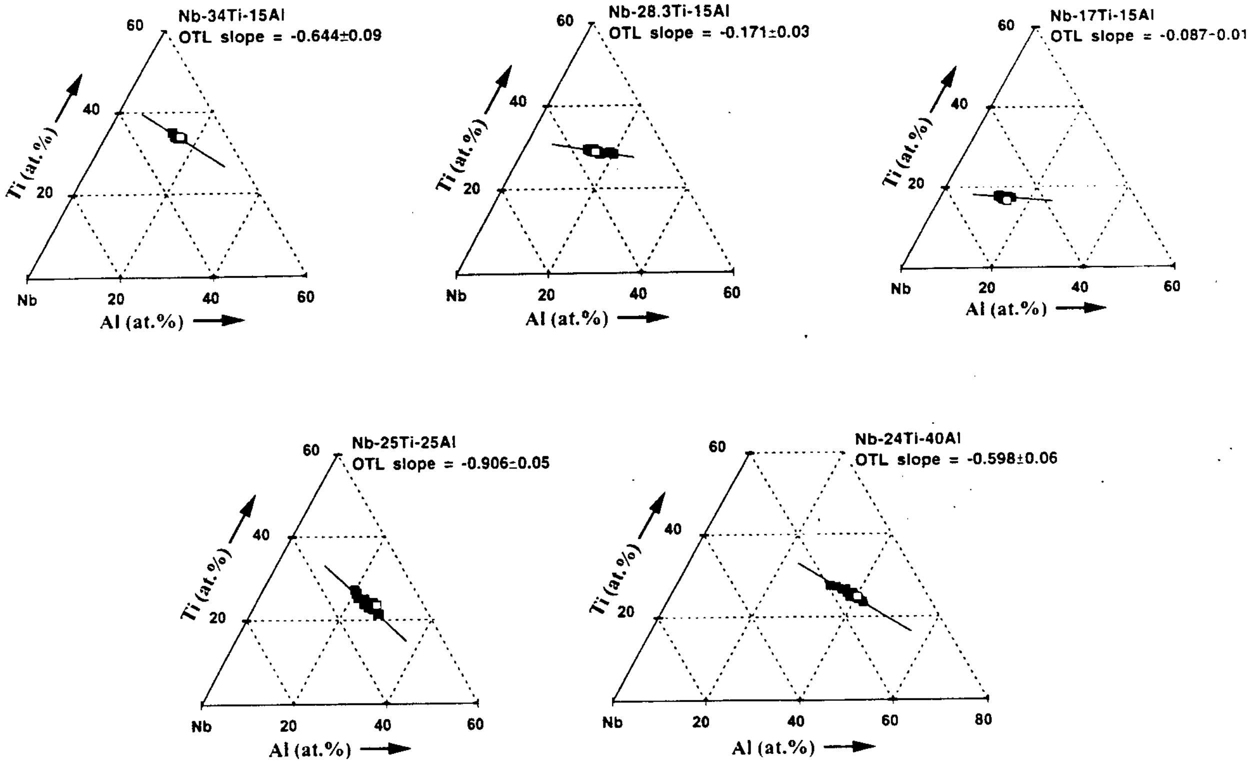

Figure 7.2 Ordering tie-lines and corresponding slopes illustrating the site occupancy preferences within the B2 ordered solid solution phase of the Nb-rich Nb-Ti-Al alloys.

8. DISCUSSION

8.1 The Extension of the β Phase Field

The investigation of the solidification structures of the Nb-Ti-Al system, just within the Nb-rich compositions, has provided valuable information on the extent to which the high temperature single-phase β field occurred within the system. The most recent liquidus projection by Zdziobeck et al. [22] is presented in Figure 8.1, with the proposed changes to the primary solidification zones represented with dashed lines. The directions of the liquidus troughs within the range of the alloys that were examined were not found to differ from all of the previous liquidus projections [15, 20, 22, 52]. From the appearance of the diagram, it is obvious that a further review of alloys closer to the Ti-Al binary is required, in particular, the refinement of the β and γ phase field boundaries in the area where they meet with the σ solidification field.

While the results of the 40 at.% Al alloys that were investigated contradict all previous liquidus projections [15, 20, 22, 52], they were supported by the experimental results of other investigators [17-19] which had been briefly described elsewhere [23]. Those experimental results, like the conclusions of this study, differed from past investigations of the liquidus projections by the most basic evidence, namely, that of confirming the high temperature β phase field through quenching treatments. While proving that the β phase field extended to Al concentrations greater than 30 at.% was not the sole intent of those studies, the use of the β field to control the morphology and distribution of desired structures was. To do this, however, accurate knowledge of the β transus temperatures and invariant reactions, which produce the subsequent microstructures, is necessary. It is possible that the reliance on DTA results, not to mention the difficulty associated with heat treating the Nb-rich compositions due to furnace and sample encapsulation constraints, had limited earlier investigations to making assumptions based solely on cast microstructures. In fact, the Nb-20Ti-40Al alloy of this study had also been investigated by Zdziobeck et al. [22], from which they concluded that the alloy had undergone σ-primary solidification. The cast microstructure, which

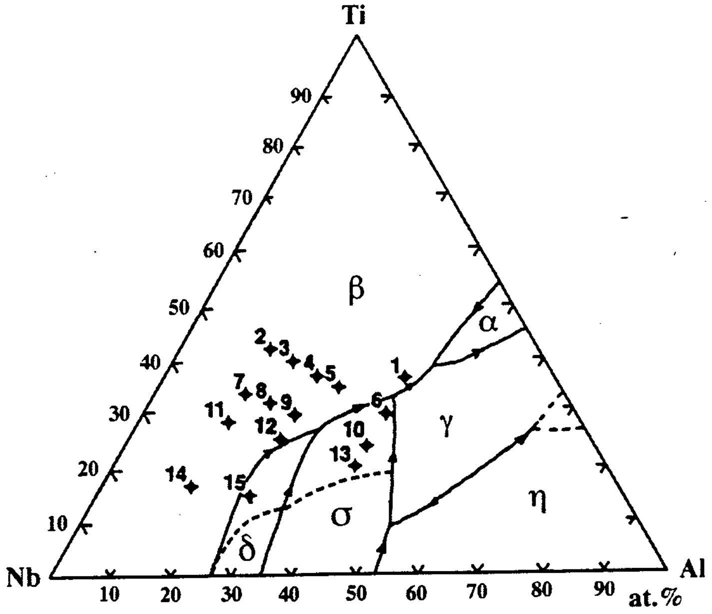

Figure 8.1 Liquidus projection of the Nb-Ti-Al system [22], with locations of the alloy compositions in the present study. Dashed lines represent proposed changes to the diagram.

they presented, was identical to the structure shown in Figure 8.2.

While the thermodynamic calculations of the liquidus projection [22] had predicted the largest extension of the δ and σ phase field in comparison with all other liquidus projections, these calculations were based on the assumption of Ti substitution occurring within the Nb$_3$Al and Nb$_2$Al crystal structures. Specifically, on the Nb sublattice due to the small difference in sizes between the Nb and Ti atoms. Therefore, the calculations had extended the δ and σ solidification fields to Nb:Ti ratios slightly less than 1:1 at relatively fixed Al concentrations. While a significant amount of Ti solubility within the ordered structures was observed at temperatures between 900 and 1400°C, the high temperature β phase field nonetheless extended to a greater solubility range than previously indicated.

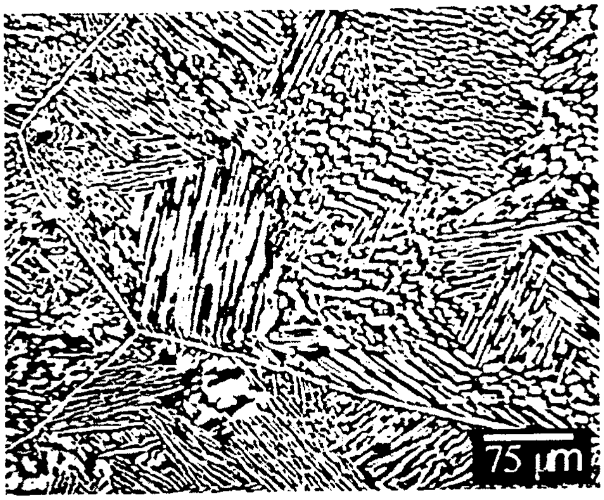

Figure 8.2 BSE-image of the cast microstructure of alloy 10.

8.2 The Ordering of the β Solid Solution

In all the alloys, quenching from the β phase field lead to the B2 ordering of the solid solution. It was observed from the slopes of the OTL's, that in all of the alloys investigated, Ti substitution had occurred for Nb on Nb sublattice sites. This site occupancy preference in Nb-rich alloys of the Nb-Ti-Al had also been previously reported [39, 53, 54]. The change in the K_α intensity ratios and the change in the slope of the OTL's indicated a change in the ordering preference of the 15% Al alloys between the 34Ti and the 28.3Ti and 17Ti concentrations, in which, decreasing concentrations of Ti produced a change in the partitioning strengths of Ti and Nb relative to the Al sublattice. The change in ordering state is estimated to have occurred near the composition of the Nb-28.3Ti-15Al alloy (#11). A similar phenomenon was observed in the Nb-xTi-15Al alloys by Hou and Fraser [54], where a change in partitioning strengths was observed between the 40 and 25Ti alloys. The larger percent difference in K_α ratios between Al:Nb and Al:Ti for the positive and negative *s* conditions, and the relatively equal Ti:Nb ratios supports the fact that ordering has been observed in the β phase of binary Nb-Al [10, 12] and not in the Nb-Ti binary [54].

The greatest changes in the K_α ratios occurred between the channeling conditions within the Nb-25Ti-25Al alloy (#12). The slope of the OTL illustrated a significant change in the ordering strengths of the elements in comparison with the slopes and behavior of the Nb-34Ti-15Al (#7) and

Nb-24Ti-40Al (#10) alloys. The K_α ratios of alloy #12 indicated that while Al predominantly occupied one sublattice opposite of Ti, the stoichiometry of the alloy produced a small partitioning of Nb to the Al sublattice rather than the Ti sublattice.

The β/β_o transition temperatures were observed to decrease from above 950°C for the alloys 7 and 11 to above 900°C for alloy #14. The trend in decreasing transition temperatures with decreasing Ti concentration towards the binary Nb-Al system was in agreement with the measured transition temperature of 800°C for Nb-10Al by Menon et al. [10]. The increase in ordering temperatures with Ti concentration appeared to be associated with the increase in Ti substitution of Nb on Nb sites in the B2 structure. Interestingly, the microhardness of the alloys decreased with the increase in Ti concentration. The decrease in hardness may have been associated with the formation of anti-sites as a result of the Ti addition.

8.3 The β+σ Phase Field

The compositions of β and σ within alloy 12 at 1400°C, and the compositions of the σ, γ and α/α_2 phases within alloy 10 at 1340 and 1475°C are plotted in Figure 8.3 against the calculated 1400°C isotherm [15]. The compositions of alloys 1 through 9, 11 and alloy 14 are also marked, however, these alloys were within the single-phase β field at 1400°C (Figure 2.1). The solubility of Ti within the Nb_3Al and Nb_2Al phases was determined to be reduced, due to the extension of the β phase field at this temperature. The β+σ phase field was determined in alloy 12 at 1400°C; alloys 12 and 15 were within the β+σ+δ three-phase field at 1340°C and 1540°C, respectively. Because the three-phase field representing the $\beta \rightarrow \sigma + \delta$ eutectoid reaction was formed from the convergence of the $L+\beta \rightarrow \delta$ and $L+\delta \rightarrow \sigma$ peritectic reactions from the Nb-Al binary (Figure 5.1), the location within the ternary field at which the β+σ+δ phase field forms from the liquid is limited to a Ti concentration slightly less than that of Nb-15Ti-25Al, alloy 15. Therefore, the addition of Ti to the Nb-Al binary greatly reduced the peritectic reaction temperatures from the binary that lead to the four-phase reaction, which produced the β+σ+δ phase field. Within alloy 15, the β+σ+δ field was estimated to have existed between 1540 and 1575°C, a substantial decrease in temperature consid-

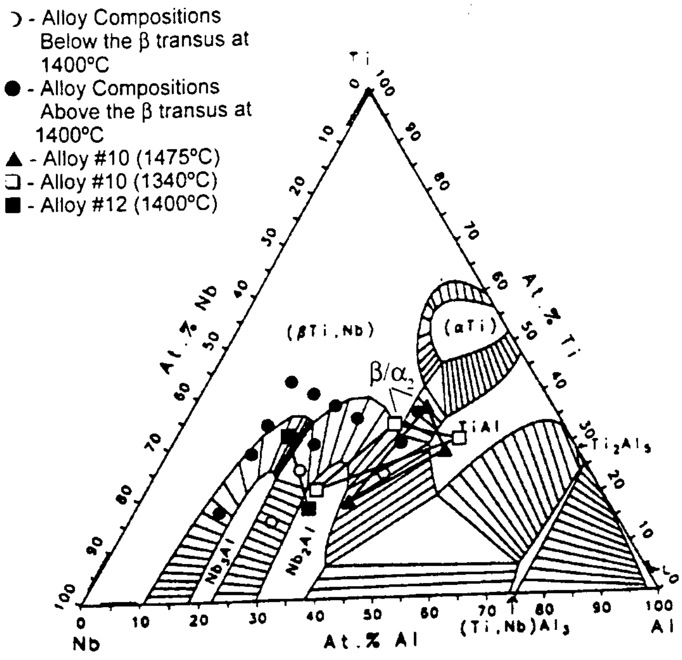

Figure 8.3 Tie-line data for alloy 12 at 1400°C and alloy 10 at 1475 and 1340°C plotted on the calculated 1400°C isotherm of Kattner and Boettinger [15]. Alloy compositions marked with black circles are above their β transus temperatures at 1400°C.

ering that the binary peritectic reactions began at 2060 and 1940°C. Therefore, with the addition of just 15 at.% Ti, the peritectic reactions must converge to form the four-phase field defining the limit of the δ solidification zone.

The phase equilibria within alloys 9, 12 and 15 does not compare well with the isopleth proposed by Majumdar et al. [55] (Figure 8.4). The isopleth was based on a 22 at.% Al composition which could have resided on the Nb-rich side of the β→δ+σ eutectoid reaction, producing a β+δ phase field at elevated temperatures instead of the β+σ field observed in the 25 at.% Al alloys.

Within alloy 10 and similarly within alloys 1 and 6, the β+σ phase field was not directly observed. Instead, the β phase had undergone transformation into α upon examination of the material. The α phase later transformed into the ordered α_2 phase during cooling, as noted by the appearance of the APB's within the retained grains. The α phase within the 1475°C (Figure 8.3) and 1340°C heat treatments had showed considerable solubility for Nb. Chemical analysis of the 1475°C oil quenched material, however, did not show a significant increase in oxygen and nitrogen

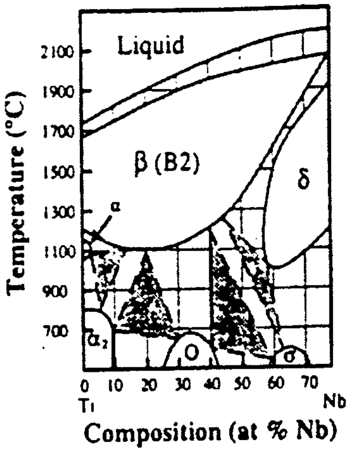

Fig. 2.12 Proposed Nb$_3$Al-Ti$_3$Al sections of the Nb-Ti-Al system by Majumdar et al. [55].

levels beyond the original values of the homogenized material.

One possibility for the formation of α could be because of phase boundary shifting and the close position of the α+β+γ phase field relative to the β+γ+σ phase field at 1400°C (Figure 8.3). Changes in the composition of the β phase either from the formation of σ or the possible effect of even fractional amounts of oxygen could have permitted the β phase to convert into α. Another possibility is that unforeseen changes to the ternary system at low Nb concentrations may have also occurred, allowing for β to transform to α upon cooling. This assumption is based on the appearance of the α$_2$/γ lamellae within the transformed regions of both alloy 10 oil quenched from 1475°C and 1340°C that contained multiple orientations, suggesting a formation directly from the β phase rather than from pre-existing grains of α. The possibility of crossing into the α phase field had been addressed by Singh and Banerjee [56, 57] as the stabilization of the α and γ phases to higher temperatures within the ternary as a result of the addition of β stabilizing elements. The scenarios which they had proposed showed complex changes within the Ti-Al-Mo diagram, based on the ternary stabilization of the α and γ phases by Mo. Little experimental information exists, however, regarding the position and movement of the α+β+γ phase field within the Nb-Ti-Al system at temperatures above 1200°C.

The most likely cause for the α/α$_2$ formation, is due to the instability of the β phase itself and the high Nb concentrations. The effect that Nb has on the formation of phases observed in hydrogen charged, Nb-lean, alloys [29, 30] was previously discussed in the section regarding the θ phase. The effects of Nb on the stability of the β phase is also of importance regarding the formation of the ω-related $P6_3/mcm$ phase and into which structure (hP16 or hP18) it forms [32, 58].

Further support of these possibilities is derived from the phase equilibria obtained after aging alloy 10 quenched from 1475°C again at 1100°C. The double-aged material contained a microstructure of only the σ and γ phases. The γ phase showed numerous {111}-type twins within its grains formed from the disappearance of the lamellar α_2/γ structure that had been present within the oil quenched microstructure (Figure 3.8). If the α which had formed at higher temperatures was stabilized from the β phase as a result of contamination, α_2 would have likely been present following the second aging at 1100°C, unless the oxygen had partitioned into either the σ or γ phases. This, however, is an unlikely scenario in reference to work on oxygen effects in the Ti-Al system [59].

Hoelzer and Ebrahimi [17] had also observed the presence of the α_2 phase well into the ternary diagram within the cast microstructure of Nb-33Ti-40Al, which is close to alloys 1 and 6 studied herein. The α_2 phase formed as needle-shaped precipitates within the β grain structure during cooling. Because of the smaller ingot sizes used in their study, a higher cooling rate during casting was obtained and the β phase did not transform into the σ+γ structures that had been observed in this study. Nonetheless, the α_2 phase from the cast material was reported to have disappeared on further aging at lower temperatures. No experimental tie-line data was reported regarding the phase fields present above 1200°C.

8.4 The 1100, 900 and 700°C Isotherms

The experimental 1100, 900 and 700°C tie-line data for the Nb-rich alloys are presented with the experimental data of previous studies in Figure 8.5. The 1100 and 700°C data are also plotted against the calculated isotherms of Kattner and Boettinger [15] in Figure 8.6. Neither theoretical calculations nor experimental work at 900°C could be found for comparison.

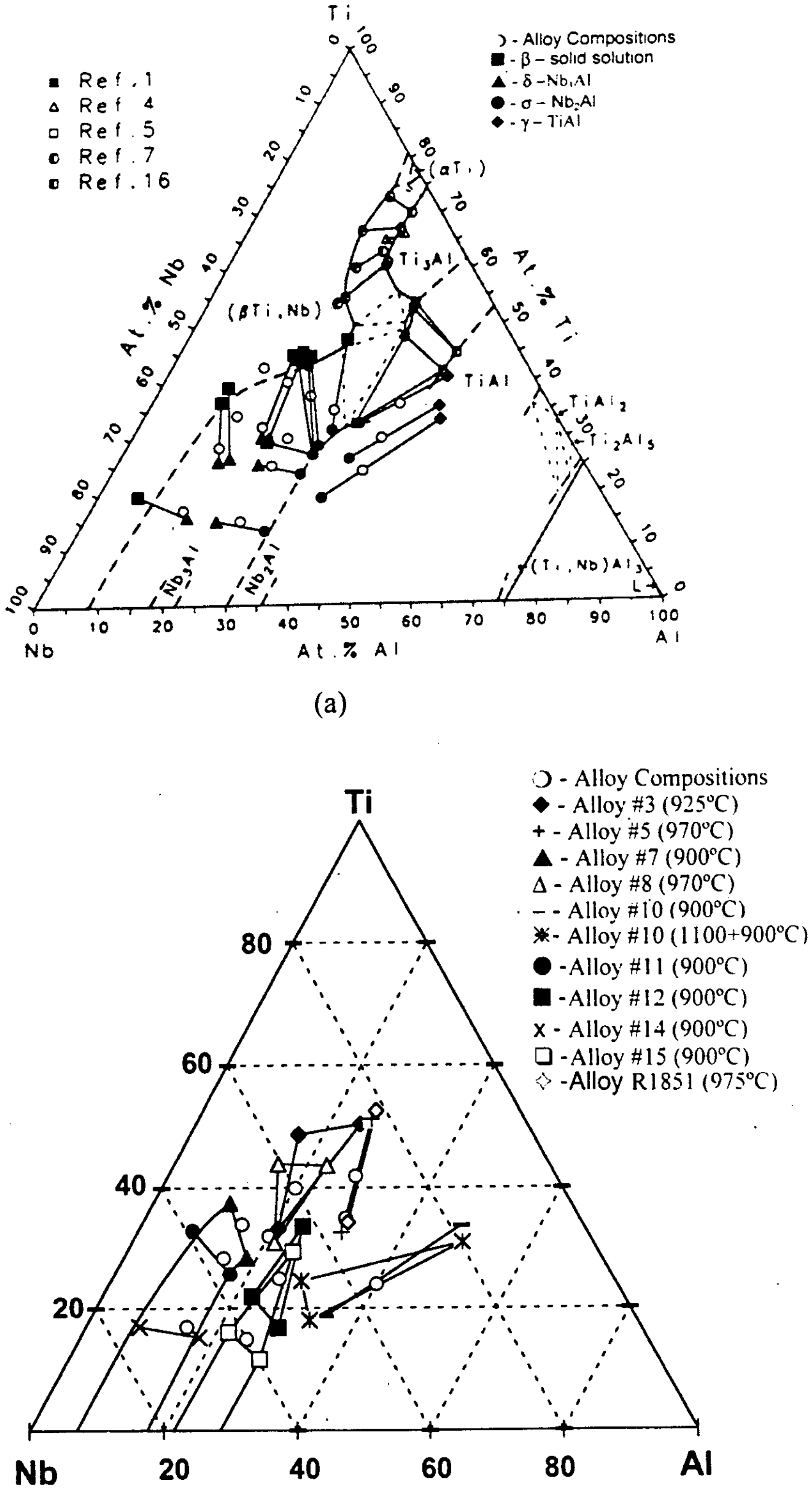

Figure 8.5 Experimental isotherms of the Nb-Ti-Al system at (a) 1100°C, (b) 900°C, and (c) 700°C. The 1100 and 700°C Ti-rich experimental data are from ref. [15].

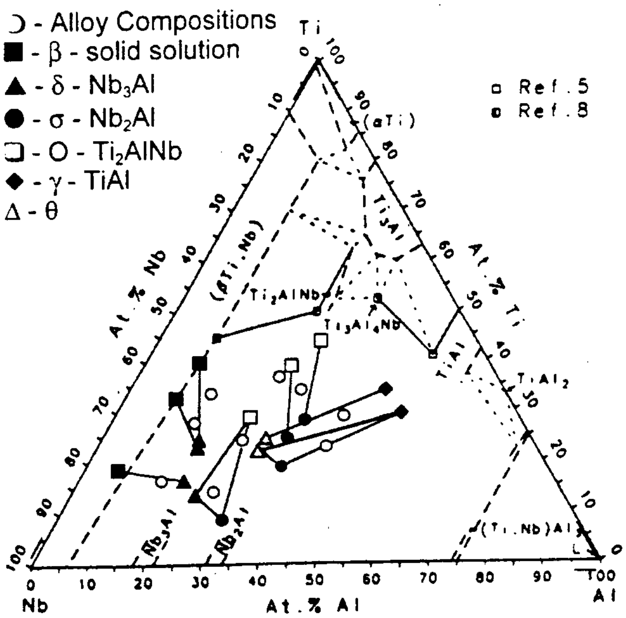

(c)

Figure 8.5 Continued

The 1100°C experimental data of the Nb-rich alloys showed close correlation to the calculated diagram (Figure 8.6(a)). The positions of the tie-lines representing the δ+σ and β+δ phase boundaries within alloys #'s 3, 5, 7, 8 and 12 fall just outside the position of the β+δ+σ tie-triangle with alloy #4 within the three-phase field. The only other significant observation was the shift of the β phase boundary to lower Al concentrations than was predicted in the calculations. The reduced solubility of Al in β was also reported by Menon et al. [8, 10].

Since experimental and theoretical information regarding the 900°C isotherm was not available, it was difficult to assess the presented information, in particular, the phase equilibria relating to the solubility of the θ phase. The difference in compositions of the θ phase between the material aged from the solutionized material and that of the 1100+900°C (Figure 8.5(b)) and 1100+700°C treatments (Figure 8.5(c)) suggested a possible range of stability of this phase. More information, however, is required to completely understand the phase equilibria at higher Al concentrations below 1100°C.

The tie-line data for the 15% Al alloys (7, 11 and 14) within the 700°C isotherm (Figure

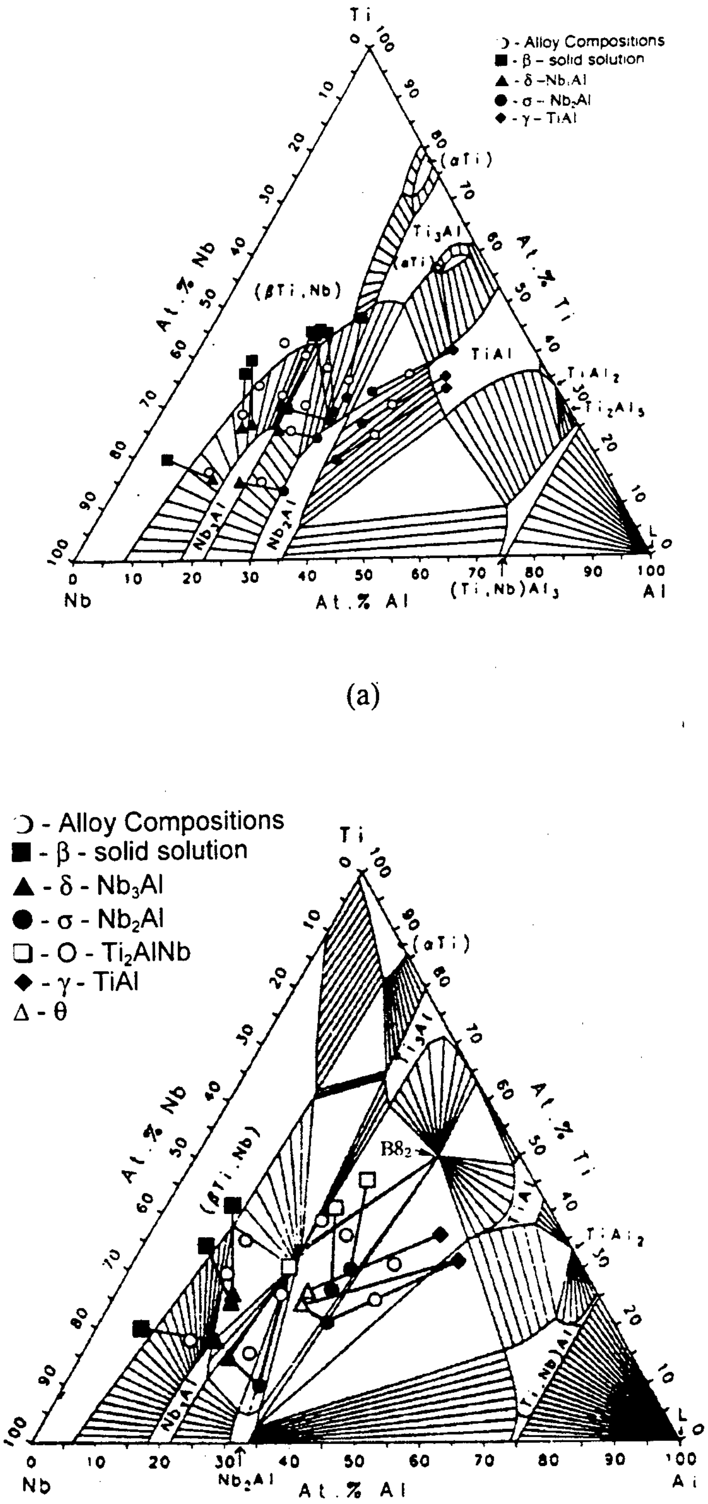

(a)

(b)

Figure 8.6 Experimental tie-line data plotted against the calculated (a) 1100°C and (b) 700°C isotherms of ref [15].

8.6(b)), were the measured compositions of the β and δ phases in the 1100+700°C samples. Aging the $\beta+\delta$ alloys at 700°C, from a single-phase β_o structure, resulted in the formation of metastable O plates. The metastable structure was found present even after 2280 hours, with only slight precipitation of presumably δ, observed along the prior β_o grain boundaries. The compositions of the β_o and δ phases within the 1100+700°C treatments were found to be close to those of the 900°C material. Although no O was detected within the 1100+700°C microstructures, the separation of the β_o-δ tie-line from alloy 7 (Nb-34Ti-15Al) may have been due to the formation of some O.

The formation of metastable β_o+O structures was also observed by Hou et al. [9] within Nb-xTi-15Al (x=10, 25, 40) alloys at low temperatures. In their work, they had reported a β_o+O structure present at 800°C, with no δ precipitation occurring until 500 hours. The addition of Ti to Nb-15Al appeared in both studies to have increased the formation of O instead of the predicted δ phase. Since δ had exhibited a large solubility for Ti at intermediate temperatures (900 and 1100°C), the structures obtained following the 1100+700°C treatment can be assumed to be stable. It is likely that due to the slow reaction kinetics of the δ phase at low temperatures, the highly unstable β_o phase reduced its energy through the kinetically favorable formation of O. The formation kinetics of δ was shown by Menon et al. [10] to dramatically decrease below 900°C for alloys near 15 at.% Al and Ti concentrations less than 22 at.% (Figure 8.7).

In alloy 12 (Nb-25Ti-25Al), the β_o phase had transformed completely into the O structure at 700°C (Figure 5.12). The nominal composition of this alloy falls within the region where the $\beta+\delta$+O and $\delta+\sigma$+O ternary fields converge (Figure 8.6(b)). Therefore, it is possible that the alloy may not have been in full equilibrium and was actually within the two-phase σ+O phase field at 700°C. In any case, the volume fraction of the second phase would have been relatively small and dificult to consider as a contributing factor in the $\beta_o \rightarrow$O transformation. The transformation of the β_o phase into a plate-like O morphology (Figure 5.12) was similar to that observed by Muraleedharan et al. [5] in a Ti-24Al-15Nb alloy aged at 800°C from the retained β_o phase. The O plate morphology, however, was only observed within Ti_3Al-Nb based alloys that contained Nb concentrations below 15 at.% [7, 40]. The β_o to O transformation which occurred at higher Nb concentrations had

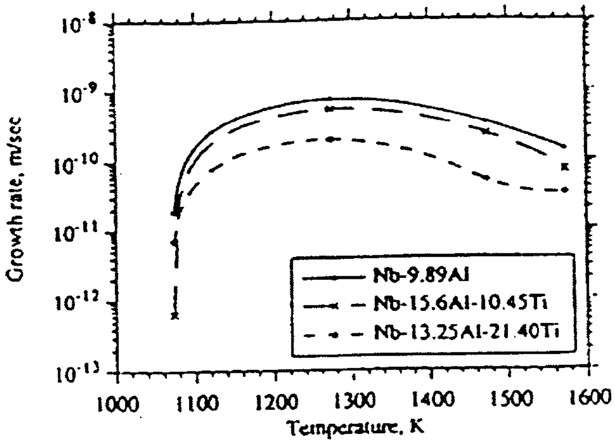

Figure 8.6 Semilog plot of the lengthening rate of Nb_3Al plates versus aging temperature for three different alloy compositions [10].

an equiaxed O morphology without defect structures, and were characterized as having been produced through a massive transformation. Alloys with Nb concentrations greater than 30 at.% Nb, which were near or along the Ti_3Al-Nb_3Al section have not been fully investigated. While the massive $\beta_o \rightarrow O$ transformation had been documented leading up to the Ti_2AlNb stoichiometry [5, 7, 40], a further increase in the Nb concentration to 50 at.% resulted in the shear induced formation of the O phase similar to that observed in the Nb-lean alloys. A mixture of twin related plates and equiaxed grain structures of the O phase was observed by Narayanan [39] within a Nb-37Ti-26Al alloy aged at 900°C for 200 hours from the solutionized β_o phase, although it was not suggested that the massive β_o to O transformation had occurred in forming the equiaxed grain structure. The massive β_o to O transformation appeared to become kinetically favorable only as the alloy composition approached the Ti_2AlNb stoichiometry.

Changes in the ordered state of the O structure were also naturally dependent on the nominal compositions. In alloy 12, ternary ordering of the O structure (O2) was observed through CBED analysis within the 700°C aged material (Figure 5.16). Upon re-aging the 700°C material at 800°C for one hour, the binary ordered O structure (O1) was identified. Within the Ti-24Al-15Nb alloy investigated by Muraleedharan et al. [5], changes between the O2 and O1 structures did not occur until 900°C. Again, it can be assumed based on stoichiometry that the stability of the O2 structure would be the greatest at compositions close to or Nb-rich of Ti_2AlNb. The lower transition temperature associated with the Nb-25Ti-25Al alloy may have been due to the large excess concentration of Nb atoms substituting on Ti sublattice sites within the O2 structure changing it into the binary ordered phase at lower temperatures.

The crossing of the tie-lines connecting the O and σ phases of alloys 4 and 5 with those of the θ, σ and γ phases in alloys 6 and 10 are the result of metastable equilibrium of alloys 4 and 5. The structures produced in alloys 4 and 5 were the result of two-stage treatments in which the β + σ structure present at 1100°C was aged again at 700°C, resulting in the conversion of the β_o phase to O. The tie-line orientations of alloys 4 and 5 at 700°C have changed little in comparison to the 1100°C results.

8.5 The New Tetragonal Phase

The observation of a body centered tetragonal phase having $a_o = 5.106$ Å and $c_o = 28.168$ Å and space group $I4_1/amd$ that appeared with a composition near that of the σ phase was new to the system. The θ phase formed in a plate-like structure with the γ phase upon aging the solutionized material at 700 and 900°C. The σ phase was not observed to form under these conditions, although, it was present within alloy 10 along the former β grain boundaries due to the solutionizing treatment. The volume fraction of σ in this alloy was low enough to have not had a significant effect on shifting the tie-line between the θ and γ phases off the point marking the alloy composition. The coarsened appearance of the θ phase within the 900°C alloys, in addition to its presence in small volumes within the samples oil quenched from 1475 and 1340°C and within the 1100+700°C and 1100+900°C double aged material, suggested that this phase had some measure of stability below 1100°C. Due to its stability and the differences between the non-isomorphic subgroup and supergroup relations of the θ and σ phases [25], it is believed that the θ phase is not a metastable precursor to σ.

The $I4_1/amd$ space group of the θ phase is, however, the same as the $TiAl_2$ intermetallic compound [27, 60-64]. In the binary Ti-Al system, the $TiAl_2$ phase can take on two different crystal structures h-$TiAl_2$ and r-$TiAl_2$ depending on temperature [27] (see Figure 3.18). Above 1216°C, h-

$TiAl_2$ is orthorhombic, whereas at lower temperatures r-$TiAl_2$ has the $I4_1/amd$ tetragonal structure [27]. The stoichiometry of the two forms is the same, but the periodicity of the Al layers normal to the [001] direction in each crystal is different. The Al layers within the r-$TiAl_2$ structure repeat ever 3 layers compared with every two in h-$TiAl_2$. The lack of experimental work below 1000°C makes it difficult to estimate the compositional range over which the $TiAl_2$ phase enters into the ternary diagram. The 1000°C experimental isotherm of Hellwig et al. [65], however, determined that the range of ternary solubility of $TiAl_2$ was less than 5 at.% Nb, with the single phase field terminating at the $\gamma+\eta+TiAl_2$ phase field.

The composition of the θ phase within the 900°C aged alloy 10 was determined to fall along a section line between the $TiAl_2$ stoichiometry and the Nb corner of the ternary, representing compositions with a Ti:Al ratio of 1:2. It is also possible that the 700°C aged alloy 10 could have fallen near to the line as well, but was skewed to lower Al concentrations due to the presence of the retained β_o/hP18 structure. The compositions of the θ phase, however, within the double aged materials and in alloys 1 and 6, fell far from the 1:2 stoichiometry of the $TiAl_2$ phase. Along with the afore mentioned 1000°C isotherm, experimental electron diffraction patterns of the θ phase did not match the intensities produced in calculated patterns of the $TiAl_2$ phase (Figure 8.8).

8.6 The γ1 Phase

The γ1 phase that had been reported as occurring near the $Nb_{30}Ti_{20}Al_{50}$ stoichiometry at temperatures up to 1400°C by Chen et al. [28], was not observed in this investigation. Certainly, the range in compositions over which the γ1 phase had been reported would have been within the location of the 40 at.% Al alloys. While experimental evidence did not indicate that the γ1 was related to the θ phase, the location of the γ1 single-phase field at 1000°C was close to the compositions of θ (Figure 8.9), supporting the possible existence of a new ternary phase within the Nb-Ti-Al system. The experimental 900 and 1100°C tie-line data from the other alloys investigated in this research, however, clearly do not match the isotherms determined through diffusion couple method by Chen et al. [28], making the existence of a stable γ1 phase questionable. In fact, the phase

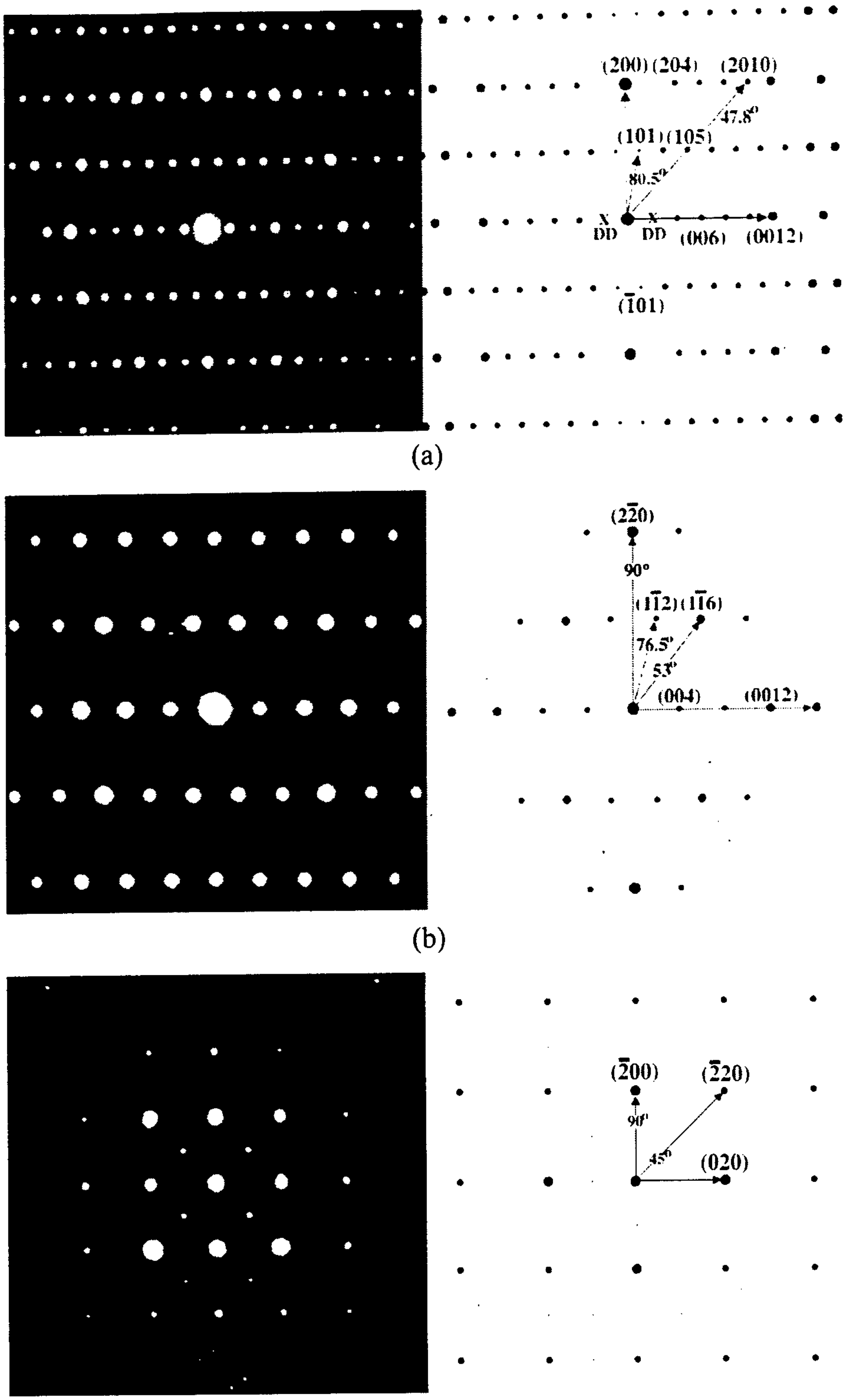

Figure 8.8 Experimental and simulated electron diffraction patterns of the new phase: (a) [010], (b) [110], and (c) [001].

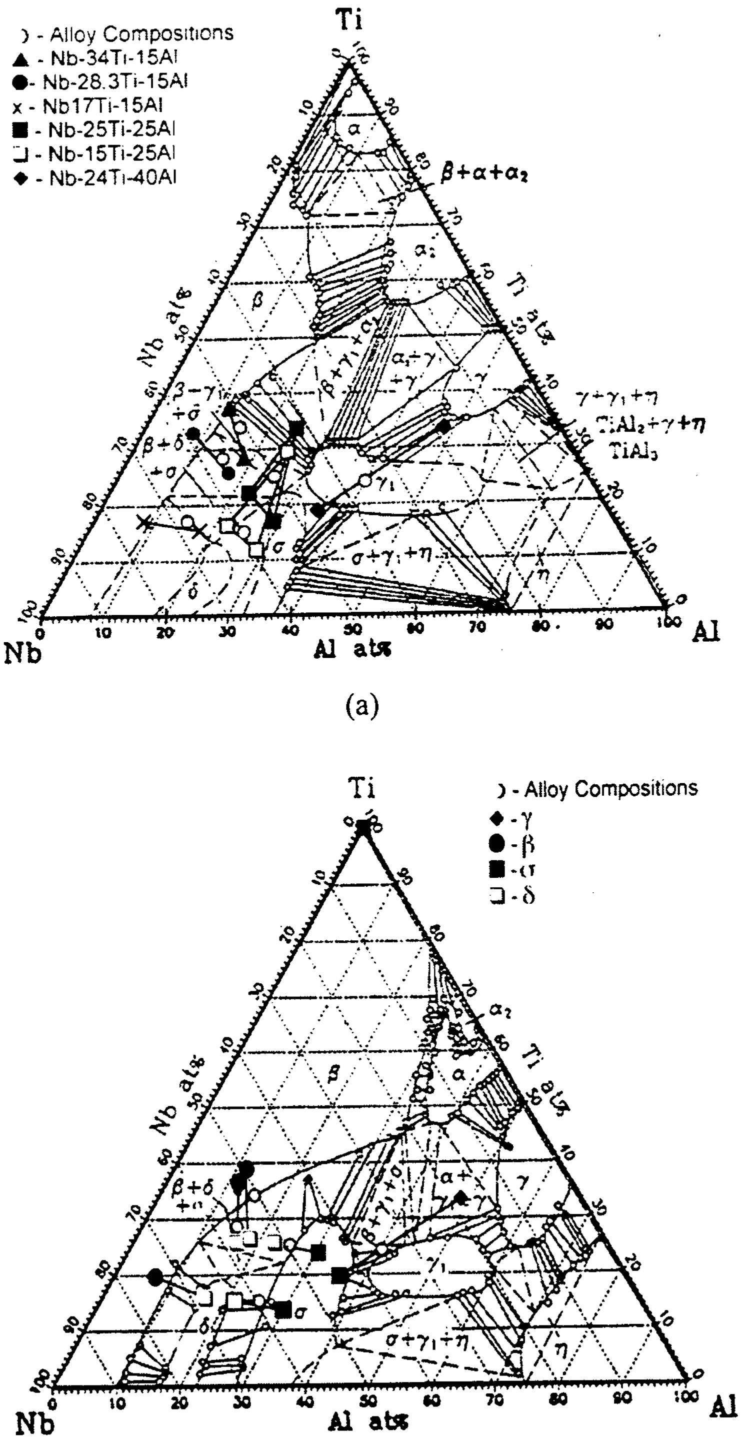

(a)

(b)

Figure 8.9 Comparison of the (a) 900, (b) 1100 and (c) 1400°C tie-line data of the Nb-rich alloys with the isothermal sections of ref. [28]. The 900°C data was plotted against the 1000°C isotherm and the 1100°C data against the 1150°C isotherm.

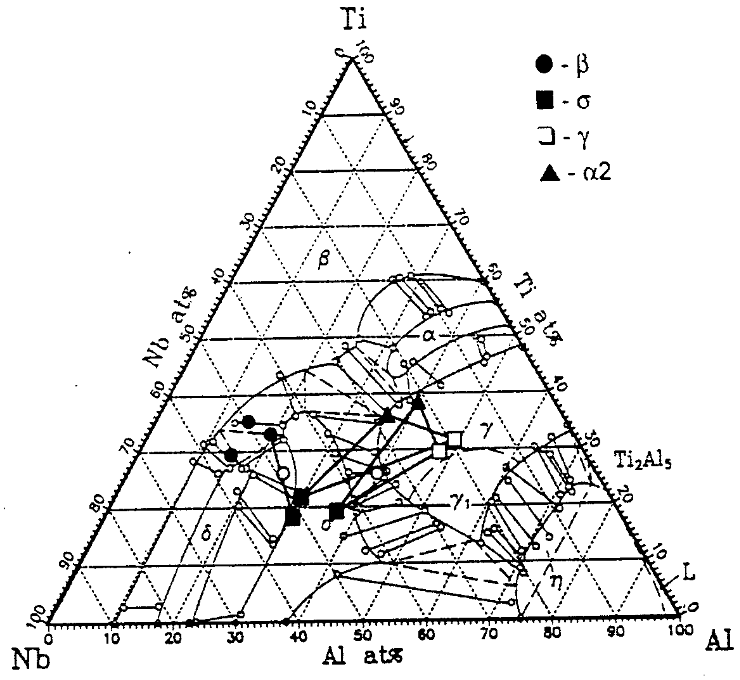

(c)

Figure 8.9 Continued.

equilibria indicated by the experimental tie-lines hardly matched the phase boundaries and phase equilibria reported. In particular, the movement of the β+δ+σ phase field toward the Nb-Al binary with decreasing temperature was clearly inconsistent with the findings of this work. In addition, when one considers the 1400°C isotherm reported (Figure 8.9(c)), more inconsistencies were apparent, since at this temperature alloys 7 and 11 were single-phase β and alloy 12 was in a two-phase β+σ phase field. Because numerous researchers have reported the γl phase [65-67] something may very well exist, however, it is more than likely a metastable formation induced through interstitial contamination [68] or possibly an incorrect determination of its structure.

While it is nearly impossible to evaluate the experimental techniques of another groups work, there appeared to be numerous inconsistencies within the reported observations of the γl phase that one must be skeptical of its occurrence [28, 65-67]. While the appearance of the θ phase within this study requires further review, there appears to be growing evidence that the phase equilibria in the Nb-Ti-Al system is much more complex at low temperature than had initially been predicted through theoretical analysis [15].

8.7 The Compositional Invariant $\beta \rightarrow \delta$ Transformation

Alloy 12 was the only material in this study to exhibit the $\beta \rightarrow \delta$ massive transformation. The transformation was most apparent within the cast material, for lack of competing phase transformations. The large colonies emanating from the β grain boundaries consisted of a lath structure growing into the β_o phase (Figure 5.9). Investigation of the β_o/δ_m interface did reveal an orientation relationship of $\beta_o(0\bar{1}1)//\delta_m(\bar{1}02)$ which was observed using the near parallel zone axis relations of $\beta_o[1\bar{1}\bar{1}]//\delta_m[100]$ and $\beta_o[100]//\delta_m[2\bar{2}1]$. Compositional differences between the two phases were not detectable. Menon et al. [10] observed a similar transformation in cast Nb-9.4Ti-16.82Al, from which they concluded that the formation of the structure was due to local Al enrichment near the β grain boundaries as a result of solute segregation from casting. The transformation was reported to have disappeared on homogenization and did not occur through subsequent thermal treatments. Although the $\beta \rightarrow \delta$ transformation had been previously observed, TEM investigations of the structures were never reported.

The $\beta \rightarrow \delta$ transformation did reoccur in alloy 12 following homogenization above the β transus. In fact, furnace cooling from the homogenization treatment had produced massive colonies along β grain boundaries that had not transformed into the δ/σ lamella from the $\beta \rightarrow \delta+\sigma$ eutectoid reaction. The $\beta \rightarrow \delta$ reaction also occurred within material air cooled from 1475°C (β phase field). The transformation was suspected within the oil quenched material from 1475°C, but due to the small volume fraction, TEM foils containing the structure could not be captured for evaluation. In all cases the δ laths exhibited the same orientation to the β_o phase, were separated by thin layers of β_o, and showed compositions that were the same as the parent phase.

While the past work of the massive transformation have invariably linked the growth of a massive phase to the advancement of an incoherent boundary [69], recent work has questioned this view [42, 43]. This is not to say, however, that all massive transformations do not occur this way [70, 71]. Low index relationships between the massive and parent phases have been observed in numerous alloy systems, such as: Ag-Al, Ti-Al, Cu-Zn, Ag-Zn, Cu-Ga, Ag-Cd [42, 43, 72-75]. A study of the nucleation rates for the β to α_m transformation in Ti-Ag and Ti-Au was performed through an incoherent nucleus model by Plichta et al. [73], from which it was determined that the predicted rate of nucleation was thousands of orders of magnitude lower than that experimentally observed; this was taken as indication that the formation of massive nuclei with partially coherent interfaces had to occur in order for detectable levels of nucleation to be observed [42, 73]. Investigation of the interface between β and massive ζ_m in Ag-26Al by Mou and Aaronson [42], revealed Burgers and near Burgers (planes or directions off by a couple of degrees) relations of $\zeta(0001)//\beta(\bar{1}10)$ and $\zeta[1\bar{2}10]//\beta[111]$ across the interface. No apparent orientation relationship was observed, however, between the ζ_m crystal and the neighboring β grain it was growing away from.

Data on previously investigated growth kinetics of massive phases form different alloy systems was analyzed by Menon et al. [76], from which they concluded that a ledge mechanism for massive growth was plausible. Growth ledges had been observed occurring along faceted massive/matrix interfaces [77, 78], but more recent work by Mou and Aaronson [42] through questionable TEM was stated to provide direct evidence confirming the presence of both interfacial structural ledges and misfit compensating ledges both at rational and irrational interfacial relationships.

While misfit compensating ledges have been observed along with rational and irrational orientation relationships between the massive and matrix phases, this does not necessarily mean that the interface is coherent or partially coherent. What is important to note is the direction of ledge growth relative to the direction of the interface (Figure 8.10). If the angle is relatively large, than the number or density of misfit compensating ledges over a given length would be high and would not be typical of a coherent interface. In addition, recent theoretical work by Dhandapani [79] had proven that incoherent nucleation of massive structures in Ti-Al was energetically favorable and that calculated nucleation rates were comparable to experimental observations. Furthermore, even if the nucleation of a massive crystal was coherent, Massalski [80] had reasoned that coherency strains would increase during growth and a coherent interface would no longer be energetically favorable. Therefore, while massive crystals may grow by means of a ledge mechanism

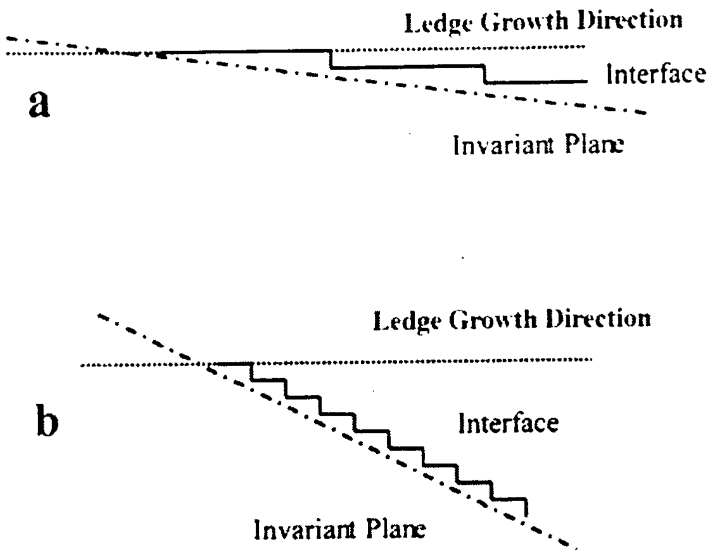

Figure 8.10 Illustration of the changes in ledge density as a function of the angle between the interface and ledge growth directions for (a) partially coherent boundary and (b) an incoherent boundary.

and show either a rational or irrational orientation relationship to the parent grain, the true spacing of the misfit compensating ledges is a determining factor between a partially coherent or incoherent boundary.

While interfacial defects were not directly observed through HREM for alloy 12, a low index orientation relationship was observed between the massive and matrix phases. The orientation between the crystallographic zones were found to be within less than 6° of each other at the outer portion of the massive colony, but within the thin β_o layer separating the δ_m laths the angle was near zero. In both cases, no measurable rotational angle was observed between the matching $\beta_o(0\bar{1}1)$ and $\delta(\bar{1}02)$ planes within the oriented zone axis. This orientation between the β_o and δ_m planes had the closest matching between the interplanar spacings of the two crystals (Table 8.1). The growth direction of the δ_m crystal within the β_o matrix was determined through trace analysis of the SAD patterns taken at the interface with that of the corresponding image corrected for rotation (Figure 8.11). It was determined that the $\beta_o[0\bar{1}1]$ vector ran nearly perpendicular to the β_o/δ_m interface, with the approximated angular difference between the vector and interface being within the statistical error of the rotation calibration. This suggests that the interface was partially coherent. however, the degree to which this is true could only be determined through HREM examination of the interfaces over a statistically significant area. The development of the δ lath structure separated by thin regions of β_o may contribute to reducing the total distance required of ledge growth within a given massive crystal compared with the distance required if the entire massive colony was one crystal. This, in turn, would allow for a reduction in the coherency strain associated with the reaction, a point that had been made by Pilchta et al. [81].

The formation of δ_m within the samples furnace cooled and air cooled from 1475°C, is not believed to have been produced by compositional changes within the β phase due to the formation of the δ/σ lamella or σ lath formations that had also occurred within the material. Composition analysis of the β and δ_m phases from the furnace cooled material, listed in Table 8.2, showed the two phases to be less than an atomic percent different in Nb, Ti and Al from each other and less than 1.5 atomic percent from the nominal alloy composition, all within or near to the estimated one atomic percent error associated with the EDS measurements based on a set standard.

Table 8.1 Measured interplanar spacings of the β_o and δ phases in as-cast alloy 12.

β_O : a_o = 3.258Å cast Nb-25Ti-25Al		δ : a_o = 5.169Å cast Nb-25Ti-25Al	
Planes	d-spacing (Å)	Planes	d-spacing (Å)
{100}	3.258	{100}	5.169
{110}	2.304	{110}	3.655
{111}	1.881	{111}	2.984
{120}	1.457	{120}	2.312
{112}	1.33	{112}	2.11
{122}	1.086	{122}	1.723

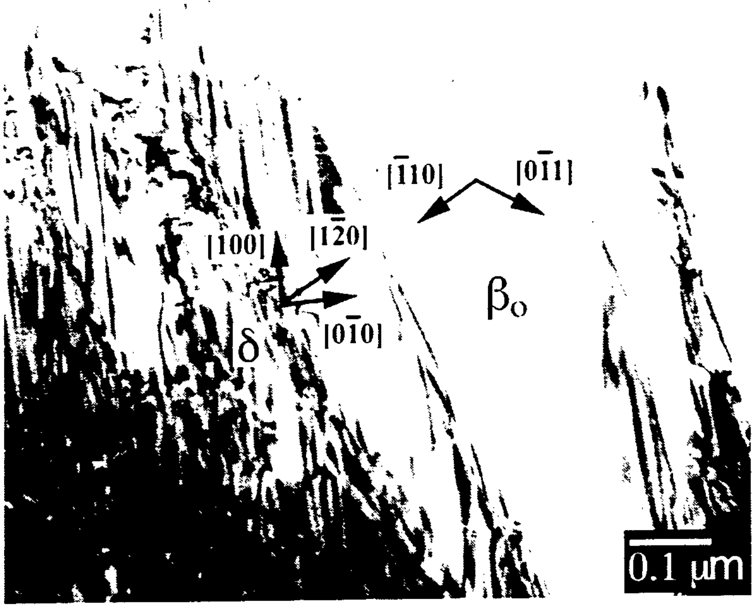

Figure 8.11 The $[01\bar{1}]$ growth direction within β_o with respect to the β_o/δ_m interface within cast alloy 12.

Table 8.2 Measured compositions (at. %) of the β_o and δ_m phases within alloy 12 furnace cooled from 1475°C.

Species	β_o	δ_m	Alloy Composition
Nb	47.16	47.99	49.57
Ti	26.18	25.25	24.80
Al	26.66	26.76	25.35

9. Conclusions

1. The fifteen Nb-rich Nb-Ti-Al alloys investigated were found to have solidified through the β phase field, extending the range of primary solidification into the ternary beyond the limits of previous liquidus projections. The presence of the high temperature β field was verified through heat treatments of each alloy. The β transus temperatures were either directly determined through DTA analysis or estimated based on results of quenching experiments.
2. The β phase could be retained upon quenching as β_o (B2) with only a small amount of ω phase formation within certain alloys. Some precipitation of σ did occur along grain boundaries in two of the 40 at.% alloys, due to quench temperatures being marginally above the β transus temperatures.
3. The β phase within the alloys was observed to have a B2 ordered structure at room temperature. The transition temperatures between the ordered and disordered structures were investigated for selected alloys.
4. The site occupancy preferences of the B2 ordered solid solution were determined within five of the alloys through the ALCHEMI technique. Ti substitution for Nb on Nb sublattice sites was observed to occur in all cases, however, the partitioning tendencies between the atomic species was determined to be dependent upon alloy composition.
5. The phase transformations and phase equilibria occurring within the alloys over their complete temperature ranges were characterized, including defect analysis and orientation relationships. Tie-line compositions defining the phase equilibrium at 1400, 1100, 900 and 700°C were plotted and compared against previous experimental and theoretical isotherms.
6. A plethel section was established for the phase equilibria between β and σ, which develops into a $\beta+\sigma\rightarrow O$ peritectoid reaction at lower temperatures. Microstructural control over alloys near this section have been investigated, in which desirable two-phase *in situ* composite structures of σ+βo have been produced. At lower temperatures, the βo phase transforms into O while the elongated σ structure remained unchanged.

7. Aging several alloys at 700°C from a single phase β structure resulted in the metastable formation of metastable O plates that restricted the precipitation and growth of the equilibrium δ or σ phases for times up to 2280 hours. The slow diffusional growth rate of the intermetallic phases at 700°C made the formation of the O plates more kinetically favorable. The O phase formation at low temperatures was avoidable in certain alloys through heat treatments at higher temperatures before aging at 700°C.

8. The β_o to O transformation kinetics at temperatures below 800°C were determined to be controlled by volume diffusion through the bulk in order to support the atomic rearrangement necessary across the interface. This required a compositional limit of Al for the formation of metastable O.

9. Two eutectoid reactions were observed in the alloys investigated. The $\beta \rightarrow \sigma + \gamma$ and $\beta \rightarrow \sigma + \delta$ reactions were observed to move to higher Ti concentrations with decreasing temperature, with the latter converging into a four-phase $\beta + \sigma + \delta + O$ plane at 980°C.

10. The βo phase within the 40 at.% Al alloys was observed to undergo ω-related transitions leading to the formation of the $P6_3/mcm$ structure. The structure was identified through X-ray diffraction and convergent beam electron diffraction as having the hP18 form, which had neither been fully identified previously in the Nb-Ti-Al system or observed within Nb-rich compositions.

11. The β phase within the 40 at.% Al alloys was also susceptible to the formation of α_2 upon quenching from the β, $\beta + \sigma$ and $\beta + \sigma + \gamma$ phase fields. The extent of the transformation and the produced microstructures were found to vary with alloy composition and cooling rate.

12. A new body centered tetragonal phase (θ) having an $I4_1/amd$ space group and lattice parameters near to $a_o = 5.10$ Å and $c_o = 28.17$ Å was observed below 1100°C within the 40 at.% Al alloys. The θ phase was observed to form in β solutionized materials, material oil quenched from elevated temperatures and after initial aging treatments above its suspected temperature limit.

13. The γ1 phase that had been observed by numerous investigators was not detected within this

study. Although the composition range of the γ1 phase was near that determined for the θ phase, to two structures were not the same.

14. A massive β→δ transformation present within cast Nb-25Ti-25Al was reproduced in both furnace and air cooled samples from 1475°C, following homogenization treatments. The massive colonies consisted of groups of laths separated by thin layers of the parent β phase. A rational orientation relationship of $\beta o[100] // \delta[2\bar{2}1]$, $\beta_o(011) // \delta(\bar{1}02)$ was observed across the interface.

10. REFERENCES

1. D. M. Dimiduk, P. R. Subramanian and M. G. Mendiratta, *Acta Met.*, **8**, p.519 (1995).
2. R. L. Fleischer and A. I. Taub, *JOM*, p. 8, Sept. (1989).
3. D. Banerjee, T. K. Nandy, A. K. Gogia and K. Muraleedharan, Microstructure and Phase Relations in the Ti_3Al-Nb Section, *Sixth World Conference on Titanium*, France (1988).
4. M. J. Kaufman, T. F. Broderick, C. H. Ward, J. K. Kim, R. G. Rowe and F. H. Froes, *Sixth World Conference on Titanium*, France (1988).
5. J. Muraleedharan, T. K. Nandy, D. Banerjee and S. Lele, *Met. Trans. A*, **23**, p. 417 (1992).
6. L. A. Bendersky and W. J. Boettinger, *Acta. Met. Mater.*, **42**, 7, p. 2337 (1994).
7. D. Banerjee, *Prog. in Mat. Sci.*, **42**, p. 135 (1997).
8. E. S. K. Menon, P. R. Subramanian and D. M. Dimiduk, *Scripta Met. et Mat.*, **27**, p. 265 (1992).
9. D.-H. Hou, S. S. Yang, J. Shyue and H. L. Fraser, *Mat. Res. Soc. Symp. Proc.*, **322**, MRS, Pittsburgh PA, p. 437 (1994).
10. E. S. K. Menon, P. R. Subramanian and D. M. Dimiduk, *Met. and Mat. Trans. A*, **27**, p. 1647 (1996).
11. T. N. Marieb, A. D. Kaiser and S. R. Nutt, *Mat. Res. Soc. Symp. Proc.*, **213**, MRS, Pittsburgh PA, p. 329 (1991).
12. S. Yang and V. K. Vasudevan, *Scripta Met. et Mat.*, **31**, 7, p. 879 (1994).
13. S. Dymek, M. Dollar and K. J. Leonard, *Mat. Sci. and Eng. A*, **239**, pp. 507 (1997).
14. F. Ye, C. Mercer and W. O. Soboyejo, *Met. Trans. A*, **29**, p. 2361 (1998).
15. U. R. Kattner and W. J. Boettinger, *Mat. Sci. and Eng. A*, **152**, p. 9 (1992).
16. S. Gama, Aluminum-Niobium-Titanium, *Ternary Alloys*, G. Petzow and G. Effenberg eds., **7**, p. 382 (1993).

17. D. T. Hoelzer and F. Ebrahimi, *Mat. Res. Soc. Symp. Proc.*, **194**, MRS, p. 393 (1990).

18. F. Ebrahimi and B. J. G. DeAragao, *Mat. Res. Soc. Proc.*, **364**, MRS, Pittsburgh PA, p.1247 (1995).

19. C. R. Feng and D. J. Michel, *Met. Sci. and Eng. A*, **152**, 6, p. 1409 (1992).

20. J. H. Perepezko, Y. A. Chang, L. E. Seitzman, J. C. Lin, N, R. Bonda, T. J. Jewett and J. C. Mishurda, *High Temperature Aluminides and Intermetallics*, Proc. Symp. Indianapolis, Ind., S. H. Whang et. Al. eds., TMS-AIME, Warrendale PA, p. 19 (1990).

21. J. H. Perepezko, T. J. Jewett, S. Das and J. C. Mishurda, *3rd International SAMPE Metals Conference*, Oct.20, p. M357-M365 (1992).

22. A. Zdziobek, M. Durand-Charre, J. Driole and F. Durand, *Z. Metallkund.*, **86**, 5, p. 334 (1995).

23. K. J. Leonard, J. C. Mishurda and V. K. Vasudevan, *Met. and Mat. Trans.*, in print (2000).

24. B. F. Burton, J. A. Eades, J. W. Steeds and G. M. Rackhaus, *Phil. Trans. Roy. Soc.*, **281A**, p. 171 (1976).

25. *International Tables for Crystallography*, Volume A, Space-Group Symmetery, T. Hahn ed., Reidel Publishing Company, Boston (1987).

26. K. J. Leonard, *Phase Equilibria and Solid-State Transformations in Nb-rich Nb-Ti-Al Intermetallic Alloys,* Ph.D. Thesis, University of Cincinnati, Cincinnati OH, (1999).

27. T. Nakano, A. Nefishi, K. Hayashi and Y. Umakoshi, *Acta Mater.*, **47**, 4, p. 1091 (1999).

28. G. L. Chen, X. T. Wang, K. Q. Ni, S. M. Hao, J. X. Cao, J. J. Ding and X. Zhang, *Intermetallics*, 4, p. 13 (1996).

29. M. DeGraef and B. Molloseau, *Personal Communication* (1999).

30. K. Li, T. M. Pollock, A. W. Thompson and M. DeGraef, *Scripta Metall. Mater.*, 32, p. 1009 (1995).

31. X. Pierron, M. De Graef and A. W. Thompson, *Phil. Mag. A.*, **77**, p. 1399 (1998).

32. R. Tewari, P. Mukhopadhyay, S. Banerjee and L. A. Bendersky, *Acta Mater.*, **47**, p. 1307 (1999).

33. G. Shao, E. Passa, P. Tsakiropoulos, A. P. Miodownik, D. N. Manh, and D. G. Pettifor, in Structural Intermetallics, ed M. V. Nathal et al., TMS, Warrendale, OH p. 825 (1997).

34. L. A. Bendersky, B. P. Burton, W. J. Boettinger and F. S. Biancaniello, *Scripta Met. et Mat.*, **24**, p. 1541 (1990).

35. L. A. Bendersky, W. J. Boettinger B. P. Burton, and F. S. Biancaniello, *Acta. Metall. Mater.*, **38**, 6, p. 931 (1990).

36. L. A. Bendersky, W. J. Boettinger and F. S. Biancaniello, *Mat. Sci. and Eng.*, **A152**, p. 41 (1992).

37. J. L. Jorda, R. Flukiger and J. Muller, *Journal of the Less-Common Metals*, **75**, p. 227 (1980).

38. B. Mozer, L. A. Bendersky and W. J. Boettinger, *Scripta Met. et Mat.*, **24**, p. 2363 (1990).

39. G. Narayanan, *Microstructural Evolution and Sequence of Transformation in a 37Nb-37Ti-26Al Intermetallic Alloy*, M. S. Thesis, University of Cincinnati, Cincinnati OH, (1997).

40. K. Muraleedharan, T. K. Nandy, D. Banerjee and S. Lele, *Intermetallics*, 3, p. 87 (1995).

41. C. E. Lundin and A. S. Yamaoto, *Trans. of the Metall. Soc. of AIME*, **236**, p. 863 (1966).

42. Y. Mou and H. I. Aaronson, *Acta Metall. Mater.*, **42**, 6, p. 2159 (1994).

43. J. F. Nie, B. C. Muddle, T. Furuhara and H. I. Aaronson, *Scripta Mat.*, **39**, 4, p. 637 (1998).

44. K. S. Jepson, A. R. G. Brown and J. A. Gray, *The Science, Technology and Application of Titanium*, Ed. R. I. Jaffee and N. E. Promisel, p. 677 (1970).

45. M. E. Brown, *Introduction to Thermal Analysis Techniques and Applications*, Chapman and Hall, (1988).

46. G. Gyulai and E. J. Greenhow, *Non-Isothermal Thermal Analysis: A Critical Examination of Some Recent Theories*, **21**, p. 131 (1974).

47. R. C. Mackenzie, *Differential Thermal Analysis, Applications*, **2**, Academic Press, (1972).

48. J. D. Verhoeven, *Fundamentals of Physical Metallurgy*, John Wiley & Sons, 1975.

49. P. Shewmon, *Diffusion in Solids*, 2nd Ed., TMS, (1989).

50. K. D. Jones, M. R. Jackson, M. Larsen, E. L. Hall and D. A. Woodford, in *Refractory Metals: Extraction, Processing and Applications*, eds. K. C. Liddell et. al., TMS, Warrendale PA, p. 321 (1990).

51. D. B. Wiliams and C. B. Carter, *Transmission Electron Microscopy*, Plenum Press, New York, NY, (1996).

52. K. Kaltenbach, S. Gama, D. G. Pinatti, K Schulze and E. Henig, *Z. Metallkd.*, **80**, p. 535 (1989).

53. D. Banerjee, T. K. Nandy and A. K. Gogia, *Scripta Met.*, **21**, p. 597 (1987).

54. D. H. Hou and H. L. Fraser, *Scripta Met.*, **36**, 6, p. 617 (1997).

55. B. S. Majumdar, C. Boehlert, A. K. Rai and D. B. Miracle, *Mat. Res. Soc. Symp. Proc.*, **364**, MRS, Pittsburgh PA, p. 1259 (1995).

56. A. K. Singh and D. Banerjee, *Met. Trans. A*, **28**, 9, p. 1735 (1997).

57. A. K. Singh and D. Banerjee, *Met. Trans. A*, **28**, 9, p. 1745 (1997).

58. K. J. Leonard, J. C. Mishurda, M. DeGraef and V. K. Vasudevan, to be published.

59. C. G. Rhodes, J. A. Graves, P. R. Smith and M. R. James,in *Structural Intermetallics*, eds. R. Darolia et al., TMS, Warrendale PA, p. 45 (1993).

60. P. Villars and L. D. Calvert, *Pearson's Handbook of Crystallographic Data For Intermetallic Phases*, ASM, Metals Park, OH (1985).

61. A. Loiseau, A. Lasalmonie, G. Van Tedeloo, J. Van Landuyt and S. Amelinckx, *Acta Cryst. B*, **41**, p. 411 (1985).

62. A. Loiseau, R. Portier, G. Van Tendeloo and F. Ducastelle, *Inst. Phys. Conf. Ser.*, 78, chapter 9, p. 351 (1985).

63. R. Miida, M. Kasahara and D. Watanabe, *Japanese Journ. of Appl. Phys.*, **19**, 11, p. L707 (1980).

64. L. Potez, A. Loiseau, S. Naka and G. Lapasset, *J. Mater. Res.*, **7**, 4, p. 876 (1992).

65. A. Hellwig, M. Palm and G. Inden, *Intermetallics*, 6, p. 79 (1998).

65. I. A. Popov and V. I. Rabezova, *Russian Journal of Inorganic Chemistry*, 7, 2, p. 222 (1962).

66. T. T. Nartova and G. G. Sopochkin, *Izv. Akad. nauk SSR, Otd. Tekhn. Nauk Met.*, **2**, p. 221 (1970).

67. A. M. Zakharov, G. V. Karsanov and L. L. Vergasova, *Russian Metall.*, **1**, p. 199 (1984).

68. T. J. Jewett, *Intermetallics*, 5, p. 157 (1997).

69. T. B. Massalski, in *Phase Transformations*, ASM, Metals Park, OH p. 433 (1968).

70. A. Akhtar, *Metall. Trans. A*, **7**, p. 1735 (1976).

71. J. C. Caretti, J. E. Kittl and H. R. Bertorello, *Acta Metall.*, **31**, 2, p. 317 (1983).

72. J. D. Ayers, *Acta Metall.*, **28**, p. 1513 (1980).

73. M. R. Plichta and H. I. Aaronson, *Acta Metall.*, **28**, p. 1041 (1980).

74. M. R. Plichta, J. H. Perepezko, H. I. Aaronson and W. F. Lange III, *Acta Metall.*, **28**, p. 1031 (1980).

75. J. D. Ayers, P. G. Moore and R. A. Masumura, *Acta Metall.*, **36**, 8, p. 2349 (1988).

76. E. S. K. Menon, M. R. Plichta and H. I. Aaronson, *Acta Metall.*, **36**, 2, p. 321 (1988).

77. J. E. Kittl, H. Serebrinski and M. P. Gomez, *Acta Metall.*, **15**, p. 1703 (1967).

78. G. Baro, H. Gleiter, J. H. Perepezko and T. B. Massalski, *Mater. Sci. Eng.*, **22**, p. 171 (1976).

79. V. Dhandapani, Kinetics, *Thermodynamics and Nucleation of the* α-γ_m *Massive Transformation in Ti-Al Alloys*, Ph.D. Thesis, University of Cincinnati, Cincinnati, OH (1998).

80. T. B. Massalski, *Acta Metall.*, **6**, p. 243 (1958).

81. M. R. Plichta, W. A. T. Clark and H. I. Aaronson, *Met. Trans. A*, **15**, p. 427 (1984).

11. Conference Presentations

1. "Site Occupancy Preferences in the B2 Ordered Solid Solution Phase of Nb-rich Nb-Ti-Al Alloys", K. J. Leonard and V. K. Vasudevan, *5th International Conference on Structural and Functional Intermetallics*, TMS, Vancouver, British Columbia, July (2000).

2. "Phase Equlibria at 1100°C in the Nb-Ti-Al System", K. J. Leonard and V. K. Vasudevan, *5th International Conference on Structural and Functional Intermetallics*, TMS, Vancouver, British Columbia, July (2000).

3. "The Observation of a New Tetragonal Phase in the Nb-Ti-Al System", K. J. Leonard and V. K. Vasudevan, *5th International Conference on Structural and Functional Intermetallics*, TMS, Vancouver, British Columbia, July (2000).

4. "Phase Transformaitons in Nb-Rich Nb-Ti-Al Alloys," K. J. Leonard and V. K. Vasudevan, *R. W. Cahn Symposium on Intermetallics for the Third Millenium*, ASMI/TMS, Cincinnati, OH, Oct./Nov. (1999).

5. "The Use of Phase Equilibria in Microstructural Control of $\sigma+\gamma$ and $\beta+\sigma$ Alloys in the Nb-Ti-Al System," J. C. Mishurda and V. K. Vasudevan, *Symposium on Refractory Metals and Alloys*, ASMI/TMS, Cincinnati, OH, Oct./Nov. (1999).

6. "A Study of Phase Equilibria and Transformations in the Nb-Ti-Al System," *AFOSR Metallic Materials Contractors' Meeting, Materials Workshop,* San Diego, CA, Mar. 4-5 (1999).

7. "Solidification Pathways and Solid State Transformations in Nb-Ti-Al Alloys," K. J. Leonard and V. K. Vasudevan, *Symposium on New and Emerging Applications for Refractory Metals and Materials*, TMS, Rosemont, IL, Oct. (1998).

8. "Decomposition of the β Phase in a Nb-25Ti-25Al Alloy," K. J. Leonard and V. K. Vasudevan, *Symposium on New and Emerging Applications for Refractory Metals and Materials*, TMS, Rosemont, IL, Oct. (1998).

9. "A Study of Phase Equilibria and Transformations in the Nb-Ti-Al System," J. C. Mishurda and V. K. Vasudevan, *Symposium on New and Emerging Applications for Refractory Metals and Materials*, TMS, Rosemont, IL, Oct. (1998).

10. “Phase Equilibria and Transformations in the Nb-Ti-Al System.” *High Temperature Materials Workshop, Wright Laboratories, Materials Directorate, WPAFB*. Dayton, OH. Oct. 15-16 (1997).

11. “A Study of Phase Equilibria and Transformations in the Nb-Ti-Al and TiAl Systems.” *AFOSR Metallic Materials Contractors' Meeting, Materials Workshop*, Bar Harbor, ME. Aug 19-21 (1996).

12. Publications

1. “Examination of Solidification Pathways and the Liquidus Surface in the Nb-Ti-Al System.” K. J. Leonard, J. C. Mishurda and V. K. Vasudevan, *Metall. Mater. Trans.*, in press (2000).

2. “Phase Equilibria and Solid-State Transformations in Nb-Rich Nb-Ti-Al Intermetallic Alloys.” K. J. Leonard and V. K. Vasudevan, *Intermetallics*, in press (2000).

3. “Identification of a New Tetragonal Phase in the Nb-Ti-Al System,” K. J. Leonard, J. C. Mishurda, B. Molloseau, M. de Graef and V. K. Vasudevan,” *Phil. Mag. Lett.* , **80(5)**, pp. 295-305 (2000).

4. “Decomposition of the β_o Phase to the ω-related hP18 Structure in Nb-Ti-40Al Alloys,” K. J. Leonard, J. C. Mishurda and V. K. Vasudevan,” *Phil. Mag. Lett.* (2000).

5. “A Study of Phase Equilibria and Transformations in the Nb-Ti-Al System,” J. C. Mishurda and V. K. Vasudevan, *Intern. J. of Refractory Alloys and Hard Compounds* , under review, (1999).

6. “The Use of Phase Equilibria in Microstructural Control of $\sigma+\gamma$ and $\beta+\sigma$ Alloys in the Nb-Ti-Al System,” J. C. Mishurda and V. K. Vasudevanys,” *Intern. J. of Refractory Alloys and Hard Compounds* , under review, (2000).

7. “Phase Equilibria at 1100°C in the nb-Ti-Al System”, K. J. Leonard, J. C. Mishurda and V. K. Vasudevan, *Mater. Sic. & Eng.*, in preparation.

8. “Site Occupancy in the β_o/B2 Phase in Nb-Ti-Al Alloys,” K. J. Leonard, N. Giridhar and V. K.

Vasudevan, *Phil. Mag Lett.*, in preparation.

9. "Phase Equilbria and Transformations in the Nb-Ti-Al System: β+σ Alloys," J. C. Mishurda and V. K. Vasudevan, *Metall. Mater. Trans.*, in preparation.

10. "Phase Equilbria and Transformations in the Nb-Ti-Al System: σ+γ Alloys," J. C. Mishurda and V. K. Vasudevan, *Metall. Mater. Trans.*, in preparation.

11. "Phase Equilbria and Transformations in the Nb-Ti-Al System: σ+δ Alloys," J. C. Mishurda, K. J. Leonard and V. K. Vasudevan, *Metall. Mater. Trans.*, in preparation.

12. "Phase Transformations in a Nb-25Ti-25Al Alloy," K. J. Leonard and V. K. Vasudevan, *Acta Mater.*, in preparation.

13. "Phase Transformations in a Nb-24Ti-40Al Alloy," K. J. Leonard and V. K. Vasudevan, *Acta Mater.*, in preparation.